MONASH University

RAFT-Mediated Polymerisation-Induced Self-Assembly: New Initiation Method and Morphologies

Jing Wan

Master of Eng. Sci. Chemical and Biochemical Engineering

The University of Western Ontario, Canada

A thesis submitted for the degree of *Doctor of Philosophy* at

Monash University in 2022

School of Chemistry

Copyright notice

Table of Contents

v

Abstract

Polymeric nano-objects with a diverse range of morphologies attracted extensive research attention in areas such as biomedicine, catalysis and coating, etc. The traditional method to prepare block copolymer amphiphilic nano-objects is solution self-assembly, which suffers multi-step synthesis and purification, and low solid contents. Polymerisation-induced self-assembly (PISA) provides an efficient strategy that allows *in situ* polymerisation and simultaneous self-assembly of amphiphilic block copolymers at high solid contents. The realisation of PISA is based on reversible deactivation radical polymerisation (RDRP) techniques, among which reversible addition-fragmentation transfer (RAFT) polymerisation is the most powerful and studied technique for PISA. Since the advent of PISA, increasing research interest has been input into this area, various morphologies including spheres, worm-like micelles, vesicles, lamellae and even higher-order complex structures were achieved using a broad range of monomers and solvents. As an emerging and burgeoning research field, PISA requires more attention to complete the puzzle pieces and explore its potential. In this thesis, several new aspects of PISA have been investigated; we used ultrasound as a new initiation method for PISA to prepare nano-objects, as well as hybrid nanoparticles with catalytic properties; meanwhile, rarely achieved "colloidal molecules" were synthesised using thermal-PISA and hierarchical self-assembly. This thesis consists of six chapters:

Chapter 1 gives a general introduction of RAFT polymerisation, PISA and sonochemistry in polymerisation.

Chapter 2 provides a detailed review on recent advances of PISA in several emerging aspects.

In Chapter 3, we demonstrated for the first time that ultrasound-initiation RAFT-mediated PISA (sono-RAFT-PISA) can be implemented at room temperature and produce nano-objects in different morphologies including spheres, short worms and uniform vesicles. The nano-objects prepared with sono-RAFT-PISA and traditional thermal-PISA were compared. The influence of ultrasound on the morphology of nano-objects was also outlined. The room-temperature process without external initiator compounds endows with the "green" feature that could open up many new prospects for the field of polymeric nano-objects synthesis.

In Chapter 4, we further extended the versatility of ultrasound. It was used for generating hydroxyl radicals to initiate sono-PISA, as well as generating reducing species that allows *in situ* formation of gold and palladium nanoparticles. This allows us to produce nanocomposites of polymeric colloids immobilised with metal nanoparticles using sono-PISA without any external initiator or reducing agent. The synthesised hybrid nanocomposites also showed plasmonic and catalytic properties.

Chapter 5 demonstrates our exploration in achieving nano-objects with new morphologies by PISA. We exploited the "host-guest" complexation between β-cyclodextrin and certain functional groups to transfer water-immiscible monomer into water-soluble complexes, which overcomes the kinetic trapping of morphology. Using this strategy, we conducted a sequential one-pot process to synthesise linear triblock terpolymers and achieved "colloidal molecules", core-shell-corona micelles, and raspberry-like nanoparticles. In addition, the particle formation mechanism driven by minimisation of interfacial energy was summarised, which provides a guideline for the rational design of linear triblock terpolymer nanoparticles.

Chapter 6 summarises the overall conclusions of each chapter and give recommendations for future investigations.

Declaration

This thesis is an original work of my research and contains no material which has been accepted for the award of any other degree or diploma at any university or equivalent institution and that, to the best of my knowledge and belief, this thesis contains no material previously published or written by another person, except where due reference is made in the text of the thesis.

Signature: ……………………

Print Name: …JING WAN……….

Date: ……20/04/2022………….

Publications during enrolment

1. **Wan, J.**; Fan, B.; Putera, K.; Kim, J.; Holl, M.; Thang, S.; *"Polymerization-Induced Hierarchical Self-Assembly: From Monomer to Complex Colloidal Molecules and Beyond"* **ACS Nano.** *2021*, 15, 13721-13731.

2. **Wan, J.**; Fan, B.; Thang, S.; *"Sonochemical Preparation of Polymer-Metal Nanocomposites with Catalytic and Plasmonic Properties"* **Nanoscale Adv.** *2021*, 3, 3306-3315.

3. **Wan, J.**; Fan, B.; Liu, Y.; Hsia, T.; Qin, K.; Junkers, T.; Teo, B. M.; Thang, S.; *"Room temperature synthesis of block copolymer nano-objects with different morphologies via ultrasound initiated RAFT polymerization-induced self-assembly (sono-RAFT-PISA)"*, **Polym. Chem.** *2020*, 11, 3564-3572.

4. Fan, B.; **Wan, J.**; Zhai. J.; Chen, X.; Thang, S.; *"Triggered degradable colloidal particles with ordered inverse bicontinuous cubic and hexagonal mesophases"* **ACS Nano** *2021*, *15, 4688-4698.*

5. Fan, B.; **Wan, J.**; Liu, Y.; Thang, S.; *"Functionalization of liquid metal nanoparticles by surface-initiated RAFT polymerization"* **Polym. Chem.** *2021*, 12, 3015-3025.

6. Hsia, T.; **Wan, J.**; Fan, B.; Thang, S.; *"Bifunctional RAFT agent directed preparation of polymer/graphene oxide composites"* **Macromol. Rapid Commun.** *2021,* 42, 2100460.

7. Fan, B.; **Wan, J.**; McKay, A.; Qu, Z.; Thang, S.; *"Facile synthesis of well-controlled poly(1-vinyl imidazole) by the RAFT process"* **Polym. Chem.** *2020*, 11, 5649-5658.

8. Fan, B.; Liu, Y.; **Wan, J.**; Crawford, S.; Thang, S.; *"Polymerization-Induced Self-Assembly (PISA) and "Host–Guest" Complexation-Directed Polymer/Gold Nanocomposites"*, **ACS Mater. Lett.** *2020*, 2, 492-498.

Acknowledgements

Foremost, I would like to give my sincere gratitude to my supervisor Prof San H. Thang AC. I thank him for accepting me as a member of this caring, mutually helping and creative research group. More importantly, I wish to acknowledge Prof San H. Thang AC for his guidance and encouragement along the way, without whom this thesis would not be achievable.

My thanks would also go to all the previous and present members of the Thang group. Thank you all for your generous sharing of information and suggestions. You leave me with lots of unforgettable memories during the past several years.

Many thanks to my co-supervisor Prof Tanja Junkers and Dr Boon Mian Teo for their valuable suggestions. Thank you to my advisory panel members A/Prof Rico Tabor and Dr Toby Bell for their time reading my milestone reports and giving advice. I would also like to thank my thesis examiners, Prof Atsushi Goto and Prof Suzie Hwang Pun taking time to read my thesis. Many thanks to all the faculty and staff in the School of Chemistry and Monash Centre of Electron Microscopy for their support in my research.

I would like to thank Monash University and Monash Graduate Research Office for providing me MITS, MGS and PPA scholarships.

Furthermore, I would like to express heartfelt appreciation to my husband Dr Bo Fan, who is also a trustworthy colleague, a role model and my best friend, for always being patient and supportive. Thank you for being candid in pointing out problems in my research, while not being stingy with compliments in our life. A shout-out goes out to my cats, Plato and Peppercorn, for being the sweetest company while I type these words.

Last but not the least, I would like to extend my deepest thanks to my parents for their unconditional love and support, and for encouraging me to keep moving forward in whatever I do.

Thank you everyone who has supported me along this meaningful journey!

List of Abbreviations

4-ATP	4-Aminothiophenol
4VP	4-Vinylpyridine
AA	Acrylic acid
AAm	Acrylamide
ACVA	4,4'-azobis(4-cyanopentanoic acid)
AFM	Atomic force microscopy
AFN-IR	Atomic force microscopy-infrared spectroscopy
AIBN	Azobis(isobutyronitrile)
AIPD	2,2'-Azobis[2-(2-imidazolin-2-yl)propane]dihydrochloride
AM	Acrylamide
AN	Acrylonitrile
ATRP	Atom transfer radical polymerisation
Au	Gold
AuNPs	Gold nanoparticles
BMA	n-Butyl methacrylate
BzMA	Benzyl methacrylate
CA	Colloidal atom
CCL	Core cross-linking
CD	Cyclodextrin
CDCl$_3$	Deuterated chloroform
CDPA	4-Cyano-4 (((dodecylthio) carbonothioyl) thio) pentanoic acid
CDTPA	4-Cyano-4 (((dodecylthio) carbonothioyl) thio) pentanoic acid
CM	Colloidal molecule
cryo-TEM	Cryogenic transmission electron microscopy
CTA	Chain transfer agent
Đ	Dispersity (molecular weight distribution)
DAAM	Diacetone acrylamide
DIC	Diisopropyl carbodiimide
DLS	Dynamic light scattering
DMA	N,N-Dimethylacrylamide
DMAEMA	2-(Dimethylamino)ethyl methacrylate
DMAP	Dimethylaminopyridine
DMF	N,N-Dimethylformamide
DMSO	Dimethyl sulfoxide
DOX	Doxorubicin
DP	Degree of polymerisation
EMS	Poly(ethylene glycol)-b-poly($tert$-butyl methacrylate)-b-polystyrene
EST	Poly(ethylene glycol)-b-polystyrene-b-poly($tert$-butyl acrylate)
ETS	Poly(ethylene glycol)-b-poly($tert$-butyl acrylate)-b-polystyrene
FFT	Fast Fourier transformation

GMA	Glycerol monomethacrylate
GOx	Glucose oxidase
GPC	Gel permeation chromatography
HAADF	High-angle annular dark-field imaging
HPMA	2-Hydroxypropyl methacrylate
HPMAm	*N*-(2-Hydroxypropyl) methacrylamide
HRTEM	High resolution transmission electron microscopy
hr	Hour
Hz	Hertz
LAM	Less activated monomer
LC	Liquid crystalline
LCST	Lower critical solution temperature
LED	Light-emitting diodes
MA	Methyl acrylate
MAA	Methacrylic acid
MAM	More activated monomer
MBA	*N,N'*-Methylenebisacrylamide
MMA	Methyl methacrylate
M_n	Number-average molecular weight
M_w	Weight-averaged molecular weight
MβCD	Methylated-β-cyclodextrin
*n*BA	*n*-Butyl acrylate
NIPAM	*N*-Isopropylacrylamide
NIR	Near-infrared
NMP	Nitroxide mediated polymerisation
NMR	Nuclear magnetic resonance spectroscopy
NTU	Nephelometric turbidity unit
OEGMA	Oligo(ethylene glycol) methyl ether methacrylate
P	Packing parameter
Pd	Palladium
PDI	Polydispersity index
PdNPs	Palladium nanoparticles
PEG	Polyethylene glycol
PET	Photo-induced electron transfer
PFS	2,3,4,5,6-Pentafluorostyrene
PISA	Polymerisation-induced self-assembly
ppm	Part per million
PS	Polystyrene
PVP	Poly(*N*-vinylpyrrolidone)
RAFT	Reversible addition-fragmentation chain transfer
RDRP	Reversible deactivation radical polymerisation
ROMP	Ring-opening metathesis polymerisation
ROS	Reactive oxygen species
SAED	Selected area electron diffraction

SAXS	Small-angle X-ray scattering
SEM	Scanning electron microscopy
SERS	Surface-enhanced Raman spectroscopy
SPR	Surface plasmon resonance
St	Styrene
STEM	Scanning transmission electron microscopy
TA	Tertiary amine
TBA	4-(4,4,5,5-Tetramethyl-1,3,2-dioxaborolan-2-yl)benzyl acrylate
*t*BA	*tert*-Butyl acrylate
*t*BMA	*tert*-Butyl methacrylate
TEM	Transmission electron microscopy
T_g	Glass transition temperature
TGA	Thermogravimetry
THF	Tetrahydrofuran
TOF	Turnover frequency
TTC	Trithiocarbonate
UA	Uranyl acetate
UCST	Upper critical solution temperature
UV	Ultraviolet
UV-Vis	Ultraviolet-Visible
VA-044	2,2'-Azobis[2-(2-imidazolin-2-yl)propane]dihydrochloride
β-CD	β-Cyclodextrin
λ	Wavelength

Chapter 1

Introduction

1.1 RAFT Polymerisation

Since its first report in 1998, the *reversible addition–fragmentation chain transfer* (RAFT) process has revolutionised the field of free radical polymerisation. It was invented in 1998 by the Commonwealth Scientific and Industrial Research Organisation (CSIRO) in Melbourne Australia, by a team led by Graeme Moad, Ezio Rizzardo and San H. Thang.[1, 2] Almost simultaneously, a group of French researchers patented a technique called *macromolecular design via the interchange of xanthates* (MADIX),[3] which proceeds in the same mechanism as the CSIRO-reported RAFT process but uses xanthates as regulating agents. RAFT is a reversible deactivation radical polymerisation (RDRP),[4] also known as living/controlled radical polymerisation, which enables the synthesis of polymer and copolymer with predictable molecular weight, low molar mass dispersity ($Đ$), high end-group fidelity, and capacity for continued chain growth.[5] Other widely applied RDRP techniques include nitroxide-mediated polymerisation (NMP)[6] and atom transfer radical polymerisation (ATRP)[7]. Over the past 24 years, more than 10,000 publications have been published on RAFT polymerisation (Figure 1.1), initially focusing on the elucidation of the mechanism and the process in homogenous and heterogeneous systems, then the demonstration of the myriad of polymeric architectures and functional materials, and recently more application-driven reports. This shows that RAFT is recognised as a widely applied technique in the areas include material science and technology.
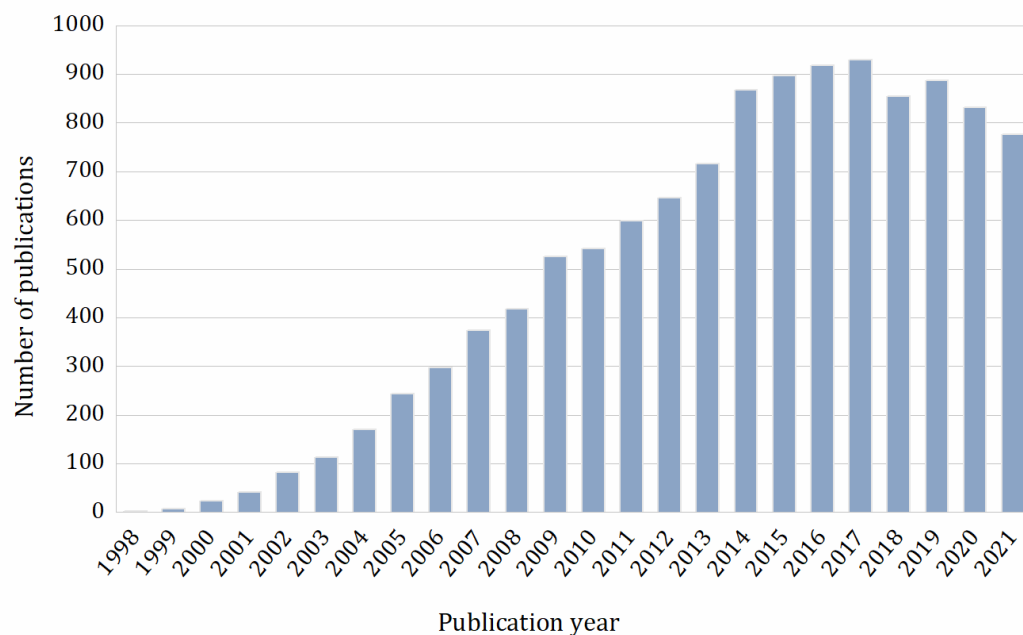
Figure 1.1 Publications per year on "RAFT polymerization" and "reversible addition–fragmentation chain transfer polymerization" (source Web of Science, February 2022).

1.1.1 Mechanism of RAFT

The mechanism of RAFT is depicted in Figure 1.2. The initiation process (step I) is activated by the radical source to generate propagating radical ($P_n{}^{\bullet}$). In the following step (II), addition of a propagating radical to the thiocarbonylthio RAFT agent **1** followed by fragmentation of the intermediate radical gives rise to a polymeric thiocarbonylthio compound [$P_nS(Z)C=S$, **3**] and a new radical ($R^{\bullet}$). Then (step III) a new propagating radical ($P_m{}^{\bullet}$) is formed by the reaction between $R^{\bullet}$ and monomer. Step IV shows the rapid equilibrium between the active propagating radicals ($P_n{}^{\bullet}$ and $P_m{}^{\bullet}$) and the dormant compound **3**, which is the key step of RAFT process. The rate of addition/fragmentation equilibrium is higher than that of the propagation, so there should be less than one monomer unit added per activation cycle; therefore, it provides equal probability for all chains to grow, and allows for the production of polymer with narrow dispersity (*Đ*). Chains undergo bi-radical termination form dead chains that cannot react further; nevertheless, this step is supressed in an ideal RAFT process.

I. Initiation

II. Reversible chain transfer/propagation

III. Reinitiation

IV. Chain equilibration/propagation

V. Termination

Figure 1.2 Mechanism of RAFT polymerisation.
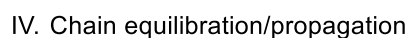
In an ideal living polymerisation, all chains survive and do not undergo termination process. However, in a realistic RAFT polymerisation initiated by thermal initiators such as diazo or peroxide compounds, the number of dead chains is known, based on the number of initiators, and thus can be controlled by controlling the addition of initiators. Therefore, the products of RAFT polymerisation are polymer chains with and without the thiocarbonylthio end-group at the ω-end (living and dead chains). In addition, polymer chains based on the α-end can be separated to chains with initiator fragment and RAFT agent R-group (Figure 1.3).
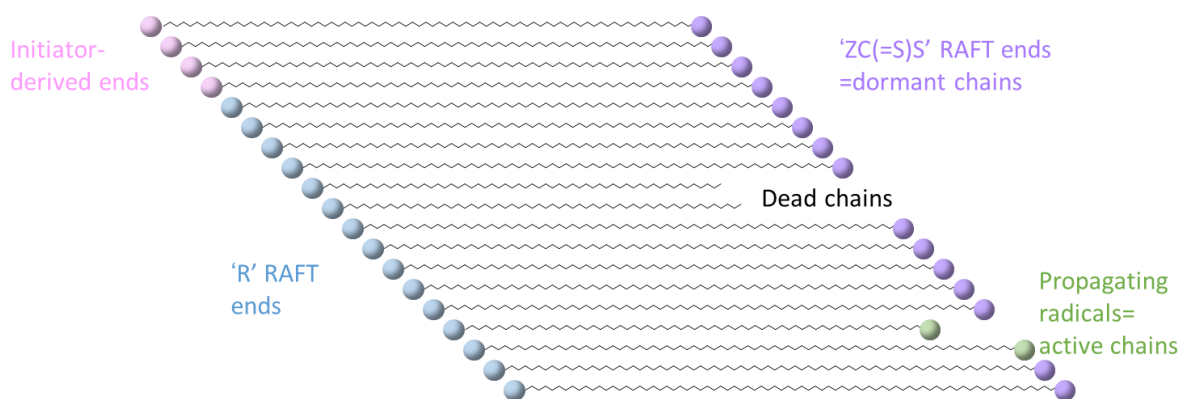
Figure 1.3 Different types of chains in RAFT polymerisation. (The number of each type shown here is not in proportion to that expected for a well-designed experiment.)

1.1.2 Monomer class and RAFT agent

RAFT technique is powerful because of its compatibility with an extensive range of functional monomers. Most vinyl monomers can be divided into "more activated" monomers (MAMs) and "less activated" monomers (LAMs). MAMs are those where the vinyl group is conjugated to a double bond (*e.g.* butadiene, isoprene); a carbonyl group (*e.g.* (meth)acrylates and (meth)acrylamides, maleic anhydride, maleimide); an aromatic ring (*e.g.* styrene, vinylpyridine); or a nitrile (*e.g.* acrylonitrile). LAMs usually have a vinyl group adjacent to saturated carbons, oxygen, nitrogen, halogen, sulphur lone pairs, or the heteroatom of a heterocyclic ring (*e.g.* diallyldimethylammonium chloride, 1-alkenes, vinyl acetate, vinyl chloride, *N*-vinylpyrrolidone). RAFT agents such as dithioesters (Z=aryl or alkyl) or trithiocarbonates (Z=alkylthio) are suitable for controlling polymerisation of MAMs but will inhibit polymerisation of LAMs.[8] *N,N*-dialkyl- or *N*-alkyl-*N*-aryl dithiocarbamates and xanthates as RAFT agents will have good control on polymerisation of LAMs but not MAMs. Figure 1.4 summarises the guideline for the selection of appropriate RAFT agent for particular monomers (adapted from a previous report[9]). For the dashed lines part, it refers to those monomer–RAFT agent combinations with partial control, usually with higher Đ or there may be substantial retardation, or a prolonged inhibition period.[10]

The Z-group of RAFT agent is most responsible for the reactivity of the C=S bond and the propagating radical. For the addition of MAMs, because of the electronic stabilisation from their substituent, they produce more stabilised radicals and therefore require a Z-group (Z = S-alkyl or Ph) that help with the

stabilisation of the intermediate radical to favour radical addition on C=S bond. On the other hand, LAMs with high reactivity make them poor homolytic groups, and thus require less stable intermediate radicals to favour the fragmentation of the propagating radical. RAFT agents such as xanthates (Z=O-alkyl) and dithiocarbamate (Z=N-alkyl) have lone pair of electrons on oxygen or nitrogen that can be delocalised in the thiocarbonyl group, therefore destabilise the intermediate radical.

The R-group plays a subtle role on the RAFT. The selection of R-group is based on (1) subsequent fragmentation from the intermediate, R-group has to be a good leaving group to fragment; and (2)

Figure 1.4 (a) Guidelines for Selection of the (a) R-Group and (b) Z-group of RAFT Agents (Z−C(=S)S−R) for various polymerisations (Adapted from Ref. 9). Reprinted from Ref. [5] with permission. Copyright 2017, American Chemical Society. Abbre*vi*ations: MMA = methyl methacrylate, HPMAm = N-(2-hydroxypropyl) methacrylamide, St = styrene, MA = methyl acrylate, AM = acrylamide, AN = acrylonitrile, VAc = vinyl acetate, NVP =N-vinylpyrrolidone, and NVC = N-vinylcarbazole

propagation ability, as R-group must have the ability to rapidly reinitiate propagation. Thus, the R-group must seek a balance between the stability and steric effects. Typically, good R-groups mimic monomer radicals or thermal initiators.[5]

1.1.3 Process of polymerisation

RAFT polymerisation as a RDRP polymerisation, like the conventional free radical polymerisation, has been applied in homogenous and heterogeneous systems. The homogeneous RAFT polymerisation can be performed in bulk and in solution (including aqueous, polar and non-polar systems, even supercritical CO_2[11]). Most solvents used in conventional free radical polymerisation are compatible with RAFT, except for strong nucleophilic solvents that may degrade the thiocarbonylthio group. Homogeneous RAFT polymerisations usually show pseudo-first-order rate plots, indicating a first-order dependence on monomer.

RAFT polymerisation has been extensively studied in various heterogeneous systems, including emulsion, miniemulsion and dispersion polymerisation. Different to homogeneous RAFT polymerisation, both theoretical and experimental studies have shown that RAFT polymerisation in compartmentalised systems can result in a significant increase in polymerisation rate while maintaining good control due to the segregation effect.[12] The rate enhancement feature enables the RAFT process for the synthesis of polymers with ultrahigh molecular weights and efficient preparation of well-defined polymeric nano-objects. Solvophilic macro-RAFT agent undergoes chain extension with a monomer that forms a solvophobic block, thus leading to the self-assembly of the amphiphilic block copolymer. The morphology of the self-assembled nano-objects could be tuned by adjusting the solvophilic/solvophobic ratio. The process was coined polymerisation-induced self-assembly (PISA).

1.2 Polymerisation-Induced Self-Assembly (PISA)

Block copolymer self-assembly in solution is a well-known approach for the fabrication of a wide range of nano-objects, including spheres, worms, rods, vesicles, lamellae, ellipsoids, and toroids.[13-15] However, this self-assembly approach is typically conducted *via* post-polymerisation processing in diluted solution, which means the industrial scale-up is not cost-effective. This significantly limits the potential commercial applications. Polymerisation-induced self-assembly (PISA) offering an *in-situ* synthesis of

nano-objects at relatively high solid content, has drawn significant research attention over the past decade.[16-19] In a typical PISA process, a solvophilic macromolecule (macro-CTA; block A) is chain-extended with a second monomer in a suitable solvent *via* either dispersion or emulsion polymerisation (depending on the monomer solubility in solvent).[20] The growth of the second block (B) which is insoluble in solvent, leads to the *in situ* self-assembly of AB diblock copolymer into nano-objects. By varying the degree of polymerisation (DP), and the ratio of A and B blocks, nano-objects with various morphologies such as spheres, worms, vesicles and even oligolamellar vesicles can be obtained at different solid contents (10 to up to 40-50 %).[20-23] PISA also enables high monomer conversions within short reaction times compared to conventional solution living polymerisation. This is because upon the micellar nucleation, the unreacted monomer transports from solvent into micellar cores, leading to high local monomer concentration. RAFT polymerisation follows pseudo-first-order kinetics, which the polymerisation rate depends on the monomer concentration. Therefore, the high local concentration of monomer inside micellar cores accelerates the rate of polymerisation. The self-assembled nano-objects have a broad range of applications, such as drug delivery,[18, 24] bio-imaging agents,[25, 26] stimuli-responsive smart nanomaterials,[27, 28] Pickering emulsifiers[29] and so forth.

The synthesis of block copolymers in PISA usually requires the use of living/controlled polymerisation techniques.[30] The common living/controlled polymerisation technique for PISA reported in literature is RDRP technique, including RAFT polymerisation, ATRP[31-33] and NMP.[34-36] Recently, Choi group reported ring-opening metathesis polymerisation (ROMP) induced self-assembly (ROMP-PISA), which had further expanded the polymerisation techniques for PISA.[37-40] Nevertheless, in practical, the most widely used technique for PISA is RAFT polymerisation, which is versatile for a broad range of monomers and solvents.[1, 10, 41-46]

Since the invention of PISA, many research groups around the world have developed new and creative approaches to broaden the scope of PISA initiations, morphologies and applications, etc. The growing interest in PISA is certainly reflected in the increasing number of publications over the past few years. A detailed literature review will be covered in Chapter 2. In the review, we summarise these recent advances in the emerging aspects of RAFT-mediated PISA. These include: 1) non-thermal initiation processes, such as photo-, enzyme-, redox- and ultrasound-initiation; the achievements of 2) high-order

structures, 3) hybrid materials, 4) stimuli-responsive nano-objects by design and adopting new monomers and new processes, 5) the efforts in the realisation of upscale production by utilisation of high throughput technologies, and 6) the applications of current PISA nano-objects in different fields and finally 7) its future directions.

1.3 Sonochemistry

Ultrasound refers to sound waves beyond 20 kHz, which cannot be detected by human ear. Ultrasound can be roughly divided into three main regions according to frequency ranges: low frequency (20–100 kHz), intermediate frequency (100 kHz–1 MHz) and high frequency (1–10 MHz).[47] The frequency range from 20 kHz to 1 MHz is commonly used in sonochemistry which refers to ultrasound-initiated chemical reactions and various processing through acoustic cavitation. The process of acoustic cavitation can be divided into three stages including the formation, growth and subsequent collapse of acoustic bubbles,[48] as shown in Figure 1.5. The collapse is highly energetic and generates extreme temperatures and pressures.[47, 49] These extreme conditions lead to several promoting chemical and physical/mechanical effects: chemical effects at high-frequencies such as radical formation and sonoluminescence; physical/mechanical effects at low-frequencies such as shear force.[47] As a result, sonochemistry has been developed as a versatile technology that has wide applications including synthesis of inorganic and organic materials, degradation of organic matters, removal of organic and biological pollutants, etc.
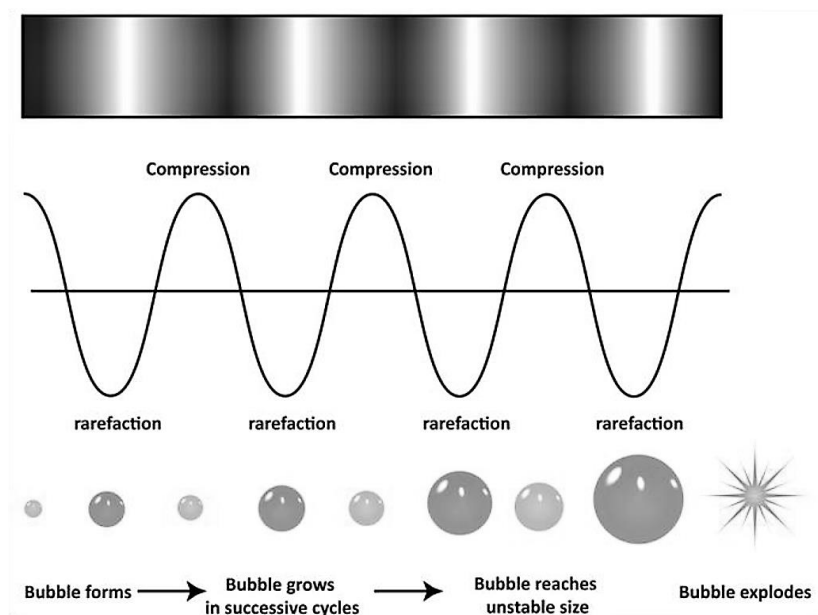
Figure 1.5 Schematic diagram of acoustic bubble formation, growth and collapse in a liquid.

1.3.1 Application of ultrasound to polymer synthesis

The majority of polymers are prepared from vinyl monomers, which undergo chain growth or addition reactions.[50] The most common and straightforward method for polymerisation of vinyl monomers is radical initiation.[51] As mentioned, acoustic cavitation can generate chemical effect of radical formation, thus it has been used extensively as an alternative method of initiation for vinyl polymer synthesis purposes.

The possibility of using ultrasound to induce polymerisation was first suggested by Henglein[52] in 1950s to prepare poly(acrylonitrile) in aqueous solution. Initially, the reaction medium of ultrasound-induced polymerisation was limited to water and it was considered that the lower degree of radical formation in organic solvent would preclude polymerisation.[50, 53] Weissler *et al.*[54] reported in 1965 that acetonitrile decomposed into methane, hydrogen and nitrogen under ultrasound irradiation, indicating the possibility of radical formation in organic solvents. Many ultrasound-initiated polymerisations in organic solvents have been reported since then.

The main role of ultrasound is to produce the initiating radicals as a replacement of radical initiators such as azo initiators. Alternatively, ultrasound can be used in combination with chemical initiators to

accelerate the decomposition of chemical initiators such as peroxides or azo compounds. Price *et al.*[51] demonstrated high-intensity ultrasound can cleave 2, 2'-azobisisobutyrylnitrile (AIBN) at 25 °C and initiate polymerisation of methyl methacrylate. This provides a possible method of initiating a polymerisation at a temperature lower than the usual decomposition temperature of the chemical initiator. Price *et al.*[51] also illustrated the number-average molecular weight of formed polymer is very high at early stages of the sonication but getting decreased over sonication time. This is because once sufficiently long chains are formed, the onset degradation becomes more pronounced, and limiting the achievable maximum molecular weight. Another complication is the increases of the viscosity during the polymerisation, which suppresses the formation of cavitation bubbles and consequent radical production, and therefore no further conversion of monomer.

1.3.2 Ultrasound-initiated polymerisation in controlled fashion

The application of ultrasound in free radical polymerisation has been extensively studied. In the 1990s, new methods such as ATRP,[7] RAFT polymerisation[1] and NMP[6] were invented which enabled control over the polymer molecular weight, dispersity, functionality and composition. However, the use of ultrasound as an initiator in controlled polymerisation was not reported until more recently. Esser-Kahn *et al.* reported a novel methodology in 2016 to perform ATRP by employing low-frequency ultrasound (20 kHz) as a stimulus.[55] The mechanoactive catalyst can be stimulated by ultrasound irradiation to reduce Cu[II] to Cu[I], which subsequently initiate an ATRP reaction. The real ultrasound-activated ATRP in aqueous medium was reported by Matyjaszewski *et al.*[56] Throughout the reaction, the hydroxyl radicals generated by ultrasound were acting as the reducing species to convert Cu[II]X$_2$/L (pre-catalyst complex) to Cu[I]X/L form (active catalyst). The latter form can activate ATRP reaction with the presence of alkyl halide and monomer. In 2017, Qiao and Ashokkumar reported the use of ultrasound derived radicals for initiation of RAFT polymerisation in aqueous medium.[57] In their study, a high frequency (414 kHz) was applied, at which the hydroxyl radical generated from H$_2$O sonolysis is enhanced and the potential of polymer degradation is minimised. It allowed the controlled polymerisation of a range of water soluble (meth) acrylate-based monomers. However, it was found the ability for ultrasonic irradiation to generate radicals is monomer-dependent. Bulky monomer or high concentration of monomer could suffer from no polymerisation. The sono-RAFT polymerisation

was observed to be switchable by simply switch ON/OFF the sonication. The successes of ultrasound-induced controlled radical polymerisation provide a "green", externally regulated, easy scalable method with a broad range of monomers.

Although many successes have been reported, however, there is still much to be explored of the ultrasound-initiated controlled polymerisation. For instance, ultrasound-initiated controlled polymerisation induced self-assembly (sono-PISA) to produce different nano-objects could find new and interesting applications. Moreover, both chain growth and degradation of polymer may occur during sonication, a detailed understanding of the dependency of rates on the factors such as ultrasound frequencies, intensities, polymer chain lengths, and medium viscosities is required. In conclusion, ultrasound-initiated controlled radical polymerisation is a very unique technique that has a potentially broad scope of application in polymer synthesis, nano-objects construction and industrial realisation.

1.4 Aims and Outline of Thesis

The overall aim of this thesis is to expand the scope and applications of PISA in dispersion polymerisation *via* RAFT. In particular, a large part of this work focuses on exploring the synthesis of well-defined nano-objects and hybrid material *via* ultrasound-initiated PISA (sono-PISA). Furthermore, polymerisation-induced hierarchical self-assembly, an expanded scope of PISA, has been investigated in aqueous system *via* a promising strategy. Some of the main outcomes of each chapter are summarised below.

Chapter 2 provides a literature review of the closely related topics of the main body of the thesis. Both pioneering and most recent works were summarised in the emerging aspects of RAFT-PISA, including non-thermal initiation, high-order and complex morphologies, hybrid and stimuli-responsive nano-objects, improved throughput of PISA and applications.

Chapter 3 demonstrates the first room-temperature synthesis of diblock copolymer nano-objects with different morphologies using ultrasound (990 kHz) initiated reversible addition–fragmentation chain transfer PISA (sono-RAFT-PISA) in an aqueous system. Sonolysis of a water molecule by high-frequency ultrasound to generate hydroxyl radicals and to initiate polymerisation has the potential to be a new "initiator-free" synthesis technique. It was found that the morphologies of the block copolymer nano-

objects prepared by sono-RAFT-PISA were different from those prepared by conventional thermal-PISA. Furthermore, the impacts of ultrasound and the presence of a cross-linker on the nano-object morphology were investigated. It was observed that the stability of worm-like micelles will be affected by ultrasound but it could be strengthened *via* core-cross-linking (CCL). Overall, the externally-regulatable, easily scalable and sustainable "green" features of ultrasound have the potential to promote the application of sono-PISA for the fabrication of nano-objects. The content of this chapter has been published: Jing Wan *et al.*, "Room Temperature Synthesis of Block Copolymer Nano-Objects with Different Morphologies *via* Ultrasound Initiated RAFT Polymerisation-Induced Self-Assembly (Sono-RAFT-PISA)", *Polym. Chem.*, 2020, **11**, 3564–3572.

In Chapter 4, we demonstrate the preparation of polymer–metal nanocomposites for improved catalytic performance by utilising ultrasound as both the initiation and reducing source. Specifically, synthesis of the macro-RAFT agent containing poly[2-(dimethylamino)ethyl methacrylate], followed by sono-RAFT-PISA, provides triblock copolymer nanoparticles containing tertiary amine groups. These polymer nanoparticles were further used as the scaffold for the *in situ* reduction of metal ions (Au and Pd ions) by radicals generated *via* sonolysis of water without additional reducing agents. Polymer–Au nanocomposites with stepwise-grown AuNPs can be applied as surface-enhanced Raman scattering (SERS) substrates for 4-aminothiophenol (4-ATP) detection. Furthermore, the catalytic performances of these prepared polymer–Au and polymer–Pd nanocomposites were examined for aerobic alcohol oxidation and the Suzuki–Miyaura cross-coupling reaction, respectively. Overall, this strategy is expected to greatly expand the utility of ultrasound in the preparation of polymer–metal nanocomposites and promote the catalytic applications of these nanocomposites. The content of this chapter has been published: Jing Wan *et al.*, "Sonochemical preparation of polymer–metal nanocomposites with catalytic and plasmonic properties", *Nanoscale Adv.*, 2021, **3**, 3306–3315.

In Chapter 5, we demonstrate a strategy achieving the challenging preparation of hierarchical strictures using a sequential one-pot synthesis of hierarchically self-assembled polymer colloids with diverse morphologies *via* aqueous PISA. Complex formation of water-immiscible monomers with cyclodextrin *via* "host–guest" inclusion, followed by sequential aqueous polymerisation, provides a linear triblock terpolymer that can *in situ* self-assemble into hierarchical nanostructures. To access polymer colloids

with different morphologies, three types of linear triblock terpolymers were synthesised through this methodology, which allows the preparation of AX_n-type colloidal molecules (CMs), core–shell–corona micelles, and raspberry-like nanoparticles. The proposed mechanism explained how the interfacial tensions and glass transition temperatures of the core-forming blocks affect the morphologies. Overall, this chapter provides a scalable method of the production of CMs and other hierarchical structures. It can be applied to different block copolymer formulations to enrich the complexity of morphology and enable diverse functions of nano-objects. The content of this chapter has been published: Jing Wan *et al.*, "Polymerisation-Induced Hierarchical Self-Assembly From Monomer to Complex Colloidal Molecules and Beyond", *ACS Nano*, 2021, **15**, 13721–13731.

Chapter 6 summarises the general conclusions from Chapter 3 to Chapter 5 and provides some recommendations for future work.

1.5 References

1. J. Chiefari, Y. K. Chong, F. Ercole, J. Krstina, J. Jeffery, T. P. T. Le, R. T. A. Mayadunne, G. F. Meijs, C. L. Moad, G. Moad, E. Rizzardo and S. H. Thang, *Macromolecules*, 1998, **31**, 5559-5562.
2. T. P. Le, G. Moad, E. Rizzardo and S. H. Thang, WO 9801478, 1998 [Chem Abstracts, 128, 115390].
3. P. Corpart, D. Charmot, T. Biadatti, S. Zard and D. Michelet, WO 9858974, 1998 [Chem Abstracts, 130, 82018].
4. A. D. Jenkins, R. G. Jones and G. Moad, *Pure Appl. Chem.*, 2009, **82**, 483-491.
5. S. Perrier, *Macromolecules*, 2017, **50**, 7433-7447.
6. D. H. Solomon, E. Rizzardo and P. Cacioli, US Pat. 4581429 [Chem Abstracts, 1986, 221335q].
7. J.-S. Wang and K. Matyjaszewski, *J. Am. Chem. Soc.*, 1995, **117**, 5614-5615.
8. Y. Luo, J. Tsavalas and F. J. Schork, *Macromolecules*, 2001, **34**, 5501-5507.
9. D. J. Keddie, G. Moad, E. Rizzardo and S. H. Thang, *Macromolecules*, 2012, **45**, 5321-5342.
10. G. Moad, E. Rizzardo and S. H. Thang, *Aust. J. Chem.*, 2012, **65**, 985-1076.
11. T. Arita, S. Beuermann, M. Buback and P. Vana, *e-Polymers*, 2004, **4**, 003.
12. P. B. Zetterlund, S. C. Thickett, S. Perrier, E. Bourgeat-Lami and M. Lansalot, *Chem. Rev.*, 2015, **115**, 9745-9800.
13. J. B. Gilroy, T. Gädt, G. R. Whittell, L. Chabanne, J. M. Mitchels, R. M. Richardson, M. A. Winnik and I. Manners, *Nat. Chem.*, 2010, **2**, 566.
14. S. G. Jang, D. J. Audus, D. Klinger, D. V. Krogstad, B. J. Kim, A. Cameron, S.-W. Kim, K. T. Delaney, S.-M. Hur, K. L. Killops, G. H. Fredrickson, E. J. Kramer and C. J. Hawker, *J. Am. Chem. Soc.*, 2013, **135**, 6649-6657.
15. D. E. Discher and A. Eisenberg, *Science*, 2002, **297**, 967-973.
16. N. J. Warren and S. P. Armes, *J. Am. Chem. Soc.*, 2014, **136**, 10174-10185.
17. B. Charleux, G. Delaittre, J. Rieger and F. D'Agosto, *Macromolecules*, 2012, **45**, 6753-6765.
18. B. Karagoz, L. Esser, H. T. Duong, J. S. Basuki, C. Boyer and T. P. Davis, *Polym. Chem.*, 2014, **5**, 350-355.
19. W.-M. Wan and C.-Y. Pan, *Polym. Chem.*, 2010, **1**, 1475-1484.
20. S. L. Canning, G. N. Smith and S. P. Armes, *Macromolecules*, 2016, **49**, 1985-2001.

21. J. Tan, H. Sun, M. Yu, B. S. Sumerlin and L. Zhang, *ACS Macro Lett.*, 2015, **4**, 1249-1253.
22. C. A. Figg, A. Simula, K. A. Gebre, B. S. Tucker, D. M. Haddleton and B. S. Sumerlin, *Chem. Sci.*, 2015, **6**, 1230-1236.
23. A. Blanazs, S. P. Armes and A. J. Ryan, *Macromol. Rapid Commun.*, 2009, **30**, 267-277.
24. B. Fan and E. R. Gillies, *Mol. Pharmaceutics*, 2017, **14**, 2548-2559.
25. M. Huo, Q. Ye, H. Che, X. Wang, Y. Wei and J. Yuan, *Macromolecules*, 2017, **50**, 1126-1133.
26. J. Huang, H. Zhu, H. Liang and J. Lu, *Polym. Chem.*, 2016, **7**, 4761-4770.
27. B. Fan, J. F. Trant, A. D. Wong and E. R. Gillies, *J. Am. Chem. Soc.*, 2014, **136**, 10116-10123.
28. B. Fan, R. E. Yardley, J. F. Trant, A. Borecki and E. R. Gillies, *Polym. Chem.*, 2018, **9**, 2601-2610.
29. C. J. Mable, K. L. Thompson, M. J. Derry, O. O. Mykhaylyk, B. P. Binks and S. P. Armes, *Macromolecules*, 2016, **49**, 7897-7907.
30. M. Lansalot, J. Rieger and F. D'Agosto, in *Macromolecular Self‑assembly*, ed. L. Billon and O. Borisovpp, John Wiley & Sons, Inc., 2006, **2**, 33-82.
31. X. Liu and W. Gao, *ACS Appl. Mater. Interfaces*, 2017, **9**, 2023-2028.
32. S. Sugihara, K. Sugihara, S. P. Armes, H. Ahmad and A. L. Lewis, *Macromolecules*, 2010, **43**, 6321-6329.
33. W.-M. Wan and C.-Y. Pan, *Macromolecules*, 2007, **40**, 8897-8905.
34. G. Delaittre, M. Save and B. Charleux, *Macromol. Rapid Commun.*, 2007, **28**, 1528-1533.
35. X. G. Qiao, P. Y. Dugas, B. Charleux, M. Lansalot and E. Bourgeat-Lami, *Macromolecules*, 2015, **48**, 545-556.
36. X. G. Qiao, M. Lansalot, E. Bourgeat-Lami and B. Charleux, *Macromolecules*, 2013, **46**, 4285-4295.
37. I.-H. Lee, P. Amaladass and T.-L. Choi, *Chem. Commun.*, 2014, **50**, 7945-7948.
38. I.-H. Lee, P. Amaladass, K.-Y. Yoon, S. Shin, Y.-J. Kim, I. Kim, E. Lee and T.-L. Choi, *J. Am. Chem. Soc.*, 2013, **135**, 17695-17698.
39. D. B. Wright, M. A. Touve, L. Adamiak and N. C. Gianneschi, *ACS Macro Lett.*, 2017, **6**, 925-929.
40. K.-Y. Yoon, I.-H. Lee, K. O. Kim, J. Jang, E. Lee and T.-L. Choi, *J. Am. Chem. Soc.*, 2012, **134**, 14291-14294.
41. Y. Chong, T. P. Le, G. Moad, E. Rizzardo and S. H. Thang, *Macromolecules*, 1999, **32**, 2071-2074.
42. G. Moad, E. Rizzardo and S. H. Thang, *Aust. J. Chem.*, 2006, **59**, 669-692.
43. G. Moad, E. Rizzardo and S. H. Thang, *Aust. J. Chem.*, 2009, **62**, 1402-1472.
44. G. Moad, E. Rizzardo and S. H. Thang, *Polymer*, 2008, **49**, 1079-1131.
45. G. Moad, E. Rizzardo and S. H. Thang, *Aust. J. Chem.*, 2005, **58**, 379-410.
46. G. Moad, E. Rizzardo and S. H. Thang, *Acc. Chem. Res.*, 2008, **41**, 1133-1142.
47. M. Ashokkumar and T. J. Mason, in *Kirk-Othmer Encycl. Chem, Tech.*, Wiley Interscience, Online, 2007.
48. T. Leong, M. Ashokkumar and S. Kentish, *Acoustics Australia*, 2011, **39**, 54-63.
49. S. K. Bhangu and M. Ashokkumar, *Topics in Current Chemistry*, 2016, **374**, 56.
50. K. S. Suslick and G. J. Price, *Annu. Rev. Mater. Sci.*, 1999, **29**, 295-326.
51. G. J. Price, D. J. Norris and P. J. West, *Macromolecules*, 1992, **25**, 6447-6454.
52. V. A. Henglein, *Die Makromolekulare Chemie*, 1954, **14**, 128-145.
53. I. Él'Piner, *Chemical, and Biological Effects, Consultants Bureau, New York*, 1964.
54. A. Weissler, I. Pecht and M. Anbar, *Science*, 1965, **150**, 1288-1289.
55. H. Mohapatra, M. Kleiman and A. P. Esser-Kahn, *Nat. Chem.*, 2016, **9**, 135-139.
56. Z. Wang, Z. Wang, X. Pan, L. Fu, S. Lathwal, M. Olszewski, J. Yan, A. E. Enciso, Z. Wang, H. Xia and K. Matyjaszewski, *ACS Macro Lett.*, 2018, **7**, 275-280.
57. T. G. McKenzie, E. Colombo, Q. Fu, M. Ashokkumar and G. G. Qiao, *Angew. Chem. Int. Ed. Engl.*, 2017, **56**, 12302-12306.

Chapter 2

Literature Review

2.1 Introduction

Since the advent of RDRP techniques, there is no doubt that they have revolutionised the synthesis of polymers by providing a robust method for controlling the polymer compositions, architectures, molecular weights and molecular weight distributions.[1] Of all the applications and development of RDRP, PISA is one of the research fields that has benefited most from it.[2] PISA is an efficient strategy for the synthesis of diverse block copolymer nano-objects at high solid contents (up to 50% w/w), which overcome many limitations of the conventional solution self-assembly process and is suitable for industrial scale-up. In a typical PISA process, the solvophilic stabliser polymer undergoes chain extension with a solvophobic block *via* RDRP, this induces the concomitant self-assembly of the amphiphilic block copolymer and the formation of nano-objects.[3] PISA usually enables high or even quantitative conversion of monomers without the need for post-purification. The required reaction time is also shorter compared to solution polymerisation because of the high local monomer concentration within the micellar cores.[4] Over the past decade, PISA has been applied to a variety of monomers in diverse solvent systems, including water, polar solvents (*e.g.* alcohols), non-polar solvents[5] (*e.g. n*-alkanes[6, 7]) and other media including ionic liquids,[8, 9] supercritical CO_2[10-12] and silicone oil[13]. Up to now, many morphologies have been realised *via* PISA, including spheres, rods, worms, vesicles, framboidal vesicles,[14, 15] multilamellar vesicles,[16] lamellae,[17] spongosomes,[18-24] hexosomes,[18-20, 25] cubosomes,[18, 19, 25] Janus particles,[26, 27] colloidal molecules,[26, 27] and many others. The synthesised particles have a broad range of applications in the areas of biomedical, coating, catalysis and Pickering emulsions and so forth.

Theoretically, all RDRP techniques can produce block copolymer nano-objects *via* PISA. Indeed, many examples of PISA process using different RDRP techniques have been reported, including RAFT polymerisation, NMP,[28-30] ATRP,[31-34] iodine-transfer polymerisation (ITP),[35] bromine-iodine

transformation reversible-deactivation radical polymerisation (BIT-RDRP),[36, 37] telluride-mediated radical polymerisation (TERP),[38] cobalt-mediated radical (CMR) polymerisation[39] and reversible complexation mediated polymerisation (RCMP)[40, 41]; other polymerisation techniques such as ring-opening metathesis polymerisation (ROMP)[42-46] have been implemented as well. However, RAFT remains the most employed and robust technique for PISA due to its high compatibility with various monomers, solvents and reaction conditions. In recent years, there are more than 100 research articles published on PISA every year, mainly on RAFT-mediated PISA (Figure 2.1). Although PISA based on other RDRP techniques also attracted much research attention, the focus of this chapter is RAFT-mediated PISA.
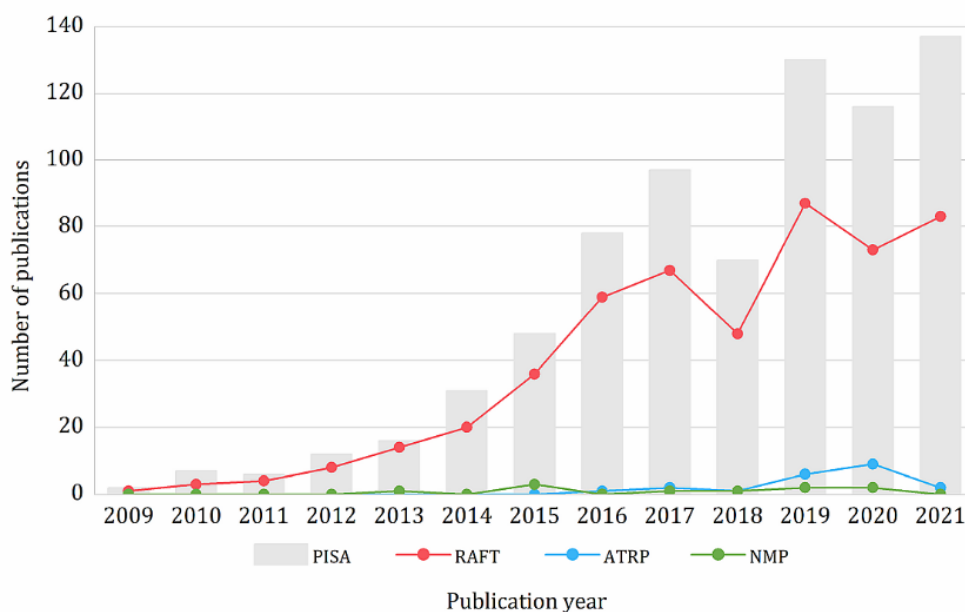
Figure 2.1 Development of PISA, RAFT-, ATRP-, and NMP-mediated PISA in 2009-2022 (Source: Web of Science 02/2022, research topic: "polymerisation-induced self-assembly", PISA: without refinement, RAFT: refined keyword "RAFT", ATRP: refined keyword "ATRP", NMP: refined keyword "NMP").

We note that a few reviews have been published since the inception of PISA, covering some important concepts of the PISA process, such as the initiation methods,[47] the biomedical applications,[48, 49] and even overview.[2, 4] However, a growing number of publications clearly reflected the interest in PISA, and many outstanding studies continue to emerge even while these lines are being read. The aim of this

chapter is not to add additional concepts in RAFT-mediated PISA, but to summarise the emerging trends in PISA and to provide an up-to-date review of this field so that the reader can better understand the development and future direction of PISA. The particular focus of this chapter is on the following topics: (1) the new initiation methods for the PISA process, (2) the emerging high-order and complex morphologies by PISA, (3) the synthesis of hybrid materials *via* PISA, (4) the stimuli-responsive nano-objects by PISA, (5) the strategies for improved throughput and continuous flow process, (6) current and potential applications.

2.2 Non-Thermal Initiation of PISA

In contrast to other RDRP techniques such as NMP or ATRP, RAFT generally requires an external source of radicals (exogenous radicals), which are generally produced by the decomposition of organic molecules under thermal conditions.[2] Most of the conventional initiators employed to implement emulsion or dispersion polymerisation are azo compounds or photoactive molecules. When the dispersing phase is water, ionic azo compounds or persulphates are preferred. The reaction is usually conducted at around the 10-hr half-life temperature of the initiator. The 10-hr half-life temperature varies with the chemical nature of the initiators, usually varies between 44 to 100 °C. For RAFT-mediated PISA the most widely employed reaction temperature is 50 -70 °C, as the solvent is usually water or methanol.

The thermal initiation of RAFT-PISA is readily applied in diverse conditions with good compatibility with different monomers and solvent systems, and could be easily realised in the industrial upscaling process. Nevertheless, the relatively high reaction temperature (> 44 °C) limits the utilisation of temperature-sensitive materials, including thermo-responsive RAFT agents, temperature-sensitive polymers, DNA, RNA and enzymes. Therefore, in the past few years, there has been a surge of interest in new initiation mechanisms that utilise visible light, microwaves, enzymes, redox/oscillatory reaction, electrochemistry, ultrasound as alternative approaches for RAFT-PISA that initiated at a lower temperature. The non-thermal approaches allow the PISA to be combined with biomolecules, which may open up new scopes of research for PISA formulations.

2.2.1 Visible light initiated PISA (Photo-PISA)

RAFT polymerisation has been extensively explored in a broad range of electromagnetic spectra including gamma,[50-52] ultraviolet (UV),[53-56] visible,[57-61] near-infrared (NIR)[62] and microwave[63]. It was then a spontaneous process that photo-initiated RAFT polymerisations were extended to the area of RAFT-mediated PISA. Visible light and NIR have attracted more research attention due to their low energy nature, induction of fewer side reactions, and also the potential to control the polymerisations temporally and spatially.[64] In this section, the visible light photo-PISA will be mainly discussed.

Initially, only photo-RAFT have been implemented in the PISA process. More recently, other RDRP techniques, such as NMP,[65] ATRP,[32] and bromine-iodine transformation (BIT),[37] as well as some other polymerisation techniques such as ring-opening polymerzation[66] have been explored for the photo-PISA process. Nevertheless, the photo-RAFT technique remains the most robust and widely employed technique for the photo-PISA process. The main types of photo-RAFT polymerisations can be summarised as: (1) photoinitiator process: photo-decomposition of external photoinitiators, similar to the mechanism of thermal initiation,[67] (2) photoiniferter (***ini***tiator-trans***fer*** agent-***ter***minator) process: photolytic cleavage of a C–S bond in the thiocarbonylthio RAFT agent without exogenous radical sources,[68-70] and (3) photocatalyst process: a photo-induced electron transfer (PET) process using photo-redox catalysts.[60, 71] Thus, the photo-RAFT-PISA can also be summarised according to these three different processes (Figure 2.2).
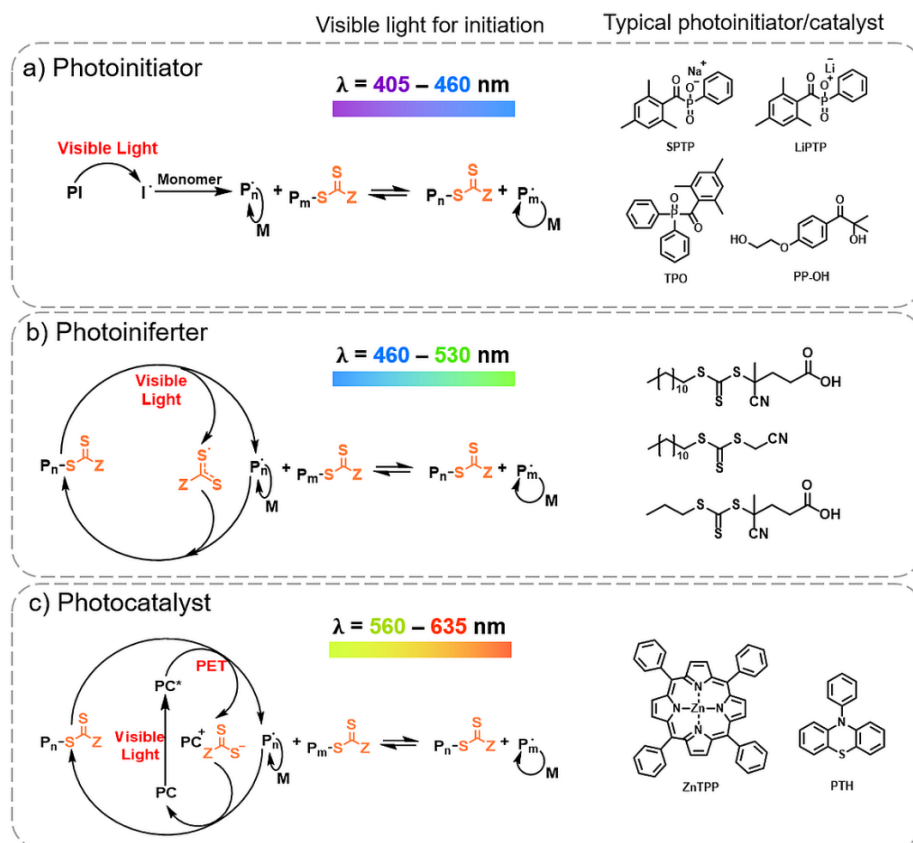
Figure 2.2 Different mechanisms for initiating PISA polymerisations under visible light: (a) photoinitiator, (b) photoiniferter and (c) photocatalyst approaches.

2.2.1.1 Photoinitiator approach

Many organic compounds are able to absorb light and generate radicals, thus providing exogenous radicals for RAFT dispersion/emulsion polymerisations. Photoinitiators can be divided into one-component (type I) and two-component (type II) initiators. Type I initiators are typically compounds that undergo unimolecular homolytic cleavage reaction, while type II initiators can absorb light to form excited molecules which then abstract a hydrogen atom from a donor molecule, producing free radical.[67]

The first example of visible light photo-PISA was reported by Cai and co-workers in 2015 using sodium phenyl-2,4,6-trimethyl-benzoylphosphinate (SPTP) as the photoinitiator.[72] In this work, poly(2-hydroxypropyl methacrylamide) (PHPMAm) macro-RAFT and diacetone acrylamide (DAAM) undergo fast aqueous dispersion polymerisation under visible light at 25 °C. The kinetics was found to be similar

to thermally initiated PISA, both containing phase transition points and rate accelerations, however, the polymerisation rates were much faster than that of traditional thermal-PISA, and the induction period was negligible. The room temperature process showed good control ($Đ$ <1.3) when targeting a series of PHPMAm-*b*-PDAAM spheres with various degree of polymerisation (DP). In addition, nanoparticles synthesised with *N*-(2-aminoethyl) acrylamide (AEAM) as a comonomer could further functionalise with metal binding motifs *via* the post-polymerisation process.

By applying the same photoinitiator SPTP reported in Cai's work, Zhang, Sumerlin and co-workers expanded this PISA process by employing 405 nm violet LED light to synthesise poly(ethylene glycol)-poly(2-hydroxypropyl methacrylate) (PEG-PHPMA) based classical nano-objects.[73] This photo-PISA achieved a diverse set of morphologies with spheres, worms, vesicles (S, W, V) by varying the target DP of PHPMA and the solid contents. In addition, ultrafast kinetics were observed in this process, with quantitative monomer conversion achieved within 30 min at room temperature. This is a tremendous improvement compared to the conventional thermal-PISA process at 70 °C, which usually requires at least 3 hr to achieve quantitative monomer conversions. This was also the first report that the full range of morphology phase diagram was generated for photo-PISA at room temperature. The mild conditions are important for the preparation of vesicles loaded with bio-related species; as a proof of concept, silica nanoparticles and bovine serum albumin (BSA) were encapsulated *in situ* within the vesicles.

In addition to S, W, V, the same technique as Cai's work has been used to synthesise an unusual collection of morphologies such as silks, ribbons, interlinked vesicles and nanotubes (Figure 2.3),[74] which expands the morphologies achieved by the photo-PISA process. Recently, a similar technique was combined with electrostatic manipulation to achieve triblock copolymer multi-compartmentalised 2D nano-objects by tuning the pH of reactions.[75]
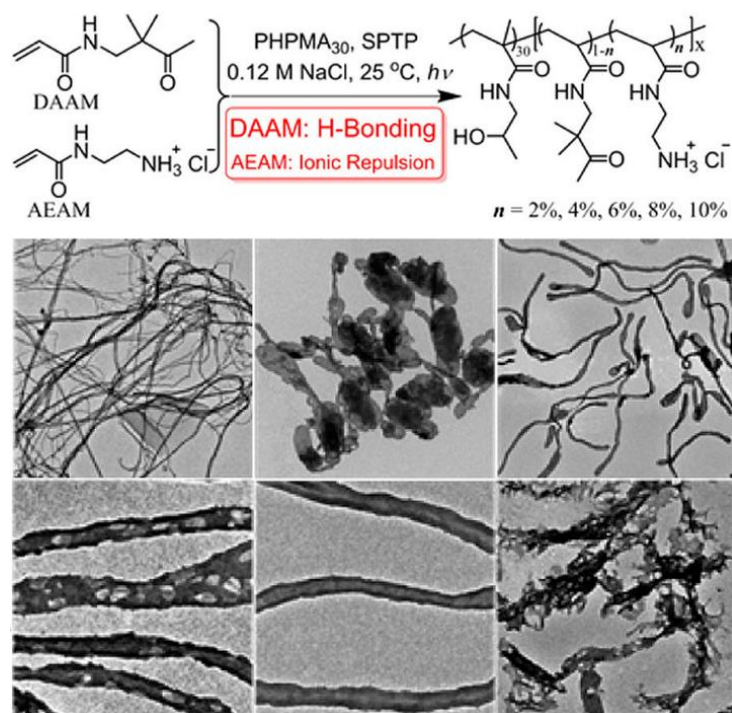
Figure 2.3 Schematic illustration of photomediated PISA at 25 °C and representative TEM images. Reprinted from Ref. [74] with permission. Copyright 2016, American Chemical Society.

Apart from SPTP, other photoinitiators such as 2,4,6-trimethylbenzoyl-diphenylphosphinate (TPO),[76, 77] 2-hydroxy-4′-2-(hydroxyethoxy)-2-methylpropiophenone (PP-OH),[78] and lithium phenyl(2,4,6-trimethylbenzoyl)phosphinate (LiPTP)[79] were also used as photoinitiators in photo-PISA. Junkers, Zetterlund, Boyer and co-workers reported the optimised batch protocol by varying the solvents, photoinitiators as well as light intensities.[80] By comparing TPO, PP-OH, 4,4'-bis(diethylamino)benzophenone, camphorquinone and eosin Y (EY) disodium salt photoinitiator and photoiniferter route, TPO was selected as the most suitable photoinitiator. EtOH/DMSO (90/10 v/v %) was chosen as the optimal solvent system to achieve both high monomer conversion and high order morphologies. The optimised batch protocol was then adapted for flow processing, showing the potential of continuous tubular reactors for alcohol-based photo-PISA.

One of the trends in photoinitiator induced photo-PISA is to minimise the use of photoinitiators or to make them dual-acting. In 2020, Dai, Jung and Boyer *et al.* reported the dual roles of doxorubicin (DOX), which can serve as an antitumor drug and co-catalyst for a photo-PISA process under blue LED light (485 nm).[81] It was found that DOX can enhance the polymerisation rates of a broad range of

monomers, including acrylate, acrylamide and methacrylates, however, the mechanism remains unclear. In 2021, Tan *et al.* developed a strategy to attach TPO to the R group of RAFT agent (TPO-CDPA), so that the type I photoinitiator could attach onto the surface of polymeric nano-objects.[82] This strategy enables the photoinitiator-RAFT agent with dual-role that can both initiate and control the polymerisation, thus overcoming some drawbacks of using small molecular type I photoinitiators. The yielded photoinitiator-functionalised block copolymer nanoparticles could be further used as heterogeneous photoinitiators to produce hydrogels with internally embedded nanoparticles.

2.2.1.2 Photoiniferter approach

It is well known that UV light can induce photolytic cleavage of the C–S bond in the RAFT agent, generating carbon centred radicals to directly initiate RAFT polymerisation. This attractive approach has been intensively investigated by several groups owing to no exogenous catalysts/initiators are required to initiate the polymerisation.[83-85] However, UV light can also cause gradual degradation of the RAFT agent, which generally results in limited control over the polymerisation, particularly at high conversion.[64] Starting in 2015, several groups including Boyer,[68] Qiao,[69] and Zhu[70] subsequently expanded on this concept by using visible light as a substitute. This process is possible because the absorption energy of the spin-forbidden n $\rightarrow$ π* electron transition of some thiocarbonyl species falls in the visible region ($\lambda_{max, n\rightarrow\pi^*}$ = 400 - 550 nm), therefore, the thiocarbonyl species can be excited by visible light.[69] In this process, the RAFT agent acted as a photoiniferter, as previously proposed by Otsu.[86]

In 2016, Boyer and co-workers reported the first example of photo-PISA without the addition of an external catalyst or initiator to yield nano-objects with different morphologies (S, W, V).[87] A POEGMA-CDTPA macro-CTA was activated under blue (460 nm) or green (530 nm) light and chain extended with benzyl methacrylate (BzMA) in the ethanolic solvent. The *in situ* encapsulation of Nile Red as a model hydrophobic drug was demonstrated as a proof-of-concept for drug loading. In 2017, O'Reilly compared the influence of initiation methods and light intensity on the final PISA morphology.[78] The preparation of PEG-*b*-PHPMA nano-objects were conducted *via* three routes: photo-PISA with 100% intensity (405 nm, no functioning initiator), thermal-PISA, and photo-PISA with 20% (405 nm, no initiator) intensity at the same temperature. Their findings suggest both reaction kinetics and end

group fidelity lead to the difference in phase diagrams generated using photo-PISA and thermal-PISA. More recently, Poly and Chemtob and co-workers reported an initiator-free photo-PISA of poly(2-hydroxyethyl acrylate)-*b*-polystyrene (PHEA-*b*-PS) spheres using 472 nm LED light at 35 °C in methanol/water co-solvent.[88] The yielded nanoparticles were further demonstrated as soft templates for the synthesis of uniform nanoscale porous carbons with large mesopores size.

The advantage of the photoiniferter approach is obvious, as no external photoinitiator or catalysts need to be added, thus eliminating the potential source of toxicity. However, this visible light-mediated RAFT is strongly dependent on both the type of RAFT agent and the effective light intensity.[64] While achieving high monomer conversion is not a problem, the rates of polymerisation could be problematically low compared to photoinitiator or photocatalyst approaches. For example, in Poly and Chemtob's study,[88] it took around 70 hr to achieve 59% conversion of styrene. Furthermore, these polymerisations require careful deoxygenation since no exogenous initiator is present, even low concentrations of oxygen can retard the polymerisation.

2.2.1.3 Photocatalyst approach

This approach refers to the PISA process mediated by photoinduced electron/energy transfer - RAFT polymerisation (PET-RAFT) with photo-redox catalysts. In 2014, Boyer reported the RAFT polymerisation using $Ir(ppy)_3$ and $[Ru(bpy)_3]Cl_2$ at ppm concentrations (typically 1 ppm to monomers) under visible light, and coined this process as PET-RAFT.[71] This process is versatile and compatible with a broad range of solvents and monomers under both homogenous and heterogeneous conditions, and even open-air systems. In the following year, the same group exploited this process in photo-PISA. This first example of PET-RAFT-PISA used $[Ru(bpy)_3]Cl_2$ as a photocatalyst to yield POEGMA-PBzMA nanoparticles with different morphologies in the ethanolic solvent.[89] The "ON/OFF" control over the dispersion polymerisation demonstrated the temporal control over the nanoparticle morphology. Although only ppm level of the photocatalyst was used, it still brings heavy metal into the system, which may be potentially toxic and limit the application in the biomedical field. Next, the utilisation of $Ir(ppy)_3$ in photo-PISA was reported by Han *et al.*, where fluorinated raspberry-like nanoparticles were achieved by the polymerisation of pentafluorostyrene in DMSO.[90]

In 2017, Pan and co-workers performed PET-RAFT dispersion polymerisation using the organic dye 10-phenylphenothiazine (PTH) as an alternative to heavy metal-based photo-redox catalysts.[91] Although the required concentration of PTH (1 ‰ to monomer) was higher than that of heavy metal-based photocatalysts (1 ppm to monomer), good control of the dispersion polymerisation was achieved. Temporal control of the polymerisation in this specific PET-RAFT process has also been demonstrated by adjusting the light source.

Furthermore, many other organic dyes have been exploited as photocatalysts for PET-RAFT polymerisation. The order of reactivity to activate PET-RAFT was reported as eosin Y (EY) $\gg$ fluorescein $\gg$ Nile red, rhodamine 6G (R6G) and methylene blue.[92] Boyer *et al.* reported an oxygen-tolerant ultralow volume RAFT polymerisation in a 96-well microtiter plate under green light irradiation (λ = 530 nm) using EY in the presence of ascorbic acid.[93] The proposed mechanism is that the photo-reduced EY is oxidised by oxygen, regenerating the original dye and converting oxygen to hydrogen peroxide. A redox reaction between the hydrogen peroxide and excess ascorbic acid then produces reactive hydroxyl radicals that initiate RAFT polymerisation. This approach allows control of a range of monomer families (acrylamides, acrylates, methacrylates) for the synthesis of homo- and block copolymers, and can be applied to PISA. Recently, R6G has also been used as a photocatalyst for the PISA process by Lin and co-workers to produce micelles and other high order structures.[94]

Another type of widely applied catalysts for photo-PISA are porphine catalysts. In 2016, the Boyer group extended to longer visible light wavelengths such as red (λ = 635 nm) and yellow (λ = 560 nm) light by the addition of the metalloporphyrin, such as 5, 10, 15, 20-tetraphenyl-21H, 23H-porphine zinc (ZnTPP).[95] In addition, encapsulation of ZnTPP into the core of nanoparticles was achieved, which makes it potentially useful in photodynamic therapy (PDT), as ZnTPP can generate singlet oxygen under visible light irradiation. This oxygen-tolerant PISA system without the traditional deoxygenation process was also demonstrated by the addition of ascorbic acid as the singlet oxygen quencher.[95] Later on, the same research group explored the oxygen-tolerant PET-RAFT PISA by addition of singlet oxygen quenchers such as 9,10-dimethylanthracene, ascorbic acid and (R)-(+)-limonene.[96] Conventional deoxygenation processes generally require the use of specialised equipment (Schlenk vessels, high-

vacuum pump, etc.) and inert gas, the open-air PISA system allows the synthesis to perform without these restrictions at ultra-low volumes.

In 2018, a water-soluble porphine photocatalyst, zinc meso-tetra(*N*-methyl-4-pyridyl) porphine tetrachloride (ZnTMPyP) was investigated for aqueous PET-RAFT dispersion polymerisation,[97] as this water-soluble photocatalyst is more suitable for aqueous PISA systems. In this study, the photo-PISA process was conducted in 96-well microtiter plates under low energy red light (λ_{max} = 595 nm, 10.2 mW/cm^2) without deoxygenation due to the addition of biotin (vitamin B$_7$) as the singlet oxygen quencher. A photo-responsive comonomer 7-[4-(trifluoromethyl)coumarin] methacrylamide (TCMAm) was added for the purpose of post-PISA photo-crosslinking, which was performed under a UV light source (λ_{max} = 365 nm, 10.2 mW/cm^2) to allow the core-cross-linked nanoparticles to retain their original morphologies when exposed to organic solvents.

Some PDT photo-sensitisers can be used to catalyse PET-RAFT polymerisations as well. In 2021, Sumerlin *et al.* reported a strategy to maximise the multifunctionality of Rose Bengal methacrylate (RBMA) as both photocatalyst and comonomer in a photo-PISA process, also a singlet oxygen generator for PDT, and a fluorophore for imaging.[98] In their work, quantitative and controlled loading of Rose Bengal (RB) was realised by converting RB to the polymerisable methacrylate that could be covalently incorporated into nanoparticles. It was further demonstrated that RB-loaded nanoparticles can be activated by visible light, and the efficiency of singlet oxygen production was higher than free RB. After post-modification of the RB-loaded nanoparticles with a DNA aptamer, *in vitro* study showed enhanced internalisation by HCT 116 cells and significant inhibition of tumor cell proliferation under yellow light.

2.2.2 Enzyme-assisted/initiated PISA

2.2.2.1 Enzyme-initiated PISA

Enzymatic catalysis, which is the basis of various biochemical reactions *in vivo*, is extensively found in nature and has been widely applied in organic synthesis and biotechnology. Because of its high efficiency, selectivity, mild reaction conditions and stability, it is emerging as a sustainable and promising strategy for the synthesis of materials, including the initiation of RDRP polymerisations. di Lena and co-workers first demonstrated in 2011 the free radical polymerisation catalysed by enzymes,

in which laccase or horseradish peroxidase (HRP), alkyl halides, and ascorbic acid act as catalysts, initiators, and reducing agents, respectively.[99, 100] In terms of enzyme-initiated RAFT polymerisation, a ternary initiation system based on HRP/H_2O_2/acetylacetone (ACAC) was first achieved at room temperature by An *et al.* in 2015.[101] Later, they reported glucose oxidase (GOx) deoxygenation and H_2O_2/AscA redox initiation for RAFT polymerisation at low temperature in air.[102] In 2017, An *et al.* also demonstrated the enzymatic cascade catalysis for the initiation of RAFT polymerisation to achieve multiblock and ultrahigh-molecular-weight polymers in a vessel open to air.[103]

In 2018, Tan and Zhang *et al.* reported the enzyme-initiated RAFT dispersion polymerisation of 2-hydroxypropyl methacrylate (HPMA) in water at room temperature, yielding nano-objects with different morphologies.[104] In their study (Figure 2.4), ACAC was oxidised by H_2O_2 with HRP as the catalyst, generating ACAC radicals to initiate the RAFT polymerisation. The enzyme-initiated RAFT-PISA enabled the rapid synthesis of nano-objects, including spheres, worms and vesicles in mild reaction conditions. The kinetics revealed that a high monomer conversion (>99%) was achieved within 20 min, indicating the fast generation of ACAC radicals and the high catalysis efficiency of HRP. SEC measurement exhibited a linear relationship between number-average molar mass (M_n) and monomer conversion, and the mPEG$_{113}$-PHPMA$_n$ diblock copolymers had low dispersities ($Đ < 1.20$) throughout the enzyme-initiated polymerisation process, indicating that good control was maintained throughout. The mild reaction conditions also allow the *in situ* loading of SiO_2 nanoparticles and bovine serum albumin (BSA) into vesicles. In this study, they also took advantage of RAFT polymerisation initiated by enzymatic cascade catalysis to develop oxygen-tolerant PISA based on GOx-HRP enzymatic cascade catalysis. As shown in Figure 2.4b, GOx catalysed the oxidation of glucose in the presence of oxygen to produce H_2O_2, which is subsequently used to generate ACAC radicals using HRP as the catalyst, allowing the RAFT dispersion polymerisation to occur in open vessels and multiwall plates at room temperature.[104] Overall, these studies demonstrated that the enzyme-initiated RAFT-PISA can serve as an efficient and facile platform for the preparation of functional nano-objects under the mild condition with oxygen tolerance.
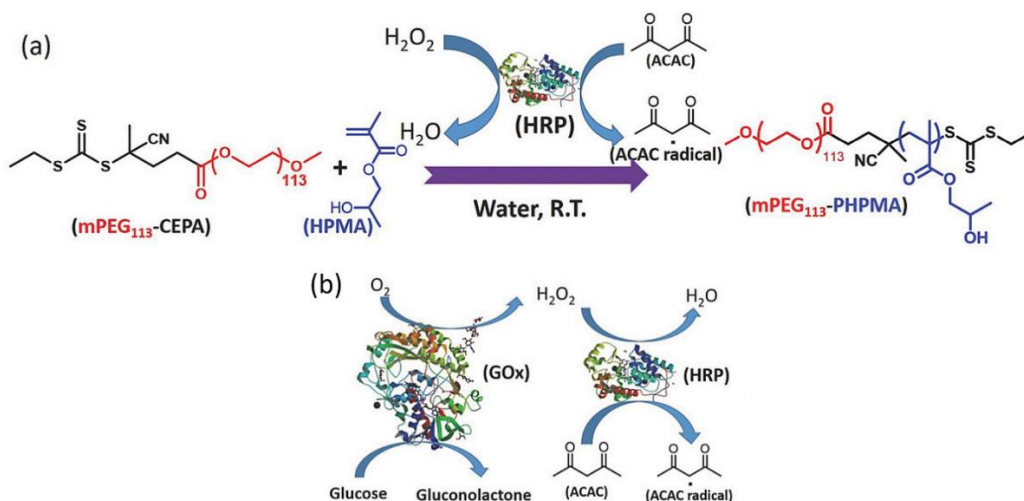
Figure 2.4 (a) Schematic illustration of enzyme-initiated aqueous RAFT dispersion polymerisation of HPMA. (b) Schematic illustration of GOx-HRP cascade reaction. Reprinted from Ref. [104] with permission. Copyright 2018, Wiley.

Later in the same year, Tan *et al.* reported the synthesis of a series of epoxy-functionalised triblock copolymer vesicles *via* enzyme-initiated PISA.[105] First, poly(glycerol monomethacrylate)-*b*-poly(2-hydroxypropyl methacrylate) (PGMA-PHPMA) diblock copolymer vesicles were prepared *via* enzyme-initiated aqueous dispersion polymerisation, and then glycidyl methacrylate (GlyMA) was used for chain extension *via* enzyme-initiated seeded emulsion polymerisation to produce epoxy-functionalised vesicles. The mild condition of enzyme-initiated RAFT polymerisation at room temperature is critical to ensure the survival of epoxy groups after the polymerisation. The synthesised triblock epoxy-functionalised vesicles were evaluated as a Pickering emulsifier in hexane-water emulsions. Furthermore, cross-linked vesicles were achieved by reacting epoxy groups with ethylenediamine.

2.2.2.2 Enzyme-assisted PISA

Enzyme catalysis has also been used for deoxygenation in the PISA process. This refers to the PISA processes that include enzymes for assisting the polymerisation but are not involved in the direct initiation. In 2014, Stevens *et al.* reported the enzyme-assisted RAFT polymerisation (Enz-RAFT) in an open vessel using GOx for deoxygenation and VA-044 as a thermal initiator.[106] GOx was used because of its high activity, the ability to completely deoxygenate the media at very low concentrations, and compatibility with organic solvents. In 2016, they further expanded the scope of Enz-RAFT to extremely

low volume (40 µL) in an open atmosphere at 45 °C, allowing for high-throughput screening applications.[107]

In 2017, Tan and Zhang *et al.* expanded the range of Enz-RAFT to dispersion polymerisation for high-throughput synthesis of well-defined AB diblock and ABC triblock copolymer nano-objects in open multiwell plates at room temperature.[108] GOx and glucose were added for deoxygenation, and SPTP and LED (λ = 405 nm) were used to initiate the polymerisation. They also demonstrated potential biologically relevant application by encapsulating HRP and BSA into vesicles without compromising protein activities. This approach facilitated high-throughput application, allowing for faster construction of the PISA phase diagram. In 2021, Tan *et al.* performed the same technique in a continuous flow reactor, offering the possibility of large-scale production of nano-objects in an oxygen-tolerant environment.[109]

Recently, the same group used a similar technique to synthesise higher-order morphologies from *tert*-butyl acrylate or *tert*-butyl methacrylate at room temperature by enzyme-assisted RAFT emulsion polymerisation.[110] The RAFT emulsion polymerisation of hydrophobic monomers usually leads to spheres because of kinetical trapping. This may be overcome by temperature-directed morphology transformation, but the high temperature hinders the preparation of thermo-sensitive or bio-related polymer nano-objects. Therefore, their study fills the gap that higher-order morphologies can be produced by emulsion polymerisation of hydrophobic methacrylic and acrylic monomers at a low temperature.

In 2020, Ng, Weil and co-authors reported a "grafting from" protocol for the preparation of DNA-polymer nanostructures from single-stranded DNA (ssDNA) under ambient conditions, aided by enzymatic degassing with glucose, glucose oxidase, and sodium pyruvate.[111] In this study, they successfully produced a series of functional DNA-polymer conjugates and DNA-diblock conjugates derived from acrylamide (DMA, NAM)/acrylate (HEA, OEGA)-based monomers.

2.2.3 Redox-PISA/oscillatory reaction

Redox initiators have been widely used in homogeneous and heterogeneous free radical polymerisations.[112-114] The low activation energy of redox initiators allow the polymerisation to proceed

at relatively lower temperatures, which is beneficial for the synthesis of thermal-sensitive polymer/drugs and bio-related materials. The applications of redox initiators in RAFT-mediated solution polymerisation at low temperature and under even freezing conditions were explored back in 2008.[115-117] Their use in RAFT-mediated dispersed system was soon reported in 2009 by Santos *et al.* Specifically, they reported the use of potassium persulphate (KPS)/sodium metabisulphite (SMB) as redox couple initiators for the mini-emulsion polymerisation of styrene with PEO-RAFT as chain transfer agent.[118] Later in 2011, An *et al.* reported an aqueous dispersion polymerisation mediated by RAFT using KPS/L-ascorbic acid sodium salt (NaAs) as redox initiator to prepare 2-methoxyethyl acrylate (MEA)-based core-cross-linked nanogels with up to 32% w/v solid content at low temperature (30 and 40 °C).[119]

KPS/ascorbic acid-based redox initiator is a classical redox couple that has been widely applied in low temperature polymerisation.[114, 120, 121] The redox initiator has a wide range of compatible reaction temperatures, which can be easily adjusted to study the effect of reaction temperature on polymerisation and morphological evolution. For example, Tan *et al.* used this redox couple for RAFT emulsion polymerisation at 25-50 °C to synthesise POEGMA-*b*-PGlyMA and yielded higher-order morphologies.[122] In this study, several factors including reaction temperature, molecular weight of macro-RAFT agent, DP of PGlyMA, and monomer concentration have been studied in detail to investigate their effects on emulsion polymerisation. The results indicated that higher temperature strongly promoted the mobility of PGlyMA (T_g= *ca.* 45 °C), and leading to morphological evolution from spheres (25 °C) to worms (37 °C) and vesicles (50 °C). More recently in 2020, Armes *et al.* reported the RAFT aqueous emulsion polymerisation with the incorporation of thermal and redox initiator at both 80 and 30 °C.[123] In this example, poly(2-(*N*-acryloyloxy)ethyl pyrrolidone) (PNAEP) was used as a new non-ionic stabliser block, and by using VA-044 as the thermal initiator at 80 °C, they achieved full conversion of styrene within 40 min while maintaining good control over dispersity ($Đ$ <1.30). Meanwhile, by using KPS/AscA redox initiator at pH=3 and 30 °C, they could achieve full conversion of *n*-butyl acrylate (*n*BA) within 25 min. Despite relatively high dispersities were observed ($Đ$ = 1.52-1.64), it is still much better control than the polymerisation of *n*BA initiated by VA-044 at 80 °C ($Đ$ > 3.00).

Oscillatory reactions are chemical systems in which one or more reacting compounds exhibit periodic changes in time or space. Most oscillating reactions involve redox reactions, and some of these are able to generate free radicals. Extensive studies have explored Belousov-Zhabotinsky (BZ) reaction for the initiation of radical polymerisations and investigated the roles of different free radicals in the BZ reaction.[124-127] The extended study of BZ reaction to PISA has not been reported until recently. In 2017, Bastakoti and Pérez-Mercader reported a one-pot synthesis of PEG-*b*-P*n*BA giant vesicles *via* PISA coupled with BZ reaction.[128] The authors proposed a mechanism (Figure 2.5) that includes the roles of different radical species in this oscillatory reaction-initiated polymerisation. The oscillations appeared after an induction time of 16 min, and the measured amplitude gradually decreased as time elapsed, which could be explained by the consumption of radicals (intermediate moieties) and the increase in viscosity during polymerisation. Due to the different chemical environments inside and outside of the self-assembled vesicles, the consumption rates and osmotic pressures become different at membrane sides, resulting in the increase in vesicle size and final formation of giant vesicles. In the same year, this group repeated this technique on a different formulation composed of acrylonitrile-based PEG-*b*-PAN diblock copolymer and succeeded in preparing giant vesicles.[129] Later on, another formulation composed of poly(ethylene glycol)-*b*-poly(ethyl acrylate) (PEG-PEA) was reported to form micelle with patchy voids.[130]
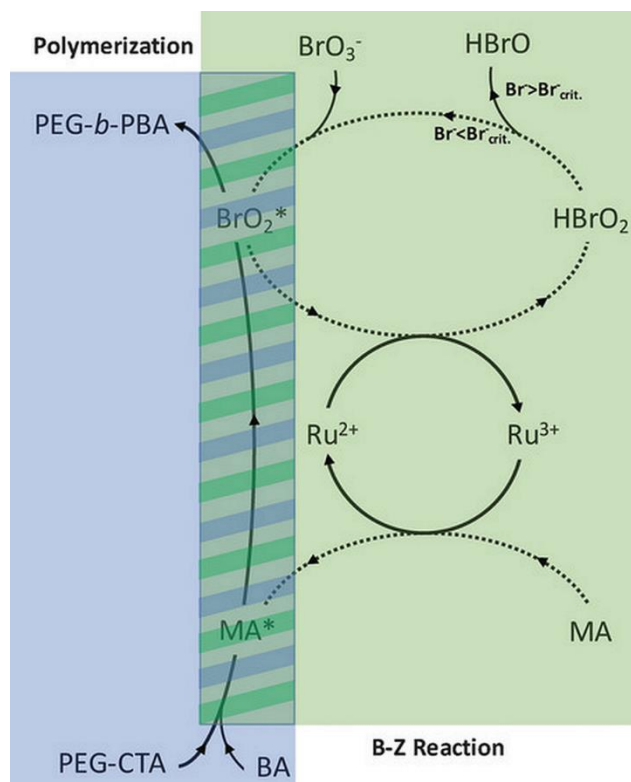
Figure 2.5 The proposed mechanism of the BZ assisted polymerisation of a PEG-*b*-PBA block co-polymer. Reprinted from Ref. [128] with permission. Copyright 2017, Wiley.

In 2019, Pérez-Mercader, Dueñas-Díez and coworkers combined the oscillatory reaction-initiated PISA with a continuously stirred tank reactor (CSTR) strategy, allowing consistent control over the PISA process and chemical properties.[131] In this study, different morphologies were obtained by tuning the residence time (τ), target DP and the BZ reactants. CSTR-BZ-PISA resembles the out-of-equilibrium and open-system characteristics of living systems, which may be suitable for studying the protolife scenarios.

More recently, Cheng and Pérez-Mercader presented a chemical fuel-driven PISA catalysed by the BZ reaction.[132] The amphiphilic block copolymers could self-organise into large multicompartmental structures, mimicking some dynamical aspects of living systems. These multicompartmental structures are highly dependent on the dissipate energy from BZ reaction. Overall, this study illustrated a strategy to design and synthesise complex microsystems that can be widely used for biosensors, microreactors, and molecular delivery.

The second group of oscillatory chemistry that successfully initiated RAFT-PISA was the pH oscillators. In 2019, the Pérez-Mercader's group reported a semi-batch bromate-sulphite (B-S) pH oscillator-driven PISA (pH-O-PISA), in which the two-way oxidation of the SO_3^{2-} by BrO_3^- generated radicals and further initiated the RAFT polymerisation of nBA on PEG-based macro-RAFT agent.[133] The complete oxidation of SO_3^{2-} to SO_4^{2-} generates H^+, while the partial oxidation of SO_3^{2-} (1-2%) to $S_2O_6^{2-}$ consumes H^+. By adjusting the H^+ concentration in the inflowed Na_2SO_3 to H_2SO_4 solution, this system can be universally adapted to different monomers. In 2021, the same group further investigated the effect of the oscillatory behaviour on polymerisation in comparison with conventional (non-oscillatory) redox initiation.[134] In this study, HPMA was chosen as the monomer, which is the first time it was used in pH-O-PISA and different morphologies, including giant vesicles, were obtained. The radical formation was switched ON/OFF by the SO_3^{2-}-BrO_3^- pH oscillator, inducing periodic polymerisation. This indicates that different kinetics have a significant impact on the final conversion (%) of a particular component and the high salt concentration in the pH oscillator was found to affect the morphology and contribute to the formation of microscale structures.

2.2.4 Ultrasound-initiated PISA

The acoustic cavitation produced by ultrasound in water can promote several physical/chemical effects including radical formation.[135] This allows the application of ultrasound in radical polymerisation, providing a "green" synthesis pathway. Ultrasound has been extensively studied to initiate free radical polymerisations in both homogeneous and heterogeneous systems, as well as to accelerate the decomposition of chemical initiators to assist polymerisation. In 2017, Qiao and Ashokkumar and co-workers reported the first use of ultrasound derived radicals to initiate RAFT polymerisation in aqueous medium.[136] In their study, a high frequency (414 kHz) was applied, at which the hydroxyl radical generation by H_2O sonolysis was enhanced and the possibility of polymer degradation is minimised. This process allowed the controlled polymerisation of a range of water-soluble acrylates and methacrylates. However, it was found the ability of ultrasonic irradiation to generate radicals is concentration dependent. Bulky monomers or monomers with high concentrations could suffer from no polymerisation. It was also observed that sono-RAFT polymerisation can be regulated ON/OFF by simply switching ON/OFF the sonication. The success of ultrasound-induced controlled radical

polymerisation provides a "green", externally regulated and easily scalable method for a range of monomers.

Later in 2018, Qiao *et al.* reported the first sono-RAFT-PISA using *N*-isopropylacrylamide (NIPAM) as the monomer to synthesise thermo-responsive spherical nanogels at 45 °C.[137] Temporal control was realised by exposing the polymerisation to an alternating "ON/OFF" period of ultrasound. Furthermore, *N,N'*-methylenebis(acrylamide) (MBA) was used as the comonomer to achieve core-cross-linked nanoparticles that would maintain the morphology below the lower critical solution temperature (LCST) of PNIPAM. The cross-linked nanogels are thermo-sensitive and can undergo reversible shrink/swell cycles in heating (45 °C)/cooling (25 °C) cycles.

2.3 Controlled and High-Order Morphologies by PISA

One of the main benefits of the PISA process is that the morphology of the self-assembled nano-objects can be easily tuned by adjusting the DP of the core-forming block. In a dispersed system without kinetic trapping, the evolution from spheres to worms to vesicles with the increasing DP is usually observed. Over the past decade, many efforts have been made to achieve morphological control, and interest in expanding the morphological library has continued unabatedly. In this section, we focus on some pioneering works and most recent studies that realised the control of morphology toward high-order structures. The order of morphology usually depends on the packing parameter (P, defined as $P = V/a_0 l_c$, in which V and l_c represent the volume and length of the hydrophobic block, respectively, and a_0 stands for the effective area of the hydrophilic headgroup), high-order structures occur when $P > 1$. This could be achieved by adjusting several factors, including DP and solvophobicity of the hydrophobic block, solvent system, and block copolymer architecture. In the following, these factors were summarised as determinants for achieving nano-objects with high-order and complex morphologies.

2.3.1 Varying the chain length or DP of the hydrophobic block

Tuning the chain length or DP of the hydrophobic block is the most direct way to control the morphology transformation from spheres to higher-order morphologies, such as worms, vesicles, lamella, spongesomes and cubosomes. As the molar mass/DP of the hydrophobic block increases, the packing parameter also increases simultaneously. Currently, there are a number of studies reported the

morphological transformation beyond vesicles, including lamella, multilamellar vesicles,[78] large compound vesicles[138] or precipitates.[139, 140] For example, in 2010, Pan and co-authors discovered that higher-order morphology vesicles with complex internal structures; the morphologies evolved from spheres to vesicles, and to multiple morphologies including nanotubes, doughnuts, spongesomes and onion-like vesicles by tuning the chain length and thus the ratio of hydrophobic to hydrophilic blocks.[141] Then in 2015, they further reported the realisation of large compound vesicles (LCVs) and hexagonally packed hollow hoops (HHHs, i.e. hexasomes) with packing parameter larger than 1 by PISA.[20] In addition, they probed the mechanism of the transformation from vesicles or LCVs to HHHs. Similar to the annealing of copolymers swollen by DMF in the nanoprecipitation approach,[142] the high feed molar ratio of St/PDMAEMA = 10000 allowed PS chains to be well swollen by the residual St monomer, which has a beneficial effect on the chain mobility and the morphological transition. The good mobility of copolymer chains also allowed deformation and fusion of vesicles, eventually leading to the formation of high order structure. This is the first study to utilise the scalable PISA approach to fabricate PS-based inverse bicontinuous mesophases. However, the high feed molar ratio of St/PDMAEMA and a high monomer concentration were necessary for the fabrication of HHHs, which would result in high residual monomer content that may limit the potential applications.

In 2019, An, Wu and Lv exploited the scalable preparation of alternating PDMA-*b*-P(St-*alt*-PFS) block copolymer particles with high order morphologies (LCVs, spongesomes, hexasomes and cubosomes).[19] High monomer conversion (typically ≥ 90%) and high solid content (40%) were achieved simultaneously, and morphological transition from spheres to final cubosomes was observed with the growth of the core-forming block. The influence of some key parameters on the morphological evolution was investigated, it was concluded that the relatively short solvophilic block and high solid content were required to promote the production of inverse bicontinuous mesophases. In addition, the effect of different co-solvent systems was also studied, and it was found that the use of ethanol with 2% toluene afforded more ordered mesophases with improved colloidal dispersity. These mesophase structures were characterised by TEM, SEM and small-angle X-ray scattering (SAXS), revealing the *Im3̄m* cubosome and *p6mm* hexosome structures. Later on, the successful preparation of inverse bicontinuous mesophases was also achieved by polymerisation-induced cooperative assembly (PICA) using RAFT agent and PDMA-CTA as a dual controlling agent.[25] In 2021, the same method has been

used to obtain poly(*N,N*-dimethylacrylamide)-*b*-poly(4-*tert*-butoxystyrene-*co*-pentafluorostyrene) inverse bicontinuous mesophases *via* PISA.[24]

In 2021, Fan, Thang and co-workers reported the first preparation of degradable inverse bicontinuous structures by PISA.[18] First, 4-(4,4,5,5-tetramethyl-1,3,2-dioxaborolan-2-yl)benzyl acrylate (TBA) was designed and synthesised as the core-forming monomer, which can promise a high conversion compared to styrene-based monomers. The pinacol boronic ester group in TBA is extremely sensitive to reactive oxygen species, such as H_2O_2, this makes the polymer and the formed nanostructures responsive to a specific stimulus. The morphological evolution from spheres to cubosomes and hexosomes with the increasing DP of PTBA was unambiguously observed and analysed by TEM (Figure 2.6b-e), SEM and SAXS. In addition, a phase diagram (Figure 2.6a) illustrating the effect of DP, solid content, and stabliser block chain length on the morphologies were also constructed. Next, the degradation study of the obtained inverse bicontinuous structures was performed by exposing the diluted cubosome suspension to H_2O_2. The stimuli-responsiveness and degradable feature of the inverse bicontinuous cubic and hexagonal mesophases make them potentially applicable for loading and triggering the release of payloads such as drugs and proteins.

In the same year, Chen and Yang *et al.* demonstrated the preparation of inverse bicontinuous structures by PISA *via* intramolecularly folded single-chain nanoparticles (SCNPs).[21] The stabliser block (P4VP-CTA) was lightly cross-linked with 1,4-diiodobutane to obtain single-chain nanoparticles. Subsequently, PISA with styrene was performed in ethanol *via* these SCNPs to achieve inverse bicontinuous structures (Figure 2.6f). The cross-linking of solvophilic chains leads to a smaller cross-sectional molecular area (a_0), which will enlarge the packing parameter (*P*), and enable the preparation of polymer cubosome with well-defined structures. The morphology of structures prepared against linear P4VP-CTA and SCNPs with different degrees of cross-linking was compared. The obtained phase diagram (Figure 2.6g) indicated the morphological evolution depends both on the cross-linking degree and DP of PS block, and the inverse bicontinuous structures can be easily achieved within a much broader window *via* this strategy.
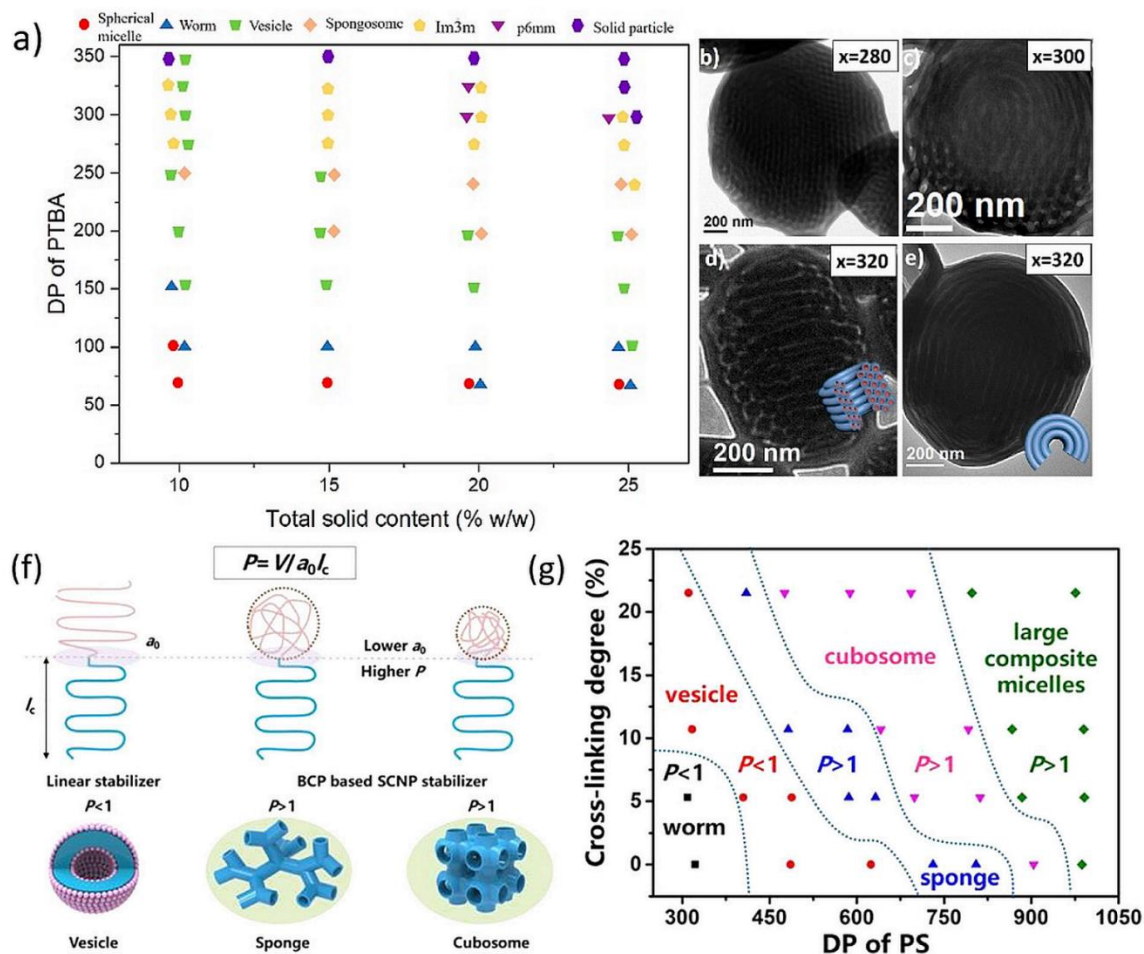
Figure 2.6 (a) Phase diagram of the PDMA$_{45}$-*b*-PTBA$_x$ block copolymer particle during PISA with different solid contents and varying DP of PTBA. (b–e) TEM images of the particle transition from cubosome to hexosome. Reprinted from Ref. [18] with permission. Copyright 2021, American Chemical Society. (f) Illustrative self-assembly of a linear block copolymer and the two SCNP-contained polymers with varied SCNP sizes and the corresponding morphologies. (g) Phase diagram of the superstructures from P4VP(SCNP)$_{35}$-PS$_n$ with various cross-linking degrees of P4VP(SCNP)$_{35}$. Reprinted from Ref. [21] with permission. Copyright 2021, American Chemical Society.

2.3.2 Varying solvophobicity of core-forming block

The hydrophobicity of core-forming monomer has a great influence on the final morphology, the effect of this factor has been revealed by many studies. For example, An *et al.* synthesised a series of alkyl α-hydroxymethyl acrylates, including methyl (MHMA), ethyl (EHMA), isopropyl (iPrHMA), and *n*-butyl

(nBHMA) α-hydroxymethyl acrylates, with different water solubility.[79] MHMA and EHMA have higher water solubility (~0.3 g/mL and ~0.2 g/mL respectively) were polymerised *via* aqueous dispersion polymerisation, and iPrHMA with moderate water solubility (~0.06 g/mL) was used for dispersion-emulsion polymerisation. The achieved morphologies by these different monomers were compared. The TEM image and DLS analysis indicated that PEG_{45}-$PMHMA_{166}$ formed spheres, which contrasts with lamellae by PEG_{45}-$PEHMA_{100}$ and vesicles by PEG_{45}-$PEHMA_{200}$. This can be inferred that core-forming block with higher hydrophobicity provides a stronger driving force for the morphology transition, and will require lower DP to achieve higher-order morphology. For PiPrHMA with higher hydrophobicity, vesicles were obtained for PEG_{45}-$PiPrHMA_{100}$ at an even lower DP. Besides, lamellae, tubular vesicles and vesicle clusters were also observed for this polymer system, which may provide a unique opportunity to access some extraordinary morphologies.

Yuan, Wei and co-workers investigated the application of three semi-fluorinated methacrylates, namely, 2-(perfluorobutyl)ethyl methacrylate (FBEMA), 2-(perfluorohexyl)ethyl methacrylate (FHEMA), and 2-(perfluorooctyl)ethyl methacrylate (FOEMA), in PISA.[143] It has been shown that the dispersion polymerisation of FBEMA in ethanol led to spheres, worms and vesicles, whereas FHEMA only produced kinetically frozen spheres because of the relatively strong associative interactions among the fluoro-containing side-chains. Cylindrical micelles were obtained for all PDMA-PFOEMA *via* PISA, due to the peculiar self-assembly behaviour from the liquid crystalline ordering of PFOEMA. This additional study demonstrates the effect of core-forming monomers on morphologies.

The hydrophobicity of some monomers and polymers can be altered by external stimuli, thus affecting the PISA morphologies. For example, the hydrophobicity of PHPMA is known to increase with increasing temperature. Tan *et al.* then designed a temperature-programmed photo-PISA by keeping the temperature maintained or changed throughout the polymerisation.[138] This resulted in a diverse set of complex morphologies, including worms, vesicles and large compound vesicles, by the same $mPEG_{113}$-$PHPMA_{400}$ with different programmed temperature profiles.

The adjustment of polymer hydrophobicity can also be achieved by interactions with comonomers. In this regard, Zhang, Hong and co-workers explored the effect of solvophobic and aromatic interactions on PISA morphology.[144] 7-(2-Methacryloyloxyethoxy)-4-methylcoumarin (CMA) was selected as the

core-forming monomer due to the aromaticity of the coumarin units, which allow aromatic interaction with other monomers. Three comonomers ranging from non-aromatic to strongly aromatic were selected to compare the effect of aromatic interaction. By inserting non-aromatic units into the PCMA block, both the aromatic and hydrophobic interactions were weakened, leading to the increased flexibility of the hydrophobic block. In clear contrast, the insertion of strongly aromatic comonomer enhanced both aromatic and solvophobic interactions, which lead to more rigid chains in membrane forming and vesicle fusion to form nanotubes. This is a good example demonstrating the control over the vesicular size and even steering the vesicle fusion to form the tubular structures that can be achieved by adjusting the type and aspect ratio of the comonomer.

The hydrophobicity of the particle core can also be tuned by zwitterionic copolymerisation. For example, Cai *et al.* showed the sequence-controlled synthesis of charge-dictated alternating or gradient terpolymer *via* polymerisation-induced electrostatic self-assembly (PIESA).[145] The oppositely-charged monomers were copolymerised by photo-switched RAFT to achieve terpolymer with controlled sequence. The hydrophobicity of the polyions was adjusted, resulting in the change of the polyion complex nanostructures from water-soluble polymer to stable nano-objects, and to precipitation. By this approach, the shape of nanostructures as well as the size and thickness of micron-sized ultrathin lamellae and vesicles could be efficiently controlled.

2.3.3 Varying solvent

In addition to varying the monomer composition, solvent quality plays a significant role in PISA, and many researchers have investigated the role of solvent quality on the morphological evolution during PISA. Co-solvent is the most straightforward strategy to determine this effect on nanoparticle morphology, and it affects the degree of solvation or plasticisation of the core-forming block.[146] For instance, Arms *et al.* reported the preparation of inverse bicontinuous phases by alternating copolymerisation of styrene with *N*-phenylmaleimide (NMI) in a 50:50 w/w ethanol/methyl ethyl ketone (MEK) co-solvent system.[22] The core-forming block has a relatively high glass transition temperature (T_g) (219 °C), which means it is extremely rigid. However, the MEK co-solvent provided better solubilisation of NMI monomer and enhanced the mobility of the growing P(St-*alt*-NMI) chains. Taking the advantage of high chain mobility induced by MEK, three inverse bicontinuous phases

(perforated ellipsoidal lamellae, bicontinuous ellipsoids and large compound micelles) were achieved in this PISA. To further investigate the role of MEK, control experiments using 50: 50 w/w ethanol/1,4-dioxane were conducted under same conditions, which only yielded kinetically trapped morphologies such as spheres, worms and worm clusters. This study also suggested that high chain mobility in an appropriate solvent system is essential for achieving high order morphologies.

An, Wu and Lv reported a rational access to poly(*N,N*-dimethylacrylamide)-*b*-poly(2,3,4,5,6-pentafluorostyrene) (PDMA-*b*-PPFS) *via* PISA in 5-20% DMF/ethanol.[146] When 5% DMF/ethanol was used, a morphological transition from spheres to vesicles and finally nanotubes were observed. In 10% DMF/ethanol, morphology transformed from spheres to vesicles, then vesicles started to fuse into vesicular dimers, followed by nanotubes and multi-wall nanotubes. When 20% DMF/ethanol was used, typical sphere-worm-vesicle-large compound vesicles morphological transition was observed, with no sign of nanotubes. The authors also deduced the hypothesis that nanotubes can be formed when the polymerisation temperature (T_p) is below or close to the solvated glass transition temperature (T_{sg}). This study revealed the effect of solvent quality on chain mobility and the subsequent morphological transition pathway. Luo also recently reported the morphological transition of PEG-*b*-PS by PISA using co-solvents.[147] When methanol and water were used, PEG-*b*-PS micellar aggregates without any internal structure were observed at 30% solid content. However, when methanol/THF/water (1.15/0.45/0.4, v/v/v) was used as co-solvent, a morphological transition from vesicles to large compound vesicles and final inverse bicontinuous phases was observed. This study once again demonstrated the effect of co-solvent on morphology, and provided a facile method for developing inverse bicontinuous phases.

Furthermore, it was demonstrated by Fielding *et al.* that the nanoparticle size could be controlled by altering the co-solvent composition. In this example, anionic poly(potassium 3-sulphopropyl methacrylate) (PKSPMA) macro-CTAs were chain-extended with BzMA in alcohol/water mixtures to form PKSPMA–PBzMA nanoparticles *via* PISA.[148] The influence of co-solvent was systematically investigated by changing the alcohol/water ratio, the alcohol type (ethanol or methanol) and relative copolymer composition. For the fixed copolymer composition, the nanoparticle diameter could be tuned

from 20 to 200 nm using different ratios of ethanol/water or methanol/water with fixed copolymer composition.

Instead of co-solvents, some additives in solvent could also play a great role in PISA. For example, cyclodextrin (CD) has been used by Yuan *et al.* to improve the solubility of styrene (St) *via* the formation of a water-soluble host-guest complex. This allowed the aqueous dispersion polymerisation of St, and morphologies including lamellae, nanotubes and dumbbell-like nanoparticles were achieved.[149] More recently, the same group obtained new nanoflower-like morphology by using host-guest modulated PISA with increased polymerisation rate.[150]

2.3.4 Varying block copolymer architecture

Varying the polymer architectures in PISA is another important strategy to achieve different morphologies and even high-order morphologies. In this regard, An *et al.* reported the star architecture of PEG-*b*-(PDAAM)$_2$, which was synthesised by RAFT polymerisation, can promote the transition to obtain higher-order morphologies at both lower solid content and lower DP.[151] In another work, Zhang, Han and co-workers synthesised a series of mono- and multifunctional trithiocarbonates, which were chain extended with P4VP to achieve macro-RAFT agents with different numbers of branches.[152] Linear and star block copolymer (BCP) nano-objects of [P4VP-*b*-PS]$_n$ with the arm number *n* at 1, 2, 3, and 4 were synthesised by PISA (Figure 2.7). The size and morphology of the [P4VP-*b*-PS]$_n$ nano-objects were found to be correlative to arm number *n*. Nano-objects formed from Star [P4VP-*b*-PS]$_n$ underwent the morphological transition from vesicles to lacunal spheres and porous nanospheres, presumably because star BCPs have better solubility (higher critical aggregation concentrations) than linear ones. Their research indicates that BCP architecture is a significant parameter to dedicate the size and morphology of nano-objects under PISA conditions.
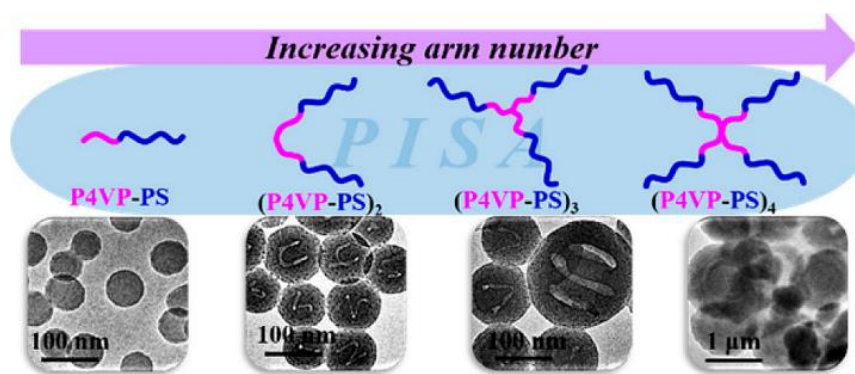
Figure 2.7 TEM images of [P4VP-*b*-PS]$_n$ nanoassemblies with different block copolymer architectures. Reprinted from Ref. [152] with permission. Copyright 2018, American Chemical Society.

Instead of star architecture, it was found that solvophobic-solvophilic-solvophobic (BAB) block copolymers allow the preparation of loop-stablised morphologies by PISA. The Zhang group reported a series of PS-*b*-PEG-*b*-PS,[153] PS-*b*-PNIPAM-*b*-PS,[154] and PS-*b*-P4VP-*b*-PS[155] loop-stablised nano-objects prepared by PISA, and investigated the morphology variations of nano-objects prepared from between AB and BAB copolymers. They found PS-*b*-PEG$_{136}$-*b*-PS forms large-sized aggregates due to the presence of a bridging linkage between the two terminal hydrophobic PS blocks compared to their AB-type counterparts.[153] In another study, it was found that the size of PS$_{167}$-*b*-PNIPAM$_{196}$-*b*-PS$_{167}$ nanospheres (25 nm) was smaller than the PNIPAM$_{98}$-*b*-PS$_{328}$ nanospheres (50 nm).[154] Furthermore, lacunal nanospheres (around 115 nm) were obtained for PS$_{282}$-*b*-P4VP$_{58}$-*b*-PS$_{282}$, which were much different from the P4VP$_{58}$-*b*-PS$_{550}$ nanospheres (67 nm) and P4VP$_{25}$-*b*-PS$_{264}$ entrapped vesicles (143 nm).[155] In addition to the work from Zhang's group, the Rieger group also studied various loop-stablised BAB particles by PISA (Flower PISA), and they found loop solvophilic chains exhibit different stablising behaviours, the bridges between the B blocks lead to the formation of gel-like dynamic polymer network.[156-158]

Using a similar strategy, Zhang, Li and co-workers demonstrated the *in situ* synthesis of ingenious nano-objects by the cooperative dispersion polymerisation with PEG-TTC and TTC-PEG-TTC macro-RAFT agents.[159] The resulted PEG-PS/PS-PEG-PS (AB/BAB) polymer blends with various ratios could lead to vesicles (ratio 6/0), compartmentalised vesicles with different sizes and wall thickness (ratio 6/1 to 6/3), and porous nanospheres (ratio 6/4).

2.3.5 Multicompartment nano-objects

Multicompartment nano-objects usually were prepared from block copolymers including one solvophilic and two or more incompatible solvophobic core-forming blocks that can lead to segmented anisotropic structures or other complex nano-objects. The Zhang group have conducted extensive studies on the preparation of multicompartment block copolymer nanoparticles (MBCNs) *via* PISA.[160-164] Nanospheres of different formulations with segregated patches on the surface were obtained by dispersion polymerisation or seeded quasi-solution/dispersion/emulsion polymerisation with subsequent solvent replacement or temperature change.[165] The phase separation between polymer blocks was triggered by the difference in solubility of one block in the new solvent or by the LCST or upper critical solution temperature (UCST) of the polymer.

Recently, *in situ* phase separation between incompatible core-forming blocks leading to multicompartment patchy particles has also been reported. For example, Yuan *et al.* reported fluoro-containing triblock terpolymer assemblies by PISA.[166] In this example, PDMA-*b*-PBzMA-*b*-PFHEMA terpolymers with different DP of PBzMA and PFHEMA were prepared by seeded RAFT dispersion polymerisation of FHEMA with spheres, worms and vesicles made from PDMA-*b*-PBzMA. Phase segregation between PBzMA and PFHEMA during polymerisation led to a series of compartmentalised nanostructures including core-shell-corona, patchy-like, ribbon-shell and raspberry-like micelles as well as core-shell-corona vesicles. The same group also reported the synthesis of PDMA-*b*-PBzMA-*b*-PFOEMA assemblies by PISA.[167] Due to the liquid crystalline alignment of PFOEMA, spheroids and cylinders with segregated PFOEMA and PBzMA nanodomains were obtained. This study demonstrated the influence of fluoro-containing mesogen on the self-assembly behaviour and morphology.

Tan *et al.* reported the preparation of patchy cylindrical micelles by seeded photo-PISA in water using cross-linked cylindrical micelles as seeds.[168] The further extension of the third block led to nanoscale phase separation within the core-forming block, which contributes to the patchy morphology. By varying the DP of the third block, the roughness of patchy cylindrical micelles could be controlled. This

study indicates that the cross-linking of the second block is required for the phase separation, and non-cross-linked control only resulted in short cylindrical micelles and vesicles.

In 2020, Yuan, Yang and co-workers demonstrated the preparation of rarely achieved colloidal molecules (CMs) by seeded dispersion polymerisation of HPMA with PDMA-*b*-PBzMA nanoparticles as seeds.[26] First, the PDMA-*b*-PBzMA colloidal atoms (CAs) were synthesised *via* PISA in ethanol, it was then dialysed against water (pH ~2) to remove ethanol. In the growth of the third block, they found that phase separation between PHPMA and PBzMA occurs as the DP of PHPMA increases. When PHPMA domains reached a critical size, they combined into PHPMA central colloidal atoms and led to colloidal clusters. When the volume ratio of PHPMA and PBzMA V_H/V_B >1, monovalent Janus intermediates would assemble hierarchically into AB_n-type CMs, with *n* increased with V_H/V_B. When $V_H/V_B \leq 1$, divalent intermediates lead to colloidal chains. This study achieved colloidal molecules with *n* from 2 to 6, and they observed the formation of "colloidal polymer", which is a beaded chain-like architecture. However, this study involved two steps and required a solvent exchange process to meet the solubility requirements of each block. Further exploration is warrant to facilitate the application of this strategy to more block copolymer systems.

2.4 Hybrid Materials Synthesised *via* PISA

Many efforts have been made to fabricate organic-polymer and inorganic-polymer nanocomposites with constituent materials such as proteins, (poly)peptides, metals, metal oxides, mineral oxides. The nanocomposites containing hybrid materials combine the attractive properties of both polymer and the constituents, which endows them with a wide range of synergistic effects. PISA offers a convenient and scalable strategy for the preparation of polymeric colloids, thus attracting extensive research interest in the preparation of hybrid materials with polymer colloids as scaffolds. The common connections between polymeric colloids and other materials *via* PISA are 1) PISA-based polymeric colloids as scaffolds with decorating materials on the surface; 2) Surface-initiated PISA from the surface of other materials; 3) *In situ* encapsulation of cargos into PISA nano-objects during the polymerisation; 4) Covalently bonded hybrid polymeric colloids with other materials attaching to either the solvophilic block or the solvophobic block. This section will introduce the design of these four types of hybrid materials by discussing some relevant examples.

2.4.1 PISA-based polymeric colloids as scaffolds for nanocomposite fabrication

One approach that allows polymeric colloids to combine with another material, such as metal nanoparticles, is to form nanocomposites by "decorating" target material on the surface of colloids. To achieve successful attaching, a common strategy is to bind on colloids by ligand exchange or complexation process; another strategy is to mix metal precursor with polymeric colloids containing docking sites, followed by *in situ* formation of metal nanoparticles on the colloid surface. In this approach, it is the solvophilic or interfacial block of the block copolymer colloids that usually acts as the docking sites to provide interaction with the other material, and maintain the stability of composites in the meantime. Therefore, the design of solvophilic or interfacial block becomes important for the successful fabrication of composites.

An example of this approach was reported by Davis and Boyer *et al.* using RAFT dispersion polymerisation of styrene to prepare various nano-objects and subsequent reduction of chloroauric acid to form gold nanoparticles on their surfaces.[169] First, the POEGMA macro-RAFT agent was chain extended with 2-(*N,N*-dimethylamino)ethyl methacrylate (DMAEMA) to synthesise POEGMA-*b*-PDMAEMA-CTA macro-RAFT agent, which contains tertiary amine on the interfacial block. The subsequent dispersion polymerisation of styrene resulted in spheres (s), worms (w) and vesicles (v) by varying the DP of PS block. Aliquots of suspension of s, w, v were mixed with chloroauric acid, then the addition $NaBH_4$ led to the reduction of chloroauric acid and the formation of gold nanoparticles. The complexation of the tertiary amine group with chloroauric acid allowed the immobilisation of gold nanoparticles between the hydrophilic and hydrophobic blocks.

The work by Zhang's group demonstrated the use of multicompartment nanoparticles (MCBNs) constructed with the brush block terpolymer as a scaffold for Au nanocatalyst.[170] First, a new brush macro-RAFT agent was synthesised by polymerisation of *p*-chloromethylstyrene (CMS) to afford PCMS$_{21}$-TTC, and then the nucleophilic substitution reaction between PCMS$_{21}$-TTC and pre-synthesised thiol-terminated P4VP$_{25}$-SH resulted in (PCMS-*g*-P4VP)-TTC. MCBNs were obtained by dispersion polymerisation of styrene mediated with (PCMS-*g*-P4VP)-TTC. Au nanoparticles were immobilised on the surface of MCBNs through the coordination between the pyridine ligand with the gold ions and the

following reduction by NaBH$_4$. The prepared Au@MCBNs were used as nanocatalyst and showed high catalytic efficiency in aerobic alcohol oxidation.

In addition to above work, many other studies have used this approach to synthesise a wide variety of hybrid nanocomposites. For example, in 2014, Davis and Boyer *et al.* reported the complexation between carboxylic acid and iron ions.[171] Similar to their work of POEGMA-*b*-PDMAEMA-*b*-PS nanoparticles, POEGMA-*b*-MAA-*b*-PS triblock terpolymer nano-objects were obtained *via* PISA. The subsequent alkaline co-precipitation of the iron (II) and (III) salts led to formation of iron oxide nanoparticles (IONP). The complexation between MAA and iron ion (Fe^{II}/Fe^{III}) mixture allowed the immobilisation of IONP in the central block. Similarly, Matyjaszweski and Pietrasik and co-workers reported the use of -*b*-PS nanoparticles as templates for the synthesis of Ag-polymer nanocomposites. The complexation between the PAA block and Ag$^+$ ions and subsequent reduction resulted in AgNPs immobilised on the shell of polymeric nanoparticles. The silver-polymer nanocomposites were applied as catalyst and SERs substrate.[172] An *et al.* employed a "multitask" monomer 2-(acetoacetoxy)ethyl methacrylate (AEMA) to produce nanospheres and vesicles bearing reactive β-ketoester groups. The β-ketoester group is multifunctional that could not only react with alkoxylamine or bisalkoxylamine to achieve oxime for cross-linking under ambient conditions, but can also complex with metal ions to produce silver nanoparticle within the nano-objects by reduction.[173]

Instead of forming metal nanoparticles *in situ*, pre-formed metal or metal oxides nanoparticles can also be immobilised with polymeric colloids *via* electrostatic charge interactions, ligand exchange, host-guest complexation, etc. For example, Semsarilar, Quemener and co-workers reported the PISA process to prepare PMAA-*b*-PMMA spheres, worms and vesicles bearing negatively charged shells.[174] Magnetic iron nanoparticles coated with poly(methacrylic acid)-*b*-poly(quaternised 2-(dimethylamino)ethyl methacrylate) (PMAA-*b*-PQDMAEMA) were synthesised and incorporated with polymeric nano-objects *via* electrostatic interaction to form nanocomposites. The mixed matrix was spin-coated to form membranes with enhanced mechanical properties. Hawkett *et al.* also prepared superparamagnetic iron oxide nanoparticles (SPIONs)-decorated nanofibres by simple mixing of SPIONs with PISA-prepared nanofibres at an appropriate pH.[175] A dibenzyl trithiocarbonate (DBTC) was employed as RAFT agent to synthesise DBTC-P(*n*BA-*co*-AA)$_2$ macro-RAFT agent, which was chain extended with PS

block to form PS-*b*-P(BA-*co*-AA)$_2$ nanofibres. At an appropriate pH, SPIONs were blended with nanofibres under high shear, the opposite charge interactions led to the absorption of SPIONs on the surface of nanofibres. Later on, the Semsarilar group reported a one-pot PISA synthesis of PMAA-*b*-PMMA block copolymer nanoparticles decorated with iron oxide nanoparticles.[176] During the PISA process with the presence of oleic acid-stablised iron oxide nanoparticles, ligand exchange occurred between oleic acid and PAA chains, resulting in the attachment of iron oxide nanoparticles on the surface of polymeric nanoparticles.

The work by Singha *et al.* presented a waterborne epoxy-based fluorescent adhesive ornamented with graphene quantum dots (GQDs).[177] The GQDs were prepared by hydrothermal process, then mixed with the poly(1-vinyl-2-pyrrolidone) (PVP) macro-RAFT agent and glycidyl methacrylate monomer to undergo surfactant-free miniemulsion PISA. The carboxyl and hydroxyl groups on the surface of GQD nanoparticles interacted with the nitrogen of the PVP block *via* noncovalent interaction, resulting in a honeycomb-like structure. The prepared block copolymer/GQD emulsions were applied to adhere ceramic and glass substrates, and showed better adhesion strength than pure block copolymer adhesive.

Recently, Fan, Thang and co-workers exploited the "host-guest" complexation between β-cyclodextrin (β-CD) and adamantane to realise combining between AuNPs and different polymeric colloids (Figure 2.8).[178] First, β-CD was attached to the R group of RAFT agent *via* esterification. The β-CD-CDPA was chain extended with OEGMA to afford macro-RAFT agent, followed by further chain extension of HPMA *via* PISA to afford spheres, worms and vesicles with β-CD on the surface. Pre-formed AuNPs stablised with polymer ligands containing adamantanyl (Ada) moiety were prepared separately. Subsequently, by incubating these polymeric nano-objects with Ada stablised-AuNPs in different ratios, a series of different polymer/gold nanocomposites, including AuNPs decorated polymer vesicles, polymer sphere nano-flowers, polymer sphere nano-patterns, and polymer nano-worms were successfully prepared. This study provided a new and efficient strategy for the preparation of polymer-metal nanocomposites with the desired ornamentation.
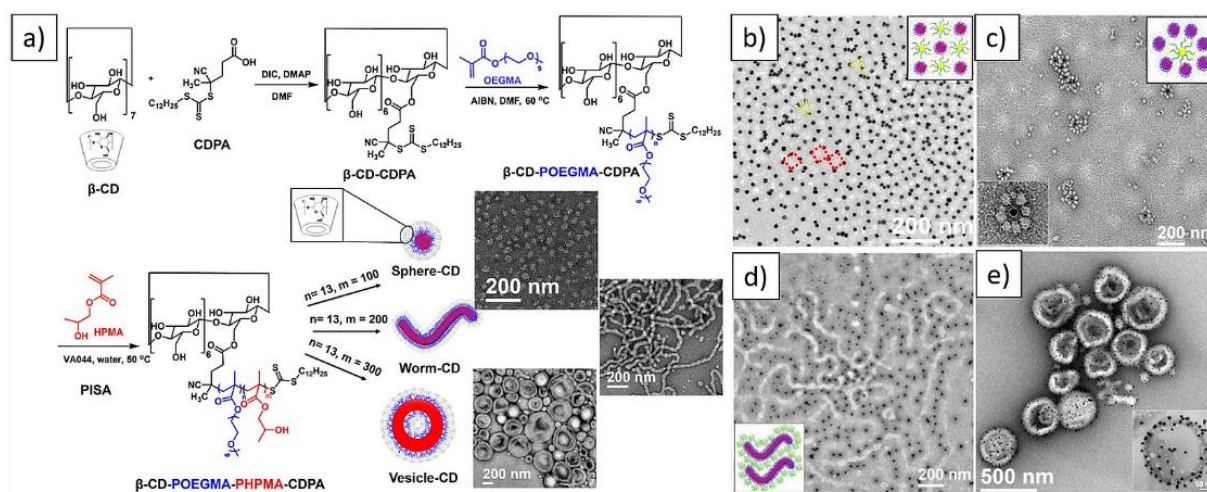
Figure 2.8 (a) Synthesis of β-CD decorated diblock copolymer nano-objects vis aqueous PISA (b-e) Representative TEM images of AuNPs decorated polymer sphere nano-pattern, sphere nano-flowers, nano-worms and vesicles. Reprinted from Ref. [178] with permission. Copyright 2020, American Chemical Society.

2.4.2 Surface-initiated PISA from the particle surface

In 2016, the Benicewicz group reported the seminal work of surface-initiated PISA from SiO_2 nanoparticles and obtained various 1-D structures, including short strings, branched long strings, and highly branched string networks.[179] The bare silica nanoparticles of diameter ~ 15 nm were attached with medium graft density (~ 0.1 chain per nm^2) of RAFT agent 2-cyano-2-propyl benzodithioate (CPDB) and chain extended with 2-hydroxyethyl methacrylate (HEMA). The medium graft density allowed both enough polymer chains to solubilise silica nanoparticles and enough space for the growth of second polymer population. The RAFT end of PHEMA chains were cleaved off and the silica nanoparticles were attached with the second round of RAFT agent to afford SiO_2-g-(PHEMA, CPDB). It was then used to mediate the surface-initiated dispersion polymerisation of BzMA in methanol. With the continuous increase of PBzMA chain length, the silica nanoparticles self-assembled into 1D silica-polymer nanocomposites (Figure 2.9). Later in the same year, they extended this method by performing polymerisation of BzMA from SiO_2-g-(PHPMA, CPDB) nanoparticles and obtained stable 3D assemblies such as single-walled hybrid vesicles.[180]
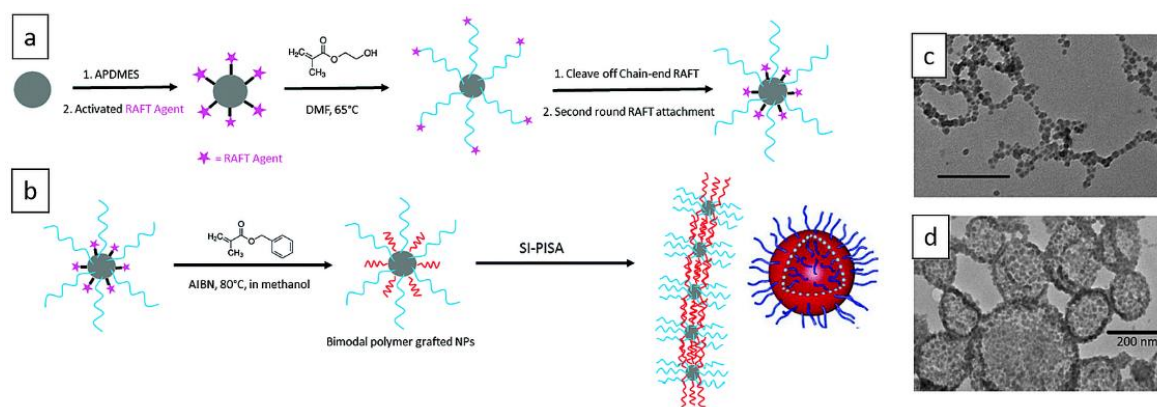
Figure 2.9 (a) Synthesis of SiO$_2$-*g*-(PHPMA, CPDB) nanoparticles. (b) One-pot surface-initiated RAFT polymerisation-induced self-assembly of grafted NPs into highly branched string networks and vesicles. TEM images of (c) highly branched string networks and (b) vesicles. Reprinted from Ref. [179, 180] with permission. Copyright 2016, Royal Society of Chemistry.

The Bourgeat-Lami group demonstrated another approach by nitroxide-mediated emulsion polymerisation of *n*-butyl methacrylate (BMA) and styrene to form multipod-like silica/polymer latexes.[28] A PEG-based macroalkoxyamine containing a small amount of styrene (P[(OEGMA$_{950}$)$_{12}$-*co*-St$_1$]-SG$_1$) was synthesised and attached to the surface of acidified silica particles through hydrogen-bonding interactions. The subsequent polymerisation of BMA and styrene initiated by the marcoalkoxyamine initiator led to the self-assembly of block copolymers around the central silica spheres. By varying the macroinitiator concentration or the silica particle size, dumbbell-, daisy- or raspberry-like hybrid composites were obtained. They also extended the surface PISA to achieve new hybrid morphologies. It was found that the morphology depends strongly on the size of the silica nanoparticles. When silica nanoparticles with diameter around 30 nm were used, "armoured" fibres and vesicles were formed. When ~136 nm silica were used, the morphologies were core-shell, "half-capped" spheres, tadpole-like and "snowman"-vesicles instead. With size around 230 nm, core-shell and "half-capped" spheres were observed.[181]

2.4.3 *In situ* encapsulation during PISA

The encapsulation of cargos into the polymeric nanoparticles during the PISA process is one of the most common methods for preparing hybrid nanocomposites. One specific example is the encapsulation of

hydrophobic drugs into the hydrophobic core of polymeric colloids. In addition to drug molecules, vesicles prepared by PISA can also serve as carriers for the encapsulation of a broad range of materials, including inorganic particles, dyes and proteins.

An early example of *in situ* encapsulation during PISA was reported by the Armes' group in 2015.[182] PGMA-*b*-PHPMA diblock copolymer vesicles were synthesised in the presence of varying concentrations of silica nanoparticles (~ 18 nm). During the PISA, an open-ended "jellyfish" structure was formed before transforming to a vesicle structure, allowing the diffusion of silica nanoparticles into "jellyfish" before the vesicle membrane formation. The *in situ* encapsulation was performed with initial silica content from 0-35 % w/w. Six centrifugation cycles were conducted to separate the silica-vesicle composites and non-encapsulated silica. The successful loading of silica was confirmed by TEM, cryo-TEM, thermogravimetry (TGA), disk centrifuge photosedimentometry (DCP) and SAXS. The thermo-responsive nature of the PGMA-*b*-PHPMA vesicles allowed the thermally induced morphological transition and the triggered release of encapsulated silica nanoparticles. This study demonstrated an encapsulation and release model system translatable to other cargoes, including globular proteins, enzymes, antibodies or other biomedical species.[182]

In 2015, Tan and Zhang *et al.* also reported the preparation of a diverse set of PEG-*b*-PHPMA polymeric nano-objects (spheres, worms, and vesicles) *via* photo-PISA at room temperature. *In situ* encapsulation of silica nanoparticles and bovine serum albumin (BSA) into vesicles could be achieved *via* photo-PISA.[73] The room-temperature process makes it possible to prepare hybrid composites containing temperature-sensitive proteins and biomedical species. Later on, the same group designed and synthesised CO_2-responsive POEGMA-*b*-P(HPMA-*co*-DMAEMA) nano-objects *via* photo-PISA at room temperature, which is suitable for encapsulating bio-related species. In such study, BSA was encapsulated into vesicles *in situ* with a loading efficiency around 24%, and the CO_2-triggered release was studied.[183] The same methodology was also used to prepare silica-polymer hybrid nanocomposites. The CO_2-responsive nature of the PDMAEMA block allowed the triggered release of silica nanoparticles under mild conditions.[184]

Recently, more cargo species have been encapsulated into PISA-prepared vesicles, including enzymes, dyes and drugs,[185-189] and the activity of the encapsulated species were investigated. For example,

Gibson and O'Reilly *et al.* reported the permeability of PHPMA vesicle membranes by showing the encapsulated enzyme remained active while inside the vesicles.[186] Subsequently, they demonstrated the *in situ* encapsulation of therapeutic enzymes within permeable nanoparticles using PISA, which provided an alternative to PEGylation for the therapeutic enzymes. A one-pot synthesis approach was performed to obtain PEG-*b*-PHPMA vesicles loaded with L-asparaginase (ASNS) at relatively high solid content (11 wt%) under the mild condition *via* photo-PISA. After encapsulation, the PHPMA membrane with size-selective permeability allows the enzyme to be protected and maintain catalytic activity. The proteolytic stability of encapsulated ASNA was shown to be higher *in vitro* and *in vivo* than the native enzyme and the PEGylated conjugate, while the binding of ASNS antibodies was reduced due to being embedded inside vesicles.[187] The benefits of this strategy is that it does not need chemical modification, demonstrating the potential application of PISA for *in situ* encapsulation and improving the stability of therapeutic enzymes. In another example, Sobotta *et al.* developed oxidation-sensitive poly(*N*-acryloylthiomorpholine) (PNAT)-based vesicles *via* PISA. The disintegration times of vesicles varied with the membrane thickness, and could be tuned by varying the DP of the hydrophobic PNAT block. They demonstrated the encapsulation of different cargo species including calcein (dye) and GOx enzyme. The encapsulated GOx not only retained its activity but also transformed the hybrid vesicle into glucose-responsive nanoreactors that can undergo self-degradation by converting glucose to H_2O_2.[189]

2.4.4 Covalently bonded biomolecule-polymer hybrid materials

Another approach to prepare hybrid materials is covalent bonding to polymer chains, especially for biomolecule-polymer hybrid materials, including (poly)peptides, proteins, DNA/RNA and amino acids. Biomolecules can be linked to the chain transfer agents and employed as stablisers for PISA; or they can be modified as polymerisable monomers and used as core-forming monomers or comonomers. The covalent bonds between biomolecules and polymers are much stronger, allowing higher loading efficiency compared to the above strategies, however, it requires additional synthesis steps.

Protein-polymer conjugates. Le Droumaguet and Velonia implemented the pioneering study on the *in situ* preparation of bovine serum albumin-*graft*-polystyrene (BSA-*g*-PS) giant self-assemblies *via* ATRP-mediated PISA.[190] The protein-polymer conjugates synthesised by RAFT-mediated PISA was not

reported until years later by Ma and co-workers, they reported the utilisation of BSA as macro-RAFT agent to synthesise giant amphiphilic protein-polymer conjugate *via* RAFT-mediated photo-PISA. In their study, BSA surface was modified with primary amino groups to provide multiple sites to couple with mercaptothiazoline-activated trithiol-RAFT agent. The obtained BSA-CTA$_8$ were used to mediate dispersion polymerisation of HPMA to afford star BSA-(PHPMA)$_8$ giant amphiphiles with sizes ranging from 164 to 255 nm.[191] Furthermore, the loading and release of cancer drug DOX and biomacromolecule DNA were demonstrated using the synthesised hybrid conjugate.

DNA-polymer conjugates. The conjugation between DNA and polymer also attracted many research interests. Lueckerath *et al.* reported the grafting-from strategy instead of conventional grafting-to approaches to afford DNA-polymer conjugates *via* solution RAFT polymerisation.[192] The same group extended the concept to prepare intricate DNA-polymer nano-objects with various morphologies by RAFT dispersion polymerisation from single-stranded DNA.[111] The conjugation of RAFT agent 2-(((butylthio)carbonothioyl)thio)propanoic acid (BTPA) to DNA was achieved by reacting 19-mer NH$_2$-ssDNA (3'-ATCATCCACCATCTCTTTT-5'-AminoC6) with the activated *N*-hydroxysuccinimide (NHS) or pentafluorophenyl (PFP) esters of the modified BTPA.[192] Enzyme degassing and VA-044 thermal initiator was used for polymerisation; sodium pyruvate was added to minimise the effects of H$_2$O$_2$ produced by enzyme degassing.[111] DNA block remained intact during polymerisation as determined by HPLC and polyacrylamide gel electrophoresis (PAGE). PISA was conducted by copolymerisation of DAAm and DMA (80:20 ratio) from BTPA-DNA. By varying the DP of polymer, different morphologies including micelles, worms and disc-like aggregates were observed by AFM and cryo-TEM.

(Poly)peptide/polypeptide-polymer conjugates. In 2016, Stayton, Convertine and co-workers first explored the PISA in acetic acid to prepare copolymers of 2-(*N*-3-sulphopropyl-*N,N*-dimethyl ammonium)ethyl methacrylate (DMAPS) with a peptide macromonomer.[193] The macro-RAFT agent was synthesised by copolymerisation of HEMA and OEGMA. Then the dispersion polymerisation of a peptide-based methacrylamide macromonomer (Mam- AhxWSGPGVWGASVK) with zwitterionic monomer DMAPS was conducted in acetic acid at 70 °C for 24 h. The use of acetic acid as a solvent is beneficial as it allows the direct polymerisation of amine-functional monomers including peptide methacrylamide, without the use of amine protecting groups or acidic buffers. In 2018, Hadjichristidis,

O'Reilly and co-workers prepared poly(sarcosine)-based diblock copolymer nano-objects *via* photo-PISA.[66] First, poly(sarcosine) was synthesised *via* ring-opening polymerisation (ROP) of sarcosine *N*-carboxyanhydride, followed by coupling with RAFT agent to afford PSar macro-CTA. The subsequent dispersion polymerisation of HPMA yielded spheres, worms, vesicles, elongated unilamellar/multilamellar vesicles and large perforated vesicles depending on the DP of PHPMA and solid contents.

Gianneschi and co-workers reported the PISA using macro-CTA containing peptide moieties. In their study, KLA peptide acrylamide monomer (KLAAm) (amino acid sequence: KLAKLAKKLAKLAK) and DMA were copolymerised in pH 5 buffer to afford peptide brush macro-CTA, followed by chain extension with DAAm and DMA *via* photo-PISA. The one-pot process yielded nanospheres with high-density of apoptotic peptides with tunable size (*da.*36-105 nm), and tunable loading of peptides (20 – 48 wt. %). In addition, enhanced proteolytic stability, cellular internalisation, and cytotoxicity were determined for the peptide-polymer spheres in comparison with free apoptotic peptides.[194]

Semsarilar *et al.* reported the use of positively charged polylysine modified with a RAFT agent moiety as hydrophilic steric stabliser and CTA for the dispersion polymerisation of HPMA.[195] First, RAFT agent 4-cyano-4-(2-phenylethanesulphanylthiocarbonyl) sulphanylpentanoic acid (PETTC) activated with NHS was used to conjugate to the amino-terminated polylysine sequence (KKK) to afford KKK-PETTC. Subsequently, it was used to conduct PISA with HPMA in water at 60 °C, resulting in the *in situ* formation of polylysine-decorated nano-objects (spheres, worm, vesicles) depending on DP of PHPMA. The positive charges of the nano-objects could bind to the negatively charged phospholipid head groups of bacterial membranes, allowing the antimicrobial properties of the nano-objects to be exerted. Both nanoparticle solution and spin-coated thin-film membrane made from these nano-objects showed great antibacterial activity against Gram negative (*Escherichia coli*) and Gram positive (*Staphylococcus epidermidis*) bacteria.

The same group employed a tripeptide methacrylamide derivative (MAm-Gly-Phe-Phe-NH$_2$, denoted as MAm-GFF) to copolymerise with GMA to produce P(GMA$_{65}$-*stat*-(MAm-GFF)$_7$) macro-RAFT agent.[196] The peptide-based macro-RAFT agent was then chain-extended with PHPMA *via* aqueous PISA at 70 °C. Different to commonly achieved spheres, worms and vesicles by PGMA-*b*-PHPMA block

copymers, the obtained P(GMA$_{65}$-$stat$-(MAm-GFF)$_7$)-b-PHPMA$_{28}$ (cooled to ambient temperature) was in fibrous structure as observed by TEM. This confirmed the influence of the GFF interactions on self-assembly. Interestingly, the self-assemblies underwent a morphological transformation with temperature change. After annealing at 70 °C for 1 h, TEM revealed the morphology changed to worm-like structures with a diameter around 25 nm. Upon cooling to 4 °C for 1 h, the fibrous structures were replaced by large spherical objects (~ 600 nm) composed of small spheres (~ 25 nm). Meanwhile, the same group explored the use of MAm-GFF and MAm-FGD (MAm-Phe-Gly-Asp-NH$_2$) as solvophobic monomers.[197] Specifically, PGMA macro-CTA were chain-extended with MAm-GFF macromonomer as core-forming monomer *via* emulsion PISA in ethanol, yielding flake-like objects and dendritic structures composed of fibrous elements (Figure 2.10a, b). PGMA-b-P((MAm-GFF)-co-HPMA) yielded a mixture of short worms and vesicles due to the insertion of a less solvophobic PHPMA block. They also investigated another peptide MAm macromonomer (MAm- FGD) as the core-forming block in aqueous PISA process, resulting in large dendritic and bow-tie shaped fibres (Figure 2.10c-e).
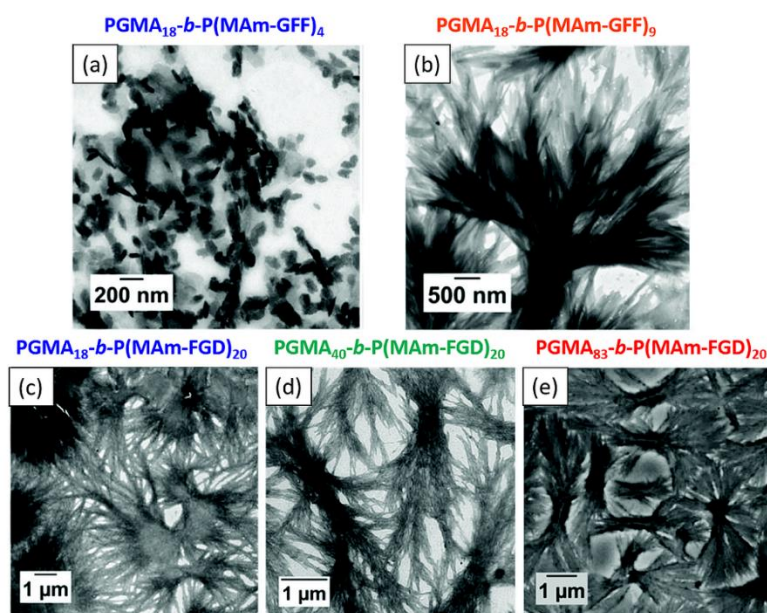

Figure 2.10 Representative TEM images of (a) flake-like objects, (b) branched bundles of fibres, (c-e) large dendritic and bow-tie shaped fibrous structures. Reprinted from Ref. [197] with permission. Copyright 2021, Royal Society of Chemistry.

Amino acid-polymer conjugates. In this area, the pioneering work of Armes and Ladmiral *et al.* reported the insertion of amino acid-based methacrylates (CysMA or GSHMA) to produce water-soluble macro-CTA.[198] When PGSHMA-CTA was used as sole macro-CTA, only spherical nanoparticles were obtained. However, PCysMA-CTA alone or a binary mixture of PGMA/PGSHMA-CTA or PGMA/PCysMA-CTA resulted in spheres, worms and vesicles. Aqueous electrophoresis studies indicated the chemical composition and type of the steric stabliser chains could impact the complicated electrophoretic activity of these nano-objects. Similar to their work, the De group synthesised Boc-protected poly(L-alanine methacryloyloxyethyl ester) (PBLAEMA)[199] and poly(L-leucine methacryloyloxyethyl ester) (PBLEMA)[200] macro-CTAs to individually mediate the dispersion polymerisation of BzMA in methanol. In both studies, a diverse set of nano-objects including spheres, worms, long fibres and polymersomes were obtained by varying the DP of PBzMA. For the PBLAEMA-*b*-PBzMA nano-objects, the interworm/interfibre entanglements led to a thermo-responsive gelation-degelation behaviour, resulting in a worm-to-spheres transformation upon heating from 25 to 65 °C. Upon addition of trifluoroacetic acid (TFA), the Boc-group deprotection of PBLAEMA units led to the morphological transition towards lower-order morphologies (vesicle-to-worm, vesicle-to-sphere).[199]

2.5 Stimuli-Responsive Particles by PISA

It is well-known that for amphiphilic self-assembled nanoparticles, the morphology undergoes stimuli-responsive transformation if one or more blocks are sensitive to stimuli, such as the temperature, pH changes and reactive species. The morphological transformation includes total disassociation of the assembly and "order-to-order" transition, *e.g.* worm-to-sphere transition. The total disassociation has been extensively exploited in conventional solution self-assembly, *i.e.* nanoprecipitation, however, the latter circumstance is rarely reported. In contrast, both transitions have been explored in depth in the PISA field, especially the order-to-order transition has gained increasing research attention and even reversible responsiveness was achieved. The stimuli-responsive morphological transformation leads to change in physical properties of polymeric colloids, and allows controlled release of conjugated or encapsulated cargos, which has great potential in drug release and other biomedical applications. Here, we summarise some of the common stimuli that have been reported for stimuli-responsive nano-objects prepared by RAFT-PISA.

2.5.1 Thermo-responsive nano-objects

Temperature-sensitive nano-objects are one of the most common stimuli-responsive polymeric nanoparticles. Typically, the design involves the incorporation of polymer blocks that exhibit either a LCST or an UCST or solubility change with temperature. Examples include thermo-responsive PNIPAM hydrogels *via* RAFT-mediated precipitation polymerisation,[201] thermal responsive spheres, worms, vesicles made from POEGMA-PFS,[202] and thermo-reversible degelation and regelation transition and thermo-responsive nanoparticles by aqueous dispersion copolymerisation of *N,N*-diethylacrylamide (DEAAm) and *N,N'*-methylene bisacrylamide (MBA) using mPEG-RAFT agent.[203] The LCST of PDEAAm at 32 °C led to a change in size of the resulted nanoparticles upon heating and cooling. In 2012, Blanazs *et al.* further extended this thermo-responsive property to PGMA-*b*-PHPMA worms that were synthesised *via* aqueous RAFT dispersion polymerisation. The variable-temperature ^{1}H NMR spectroscopy indicated the PHPMA block has a greater hydration degree at lower temperature, which can induce reversible worm-to-sphere morphological transition upon cooling from 21 to 4 °C.[204] Similar cooling triggered worm-to-sphere transition was observed for poly(lauryl methacrylate)-*b*-poly(benzyl methacrylate) synthesised *via* PISA in *n*-dodecane.[205] For PEG-*b*-PHPMA worms with a relatively long PEG chain (DP=113), they exhibited thermo-responsiveness but not reversible morphological transition. Degelation of worms to spheres occurred upon cooling, but regelation failed upon return to room temperature.[206] However, in a later study, the use of a binary mixture of long PEG_{113} and short PEG_{45} macro-RAFT agents in PISA process enabled the formation of nano-objects with thermo-reversible behaviour.[207] In this study, a systematic variation of the proportions of two PEG-RAFT agents and the DP of PHPMA were performed to obtain [x PEG_{45} + z PEG_{113}]-*b*-$PHPMA_n$ block copolymer spheres, worms, or vesicles. Interestingly, only a single worm dispersion [0.70 PEG_{45} + 0.30 PEG_{113}]-*b*-$PHPMA_{115}$ underwent full degelation/regelation cycle.

For PISA morphologies with the utilisation of UCST behaviour, Tran *et al.* synthesised hydrogen-bonding poly(*N*-acryloyl glycinamide) (PNAGA)-based thermo-sensitive nanogels driven by UCST *via* photo-PISA at 3 °C.[208] POEMGA was used as macro-CTA for the polymerisation of NAGA and MBA cross-linker. The opalescent solution was observed, and hydrodynamic diameter decreased upon cooling to 5 °C, which was related to the collapse of the core-cross-linked P(NAGA-*co*-MBA). Upon

heating to 55 °C, the solution became transparent with an increase in hydrodynamic diameter. This behaviour was reversible and reproducible over successive shrink/swell cycles. Rieger and Stoffelbach and co-workers reported the synthesis of UCST-thermo-responsive nano-objects using PDMA as macro-CTA, acrylamide (AAm) and acrylonitrile (AN) as monomers *via* aqueous PISA at 45 °C.[209] The molar fraction of AN (F_{AN}) and DP of core-forming block were varied systematically. The turbidity test indicated the cloud point temperature was tunable between ~20 to ~80 °C by increasing the F_{AN}. The thermo-responsiveness and morphology were greatly influenced by F_{AN} and DP. For intermediated F_{AN} and high DP, the formed worms transformed to spheres upon heating due to the increased hydration of the core-forming block.

While most studies reported the LCST/UCST-driven transition, Derry *et al.* reported the thermo-reversible crystallisation-driven aggregation. A series of nanoparticles were prepared *via* dispersion polymerisation of BzMA with poly(behenyl methacrylate)$_{37}$ (PBeMA$_{37}$) macro-CTA as a steric stabliser at 90 °C in mineral oil. Turbidity and DSC studies of PBeMA$_{37}$ homopolymer in mineral oil solution indicated the thermo-sensitive nature of PBeMA$_{37}$ stabliser. On cooling to 20 °C, unstable PBeMA$_{37}$-*b*-PBzMA$_{x}$ spheres formed turbid pastes because of the crystallisation of insoluble PBeMA block, and returned to free-flowing dispersions when heating to 50 °C. SAXS studies confirmed the strong interaction between PBeMA$_{37}$-*b*-PBzMA$_{100}$ spheres forming loose mass fractals at 20 °C.[210]

In most of the previous studies reported on thermo-responsive morphological transitions, a single diblock copolymer typically transforming between two morphologies (*e.g.*, worms to spheres). Few reports have shown that a single diblock copolymer can undergo transitions between three morphologies. For example, Ratcliffe *et al.* reported a single copolymer composition, poly(*N*-(2-hydroxypropyl) methacrylamide)$_{41}$-poly(2-hydroxypropyl methacrylate)$_{180}$ (PHPMAm$_{41}$-*b*-PHPMA$_{180}$), can form spheres (4 °C), worms (22 °C) or vesicles (50 °C) upon temperature change. On cooling from 50 to 4 °C after dispersion polymerisation, the appearance of the PHPMAC$_{41}$-*b*-PHPMA$_{180}$ exhibited three distinct states: milky-white free-flowing dispersion at 50 °C, free-standing gel at 22 °C, and slightly turbid fluid at 4 °C. TEM of the diluted dispersions equilibrated for 24 h at a specific temperature indicated the morphologies were well-defined vesicles, worms, and spheres respectively. Other characterisations such as SAXS, DLS and rheology studies all supported the observation.

Theoretical analysis of the diblock copolymer system using numerical lattice computations based on a self-consistent mean field theory supported the observation as well.[211]

2.5.2 pH value as stimulus

When polyelectrolytes or polymers with ionisable functional groups are used as stablisers, the morphological transition can be triggered by pH change. In 2014, Armes *et al.* reported the synthesis of PGMA-*b*-PHPMA nano-objects using a carboxylic acid-based RAFT agent.[212] The carboxylic acid end-group on the R-group of the RAFT agent allowed the ionisable single terminal on each stabliser chain to be exposed to the aqueous solution. The resulting HOOC-PGMA-*b*-PHPMA worms obtained at approximately pH 3.5 underwent worm-to-sphere morphological transition when increasing solution pH from 3.5 to 6.0 using NaOH. The pH-responsive behaviour is reversible, returning the pH to its original value resulted in sphere-to-worm transition and thus regelation. Similarly, a vesicle-to-worm morphological transition upon pH change was observed; however, in this case, the transition was not reversible.

Subsequently, the same group further explored the effects of polymer end-groups on nano-objects in response to external stimuli. A morpholine-functional RAFT agent (MPETTC) was synthesised and used to prepare PGMA macro-CTA containing the terminal morpholine functional group (pK_a ~6.3).[213] Dispersion polymerisation of HPMA was performed at pH 7.0-7.5. DLS, TEM and rheology studies all indicated the pH-responsiveness of the obtained worms. By lowering the solution pH from 7 to 3, the protonation of the morpholine end-group induced worm-to-sphere morphological transition and degelation. However, further reduction of the solution pH to 1 led to the reformation of worms. The increase in pH from 3 to 7 led to deprotonation of the morpholine end-group, inducing the sphere-to-worm transition. The control experiments were performed using a non-ionic RAFT agent (the carboxylic acid group was methylated), and the morphology of obtained worms remained unchanged at varied pH values.

Instead of introducing a pH-responsive end-group at the polymer chain terminal, ionic monomer could be used in stabliser block to generate nano-objects with ionic shells. North and Armes observed size reduction of PISA-prepared PMAA-*b*-PHPMA nanoparticles by increasing pH from 5.5 to 10. This was

because the multiple acid groups on the PMAA stabliser were ionised and resulting in a decrease in the mean aggregation number.[214] The sterically stablised nanoparticles at pH 10 were also thermo-responsive due to the presence of PHPMA block.

Ionisable core-forming monomers could also be used to prepare pH-responsive nanoparticles *via* PISA. For example, Zhang and Hong *et al.* reported the PISA process using PEG-based macro-CTA for copolymerisation of (diisopropylamino)ethyl methacrylate (DIPEMA) and BzMA. DIPEMA (pK_a ~6.3) with tertiary amine group enabled pH sensitivity of the formed vesicles. The immediate disaggregation of vesicles in acidic solution (pH 4.0 buffer) was observed, allowing burst release of encapsulated Rhodamine B.[215] In another example, Tan *et al.* reported the photo-PISA using HPMA and DMAEMA as core-forming monomers for preparing CO_2-responsive vesicles. After treating with CO_2, the solution pH decreased, a certain number of tertiary amine groups in the PDMAEMA block were protonated, inducing the increased hydrophilicity and subsequent impaired vesicle structure. After removal of CO_2 by purging with N_2 or Ar, the solution pH was restored, and the deprotonation of tertiary amine groups led to a decrease in conductivity and hydrodynamic diameter.[216]

Ampholytic diblock copolymer nanoparticles with dual pH-responsiveness were also studied. Armes *et al.* firstly reported the use of PISA for the synthesis of ampholytic schizophrenic nanoparticles with poly(2-(diethylamino)ethyl methacrylate) (PDEA) as stabilising block and PMAA-*st*-PBzMA as core-forming block. After PISA nanoparticles were prepared at pH 2.5, the ionisation of PMAA and deprotonation of PDEA could induce nanoparticle inversion when solution pH was increased to 10. At pH 6-8, the dispersion was highly turbid with a large hydrodynamic diameter, which, combined with the zeta potential results, confirmed the isoelectric point at which flocculation occurred.[217] Similar schizophrenic nanoparticles with dual pH-responsiveness were also reported by North and Armes. In this case, PEDA macro-CTA was chain extended with 2-carboxyethyl acrylate (CEA) *via* PISA in an acidic solution.[218]

2.5.3 Light-responsive nano-objects

For light/photo-responsive nano-objects, it usually involves the incorporation of some conventional photo-responsive functional groups such as azobenzene, pyrene and *ortho*-nitrobenzyl group. For

example, Chen *et al.* reported the scalable synthesis of azobenzene-containing photo-responsive block copolymer nano-objects *via* PISA.[219] PMAA macro-CTA was used as a stabliser for the dispersion polymerisation of 11-(4-(4-butylphenylazo)phenoxy)undecyl methacrylate in ethanol. During PISA, the liquid crystalline (LC) feature of azobenzene allowed internal LC ordering in the core-forming block and led to hierarchical self-assembly into worms, short belts, lamellar and rarely achieved cuboid and ellipsoidal vesicles (Figure 2.11). LC behaviour of azobenzene at its *trans* state would diminish at its *cis* state under UV irradiation, thus the obtained LC nanoparticles were photo-responsive. After UV irradiation, the original cuboids changed to spherical particles, and the ellipsoidal micelles changed to large compound micelles. Yuan *et al.* also reported the use of azobenzene-containing monomer for the synthesis of poly(*N,N*-dimethylaminoethyl methacrylate)-*b*-poly[(benzyl methacrylate)-*co*-(4-phenylazophenyl methacrylate)] [PDMA-*b*-P(BzMA-*co*-AzoMA)] *via* PISA.[220] Spheres, worms and vesicles were obtained with various DP of P(BzMA-*co*-AzoMA). Under UV irradiation, the worms underwent worm-to-vesicle transformation due to *trans*-to-*cis* transition of azobenzene groups. During the morphological evolution, some intermediate morphologies such as "octopus" and "jellyfish"-like structures were observed before reaching vesicles.
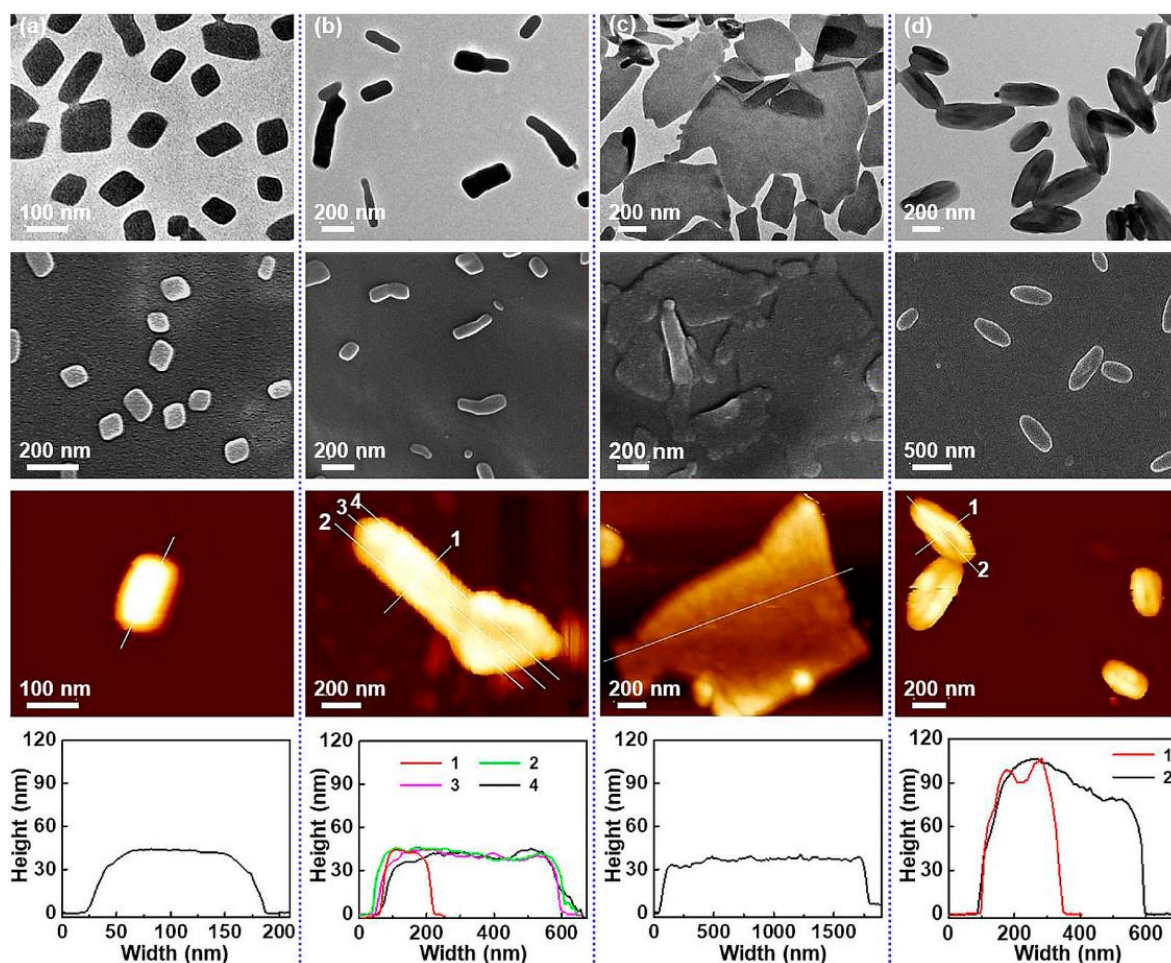
Figure 2.11 TEM, SEM, AFM images, and the corresponding height profiles of $PMAA_{112}$-*b*-$PMAAz_n$ NPs, respectively: (a) $PMAA_{112}$-*b*-$PMAAz_{66}$ cuboids, (b) $PMAA_{112}$-*b*-$PMAAz_{89}$ short belts, (c) $PMAA_{112}$-*b*-$PMAAz_{115}$ lamellar, (d) $PMAA_{112}$-*b*-$PMAAz_{142}$ ellipsoidal vesicles. Reprinted from Ref. [219] with permission. Copyright 2018, American Chemical Society.

Boyer *et al.* demonstrated a one-pot PISA process for the preparation of light-responsive pyrene-containing nanoparticles. POEGMA macro-CTA was chain extended with 1-pyrenemethyl methacrylate (PyMA) and comonomer to yield spheres, worms and vesicles.[221] The addition of comonomers such as BMA or MMA reduced the π-π stacking between pyrene moieties, this was essential for achieving relatively high PyMA conversion. The light-responsive feature of pyrene enabled light-induced gradual cleavage of pyrene moieties and gradual disassembly of nanoparticles. When exposed to UV irradiation, the POEGMA-*b*-PPyMA spheres and worms, POEGMA-*b*-P(PyMA-*co*-BMA) vesicles all underwent dissociation. Chemtob *et al.* reported the synthesis of poly(hydroxyethyl acrylate)-*b*-poly(*o*-nitrobenzyl

acrylate) (PHEA-*b*-PNBA) to prepare photo-responsive nanoparticles *via* PISA.[222] By exposing the PHEA-*b*-PNBA latex to UV irradiation, the degradation of PNBA block led to a gradual decrease in turbidity with the irradiation time. The latex also turned brown due to the decomposition of aromatic nitro products.

2.5.4 Reactive oxygen species as stimulus

The polymer nanoparticles with responsiveness to reactive oxygen species (ROS) have attracted many research interests, especially the ROS such as hydrogen peroxide and hypochlorite are typically found in inflammatory reactions. It is well-known that the thioether group could be oxidised by ROS, thus the thioether functionalised vinyl monomers could be used to prepare ROS-responsive nano-objects *via* PISA. Yeow, Boyer and co-workers reported the use of thioether group-containing monomer, 2-(methylthio)ethyl methacrylate (MTEMA), for the preparation of vesicles *via* PET-RAFT-mediated PISA.[223] A series of POEGMA-*b*-PMTEMA with different DP of PMTEMA resulted in spheres, worms and vesicles with encapsulated ZnTPP. These nano-objects can rapid disassemble after exposure to visible light in the presence of air. This was because the thioether moiety was oxidised to hydrophilic sulphoxide by the singlet oxygen generated by the encapsulated ZnTPP under visible light.

Similarly, thioether-containing monomer *N*-acryloylthiomorpholine (NAT) was used to prepare oxidation-responsive nanoparticles *via* PISA.[188, 189] Brendel *et al.* synthesised poly(*N*-acryloylmorpholine) (PNAM)-based macro-CTA for the dispersion polymerisation of NAT, and the obtained biocompatible spherical micelles exhibited different diameters. Upon exposure to H_2O_2, the oxidation of thioether moiety led to a gradual increase in the hydrophilicity of the core and the ultimate disassembly.[188] More recently, they demonstrated unilamellar vesicles could be obtained by PISA of PNAM-*b*-PNAT. Calcein was encapsulated into the vesicles as a model dye, which could be released in a time-controlled manner when expose to H_2O_2. In addition, GOx enzyme was successfully encapsulated into vesicles as well, transforming the vesicles into glucose-responsive vesicles. With the addition of glucose, H_2O_2 was generated by GOx catalysis, leading to the full disassembly of vesicles.[189]

In 2021, Fan, Thang and co-workers reported the preparation of rarely achieved inverse bicontinuous mesophases using boronic ester group-containing monomer *via* PISA.[18] Upon exposure to H_2O_2, the

boronic ester moiety was oxidised and hydrolysed to phenol, which further initiated the generation of quinone methide and hydrophilic PAA, thus the ultimate degradation of cubosomes and other nano-objects (Figure 2.12). This allows potential application in the triggered release of payloads.
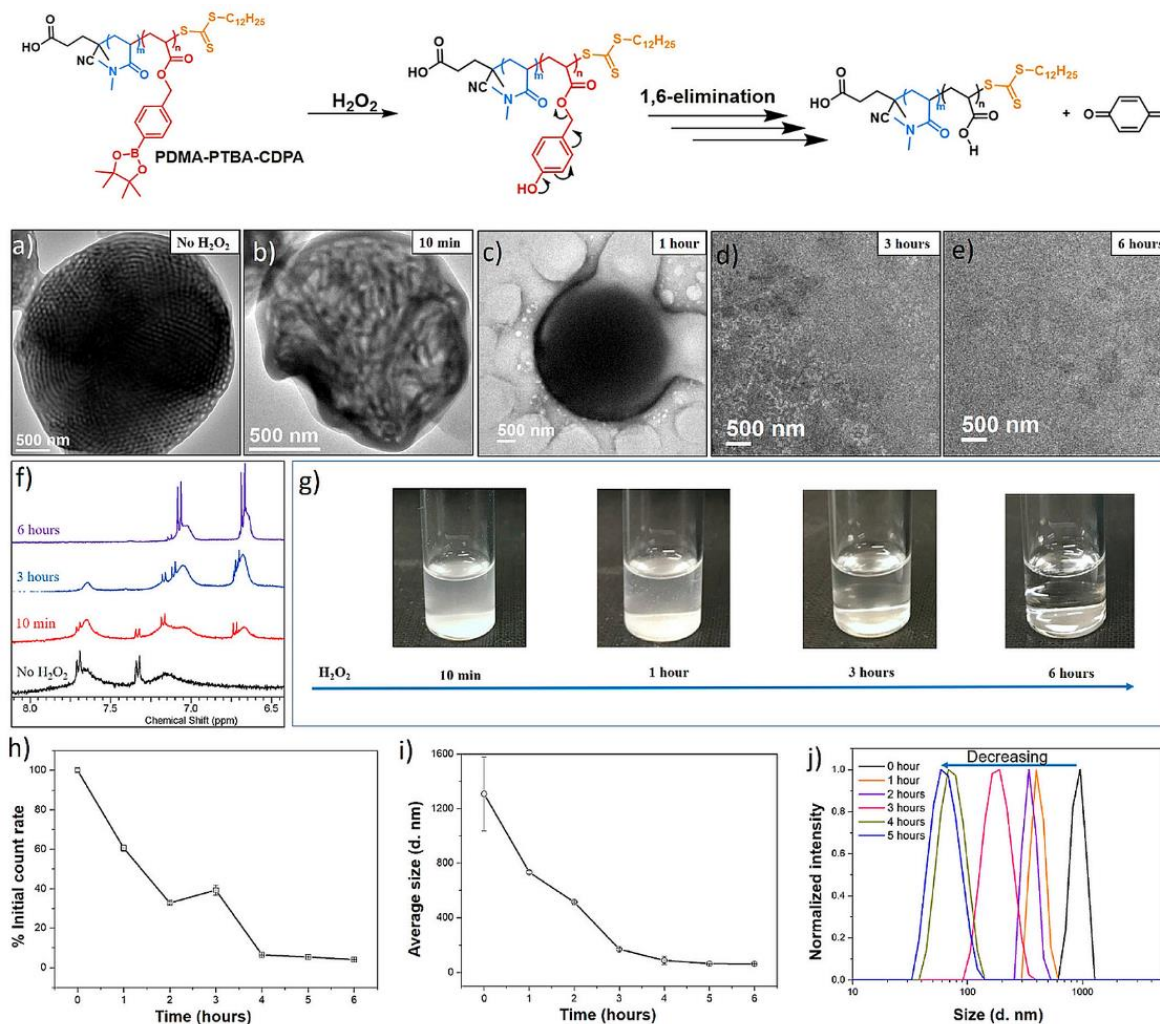

Figure 2.12 Disassembly of the PDMA-*b*-PTBA-based cubosomes in response to H_2O_2. (a-e) TEM images of the cubosome degradation process at selected time points. (f) ^{1}H NMR spectra evolution of the block copolymer after the addition of H_2O_2. (g) Digital photos of the particle suspension after the addition of H_2O_2. (h-j) DLS-monitored disassembly process. Reprinted from Ref. [18] with permission. Copyright 2021, American Chemical Society.

2.5.5 Reduction-responsive nano-objects

Instead of oxidising species, reducing species can work as an external stimulus for some polymers as well. For example, Zhou *et al.* reported using an azobenzene-derived methacrylate with a TPE (tetraphenylethylene) fluorescence probe moiety (TPE-AZO-MA) as the commoner for the dispersion copolymerisation with BMA.[224] A series of drug-loaded micelles and vesicles were obtained by *in situ* doxorubicin (DOX) loading during PISA. Azoreductase was used as the reducing agent for azo bond cleavage and resulted in micellar destruction. During enzyme hydrolysis, a slow release of DOX was observed. Meanwhile, strong fluorescence emission was detected due to the aggregation-induced emission of TPE. Goto *et al.* synthesised cross-linked nano-objects using a cross-linker containing disulphide group.[41] Due to the stablising effect of the cross-linker, the morphology of the nano-objects was retained after the hydrophobic block were hydrolysed to hydrophilic block. Subsequent addition of the reducing agent glutathione (GSH) resulted in the reduction of disulphide bonds to thiols and cleavage of cross-linking units, inducing the decomposition of nano-objects.

2.5.6 Dual and multi-responsive nano-objects

Finally, another emerging trend in PISA for the synthesis of stimuli-responsive nanoparticles is to allow responsiveness triggered by two or more stimuli, which makes nanoparticles versatile in their applications. Lovett *et al.* reported pH and temperature dual-responsive HOOC-PGMA-PHPMA worms and vesicles.[212, 225] More specifically, the thermo-responsiveness of PHPMA block led to worm-to-sphere/ vesicle-to-worm transitions on cooling; pH increase from 3.5 to 6.0 caused the ionisation of the terminal carboxylic acid group located at the end of PGMA block and resulted in worm-to-sphere/ vesicle-to-worm/ vesicle-to-sphere transitions.

Mahda*vian et al.* reported P(St-*co*-MMA) nanoparticles that could be triggered by pH change and UV irradiation. PDMAEMA macro-CTA was used for the preparation of P(St-*co*-MMA) along with the incorporation of spiropyranethyl acrylate (SPEA) comonomer *via* RAFT surfactant-free emulsion polymerisation.[226] The pH-responsiveness resulted in the dispersion/aggregation of the obtained latexes. The latexes were well-dispersed in acidic condition due to water-soluble PDMAEMA$^+$Cl$^-$, and aggregated at pH above 8 due to deprotonation. UV irradiation (λ = 365 nm) dissociated the C-O bond

in the spirocarbon to form a conjugated zwitterionic merocyanine dye isomer and led to hyperchromic behaviour, which could be returned by visible light.

Zhang, You and co-workers demonstrated the preparation of pH- and reduction-responsive prodrug nanoparticles with anticancer activity. First, biocompatible poly(*N*-(2-hydroxypropyl) methacrylamide (PHPMAm-CPDB) was chain extended with DIPEMA and camptothecin prodrug monomer (CPTM) *via* RAFT solution polymerisation.[227] The obtained PHPMAm-*b*-P(DIPEMA-*co*-CPTM) macro-CTA was used for the dispersion polymerisation of BzMA to afford prodrug nanoparticles. Upon appropriated stimulus, PDIPEMA underwent solvophobic to solvophilic transition in acidic condition, allowing faster diffusion of GSH reducing agent into the CPTM units. The reduction of the disulphide bond in the CPTM by GSH led to the release of camptothecin. The drug delivery and anticancer activity of these nanoparticles were verified by *in vitro* cytotoxicity study. More recently, the same group reported similar pH- and reduction-responsive prodrug nanoparticles with formulations of PHPMAm-*b*-PCPTM, PHPMAm/PDEAEMA-*b*-PCPTM, PHPMAm/PDMAEMA-*b*-PCPTM.[228] Different to their previous study, the CPTM was used as the only core-forming monomer. HPMAm/PDEAEMA-*b*-PCPTM nanoparticles underwent fast hydrophobic-hydrophilic transition and charge reversal at the physiological pH value (pH= 6.8), which facilitated enhanced cell internalisation. In contrast, PHPMAm-*b*-PCPTM without charge-reversible property showed slower cell internalisation and lower anticancer activity.[228]

2.6 Improved Throughput of PISA

Compared to conventional solution self-assembly, the high solid content property of PISA has dramatically improved the throughput of nanoparticle production. Based on this, many efforts have been made to further improve the throughput of PISA for the purpose of future upscale production. For instance, an automated parallel synthesiser has been employed in the RDRP polymerisation[229, 230] and PISA[231] subsequently. However, the oxygen inhibition in RDRP could be the bottleneck for high-throughput PISA. The previously reported protocols for deoxygenation are that automated parallel living polymerisation performed under inert atmosphere or with automated deoxygenation process[232], which however require specialised equipment. Alternatively, as mentioned in above sections, oxygen-tolerant PISA processes have been reported using photo-PISA[93, 96] or enzyme-PISA[104, 233], which could eliminate the time and energy needed for deoxygenation.

In 2018, Cockram *et al.* demonstrated the first high-throughput synthesis of block copolymer nanoparticles in water *via* RAFT-mediated PISA.[231] First, a large batch of PMAA macro-CTA was synthesised *via* conventional solution RAFT polymerisation. Then BzMA or BMA was added as the first core-forming monomer for RAFT aqueous emulsion polymerisation targeting $PMMA_{56}$-$PBzMA_{500}$ or $PMMA_{56}$-$PBMA_{500}$ nanoparticles using Chemspeed Autoplant A100. The deoxygenation protocol was performed by blowing N_2 gas through all reaction vessels for 20 min (~20 reaction vessels). Different types of stirrers and stirring speeds (propeller-type stirrer 350-650 rpm and anchor-type stirrer 150-350 rpm) were used to optimise the PISA process. The same protocol was employed to produce triblock and tetrablock copolymer nanoparticles using BMA or BzMA as the second or third water-immiscible monomer. The optimised protocols indicated that a propeller-type stirrer at stirring rates of 550-900 rpm was required to produce sufficiently small droplets of monomers. The preliminary study provided the basis for further high-throughput screening of PISA formulations. For instance, one-pot automated synthesis of both macro-CTA and block copolymer nanoparticles may be more attractive. Only spheres were achieved in this study, future study regarding the screening of different formulations to obtain various morphologies and rapid establishment of the phase diagram is foreseeable with the increasing demand from industry.

As automated synthesisers are still not readily available in most academic settings, alternative oxygen-tolerant polymerisation protocols have been developed for high-throughput PISA. These protocols are more suitable for laboratory scale with even ultralow volumes, and suitable for rapid optimisation especially for those with many reaction variables (monomer type, monomer concentration, targeting DP, temperature, solvent composition, solid content, etc.). In 2017, Boyer *et al.* demonstrated that oxygen-tolerant photo-PISA in the presence of AscA and eosin Y could be conducted in 96-well microplates.[93] In the same year, Tan *et al.* also reported an enzyme-assisted photo-PISA in open vessels and microplates.[108] The oxygen tolerance was endowed by the catalytic ability of GOx. These methods facilitate a high-throughput PISA that allows multiple parallel PISA processes to be performed simultaneously, which could realise rapid construction of phase diagrams and fast screening of reaction parameters.

On the basis of these methods, the oxygen-tolerant PISA strategy in low volumes has been extended to study the wavelength orthogonality of the [2 + 2] coumarin cycloaddition reaction and PET-RAFT PISA. Under the red light (λ = 595 nm) irradiation, exclusive activation of PET-RAFT PISA occurred, resulting in the formation of various nano-objects (spheres, worms, vesicles) with no evidence of dimerisation. Rapid cross-linking of polymer chains occurred by switching to UV irradiation (λ = 365 nm), allowing the retained morphology of the nano-objects in organic solvents.[97] The wavelength orthogonality of photo-induced deoxygenation and photoinitiation of PISA was reported by Tan *et al.* using a high-throughput multiwell strategy. Dual-wavelength photo-PISA of HPMA using PGMA$_n$-CDPA (n= 28, 53, 69) was achieved in a fast manner using 96-well microplates.[234] Furthermore, Gianneschi *et al.* combined UV-initiated PISA on small scales in a 96-well microplate with an automated sampling of every well and automated TEM and image analysis for the rapid generation of phase diagrams.[235] Selected compositions were repeated by scaled-up experiments, which showed identical morphologies and sizes with the low volume version. This approach could be readily applied for handling fast screening of a large number of samples. In summary, high throughput PISA and characterisation could serve as a robust method for rapid discovery of target materials and subsequent optimisation of formulations and experimental conditions, which promise great potential in future industrial mass production.

It is generally accepted that PISA under continuous flow is a more favourable method for scaling up PISA over batch synthesis, as it provides better heat/mass transfer, increased reaction rates and the ability to integrate into feedback control loops. In 2017, Zhu and Zhang *et al.* firstly reported the thermal-initiated PISA performed under continuous flow conditions, where POEGMA-CTA and MMA were used as a steric block and core-forming monomer in water/ethanol co-solvent system in a lab-scale two-stage continuous tubular reactor.[236] The concentration and flow rate of each feedstock were kept constant, and the target DP was achieved by varying the concentration of POPEMGA macro-CTA. Only spheres were obtained due to the hindered morphological transition resulting from the high amount of water (56% v/v). Later on, Parkinson *et al.* reported an all-aqueous synthesis of both PDMA macro-CTA and PDMA-PDAAm diblock copolymer spheres, worms and vesicles by thermal-initiated RAFT polymerisations in coil continuous flow reactors.[237]

Recently, researchers in Junkers, Boyer and Zetterlund groups attempted to convert light-initiated RAFT polymerisation and PISA from batch to continuous flow systems.[80, 238-240] In their report in 2018, different morphologies including spheres worms and vesicles were obtained *via* photoiniferter RAFT PISA in a continuous flow reactor under blue LED light. A rapid polymerisation was found, which reached full monomer conversion in only 75 min, compared to 6 h in batch process. Their study also optimised the protocol by varying the experimental conditions including light intensity, solid content, and residence time, allowing the production of 60 g polymeric nanoparticles per day in the lab.[238] Warren *et al.* reported the ultrafast continuous-flow RAFT dispersion polymerisation which achieved conversions > 90% within 8 min for target PDAAM DPs of 50 and 100, and achieved 79% conversion of DP of 200 within 20 min.[241] In the further study (Figure 2.13), PET-RAFT dispersion polymerisation with oxygen tolerance employing eosin Y/triethanol amine as catalytic system was exploited for the synthesis of poly(dimethyl acrylamide)-*b*-(poly(diacetone acrylamide)-co-poly(dimethyl acrylamide)) (PDMAA-*b*-(PDAAm-*co*-PDMAA)) in one-step continuous-flow process without intermediate purification.[239] The photo-PISA in less polar solvents *via* continuous flow process was investigated as well.[80] Several parameters including solvents, photoinitiators, and light intensities were optimised in the batch process. The optimised protocol was then performed in continuous flow reactors, which realised non-aqueous photo-PISA in flow with high order morphologies.
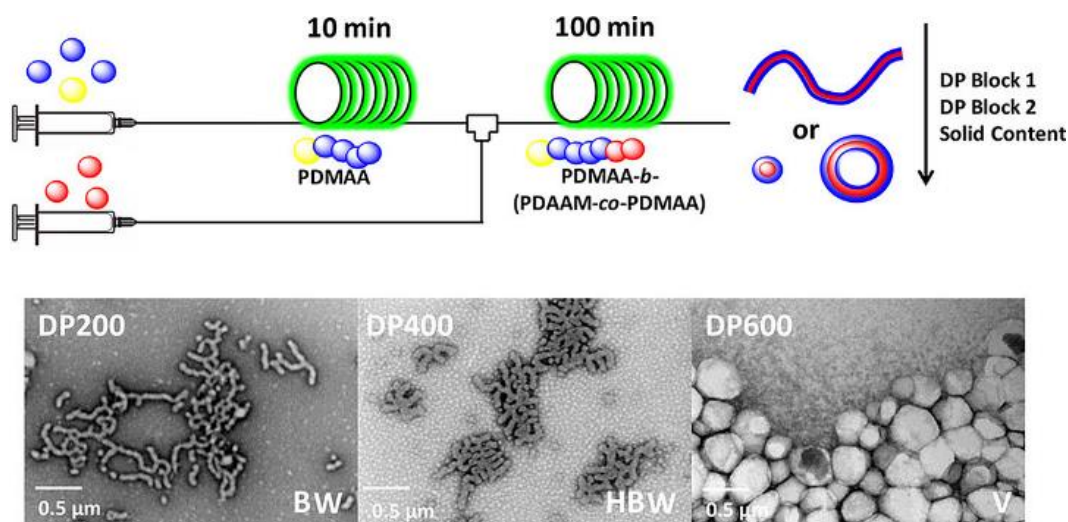
Figure 2.13 Schematic diagram of the flow reactor setup coupling two reactors, and TEM micrographs of PDMAA-*b*-(PDAAm-*stat*-PDMAA) nano-objects with DP 200-600 solvophobic block. Reprinted from Ref. [239] with permission. Copyright 2019, American Chemical Society.

More recently, the enzyme-assisted photo-PISA using GOx and glucose catalytic system was converted from batch to flow process as well. Tan *et al.* reported the oxygen-tolerant process conducted in a flow reactor, which constructed a PEG-*b*-PHPMA morphological phase diagram by systematically varying the DP of PHPMA.[109] Another oxygen-tolerant in-flow PISA system was reported by Hou *et al.* based on the oscillatory BZ redox reaction. Dispersion polymerisation of DAAM from PEG macro-CTA was implemented in a CSTR yielded spheres, worms, vesicles and giant vesicles, depending on the factors including residence time, BZ oscillation and DP of PDAAM.[131]

2.7 Applications

PISA allows the production of nanoparticles in various morphologies in relatively high solid contents, which opens up the applications of PISA in a broad range of areas. The most common applications for polymeric nanoparticles including those prepared by the PISA process, is drug delivery and other biomedical applications. Besides, PISA-prepared nano-objects have been explored as catalysts,[170, 242-245] Pickering emulsifiers, [15, 246-249] imaging agents,[250, 251] lubricants,[252] templating agents,[253-255] pigments,[256, 257] etc. The following section summarises some applications of PISA-prepared nano-objects.

Due to the versatility of PISA, nanoparticles with biocompatible formulations could be efficiently synthesised, which have drawn increasing interest in exploring their applications in the biomedical field. As early as in 2012, Armes group reported that PISA-derived worms could form free-standing hydrogels with thermo-reversible behaviour, which allowed the facile preparation of sterile gels with potential biomedical applications.[204] Later on, the loading of guest compounds into PISA-derived nano-objects during polymerisation were investigated by Boyer and Davis using Nile Red as a guest molecule,[258] as well as Mable *et al.* by loading silica nanoparticles into vesicles *via in situ* encapsulation.[182] The successful loading of guest compounds make it possible to load drug molecules during PISA as well. O'Reilly *et al.* demonstrated efficient loading of L-asparaginase (ASNS) to vesicles during PISA. After encapsulation, the morphology of vesicles remained, and the enzyme remained catalytically active. In addition, the encapsulated enzyme showed higher proteolytic stability than the free enzyme *in vitro* and *in vivo*.[187] Recently, Malmström *et al.* reported the *in situ* physical encapsulation of hydrophobic drug (DOX) during aqueous PISA. The hydrophobic core of PDMAPMA-*b*-PMMA nanoparticles allowed the migration of DOX into the core. The DOX-loaded nanoparticles showed higher cell toxicity than free DOX toward macrophages cell line.[185] Another approach for drug loading is to use prodrug monomers as a sole core-forming monomer or comonomer.[193, 227, 228, 259, 260] Drug molecules are covalently linked to polymer chains, leading to high loading efficiencies, even up to 100% when full monomer conversion is achieved. For example, Zhang *et al.* synthesised PEG-*b*-P(MEO$_2$MA-*co*-CPTM) prodrug macro-CTA, which contains camptothecin linked to the polymer chains *via* reductive-sensitive linkage. The prodrug macro-CTA was then extended with BzMA as core-forming monomer and *N,N*-cystaminebismethacrylamide (CBMA) as cross-linker, obtaining core-cross-linked nanoparticles with enhanced structural stability. The presence of disulphide bond allowed the controlled release of camptothecin under the trigger of reductive species, such as GSH in the cytosol (Figure 2.14a). The prodrug nanoparticles also exhibited excellent anticancer efficiency against HeLa cells.[259] Recently, Zhang *et al.* used camptothecin prodrug monomer synthesised anticancer nanoparticles with both pH- and reductive-regulated drug release,[227] and pH-responsive charge-reversible property.[228] In more recent reports by Stenzel *et al.*, the anticancer drug 4-(*N*-(S-penicillaminylacetyl)amino) phenylarsenonous acid (PENAO) methacrylate prodrug was copolymerised with OEGMA or zwitterionic 2-methacryloyloxyethyl phosphorylcholine (MPC) to

synthesise macro-CTAs for PISA.[261, 262] The prepared nanoparticles with drug covalently linked to shell block were compared in terms of cytotoxicities, cellular uptakes, spheroid penetration, and cell localisation profiles.

Apart from the above mentioned loading before or during polymerisation, many other studies explored the post-polymerisation loading, including post-encapsulation and modification.[263, 264] Zhang *et al*. exhibited the fabrication of intelligent vesicles with tunable size-selective membrane permeability.[265] In this example, PHPMAm macro-CTA was chain extended with 2-(diisopropylamino)ethyl methacrylate (DIPEMA) and 7-(2-methacryloyloxyethoxy)-4-methylcoumarin (CMA) to afford vesicles. The post-polymerisation dimerisation of coumarin groups was achieved under UV irradiation, leading to cross-linking of the vesicular membrane. The pore size range of the transmembrane traffic could be tuned by cross-linking density *via* changing the UV irradiation time. Post-loading of gold nanoparticles with different sizes (5, 10, 15 nm) into vesicles in acidic solution was performed, indicating vesicles with different cross-linking densities exhibited size-selective permeability.[265] In 2013, Boyer, Davis and co-workers conducted post-modification of PISA-generated nanoparticles for the synthesis of DOX-loaded nanoparticles with the therapeutic application.[266] First, POEMGA macro-CTA was extended with styrene and vinyl benzaldehyde (VBA) *via* dispersion polymerisation to obtain spheres, worms and vesicles. The aldehyde groups of VBA were conjugated with DOX *via* pH-sensitive bonds (drug loading 5 wt%). Cell *via*bility study using MCF-7 breast cancer cells indicated the cytotoxicity of the DOX-loaded nano-objects was significantly affected by morphology.[266] The conjugation between aldehyde group and primary amine group in DOX for drug-loading was also reported by Hong and Pan *et al*.[267] Dispersion polymerisation of *p*-(methacryloxyethoxy)benzaldehyde (MAEBA) using PDMAEMA macro-CTA obtained four different nano-objects with aldehyde-based polymer as core, followed by conjugation between MAEBA and DOX (Figure 2.14b). The DOX-loaded nano-objects displayed cytotoxicity in the order of nanorods-DOX > vesicles-DOX > spheres-DOX > nanowires-DOX, which also indicated the correlation between cytotoxicity and morphology. Recently, Mable *et al*. demonstrated the design and synthesis of Dengue virus-mimicking framboidal vesicles containing rhodamine B piperazine (Rh) for targeting triple-negative breast cancer cells.[268] Two macro-CTAs PGMA and poly(2-(methacryloyloxy)ethyl phosphorylcholine (PMPC) (pure PGMA and 97:3 binary mixture) were chain-extended *via* copolymerisation of HPMA and GlyMA, obtaining triblock copolymer vesicles. The epoxy

groups of GlyMA were reacted with Rh, this allowed post-PISA loading in the vesicular membrane. Further extension with 2-(diisopropylamino)ethyl methacrylate (DPA) led to the formation of pH-responsive framboidal vesicles. *In vitro* studies indicated that the introducing of phosphorylcholine-based targeting ligand is essential for intracellular uptake by MDA-MB-231 breast cancer cells.[268]
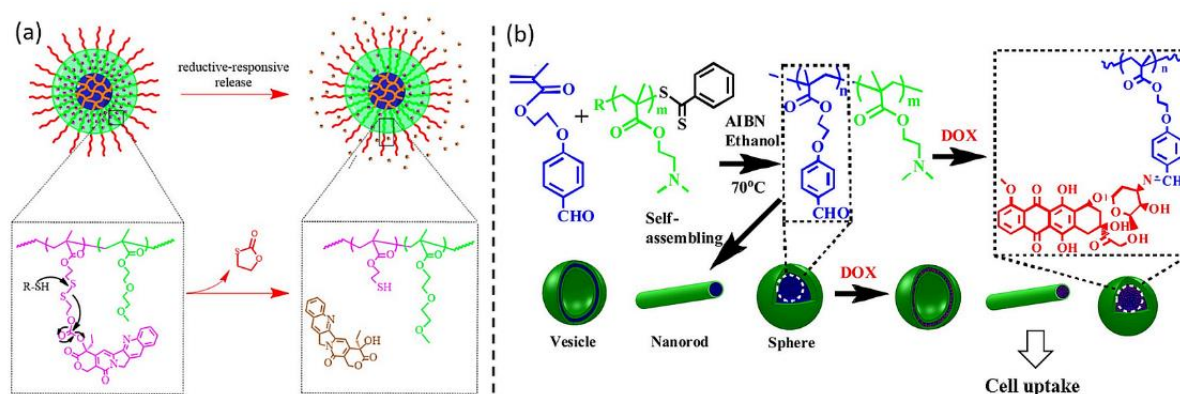

Figure 2.14 (a) Proposed mechanism of reductive-responsive release of CPT from the prodrug nanoparticles. Reprinted from Ref. [259] with permission. Copyright 2016, American Chemical Society. (b) Synthesis of PDMAEMA-*b*-PMAEBA diblock copolymer nano-objects *via* PISA, and conjugation between MAEBA and DOX. Reprinted from Ref. [267] with permission. Copyright 2016, American Chemical Society.

In addition to drug delivery applications, PISA-prepared vesicles have drawn interest as mimicking systems for living cells.[269, 270] Researchers have modulated vesicles with controllable permeability,[186, 271] and used vesicles as enzymatic nanoreactors.[187, 272] Other biomedical applications of PISA include cellular imaging, where nanoparticles with fluorescent property and biocompatibility were prepared *via* PISA.[250, 251]

Catalysis is another application of nanoparticles prepared by PISA. Polymeric nanoparticles derived by PISA are usually not catalytically active but can serve as scaffolds for catalytic species, allowing better dispersion in solvents, higher stability, higher recyclability and less leaching. A series of studies investigated the synthesis of triphenylphosphine[273-276] or nixantphos[277] ligand-containing polymer nanoparticles *via* PISA. The catalytic composite produced by complexation between rhodium and triphenylphosphine proved to be useful for the aqueous biphasic hydroformylation of 1-octane. Oble

and Rieger *et al.* synthesised core-cross-linked nanogels *via* PISA to stablise and support Pd nanoparticles. The hybrid polymer-Pd nanomaterial was applied as quasi-homogeneous catalyst for the Mizoroki-Heck reaction between *n*-butyl acrylate and bromo- or iodoarenes.[242] The complexations between metal nanoparticles and functional groups in nanoparticles derived by PISA were also used to prepare polymer-Ag and polymer-Au nanocomposites with catalytic activities.[170, 243, 244] Recently, our group used ultrasound for the synthesis of both polymeric nanoparticles and the *in situ* formation of Au and Pd nanoparticles.[245] The metal nanoparticles were immobilised on the PDMAEMA block, which was in between the hydrophilic shell and hydrophobic core, resulting in a larger exposed area of metal nanoparticles and more accessible active sites. The synthesised polymer-Au and polymer-Pd showed good catalytic activity and recyclability.

The merits of PISA, including high solid contents, tuneable morphology and functionality, also make nanoparticles suitable candidates for Pickering emulsifiers. In this regard, Armes and co-workers conducted some seminal work of Pickering emulsifiers based on block copolymer nano-objects prepared by PISA.[15, 246-249] Since then, block copolymer nano-objects including spheres,[247, 248, 278] worms,[246, 247, 279] vesicles[249] and even framboidal particles[15] have been used to prepare oil-in-water,[15, 278, 280] water-in-oil,[279, 281] and double[246, 282] emulsions. Armes *et al.* reported that the oil-in-water-in-oil transparent Pickering double emulsions could be obtained by using refractive index-matched nanoparticles with appropriate core-forming block.[282] Recently, Yuan *et al.* studied the effect of solvophilic chain length of nanoparticles on Pickering emulsion, and found a positive correlation between the stability of emulsion and the chain length.[280] For more details on Pickering emulsifier application of PISA-prepared nanoparticles, the reader is referred to a recent review for good insight.[283]

Other applications of PISA-derived nano-objects are emerging in different fields as well. For example, Derry, Armes and co-workers synthesised core-cross-linked poly(stearyl methacrylate)–poly(benzyl methacrylate)–poly(ethylene glycol dimethacrylate) nanoparticles *via* PISA, which offer excellent boundary lubrication performance and ultralow-viscosity.[252] PISA-derived nano-objects can also serve as templating agents for the fabrication of silica nanotubes.[253] Nanoparticle occlusion of silica/dye-loaded nano-objects offers a "Trojan horse" strategy to incorporate payloads into host inorganic crystals such as calcite.[254, 255] PISA also plays an important role in coating industry, such as producing

surfactant-free latexes to solve free surfactants issue, and preparing hollow particles[256] or encapsulating pigments[257] for opacity enhancement.

2.8 Summary and Future Perspective

This chapter summarises the new aspects in PISA including non-thermal initiation methods, high order morphologies, hybrid materials, stimuli-responsive nano-objects, improved throughput and applications of PISA. As elaborated in the previous sections, PISA has proven to be an efficient process for the preparation of polymeric nano-objects. To date, many morphologies observed in conventional solution self-assembly have been realised by PISA in a more efficient way, however, there are still some complex structures that have yet to be realised, for example, Janus cylinder, ellipsoidal particle stacked internal lamellae and oblate ellipsoids. More efforts to achieve complex structures by PISA are expected, where hierarchical self-assembly will attract more attention to achieve 2D and 3D hierarchical structures, and eventually leading to higher-level architecture by PISA. Meanwhile, aqueous formulations will be the focus of future PISA, as the "green" solvent benefits most in industrial applications. The non-thermal initiation methods include photo-, enzyme- and redox-initiation, providing oxygen-tolerant PISA in open vessels, which allow for high throughput PISA and eliminate the requirement for specialised equipment. This may lead to a platform technology for rapid screening of formulations and the establishment of phase diagrams. In the meantime, PISA performed in a continuous-flow fashion has provided a possible route for mass production. Another emerging trend in the PISA process is the concept of "multifunctionality" of nano-objects, for example, where the core-forming monomer containing a therapeutic drug is also stimuli-responsive, or where the synthesised nanoparticles are responsive to multiple triggers. With the addition of multifunctional components, fewer building blocks will be required and the process will become more user-friendly, thus, the versatility of PISA can be further leveraged. Automated or even artificial intelligence-controlled PISA will be another future direction in this field, by which the hands of experienced chemists can be freed. PISA has evolved into a more powerful tool than it was a decade ago, and it is foreseeable that it will perform better and attract more attention in the future, gaining enhanced performance in existing applications or being applied to new fields.

2.9 References

1. N. Corrigan, K. Jung, G. Moad, C. J. Hawker, K. Matyjaszewski and C. Boyer, *Prog. Polym. Sci.*, 2020, **111**, 101311.
2. F. D'Agosto, J. Rieger and M. Lansalot, *Angew. Chem. Int. Ed.*, 2020, **59**, 8368-8392.
3. N. J. Warren and S. P. Armes, *J. Am. Chem. Soc.*, 2014, **136**, 10174-10185.
4. N. J. W. Penfold, J. Yeow, C. Boyer and S. P. Armes, *ACS Macro Lett.*, 2019, **8**, 1029-1054.
5. M. J. Derry, L. A. Fielding and S. P. Armes, *Polym. Chem.*, 2015, **6**, 3054-3062.
6. L. A. Fielding, M. J. Derry, V. Ladmiral, J. Rosselgong, A. M. Rodrigues, L. P. D. Ratcliffe, S. Sugihara and S. P. Armes, *Chem. Sci.*, 2013, **4**, 2081-2087.
7. B. Darmau, M. J. Rymaruk, N. J. Warren, R. Bening and S. P. Armes, *Polym. Chem.*, 2020, **11**, 7533-7541.
8. Q. Zhang and S. Zhu, *ACS Macro Lett.*, 2015, **4**, 755-758.
9. H. Zhou, C. Liu, C. Gao, Y. Qu, K. Shi and W. Zhang, *J. Polym. Sci., Part A: Polym. Chem.*, 2016, **54**, 1517-1525.
10. X. Wang, L. Shen and Z. An, *Prog. Polym. Sci.*, 2018, **83**, 1-27.
11. A. Xu, Q. Lu, Z. Huo, J. Ma, B. Geng, U. Azhar, L. Zhang and S. Zhang, *RSC Adv.*, 2017, **7**, 51612-51620.
12. J. Jennings, M. Beija, A. P. Richez, S. D. Cooper, P. E. Mignot, K. J. Thurecht, K. S. Jack and S. M. Howdle, *J. Am. Chem. Soc.*, 2012, **134**, 4772-4781.
13. M. J. Rymaruk, S. J. Hunter, C. T. O'Brien, S. L. Brown, C. N. Williams and S. P. Armes, *Macromolecules*, 2019, **52**, 2822-2832.
14. P. Chambon, A. Blanazs, G. Battaglia and S. P. Armes, *Macromolecules*, 2012, **45**, 5081-5090.
15. C. J. Mable, N. J. Warren, K. Thompson, O. Mykhaylyk and S. P. Armes, *Chem. Sci.*, 2015, **6**, 6179-6188.
16. W.-J. Zhang, C.-Y. Hong and C.-Y. Pan, *Macromolecules*, 2014, **47**, 1664-1671.
17. P. Yang, L. P. D. Ratcliffe and S. P. Armes, *Macromolecules*, 2013, **46**, 8545-8556.
18. B. Fan, J. Wan, J. Zhai, X. Chen and S. H. Thang, *ACS Nano*, 2021, **15**, 4688-4698.
19. F. Lv, Z. An and P. Wu, *Nat. Commun.*, 2019, **10**, 1397.
20. W.-J. Zhang, C.-Y. Hong and C.-Y. Pan, *Macromol. Rapid Commun.*, 2015, **36**, 1428-1436.
21. W. Wen, S. Guan, Z. Yang and A. Chen, *ACS Macro Lett.*, 2021, **10**, 603-608.
22. P. Yang, Y. Ning, T. J. Neal, E. R. Jones, B. R. Parker and S. P. Armes, *Chem. Sci.*, 2019, **10**, 4200-4208.
23. X. Luo and Z. An, *Macromol. Rapid Commun.*, 2020, **41**, 2000209.
24. X. Luo and Z. An, *Chin. J. Chem*. 2021, **39**, 1819-1824.
25. F. Lv, Z. An and P. Wu, *CCS Chemistry*, 2021, **3**, 2211-2222.
26. D. Li, X. Chen, M. Zeng, J. Ji, Y. Wang, Z. Yang and J. Yuan, *Chem. Sci.*, 2020, **11**, 2855-2860.
27. J. Wan, B. Fan, K. Putera, J. Kim, M. M. Banaszak Holl and S. H. Thang, *ACS Nano*, 2021, **15**, 13721-13731.
28. X. G. Qiao, P. Y. Dugas, B. Charleux, M. Lansalot and E. Bourgeat-Lami, *Macromolecules*, 2015, **48**, 545-556.
29. X. G. Qiao, M. Lansalot, E. Bourgeat-Lami and B. Charleux, *Macromolecules*, 2013, **46**, 4285-4295.
30. G. Delaittre, M. Save and B. Charleux, *Macromol. Rapid Commun.*, 2007, **28**, 1528-1533.
31. S. Sugihara, K. Sugihara, S. P. Armes, H. Ahmad and A. L. Lewis, *Macromolecules*, 2010, **43**, 6321-6329.
32. A. Shahrokhinia, R. A. Scanga, P. Biswas and J. F. Reuther, *Macromolecules*, 2021, **54**, 1441-1451.
33. X. Liu and W. Gao, *ACS Appl. Mater. Interfaces*, 2017, **9**, 2023-2028.
34. W.-M. Wan and C.-Y. Pan, *Macromolecules*, 2007, **40**, 8897-8905.

35. S. Sue-eng, T. Boonchuwong, P. Chaiyasat, M. Okubo and A. Chaiyasat, *Polymer*, 2017, **110**, 124-130.
36. Q. Xu, C. Tian, L. Zhang, Z. Cheng and X. Zhu, *Macromol. Rapid Commun.*, 2019, **40**, 1800327.
37. H. Li, Q. Xu, X. Xu, L. Zhang, Z. Cheng and X. Zhu, *Polymers*, 2020, **12**, 150.
38. Y. Kitayama, H. Moribe, K. Kishida and M. Okubo, *Polym. Chem.*, 2012, **3**, 1555-1559.
39. D. Cordella, A. Debuigne, C. Jérôme, Z. Kochovski, D. Taton and C. Detrembleur, *Macromol. Rapid Commun.*, 2016, **37**, 1181-1187.
40. J. Sarkar, L. Xiao, A. W. Jackson, A. M. van Herk and A. Goto, *Polym. Chem.*, 2018, **9**, 4900-4907.
41. J. Sarkar, K. B. J. Chan and A. Goto, *Polym. Chem.*, 2021, **12**, 1060-1067.
42. D. B. Wright, M. A. Touve, L. Adamiak and N. C. Gianneschi, *ACS Macro Lett.*, 2017, **6**, 925-929.
43. S. Varlas, J. C. Foster and R. K. O'Reilly, *Chem. Commun.*, 2019, **55**, 9066-9071.
44. L. Zhang, C. Song, J. Yu, D. Yang and M. Xie, *J. Polym. Sci., Part A: Polym. Chem.*, 2010, **48**, 5231-5238.
45. K.-Y. Yoon, I.-H. Lee, K. O. Kim, J. Jang, E. Lee and T.-L. Choi, *J. Am. Chem. Soc.*, 2012, **134**, 14291-14294.
46. I.-H. Lee, P. Amaladass, K.-Y. Yoon, S. Shin, Y.-J. Kim, I. Kim, E. Lee and T.-L. Choi, *J. Am. Chem. Soc.*, 2013, **135**, 17695-17698.
47. N. An, X. Chen and J. Yuan, *Polym. Chem.*, 2021, **12**, 3220-3232.
48. W.-J. Zhang, C.-Y. Hong and C.-Y. Pan, *Macromol. Rapid Commun.*, 2019, **40**, 1800279.
49. S. Y. Khor, J. F. Quinn, M. R. Whittaker, N. P. Truong and T. P. Davis, *Macromol. Rapid Commun.*, 2019, **40**, 1800438.
50. P.-E. Millard, L. Barner, M. H. Stenzel, T. P. Davis, C. Barner-Kowollik and A. H. E. Müller, *Macromol. Rapid Commun.*, 2006, **27**, 821-828.
51. J. F. Quinn, L. Barner, E. Rizzardo and T. P. Davis, *J. Polym. Sci., Part A: Polym. Chem.*, 2002, **40**, 19-25.
52. R.-K. Bai, Y.-Z. You and C.-Y. Pan, *Macromol. Rapid Commun.*, 2001, **22**, 315-319.
53. M. Y. Khan, M.-S. Cho and Y.-J. Kwark, *Macromolecules*, 2014, **47**, 1929-1934.
54. M. A. Tasdelen, Y. Y. Durmaz, B. Karagoz, N. Bicak and Y. Yagci, *J. Polym. Sci., Part A: Polym. Chem.*, 2008, **46**, 3387-3395.
55. S. Muthukrishnan, E. H. Pan, M. H. Stenzel, C. Barner-Kowollik, T. P. Davis, D. Lewis and L. Barner, *Macromolecules*, 2007, **40**, 2978-2980.
56. L. Lu, N. Yang and Y. Cai, *Chem. Commun.*, 2005, 5287-5288.
57. P. Maximiano, P. V. Mendonça, J. R. C. Costa, N. L. Haworth, A. C. Serra, T. Guliashvili, M. L. Coote and J. F. J. Coelho, *Macromolecules*, 2016, **49**, 1597-1604.
58. S. Shanmugam, J. Xu and C. Boyer, *J. Am. Chem. Soc.*, 2015, **137**, 9174-9185.
59. M. Chen, M. J. MacLeod and J. A. Johnson, *ACS Macro Lett.*, 2015, **4**, 566-569.
60. J. Xu, K. Jung and C. Boyer, *Macromolecules*, 2014, **47**, 4217-4229.
61. G. Liu, H. Shi, Y. Cui, J. Tong, Y. Zhao, D. Wang and Y. Cai, *Polym. Chem.*, 2013, **4**, 1176-1182.
62. S. Shanmugam, J. Xu and C. Boyer, *Angew. Chem. Int. Ed.*, 2016, **55**, 1036-1040.
63. S. L. Brown, C. M. Rayner, S. Graham, A. Cooper, S. Rannard and S. Perrier, *Chem. Commun.*, 2007, 2145-2147.
64. J. Yeow and C. Boyer, *Adv. Sci.*, 2017, **4**, 1700137.
65. E. Yoshida, *J. Dispersion Sci. Technol.*, 2020, **41**, 763-770.
66. S. Varlas, P. G. Georgiou, P. Bilalis, J. R. Jones, N. Hadjichristidis and R. K. O'Reilly, *Biomacromolecules*, 2018, **19**, 4453-4462.
67. J.-P. Fouassier and J. Lalevée, *Photoinitiators for polymer synthesis: scope, reactivity, and efficiency*, John Wiley & Sons, 2012.
68. J. Xu, S. Shanmugam, N. A. Corrigan and C. Boyer, in *Controlled Radical Polymerization: Mechanisms*, American Chemical Society, 2015, vol. 1187, ch. 13, pp. 247-267.

69.   T. G. McKenzie, Q. Fu, E. H. H. Wong, D. E. Dunstan and G. G. Qiao, *Macromolecules*, 2015, **48**, 3864-3872.

70.   C. Ding, C. Fan, G. Jiang, X. Pan, Z. Zhang, J. Zhu and X. Zhu, *Macromol. Rapid Commun.*, 2015, **36**, 2181-2185.

71.   J. Xu, K. Jung, A. Atme, S. Shanmugam and C. Boyer, *J. Am. Chem. Soc.*, 2014, **136**, 5508-5519.

72.   Y. Jiang, N. Xu, J. Han, Q. Yu, L. Guo, P. Gao, X. Lu and Y. Cai, *Polym. Chem.*, 2015, **6**, 4955-4965.

73.   J. Tan, H. Sun, M. Yu, B. S. Sumerlin and L. Zhang, *ACS Macro Lett.*, 2015, **4**, 1249-1253.

74.   P. Gao, H. Cao, Y. Ding, M. Cai, Z. Cui, X. Lu and Y. Cai, *ACS Macro Lett.*, 2016, **5**, 1327-1331.

75.   L. Cao, Q. Zhao, Q. Liu, L. Ma, C. Li, X. Wang and Y. Cai, *Macromolecules*, 2020, **53**, 2220-2227.

76.   J. He, Q. Xu, J. Tan and L. Zhang, *Macromol. Rapid Commun.*, 2019, **40**, 1800296.

77.   J. Tan, J. He, X. Li, Q. Xu, C. Huang, D. Liu and L. Zhang, *Polym. Chem.*, 2017, **8**, 6853-6864.

78.   L. D. Blackman, K. E. B. Doncom, M. I. Gibson and R. K. O'Reilly, *Polym. Chem.*, 2017, **8**, 2860-2871.

79.   X. Wang, S. Man, J. Zheng and Z. An, *ACS Macro Lett.*, 2018, **7**, 1461-1467.

80.   N. Zaquen, W. A. A. W. Azizi, J. Yeow, R. P. Kuchel, T. Junkers, P. B. Zetterlund and C. Boyer, *Polym. Chem.*, 2019, **10**, 2406-2414.

81.   L. Zhang, L. Xie, S. Xu, R. P. Kuchel, Y. Dai, K. Jung and C. Boyer, *Biomacromolecules*, 2020, **21**, 3887-3897.

82.   Y. Du, S. Jia, Y. Chen, L. Zhang and J. Tan, *ACS Macro Lett.*, 2021, **10**, 297-306.

83.   H. Zhou and J. A. Johnson, *Angew. Chem. Int. Ed.*, 2013, **52**, 2235-2238.

84.   Y.-Z. You, C.-Y. Hong, R.-K. Bai, C.-Y. Pan and J. Wang, *Macromol. Chem. Phys.*, 2002, **203**, 477-483.

85.   J. F. Quinn, L. Barner, C. Barner-Kowollik, E. Rizzardo and T. P. Davis, *Macromolecules*, 2002, **35**, 7620-7627.

86.   T. Otsu, *J. Polym. Sci., Part A: Polym. Chem.*, 2000, **38**, 2121-2136.

87.   J. Yeow, O. R. Sugita and C. Boyer, *ACS Macro Lett.*, 2016, **5**, 558-564.

88.   V. Tkachenko, C. Matei Ghimbeu, C. Vaulot, L. Vidal, J. Poly and A. Chemtob, *Polym. Chem.*, 2019, **10**, 2316-2326.

89.   J. Yeow, J. Xu and C. Boyer, *ACS Macro Lett.*, 2015, **4**, 984-990.

90.   S. Han, Y. Gu, M. Ma and M. Chen, *Chem. Sci.*, 2020, **11**, 10431-10436.

91.   J. Zhou, C. Hong and C. Pan, *Materials Chemistry Frontiers*, 2017, **1**, 1200-1206.

92.   J. Xu, S. Shanmugam, H. T. Duong and C. Boyer, *Polym. Chem.*, 2015, **6**, 5615-5624.

93.   J. Yeow, R. Chapman, J. Xu and C. Boyer, *Polym. Chem.*, 2017, **8**, 5012-5022.

94.   C. Lin, S. K. Katla and J. Perez-Mercader, *Journal of Photochemistry and Photobiology A: Chemistry*, 2021, **406**, 112992.

95.   J. Yeow, S. Shanmugam, N. Corrigan, R. P. Kuchel, J. Xu and C. Boyer, *Macromolecules*, 2016, **49**, 7277-7285.

96.   G. Ng, J. Yeow, J. Xu and C. Boyer, *Polym. Chem.*, 2017, **8**, 2841-2851.

97.   S. Xu, J. Yeow and C. Boyer, *ACS Macro Lett.*, 2018, **7**, 1376-1382.

98.   A. B. Korpusik, Y. Tan, J. B. Garrison, W. Tan and B. S. Sumerlin, *Macromolecules*, 2021, **54**, 7354-7363.

99.   Y.-H. Ng, F. di Lena and C. L. L. Chai, *Chem. Commun.*, 2011, **47**, 6464-6466.

100.   Y.-H. Ng, F. di Lena and C. L. L. Chai, *Polym. Chem.*, 2011, **2**, 589-594.

101.   B. Zhang, X. Wang, A. Zhu, K. Ma, Y. Lv, X. Wang and Z. An, *Macromolecules*, 2015, **48**, 7792-7802.

102.   Y. Lv, Z. Liu, A. Zhu and Z. An, *J. Polym. Sci., Part A: Polym. Chem.*, 2017, **55**, 164-174.

103.   Z. Liu, Y. Lv and Z. An, *Angew. Chem. Int. Ed.*, 2017, **56**, 13852-13856.

104.   J. Tan, Q. Xu, X. Li, J. He, Y. Zhang, X. Dai, L. Yu, R. Zeng and L. Zhang, *Macromol. Rapid Commun.*, 2018, **39**, 1700871.

105.   Q. Xu, Y. Zhang, X. Li, J. He, J. Tan and L. Zhang, *Polym. Chem.*, 2018, **9**, 4908-4916.

106.   R. Chapman, A. J. Gormley, K.-L. Herpoldt and M. M. Stevens, *Macromolecules*, 2014, **47**, 8541-8547.
107.   R. Chapman, A. J. Gormley, M. H. Stenzel and M. M. Stevens, *Angew. Chem. Int. Ed.*, 2016, **55**, 4500-4503.
108.   J. Tan, D. Liu, Y. Bai, C. Huang, X. Li, J. He, Q. Xu and L. Zhang, *Macromolecules*, 2017, **50**, 5798-5806.
109.   W.-B. Cai, D.-D. Liu, Y. Chen, L. Zhang and J.-B. Tan, *Chin. J. Polym. Sci.*, 2021, **39**, 1127-1137.
110.   J. Tan, X. Dai, Y. Zhang, L. Yu, H. Sun and L. Zhang, *ACS Macro Lett.*, 2019, **8**, 205-212.
111.   T. Lückerath, K. Koynov, S. Loescher, C. J. Whitfield, L. Nuhn, A. Walther, C. Barner-Kowollik, D. Y. W. Ng and T. Weil, *Angew. Chem. Int. Ed.*, 2020, **59**, 15474-15479.
112.   N. Kohut-Svelko, R. Pirri, J. M. Asua and J. R. Leiza, *J. Polym. Sci., Part A: Polym. Chem.*, 2009, **47**, 2917-2927.
113.   T.-P. Chiu and T.-M. Don, *J. Appl. Polym. Sci.*, 2008, **109**, 3622-3630.
114.   G. S. Misra and C. V. Gupta, *Macromol. Chem. Phys.*, 1973, **165**, 205-216.
115.   X.-L. Sun, W.-D. He, T.-T. Pan, Z.-L. Ding and Y.-J. Zhang, *Polymer*, 2010, **51**, 110-114.
116.   H. Zheng, W. Bai, K. Hu, R. Bai and C. Pan, *J. Polym. Sci., Part A: Polym. Chem.*, 2008, **46**, 2575-2580.
117.   X.-L. Sun, W.-D. He, J. Li, L.-Y. Li, B.-Y. Zhang and T.-T. Pan, *J. Polym. Sci., Part A: Polym. Chem.*, 2009, **47**, 6863-6872.
118.   A. M. dos Santos, T. Le Bris, C. Graillat, F. D'Agosto and M. Lansalot, *Macromolecules*, 2009, **42**, 946-956.
119.   G. Liu, Q. Qiu, W. Shen and Z. An, *Macromolecules*, 2011, **44**, 5237-5245.
120.   H. Narain, S. M. Jagadale and N. D. Ghatge, *J. Polym. Sci., Polym. Chem. Ed.*, 1981, **19**, 1225-1238.
121.   D. E. Cabelli and B. H. J. Bielski, *J. Phys. Chem.*, 1983, **87**, 1809-1812.
122.   X. Dai, L. Yu, Y. Zhang, L. Zhang and J. Tan, *Macromolecules*, 2019, **52**, 7468-7476.
123.   O. J. Deane, O. M. Musa, A. Fernyhough and S. P. Armes, *Macromolecules*, 2020, **53**, 1422-1434.
124.   J. A. Pojman, D. C. Leard and W. West, *J. Am. Chem. Soc.*, 1992, **114**, 8298-8299.
125.   R. P. Washington, W. W. West, G. P. Misra and J. A. Pojman, *J. Am. Chem. Soc.*, 1999, **121**, 7373-7380.
126.   B. Venkataraman and P. G. Soerensen, *J. Phys. Chem.*, 1991, **95**, 5707-5712.
127.   H. D. Foersterling, S. Muranyi and Z. Noszticzius, *J. Phys. Chem.*, 1990, **94**, 2915-2921.
128.   B. P. Bastakoti and J. Perez-Mercader, *Angew. Chem. Int. Ed.*, 2017, **56**, 12086-12091.
129.   B. P. Bastakoti and J. Perez-Mercader, *Adv. Mater.*, 2017, **29**, 1704368.
130.   B. P. Bastakoti, S. Guragain and J. Perez-Mercader, *Chem. - Eur. J.*, 2018, **24**, 10621-10624.
131.   L. Hou, M. Dueñas-Díez, R. Srivastava and J. Pérez-Mercader, *Commun. Chem.*, 2019, **2**, 139.
132.   G. Cheng and J. Perez-Mercader, *Chem*, 2020, **6**, 1160-1171.
133.   J. Guo, E. Poros-Tarcali and J. Perez-Mercader, *Chem. Commun.*, 2019, **55**, 9383-9386.
134.   J. Guo, E. Poros-Tarcali and J. Pérez-Mercader, *Front. Chem.*, 2021, **9**, 576349.
135.   T. J. Mason, *Chem. Soc. Rev.*, 1997, **26**, 443-451.
136.   T. G. McKenzie, E. Colombo, Q. Fu, M. Ashokkumar and G. G. Qiao, *Angew. Chem. Int. Ed. Engl.*, 2017, **56**, 12302-12306.
137.   S. Piogé, T. N. Tran, T. G. McKenzie, S. Pascual, M. Ashokkumar, L. Fontaine and G. Qiao, *Macromolecules*, 2018, **51**, 8862-8869.
138.   Y. Zhang, J. He, X. Dai, L. Yu, J. Tan and L. Zhang, *Polym. Chem.*, 2019, **10**, 3902-3911.
139.   M. Sponchioni, C. T. O'Brien, C. Borchers, E. Wang, M. N. Rivolta, N. J. W. Penfold, I. Canton and S. P. Armes, *Chem. Sci.*, 2020, **11**, 232-240.
140.   D. Le, F. Wagner, M. Takamiya, I. L. Hsiao, G. Gil Alvaradejo, U. Strähle, C. Weiss and G. Delaittre, *Chem. Commun.*, 2019, **55**, 3741-3744.
141.   W.-M. Wan and C.-Y. Pan, *Polym. Chem.*, 2010, **1**, 1475-1484.
142.   K. Yu, C. Bartels and A. Eisenberg, *Macromolecules*, 1998, **31**, 9399-9402.

143. M. Huo, D. Li, G. Song, J. Zhang, D. Wu, Y. Wei and J. Yuan, *Macromol. Rapid Commun.*, 2018, **39**, 1700840.
144. X.-F. Xu, R.-M. Zhu, C.-Y. Pan, Y.-Z. You, W.-J. Zhang and C.-Y. Hong, *Macromolecules*, 2021, **54**, 2729-2739.
145. L. Wang, Y. Ding, Q. Liu, Q. Zhao, X. Dai, X. Lu and Y. Cai, *ACS Macro Lett.*, 2019, **8**, 623-628.
146. F. Lv, Z. An and P. Wu, *Macromolecules*, 2020, **53**, 367-373.
147. X. Luo, *Eur. Polym. J.*, 2021, **158**, 110639.
148. S.-P. Wen, J. G. Saunders and L. A. Fielding, *Polym. Chem.*, 2020, **11**, 3416-3426.
149. X. Chen, L. Liu, M. Huo, M. Zeng, L. Peng, A. Feng, X. Wang and J. Yuan, *Angew. Chem. Int. Ed.*, 2017, **56**, 16541-16545.
150. X. Chen, N. An, M. Zeng and J. Yuan, *Chem. Commun.*, 2021, **57**, 13720-13723.
151. X. Wang, C. A. Figg, X. Lv, Y. Yang, B. S. Sumerlin and Z. An, *ACS Macro Lett.*, 2017, **6**, 337-342.
152. Y. Zhang, M. Cao, G. Han, T. Guo, T. Ying and W. Zhang, *Macromolecules*, 2018, **51**, 5440-5449.
153. C. Gao, S. Li, Q. Li, P. Shi, S. A. Shah and W. Zhang, *Polym. Chem.*, 2014, **5**, 6957-6966.
154. W. Wang, C. Gao, Y. Qu, Z. Song and W. Zhang, *Macromolecules*, 2016, **49**, 2772-2781.
155. Y. Qu, S. Wang, H. Khan, C. Gao, H. Zhou and W. Zhang, *Polym. Chem.*, 2016, **7**, 1953-1962.
156. P. Biais, M. Engel, O. Colombani, T. Nicolai, F. Stoffelbach and J. Rieger, *Polym. Chem.*, 2021, **12**, 1040-1049.
157. P. Biais, O. Colombani, L. Bouteiller, F. Stoffelbach and J. Rieger, *Polym. Chem.*, 2020, **11**, 4568-4578.
158. P. Biais, P. Beaunier, F. Stoffelbach and J. Rieger, *Polym. Chem.*, 2018, **9**, 4483-4491.
159. C. Gao, J. Wu, H. Zhou, Y. Qu, B. Li and W. Zhang, *Macromolecules*, 2016, **49**, 4490-4500.
160. P. Shi, Q. Li, X. He, S. Li, P. Sun and W. Zhang, *Macromolecules*, 2014, **47**, 7442-7452.
161. X. He, Q. Li, P. Shi, Y. Cui, S. Li and W. Zhang, *Polym. Chem.*, 2014, **5**, 7090-7099.
162. Z. Song, X. He, C. Gao, H. Khan, P. Shi and W. Zhang, *Polym. Chem.*, 2015, **6**, 6563-6572.
163. X. Shen, F. Huo, H. Kang, S. Zhang, J. Li and W. Zhang, *Polym. Chem.*, 2015, **6**, 3407-3414.
164. F. Huo, S. Li, Q. Li, Y. Qu and W. Zhang, *Macromolecules*, 2014, **47**, 2340-2349.
165. J. Huang, Y. Guo, S. Gu, G. Han, W. Duan, C. Gao and W. Zhang, *Polym. Chem.*, 2019, **10**, 3426-3435.
166. M. Huo, M. Zeng, D. Li, L. Liu, Y. Wei and J. Yuan, *Macromolecules*, 2017, **50**, 8212-8220.
167. M. Huo, Y. Zhang, M. Zeng, L. Liu, Y. Wei and J. Yuan, *Macromolecules*, 2017, **50**, 8192-8201.
168. X. Dai, Y. Zhang, L. Yu, X. Li, L. Zhang and J. Tan, *ACS Macro Lett.*, 2019, **8**, 955-961.
169. R. Bleach, B. Karagoz, S. M. Prakash, T. P. Davis and C. Boyer, *ACS Macro Lett.*, 2014, **3**, 591-596.
170. P. Shi, C. Gao, X. He, P. Sun and W. Zhang, *Macromolecules*, 2015, **48**, 1380-1389.
171. B. Karagoz, J. Yeow, L. Esser, S. M. Prakash, R. P. Kuchel, T. P. Davis and C. Boyer, *Langmuir*, 2014, **30**, 10493-10502.
172. Y. Zhang, P. Filipczak, G. He, G. Nowaczyk, L. Witczak, W. Raj, M. Kozanecki, K. Matyjaszewski and J. Pietrasik, *Polymer*, 2017, **129**, 144-150.
173. W. Zhou, Q. Qu, W. Yu and Z. An, *ACS Macro Lett.*, 2014, **3**, 1220-1224.
174. L. Upadhyaya, M. Semsarilar, S. Nehache, D. Cot, R. Fernández-Pacheco, G. Martinez, R. Mallada, A. Deratani and D. Quemener, *Macromolecules*, 2016, **49**, 7908-7916.
175. D. Nguyen, V. Huynh, N. Pham, B. Pham, A. Serelis, T. Davey, C. Such and B. Hawkett, *Macromol. Rapid Commun.*, 2019, **40**, 1800402.
176. L. Upadhyaya, C. Egbosimba, X. Qian, R. Wickramasinghe, R. Fernández-Pacheco, I. M. Coelhoso, C. A. M. Portugal, J. G. Crespo, D. Quemener and M. Semsarilar, *Macromol. Rapid Commun.*, 2019, **40**, 1800333.
177. S. Samanta, S. L. Banerjee, K. Bhattacharya and N. K. Singha, *ACS Appl. Mater. Interfaces*, 2021, **13**, 36307-36319.
178. B. Fan, Y. Liu, J. Wan, S. Crawford and S. H. Thang, *ACS Mater. Lett.*, 2020, **2**, 492-498.
179. Y. Zheng, Y. Huang, Z. M. Abbas and B. C. Benicewicz, *Polym. Chem.*, 2016, **7**, 5347-5350.

180. Y. Zheng, Y. Huang, Z. M. Abbas and B. C. Benicewicz, *Polym. Chem.*, 2017, **8**, 370-374.

181. X. G. Qiao, O. Lambert, J. C. Taveau, P. Y. Dugas, B. Charleux, M. Lansalot and E. Bourgeat-Lami, *Macromolecules*, 2017, **50**, 3796-3806.

182. C. J. Mable, R. R. Gibson, S. Prevost, B. E. McKenzie, O. O. Mykhaylyk and S. P. Armes, *J. Am. Chem. Soc.*, 2015, **137**, 16098-16108.

183. J. Tan, X. Zhang, D. Liu, Y. Bai, C. Huang, X. Li and L. Zhang, *Macromol. Rapid Commun.*, 2017, **38**, 1600508.

184. J. Tan, D. Liu, X. Zhang, C. Huang, J. He, Q. Xu, X. Li and L. Zhang, *RSC Adv.*, 2017, **7**, 23114-23121.

185. J. Engström, H. Asem, H. Brismar, Y. Zhang, M. Malkoch and E. Malmström, *Macromol. Chem. Phys.*, 2020, **221**, 1900443.

186. L. D. Blackman, S. Varlas, M. C. Arno, A. Fayter, M. I. Gibson and R. K. O'Reilly, *ACS Macro Lett.*, 2017, **6**, 1263-1267.

187. L. D. Blackman, S. Varlas, M. C. Arno, Z. H. Houston, N. L. Fletcher, K. J. Thurecht, M. Hasan, M. I. Gibson and R. K. O'Reilly, *ACS Central Science*, 2018, **4**, 718-723.

188. F. H. Sobotta, F. Hausig, D. O. Harz, S. Hoeppener, U. S. Schubert and J. C. Brendel, *Polym. Chem.*, 2018, **9**, 1593-1602.

189. F. H. Sobotta, M. T. Kuchenbrod, F. V. Gruschwitz, G. Festag, P. Bellstedt, S. Hoeppener and J. C. Brendel, *Angew. Chem. Int. Ed.*, 2021, **60**, 24716-24723.

190. B. Le Droumaguet and K. Velonia, *Angew. Chem. Int. Ed.*, 2008, **47**, 6263-6266.

191. C. Ma, X. Liu, G. Wu, P. Zhou, Y. Zhou, L. Wang and X. Huang, *ACS Macro Lett.*, 2017, **6**, 689-694.

192. T. Lueckerath, T. Strauch, K. Koynov, C. Barner-Kowollik, D. Y. W. Ng and T. Weil, *Biomacromolecules*, 2019, **20**, 212-221.

193. D. Das, D. Gerboth, A. Postma, S. Srinivasan, H. Kern, J. Chen, D. M. Ratner, P. S. Stayton and A. J. Convertine, *Polym. Chem.*, 2016, **7**, 6133-6143.

194. H. Sun, W. Cao, N. Zang, T. D. Clemons, G. M. Scheutz, Z. Hu, M. P. Thompson, Y. Liang, M. Vratsanos, X. Zhou, W. Choi, B. S. Sumerlin, S. I. Stupp and N. C. Gianneschi, *Angew. Chem. Int. Ed.*, 2020, **59**, 19136-19142.

195. L. Luppi, T. Babut, E. Petit, M. Rolland, D. Quemener, L. Soussan, M. A. Moradi and M. Semsarilar, *Polym. Chem.*, 2019, **10**, 336-344.

196. T. P. T. Dao, L. Vezenkov, G. Subra, M. Amblard, M. In, J.-F. Le Meins, F. Aubrit, M.-A. Moradi, V. Ladmiral and M. Semsarilar, *Macromolecules*, 2020, **53**, 7034-7043.

197. T. P. T. Dao, L. Vezenkov, G. Subra, V. Ladmiral and M. Semsarilar, *Polym. Chem.*, 2021, **12**, 113-121.

198. V. Ladmiral, A. Charlot, M. Semsarilar and S. P. Armes, *Polym. Chem.*, 2015, **6**, 1805-1816.

199. K. Bauri, A. Narayanan, U. Haldar and P. De, *Polym. Chem.*, 2015, **6**, 6152-6162.

200. K. Bauri, B. Maiti and P. De, *Macromol. Symp.*, 2016, **369**, 101-107.

201. Z. An, Q. Shi, W. Tang, C.-K. Tsung, C. J. Hawker and G. D. Stucky, *J. Am. Chem. Soc.*, 2007, **129**, 14493-14499.

202. N. Busatto, V. Stolojan, M. Shaw, J. L. Keddie and P. J. Roth, *Macromol. Rapid Commun.*, 2019, **40**, 1800346.

203. J. Rieger, C. Grazon, B. Charleux, D. Alaimo and C. Jérôme, *J. Polym. Sci., Part A: Polym. Chem.*, 2009, **47**, 2373-2390.

204. A. Blanazs, R. Verber, O. O. Mykhaylyk, A. J. Ryan, J. Z. Heath, C. W. I. Douglas and S. P. Armes, *J. Am. Chem. Soc.*, 2012, **134**, 9741-9748.

205. L. A. Fielding, J. A. Lane, M. J. Derry, O. O. Mykhaylyk and S. P. Armes, *J. Am. Chem. Soc.*, 2014, **136**, 5790-5798.

206. N. J. Warren, O. O. Mykhaylyk, D. Mahmood, A. J. Ryan and S. P. Armes, *J. Am. Chem. Soc.*, 2014, **136**, 1023-1033.

207. N. J. W. Penfold, J. R. Whatley and S. P. Armes, *Macromolecules*, 2019, **52**, 1653-1662.

208. T. N. Tran, S. Piogé, L. Fontaine and S. Pascual, *Macromol. Rapid Commun.*, 2020, **41**, 2000203.

209. N. Audureau, F. Coumes, J.-M. Guigner, T. P. T. Nguyen, C. Ménager, F. Stoffelbach and J. Rieger, *Polym. Chem.*, 2020, **11**, 5998-6008.
210. M. J. Derry, O. O. Mykhaylyk, A. J. Ryan and S. P. Armes, *Chem. Sci.*, 2018, **9**, 4071-4082.
211. L. P. D. Ratcliffe, M. J. Derry, A. Ianiro, R. Tuinier and S. P. Armes, *Angew. Chem. Int. Ed.*, 2019, **58**, 18964-18970.
212. J. R. Lovett, N. J. Warren, L. P. D. Ratcliffe, M. K. Kocik and S. P. Armes, *Angew. Chem. Int. Ed.*, 2015, **54**, 1279-1283.
213. N. J. W. Penfold, J. R. Lovett, N. J. Warren, P. Verstraete, J. Smets and S. P. Armes, *Polym. Chem.*, 2016, **7**, 79-88.
214. S. M. North and S. P. Armes, *Polym. Chem.*, 2020, **11**, 2147-2156.
215. X.-F. Xu, C.-Y. Pan, W.-J. Zhang and C.-Y. Hong, *Macromolecules*, 2019, **52**, 1965-1975.
216. L. Yu, Y. Zhang, X. Dai, Q. Xu, L. Zhang and J. Tan, *Chem. Commun.*, 2019, **55**, 11920-11923.
217. S. L. Canning, T. J. Neal and S. P. Armes, *Macromolecules*, 2017, **50**, 6108-6116.
218. S. M. North and S. P. Armes, *Polym. Chem.*, 2021, **12**, 5842-5850.
219. S. Guan, C. Zhang, W. Wen, T. Qu, X. Zheng, Y. Zhao and A. Chen, *ACS Macro Lett.*, 2018, **7**, 358-363.
220. Q. Ye, M. Huo, M. Zeng, L. Liu, L. Peng, X. Wang and J. Yuan, *Macromolecules*, 2018, **51**, 3308-3314.
221. A. Bagheri, C. Boyer and M. Lim, *Macromol. Rapid Commun.*, 2019, **40**, 1800510.
222. E. Chaabouni, V. Tkachenko, L. Vidal, N. Allouche and A. Chemtob, *Eur. Polym. J.*, 2021, **156**, 110633.
223. S. Xu, G. Ng, J. Xu, R. P. Kuchel, J. Yeow and C. Boyer, *ACS Macro Lett.*, 2017, **6**, 1237-1244.
224. Y. Zhou, Z. Wang, Y. Wang, L. Li, N. Zhou, Y. Cai, Z. Zhang and X. Zhu, *Polym. Chem.*, 2020, **11**, 5619-5629.
225. J. R. Lovett, N. J. Warren, S. P. Armes, M. J. Smallridge and R. B. Cracknell, *Macromolecules*, 2016, **49**, 1016-1025.
226. F. Khakzad, A. R. Mahdavian, H. Salehi-Mobarakeh and M. H. Sharifian, *J. Colloid Interface Sci.*, 2018, **515**, 58-69.
227. M. Chen, W.-G. Zhang, J.-W. Li, C.-Y. Hong, W.-J. Zhang and Y.-Z. You, *Science China Chemistry*, 2018, **61**, 1159-1166.
228. X. Zhao, M. Chen, W.-G. Zhang, C.-H. Wang, F. Wang, Y.-Z. You, W.-J. Zhang and C.-Y. Hong, *Macromol. Rapid Commun.*, 2020, **41**, 2000260.
229. C. Chen, F. Richter, J. Zhang, C. Guerrero-Sanchez, A. Traeger, U. S. Schubert, A. Feng and S. H. Thang, *Eur. Polym. J.*, 2021, **160**, 110777.
230. C. Guerrero-Sanchez, R. M. Paulus, M. W. M. Fijten, M. J. de la Mar, R. Hoogenboom and U. S. Schubert, *Appl. Surf. Sci.*, 2006, **252**, 2555-2561.
231. A. A. Cockram, R. D. Bradley, S. A. Lynch, P. C. D. Fleming, N. S. J. Williams, M. W. Murray, S. N. Emmett and S. P. Armes, *React. Chem. Eng.*, 2018, **3**, 645-657.
232. C. Guerrero-Sanchez, D. J. Keddie, S. Saubern and J. Chiefari, *ACS Combinatorial Science*, 2012, **14**, 389-394.
233. M. Wang, J. Zhang, C. Guerrero-Sanchez, U. S. Schubert, A. Feng and S. H. Thang, *ACS Combinatorial Science*, 2019, **21**, 643-649.
234. D. Liu, W. Cai, L. Zhang, C. Boyer and J. Tan, *Macromolecules*, 2020, **53**, 1212-1223.
235. M. A. Touve, D. B. Wright, C. Mu, H. Sun, C. Park and N. C. Gianneschi, *Macromolecules*, 2019, **52**, 5529-5537.
236. J. Peng, C. Tian, L. Zhang, Z. Cheng and X. Zhu, *Polym. Chem.*, 2017, **8**, 1495-1506.
237. S. Parkinson, N. S. Hondow, J. S. Conteh, R. A. Bourne and N. J. Warren, *React. Chem. Eng.*, 2019, **4**, 852-861.
238. N. Zaquen, J. Yeow, T. Junkers, C. Boyer and P. B. Zetterlund, *Macromolecules*, 2018, **51**, 5165-5172.
239. N. Zaquen, H. Zu, A. M. N. B. P. H. A. Kadir, T. Junkers, P. B. Zetterlund and C. Boyer, *ACS Applied Polymer Materials*, 2019, **1**, 1251-1256.

240. N. Zaquen, A. M. N. B. P. H. A. Kadir, A. Iasa, N. Corrigan, T. Junkers, P. B. Zetterlund and C. Boyer, *Macromolecules*, 2019, **52**, 1609-1619.
241. S. Parkinson, S. T. Knox, R. A. Bourne and N. J. Warren, *Polym. Chem.*, 2020, **11**, 3465-3474.
242. A. Pontes da Costa, D. R. Nunes, M. Tharaud, J. Oble, G. Poli and J. Rieger, *ChemCatChem*, 2017, **9**, 2167-2175.
243. M. Tan, Y. Shi, Z. Fu and W. Yang, *Polym. Chem.*, 2018, **9**, 1082-1094.
244. Y. Zhang, Z. Wang, K. Matyjaszewski and J. Pietrasik, *Eur. Polym. J.*, 2019, **110**, 49-55.
245. J. Wan, B. Fan and S. H. Thang, *Nanoscale Adv.*, 2021, **3**, 3306-3315.
246. K. L. Thompson, C. J. Mable, J. A. Lane, M. J. Derry, L. A. Fielding and S. P. Armes, *Langmuir*, 2015, **31**, 4137-4144.
247. K. L. Thompson, C. J. Mable, A. Cockram, N. J. Warren, V. J. Cunningham, E. R. Jones, R. Verber and S. P. Armes, *Soft Matter*, 2014, **10**, 8615-8626.
248. V. J. Cunningham, A. M. Alswieleh, K. L. Thompson, M. Williams, G. J. Leggett, S. P. Armes and O. M. Musa, *Macromolecules*, 2014, **47**, 5613-5623.
249. K. L. Thompson, P. Chambon, R. Verber and S. P. Armes, *J. Am. Chem. Soc.*, 2012, **134**, 12450-12453.
250. J. Wang, Y. Zhu, S. Zhou, W. Wu, Q. Tong, J. Hu, S. Min, G. Hou, B. Dong and B. Song, *Dyes and Pigments*, 2021, **190**, 109353.
251. Y. Wang, D. Yang, Y. Hu, Y. Wang, W. J. Yang and L. Wang, *Talanta*, 2021, **232**, 122182.
252. M. J. Derry, T. Smith, P. S. O'Hora and S. P. Armes, *ACS Appl. Mater. Interfaces*, 2019, **11**, 33364-33369.
253. W.-J. Zhang, C.-Y. Hong and C.-Y. Pan, *Journal of Materials Chemistry A*, 2014, **2**, 7819-7828.
254. Y. Ning, D. J. Whitaker, C. J. Mable, M. J. Derry, N. J. W. Penfold, A. N. Kulak, D. C. Green, F. C. Meldrum and S. P. Armes, *Chem. Sci.*, 2018, **9**, 8396-8401.
255. Y. Ning, L. Han, M. J. Derry, F. C. Meldrum and S. P. Armes, *J. Am. Chem. Soc.*, 2019, **141**, 2557-2567.
256. B. T. T. Pham, D. Nguyen, V. T. Huynh, E. H. Pan, B. Shirodkar-Robinson, M. Carey, A. K. Serelis, G. G. Warr, T. Davey, C. H. Such and B. S. Hawkett, *Langmuir*, 2018, **34**, 4255-4263.
257. D. Nguyen, V. Huynh, M. Lam, A. Serelis, T. Davey, O. Paravagna, C. Such and B. Hawkett, *Macromol. Rapid Commun.*, 2021, **42**, 2100008.
258. B. Karagoz, C. Boyer and T. P. Davis, *Macromol. Rapid Commun.*, 2014, **35**, 417-421.
259. W.-J. Zhang, C.-Y. Hong and C.-Y. Pan, *Biomacromolecules*, 2016, **17**, 2992-2999.
260. C. Tian, J. Niu, X. Wei, Y. Xu, L. Zhang, Z. Cheng and X. Zhu, *Nanoscale*, 2018, **10**, 10277-10287.
261. J.-M. Noy, F. Chen and M. Stenzel, *Beilstein journal of organic chemistry*, 2021, **17**, 2302-2314.
262. J.-M. Noy, F. Chen, D. T. Akhter, Z. H. Houston, N. L. Fletcher, K. J. Thurecht and M. H. Stenzel, *Biomacromolecules*, 2020, **21**, 2320-2333.
263. H. Asem, W. Zheng, F. Nilsson, Y. Zhang, M. S. Hedenqvist, M. Hassan and E. Malmström, *ACS Applied Bio Materials*, 2021, **4**, 1045-1056.
264. W.-J. Zhang, C.-Y. Hong and C.-Y. Pan, *Biomacromolecules*, 2017, **18**, 1210-1217.
265. W.-J. Zhang, C.-Y. Hong and C.-Y. Pan, *ACS Appl. Mater. Interfaces*, 2017, **9**, 15086-15095.
266. B. Karagoz, L. Esser, H. T. Duong, J. S. Basuki, C. Boyer and T. P. Davis, *Polym. Chem.*, 2014, **5**, 350-355.
267. L. Qiu, C.-R. Xu, F. Zhong, C.-Y. Hong and C.-Y. Pan, *ACS Appl. Mater. Interfaces*, 2016, **8**, 18347-18359.
268. C. J. Mable, I. Canton, O. O. Mykhaylyk, B. Ustbas Gul, P. Chambon, E. Themistou and S. P. Armes, *Chem. Sci.*, 2019, **10**, 4811-4821.
269. S. Varlas, L. D. Blackman, H. E. Findlay, E. Reading, P. J. Booth, M. I. Gibson and R. K. O'Reilly, *Macromolecules*, 2018, **51**, 6190-6201.
270. M. Garni, R. Wehr, S. Y. Avsar, C. John, C. Palivan and W. Meier, *Eur. Polym. J.*, 2019, **112**, 346-364.

271. S. Varlas, J. C. Foster, P. G. Georgiou, R. Keogh, J. T. Husband, D. S. Williams and R. K. O'Reilly, *Nanoscale*, 2019, **11**, 12643-12654.
272. J. He, J. Cao, Y. Chen, L. Zhang and J. Tan, *ACS Macro Lett.*, 2020, **9**, 533-539.
273. E. Lobry, A. F. Cardozo, L. Barthe, J.-F. Blanco, H. Delmas, S. Chen, F. Gayet, X. Zhang, M. Lansalot, F. D'Agosto, R. Poli, E. Manoury and C. Julcour, *J. Catal.*, 2016, **342**, 164-172.
274. A. F. Cardozo, C. Julcour, L. Barthe, J.-F. Blanco, S. Chen, F. Gayet, E. Manoury, X. Zhang, M. Lansalot, B. Charleux, F. D'Agosto, R. Poli and H. Delmas, *J. Catal.*, 2015, **324**, 1-8.
275. S. Chen, A. F. Cardozo, C. Julcour, J.-F. Blanco, L. Barthe, F. Gayet, M. Lansalot, F. D'Agosto, H. Delmas, E. Manoury and R. Poli, *Polymer*, 2015, **72**, 327-335.
276. X. Zhang, A. F. Cardozo , S. Chen , W. Zhang, C. Julcour , M. Lansalot, J.-F. Blanco , F. Gayet , H. Delmas , B. Charleux , E. Manoury , F. D'Agosto and R. Poli *Chem. - Eur. J.*, 2014, **20**, 15505-15517.
277. A. Joumaa, F. Gayet, E. J. Garcia-Suarez, J. Himmelstrup, A. Riisager, R. Poli and E. Manoury, *Polymers*, 2020, **12**, 1107.
278. M. Zeng, X. Li, Y. Zhang, X. Chen, X. Sui and J. Yuan, *Polymer*, 2020, **206**, 122853.
279. K. L. Thompson, J. A. Lane, M. J. Derry and S. P. Armes, *Langmuir*, 2015, **31**, 4373-4376.
280. M. Zeng, S. Zhou, X. Sui and J. Yuan, *Chin. J. Chem* . 2021, **39**, 3448-3454.
281. K. L. Thompson, L. A. Fielding, O. O. Mykhaylyk, J. A. Lane, M. J. Derry and S. P. Armes, *Chem. Sci.*, 2015, **6**, 4207-4214.
282. M. J. Rymaruk, K. L. Thompson, M. J. Derry, N. J. Warren, L. P. D. Ratcliffe, C. N. Williams, S. L. Brown and S. P. Armes, *Nanoscale*, 2016, **8**, 14497-14506.
283. S. J. Hunter and S. P. Armes, *Langmuir*, 2020, **36**, 15463-15484.

Chapter 3

Ultrasound Initiated RAFT Polymerisation-Induced Self-Assembly (Sono-RAFT-PISA)

3.1 Introduction

Polymerisation-induced self-assembly (PISA), which has drawn significant research attention in the past decade,[1-4] is a relatively new and powerful methodology for *in situ* fabrication of nano-objects during polymerisation. In a typical PISA process, a solvophilic macromolecules (macro-CTA; block A) is chain-extended using a second monomer in a suitable solvent *via* either dispersion or emulsion polymerisation (depending on the monomer solubility in solvent).[5] The growth of the second block (B) which is insoluble in solvent, leads to the *in situ* self-assembly of AB diblock copolymer into nano-objects. By varying the degree of polymerisation (DP), and the volume fraction of A and B blocks, nano-objects with various morphologies such as spheres, worms, vesicles and even oligo-lamellar vesicles can be obtained at different solid contents (10 to up to 40-50 % w/w).[5-8] The self-assembled nano-objects have broad range of applications, such as drug delivery,[3, 9] bio-imaging agents,[10, 11] stimuli-responsive smart nanomaterials,[12, 13] Pickering emulsifiers[14] and so forth.

The synthesis of block copolymers in PISA usually requires the use of living/controlled polymerisation techniques.[15] The common controlled polymerisation technique for PISA reported in the literature is RDRP technique, including RAFT polymerisation, ATRP[16-18] and NMP[19-21]. Recently, Xie and Choi groups reported ROMP induced self-assembly (ROMP-PISA), which had further expanded the polymerisation techniques for PISA.[22-25] Nevertheless, for practical applications, the most widely used technique for PISA is RAFT polymerisation, which is versatile for a broad range of monomers and solvents.[26-30]

Thermal initiation and photo-initiation are the most widely employed methods for generating radicals required for RAFT polymerisation in the PISA process. However, in the past few years, there has been a growing interest in new initiation mechanisms that provide alternative approaches for PISA. This trend and new initiation mechanisms were thoroughly reviewed by Armes and Boyer recently.[31]

Thermally initiated RAFT-PISA is usually conducted at elevated temperature (usually ≥ 50 °C) with the utilisation of water-soluble azo-compound initiator regarding the aqueous dispersion polymerisation.[32-35] Photo-initiated RAFT-PISA[36, 37] provides a successful strategy for low temperature and room temperature reaction; Boyer's group reported the iniferter approach to proceed PISA process without the addition of external initiator or catalyst,[38] however, it still involves the addition of photo-initiators in most photo-PISA processes.

The promising strategy of RAFT-PISA initiated by ultrasound without the addition of external initiators or additives have not been explored until recently by Qiao and Ashokkumar.[39]Ultrasound is a sound wave with frequency higher than 20 kHz which has been applied in the fields of imaging,[40] chemical synthesis[41] and guided drug delivery.[42] In polymer synthesis, emulsion polymerisation of hydrophobic monomers has been achieved using low frequency (20-100 kHz) ultrasound.[43, 44] In this sono-polymerisation process, the ultrasound was used as source of external energy and initiating radical generation for preparation of miniemulsion or microemulsion. Comparing to low frequency ultrasound, high-frequency (> 200 kHz) ultrasound creates larger number of cavitation bubbles with smaller size, and it leads to notably increase of radical generation and decrease in the shear forces so that no polymer degradation occurs.[45] In a recent study by Qiao and Ashokkumar,[39] high frequency ultrasound was employed for the synthesis of poly(poly(ethylene glycol) methyl ether acrylate)-*block*-poly[(*N*-isopropyl acrylamide)-*co*-(*N,N′*-methylenebisacrylamide)] (PPEGA-*b*-P(NIPAM-*co*-MBA)) thermosensitive nanogel *via* dispersion polymerisation at 45 °C. MBA was employed as crosslinker in order to maintain the PNIPAM-based copolymer micelles at temperature below the lower critical solution temperature (LCST). However, only spherical micelles were prepared *via* this strategy at elevated temperature. The possibility of proceeding sono-RAFT-PISA at room temperature and the formation of polymeric nano-objects in other morphologies are worth investigating.

In this chapter, we describe the first room temperature sono-RAFT-PISA to obtain PEG-based nano-objects with various morphologies (Scheme 3.1). First, the PEG macro-CTA (PEG$_{113}$-RAFT) was synthesised using a modified procedure from literature.[46] In the next step, 2-hydroxypropyl methacrylate (HPMA) was employed as core-forming monomer (B), which has been reported to generate a range of morphologies including spheres, worms and vesicles in thermal and photo-initiated

PISA.[35, 47] High frequency ultrasound (990 kHz) was applied to generate hydroxyl radicals by sonolysis of water molecules, and induce the polymerisation reaction. *Via* this strategy, we successfully achieved the first room temperature sono-RAFT-PISA and obtained not only spherical micelles but also worm-like micelles and small vesicles for the first time.
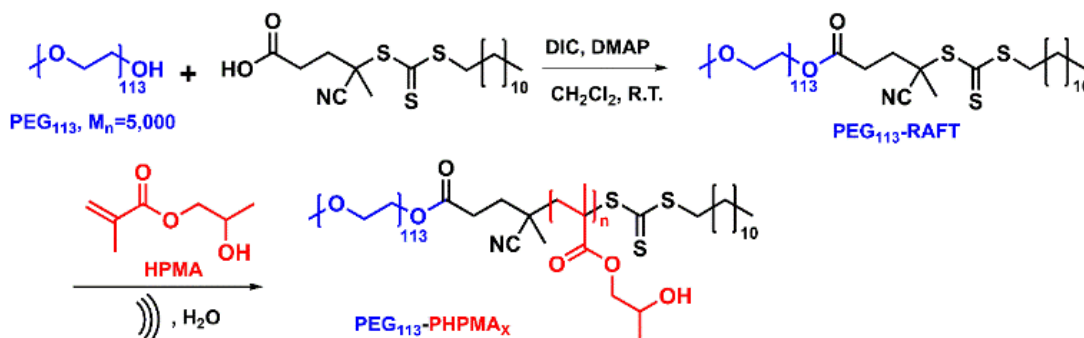
Scheme 3.1 Synthesis of PEG$_{113}$-RAFT and PEG$_{113}$-PHPMA$_X$ copolymers *via* sono-RAFT-PISA process.

3.2 Materials and Methods

3.2.1 Materials

Diisopropyl carbodiimide (DIC; >99%) was purchased from Oakwood Chemical (USA). 4-Dimethylaminopyridine (DMAP; 99%) was purchased from Alfa Aesar. 4-Cyano-4 (((dodecylthio) carbonothioyl) thio) pentanoic acid (CDTPA; 97%) was purchased from Boron Molecular (Australia). Poly(ethylene glycol) methyl ether (mPEG$_{113}$, average M_n 5,000), hydroxypropyl methacrylate (HPMA, mixture of 2-hydroxypropyl and 2-hydroxyisopropyl methacrylate; 97%), $(NH_4)_6Mo_7O_{24} \cdot 4H_2O$ and $C_8H_5KO_4$ were purchased from Sigma Aldrich (Australia). 2,2'-Azobis[2-(2-imidazolin-2-yl)propane]dihydrochloride (AIPD, VA-044) was purchased from Wako Pure Chemical Industries, Ltd. All the other solvents were obtained from commercial source and were used as received unless noted otherwise.

3.2.2 Synthesis of poly(ethylene glycol) trithiocarbonate (PEG$_{113}$-CDTPA) macro-CTA

mPEG$_{113}$ (6.0 g, 1.2 mmol) was dissolved in 30 mL toluene in a round bottom flask to remove water azeotropically that associated with PEG by rotary-evaporation (repeated 3 times). Dichloromethane (30 mL) was then added to the flask containing mPEG$_{113}$ (6.0 g, 1.2 mmol). CDTPA (970.0 mg, 2.4 mmol),

DIC (0.3 g, 2.4 mmol) and DMAP (29.0 mg, 0.24 mmol) were added to the flask in order. The flask was sealed with a rubber septum. The esterification reaction was allowed to proceed with stirring at room temperature for 24 hr. The polymer was collected by precipitation of the reaction mixture in cold diethyl ether for 3 times. PEG$_{113}$-RAFT was obtained as pale yellow solid after drying under reduced pressure (76 % yield). ^{1}H NMR (400 MHz, CDCl$_3$) (Figure 3.4a): δ 4.25 (t, 3H), 3.45-3.81 (m, 452H), 3.37 (s, 3H), 3.31 (t, 3H), 2.37-2.65 (m, 4H), 1.86 (s, 3H), 1.68 (m, 2H), 1.25-1.38 (b, 18H), 0.87 (t, 3H). ^{13}C NMR (150 MHz, CDCl$_3$)(Figure 3.4b): δ 216.8, 171.3, 118.9, 71.8, 70.4, 68.8, 64.0, 58.9, 46.2, 33.7, 31.8, 29.2, 24.7, 22.6, 14.0.

3.2.3 RAFT dispersion polymerisation of HPMA *via* ultrasound initiation

The following representative protocol was used for ultrasound-initiated RAFT dispersion polymerisation-induced self-assembly (sono-RAFT-PISA) process for the synthesis of PEG$_{113}$-PHPMA$_{600}$ at 10 % w/w solid content at room temperature (~23 °C). HPMA monomer was disinhibited by passing through a column of basic alumina, then passing through a silica gel column (*n*-hexane: diethyl ether= 1:1 eluent) to remove dimethacrylate impurity. PEG$_{113}$-CDTPA macro-CTA (11.7 mg, 2.2 µmol) and HPMA monomer (188.3 mg, 1.32 mmol, target DP= 600) were weighed in a 12 mL glass test tube with socket and dissolved in DI water (1.80 mL, 10 % w/w). The test tube was sealed using a rubber septum and deoxygenated by purging with argon using needles through the liquid for 30 min. The test tube was then immersed in ultrasonic water bath with circulated cooling water jacket maintained at room temperature (~23 °C) during reaction. The distance between the bottom of the test tube and transducer plate was kept as 5 cm (as shown in Figure 3.1). The ultrasonic generator (Meinhardt Ultrasonics, model M11-010, output power 250 W) was then switched on (990 kHz, 80% intensity). For kinetic studies, aliquots were removed periodically for analyses by ^{1}H NMR spectroscopy (Figure 3.2) and GPC. The reaction was stopped by switching off the ultrasonic generator and exposure to air after 1-2 hr irradiation.
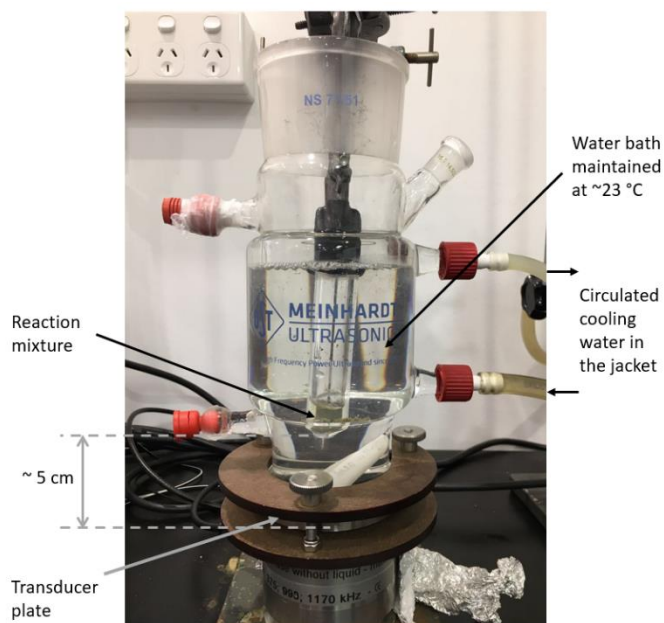
Figure 3.1 Experimental setup of ultrasound transducer and reaction vessel for PEG$_{113}$-PHPMA$_{103}$ sono-RAFT-PISA experiment at room temperature, water batch temperature measured 23.8 °C at the end of polymerisation (ultrasound amplifier and water circulation pump not shown).
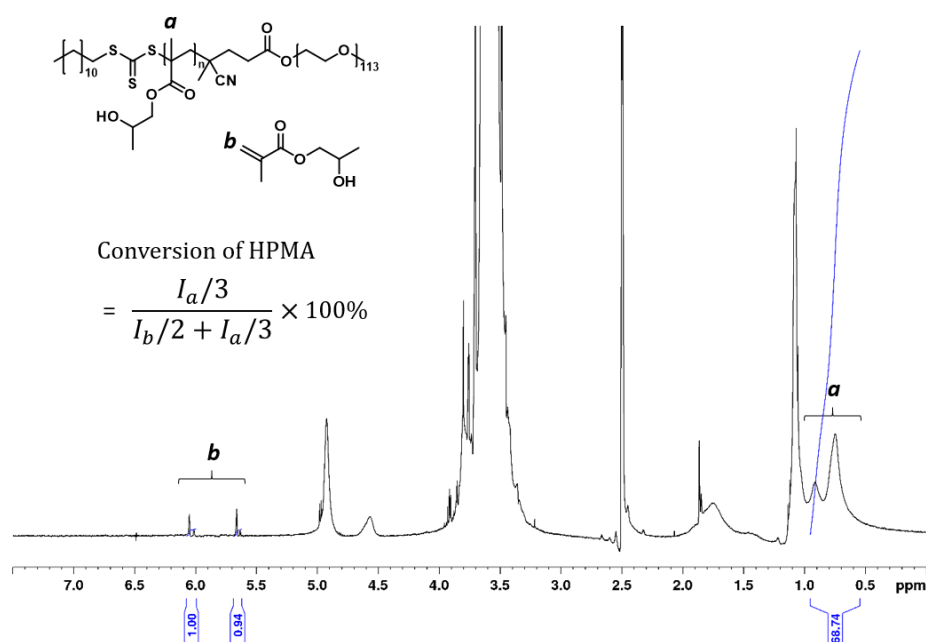
Figure 3.2 Exemplary ^{1}H NMR spectrum (400 MHz, DMSO-d_6) of PEG$_{113}$-PHPMA$_x$ crude (target DP 400) synthesised *via* sono-RAFT-PISA showing monomer conversion calculation.

Conversion=(68.74/3)/[(1.00+0.94)/2+68.74/3]×100%=95.9 %.

3.2.4 RAFT dispersion polymerisation of HPMA *via* thermal initiation

The following protocol was used for thermal-initiated RAFT dispersion polymerisation-induced self-assembly (thermal-PISA) for the synthesis of PEG$_{113}$-PHPMA$_{400}$ at 10 % w/w solid content at 50 °C. HPMA monomer was pre-treated as described above. PEG$_{113}$-CDTPA macro-CTA (17.1 mg, 3.2 µmol), HPMA monomer (182.9 mg, 1.28 mmol, target DP= 400) and VA-044 (32 µL of 10 mg/ml stock solution, 1.0 µmol) were added in a round-bottom flask containing a stirrer bar and dissolved in DI water (1.80 mL, 10 % w/w). The flask was sealed using a rubber septum and deoxygenated by purging with argon using needles through the liquid for 60 min. The mixture was stirred at 700 rpm for 30 min, followed by immersing the flask in an oil bath at 50 °C. The stirring speed was kept at 700 rpm throughout the reaction. The reaction was stopped by cooling to 20 °C and exposure to air after 4 hr.

3.2.5 Quantification of generated hydrogen peroxide (H_2O_2)

By assuming the produced hydroxyl radicals mostly recombine to form hydrogen peroxide, the quantification of hydrogen peroxide was used to estimate the formation of radicals. The spectroscopic method described by Hochanadel[48] was used, in which I^- is oxidised to I_3^- by H_2O_2 in 1:1 ratio. In detail, 1 mL of freshly sonicated sample was mixed with 1 mL of solution A (0.4 M KI, 0.1 M NaOH, and 0.02 mM $(NH_4)_6Mo_7O_{24}\cdot4H_2O$) and 1 mL of solution B (0.1 M $C_8H_5KO_4$). The solution was allowed to stand for 5 min for the reaction to proceed. The solution was then analysed by UV/Vis spectrophotometer and the absorption at 353 nm was recorded. The molar extinction coefficient for I_3^- of 26400 $M^{-1}cm^{-1}$ was used.

3.2.6 Disassembly/reassembly after sono-PISA

100 µL suspension of PEG_{113}-$PHPMA_{400}$ prepared *via* sono-PISA (10% w/w) was lyophilised overnight to obtain ~ 10 mg dried polymer. Tetrahydrofuran (THF) was added to the dried polymer to make 10 mg polymer/mL THF solution. The solution was stirred for 4 hr to ensure polymer is well dissolved. Take 0.1 mL 10 mg/mL THF solution into a small *vial* with a stirrer bar, add 0.9 mL DI water to THF solution drop by drop with constant stirring (100 rpm) to make a cloudy solution with concentration of 1 mg polymer/ mL (water: THF=9:1). The cloudy solution was dialysed against DI water using 2 kDa dialysis membrane for 24 hr to remove THF. The dialysed solution was used to prepare TEM sample without further dilution.

3.2.7 Characterisation

Dynamic light scattering (DLS) measurements were performed at 20 °C using Brookhaven Nanobrook Omni Particle Size Analyser. The aqueous dispersions containing the diblock copolymer nano-objects were diluted to 0.10 % w/v by DI water. Light scattering was detected at 90° and hydrodynamic diameters were determined by assuming spherical, non-interacting, perfectly monodisperse particles. ^{1}H Nuclear magnetic resonance spectroscopy (NMR) spectra were recorded on a Bruker Avance 400 NMR spectrometer at frequencies of 400 MHz. NMR chemical shifts (δ) are reported in ppm and were calibrated against residual solvent signals of $CDCl_3$ (δ 7.26), DMSO-d_6 (δ 2.50). Samples were dissolved in $CDCl_3$ or DMSO-d_6 at 5-10 mg mL^{-1}. The data are reported as chemical shift (δ). Gel permeation

chromatography (GPC) was performed on a system comprising a Shimadzu LC-20AT pump, Shimadzu RID-20A refractive index detector, and SPD-20A UV–visible detector. The GPC is equipped with a guard column (WAT054415) and 3×Waters GPC columns (WAT044238, WAT044226, WAT044235, 300 mm×7.8 mm). The eluent is DMF with 10 mM LiBr and eluted at 1 mL/min for 45 min in total. The samples were dissolved in DMF with 10 mM LiBr, filtered through 0.20 µm syringe filters. A calibration curve was obtained from poly(methylmethacrylate) (PMMA) standards (Agilent) ranging from 960 to 1,568,000 g mol^{-1}. Transmission electron microscopy (TEM): copper grids (formvar/carbon coated, 400 mesh) were plasma glow-discharged for 10 seconds to create a hydrophilic surface. After glow discharge, the grid was contacted with a drop (about 15 µL) of 0.10 % w/v aqueous dispersions containing the diblock copolymer nano-objects for 3 min. After blotting to remove excess sample dispersion, the grids was negatively stained by contacting with a drop (about 15 µL) of uranyl acetate solution (2.0 % w/v) for 1 min. The grid was blotted again to remove excess stain and dried using a gentle nitrogen blow. Imaging was performed using a FEI Tecnai G2 T20 TWIN TEM instrument equipped with Orius SCD200D wide-angle CCD camera operating at 200 kV. Cryogenic transmission electron microscopy (Cryo-TEM): the image was taken using a FEI Tecnai Spirit G2 TEM. Briefly, copper grids (200-mesh) coated with holey carbon film (Quantifoil R2/2) were glow discharged in a Pelco glow discharge unit to render them hydrophilic. 5 µL of sample (0.1 mg/mL) were applied onto the grids, which were blotted against two filter papers for 3 seconds at a blot force of -3 in a Vitrobot plunge freezer system (FEI). The resulting thin sample film was vitrified in a controlled environment vitrification system at 4 °C and 70% relative humidity by plunging the sample into liquid ethane, which was maintained at its melting point with liquid nitrogen. The vitrified specimens were transferred to a Gatan 626 cryoholder and observed at an operating voltage of 120 kV in a Tecnai Transmission Electron Microscope (FEI) at a temperatures -179 °C. Images were recorded with a Gatan Eagle high-resolution CCD camera (4k x 4k) at magnifications ranging from 15,000x to 110,000x and digitised with the Tecnai Image Acquisition (TIA) program. Scanning electron microscopy (SEM): the SEM sample was prepared by casting a drop (about 10 µL) of 0.10 % w/v aqueous dispersions containing the diblock copolymer nano-objects on a silicon wafer. The dispersion was then dried by a gentle nitrogen blow. The sample was then coated with a thin layer (~2 nm) of iridium to be conductive. Imaging was performed using a FEI Nova NanoSEM 450 FEGSEM instrument operating at 3.0 or 5.0 kV.

3.3 Results and Discussion

3.3.1 Formation of radicals by ultrasound

Before any PISA attempts, we confirmed the formation of radicals by the high-frequency (990 kHz) ultrasound transducer through the quantification of hydrogen peroxide in argon-purged water, with the assumption that the produced hydroxyl radicals mostly recombine to form hydrogen peroxide. It was observed that the generation of H_2O_2 is proportional to ultrasound irradiation time and frequency (Figure 3.3). With 2 hr of irradiation at 990 kHz, the concentration of H_2O_2 increased to ~630 μM, which corresponds to 1.26 mM of hydroxyl radicals (by assuming one H_2O_2 is formed by two hydroxyl radicals).
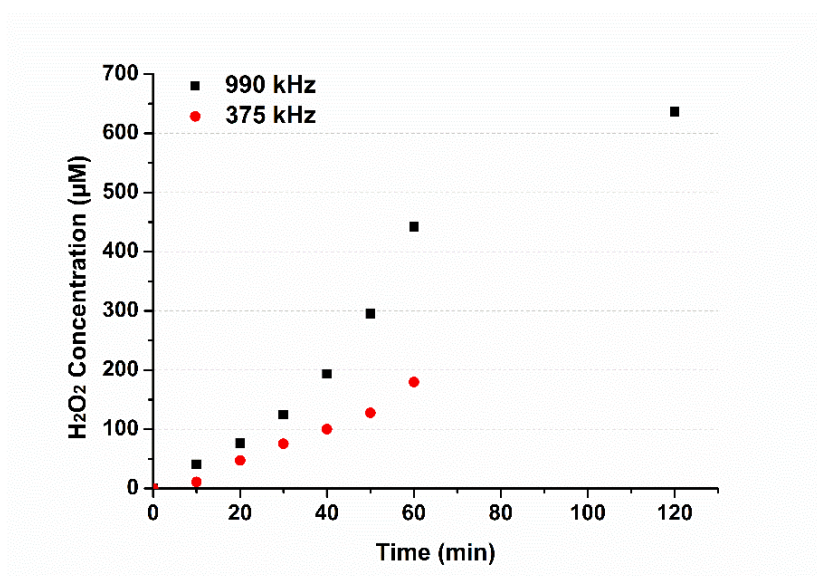
Figure 3.3 Quantification of H_2O_2 (and indirectly, HO˙) generated ultrasonically at 375 kHz and 990 kHz.

3.3.2 Synthesis of PEG$_{113}$-CDTPA and PEG$_{113}$-PHPMA$_x$

The macro-RAFT agent (PEG$_{113}$-CDTPA) was synthesised by coupling of hydrophilic poly(ethylene glycol) methyl ether (PEG$_{113}$, average M_n 5,000) with 4-cyano-4-(((dodecylthio) carbonothioyl) thio) pentanoic acid (CDTPA) through Steglich esterification, with diisopropyl carbodiimide (DIC) as coupling agent and 4-dimethylaminopyridine (DMAP) as catalyst. The success of coupling and the

purity of macro-RAFT agent PEG₁₁₃-CDTPA were confirmed by ¹H NMR and ¹³C NMR spectroscopy (Figure 3.4a and 3.4b).
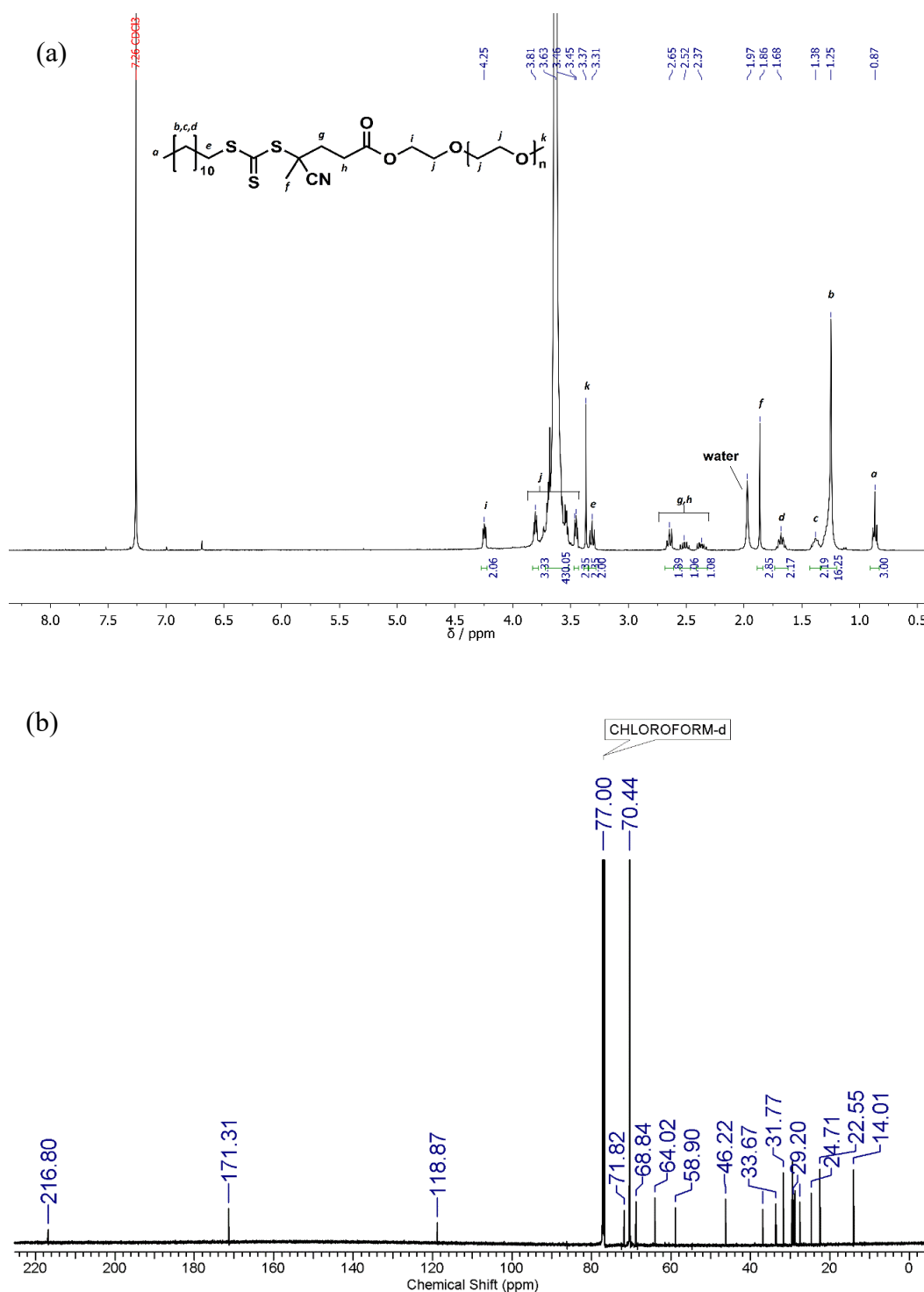
Figure 3.4 (a) ¹H NMR spectrum (400 MHz, CDCl₃) and (b) ¹³C NMR spectrum (150 MHz, CDCl₃) of PEG₁₁₃-CDTPA synthesised.

Next, PEG$_{113}$-CDTPA was chain extended with purified monomer (HPMA) in aqueous environment under ultrasound irradiation. As shown in the kinetics data (Figure 3.5), the sono-PISA could be roughly separated to two regimes, which are in a very similar pattern to the kinetics of thermal-PISA investigated by Armes group[35] and photo-PISA reported by Tan *et al.*[36] The first regime, which occurs between 0 to 60 min, has a relatively slow polymerisation rate, corresponding to the formation of diblock copolymer chains which are still in molecularly dissolved state. The point of intersection of two lines indicates the micellar nucleation occurs at around 70 min, which corresponds to 41.5 % conversion of HPMA for this formulation. This conversion corresponds to a mean DP of 250 for the nucleation of PHPMA block. Beyond this point, the polymerisation rate drastically increases. This is due to micelles cores acting as multiple mini-reactors, unreacted HPMA monomer enters into the core to solvate the hydrophobic PHPMA chains.[35, 49] The critical DP of 250 is much higher than the critical DP of 110 previously reported by Tan *et al.* for a PPEGMA$_{14}$-CDPA macro-CTA utilised to polymerise HPMA (target DP = 200) at room temperature;[36] also higher than critical DP of 135 reported by Warren *et al.* for PEG$_{113}$-PHPMA (target DP=600) at 50 $^{\circ}$C.[35] Temperature of polymerisation is one of the factors that leads to different critical DP, since the degree of hydration for the PHPMA block is temperature-dependent as previously reported.[50, 51] The other possible reason is suspected to be ultrasound effect. This will be discussed in the morphology studies section.
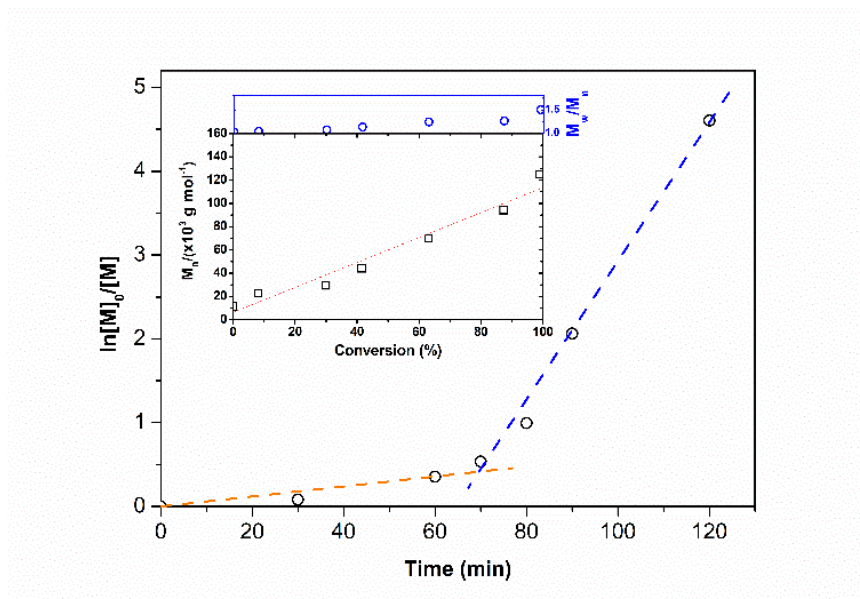
Figure 3.5 Polymerisation kinetics of HPMA (PEG$_{113}$-PHPMA$_{600}$ targeted) *via* ultrasound (990 kHz, 80%) initiated RAFT aqueous dispersion polymerisation at room temperature (~23 °C) and 10 % w/w solid content.

The GPC results show a linear relationship between M_n and PHPMA conversion (Figure 3.5 inset), which confirmed the living characteristics of this ultrasound-initiated RAFT polymerisation. Meanwhile, the dispersity ($Đ$) increases with the chain length of polymer (Figure 3.5 inset), and the final $Đ$ of PEG$_{113}$-PHPMA$_{600}$ is still relatively low ($Đ$ =1.50). These characteristics indicate that good control is maintained throughout for dispersion polymerisation initiated by ultrasound. The GPC analysis of PEG$_{113}$-PHPMA$_X$ (target DP from 250 - 800) confirms a systematic increase in M_n and relatively low $Đ$ of 1.13-1.61 (Figure 3.6). It should be noted that the GPC trace of PEG$_{113}$-RAFT is bimodal, the M_n of PEG$_{113}$-RAFT is around 11,400 (based on poly(methyl methacrylate) calibration standards) and 21,300 for the side peak. The presence of side peak impurity is not from the synthesis of PEG$_{113}$-RAFT but from the purchased mPEG$_{113}$ because same side peak appears on the GPC trace of mPEG$_{113}$ (Figure 3.7). By comparing the GPC results of diblock polymer with same DP but prepared by sono-PISA and thermal-PISA (Table 3.1), the M_n values are very close but $Đ$ of sono-PISA are not as low as thermal-PISA. This could result from the different concentration of radicals generated through polymerisation. Taking PEG$_{113}$-PHPMA$_{400}$ thermal synthesis as an example, the total radical concentration generated by VA-044 is 0.49 mM (50 °C, 4 hr, calculation as described in Section 3.5.1);

whereas the hydroxyl radical concentration is around 1.26 mM at the end of 2 hr sonication. The relatively high hydroxyl radical concentration during sono-PISA, which can be considered as a relatively low CTA/initiator ratio (around 1.0 : 0.78 in the case of PEG_{113}-$PHPMA_{400}$ sono-PISA) and can contribute to the formation of dead chains.[29, 52, 53] The essentiality of removing dimethacrylate impurity in HPMA (as described in section 3.2.3) is also showed by GPC studies. GPC trace with bimodal polymer peaks was obtained from same experiments using HPMA without the removal of dimethacrylate (Figure 3.8), showing significant elimination of cross-linking *via* the use of purified HPMA.
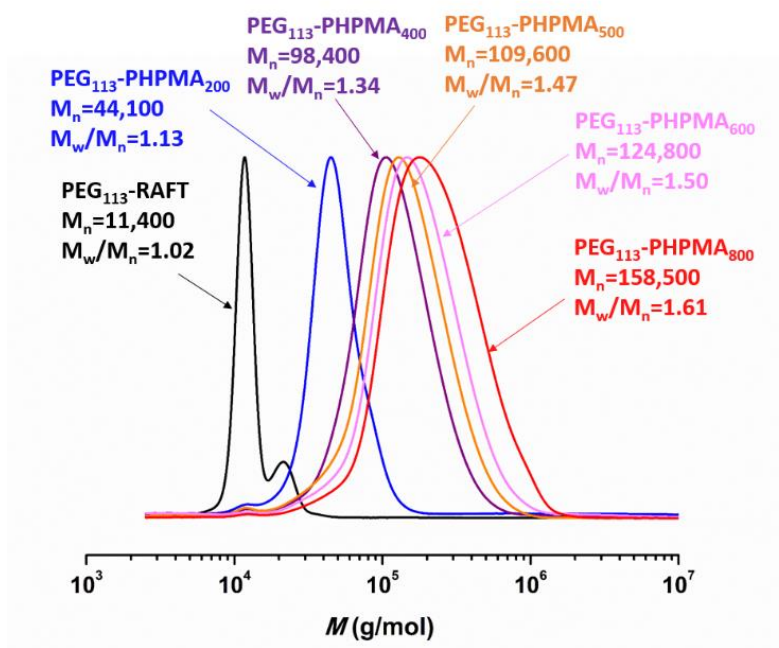
Figure 3.6 Gel permeation chromatography traces (PMMA standards) obtained for PEG_{113}-$PHPMA_X$ (target DP x=200-800) copolymers synthesised *via* sono-PISA at room temperature (~23 °C).

95
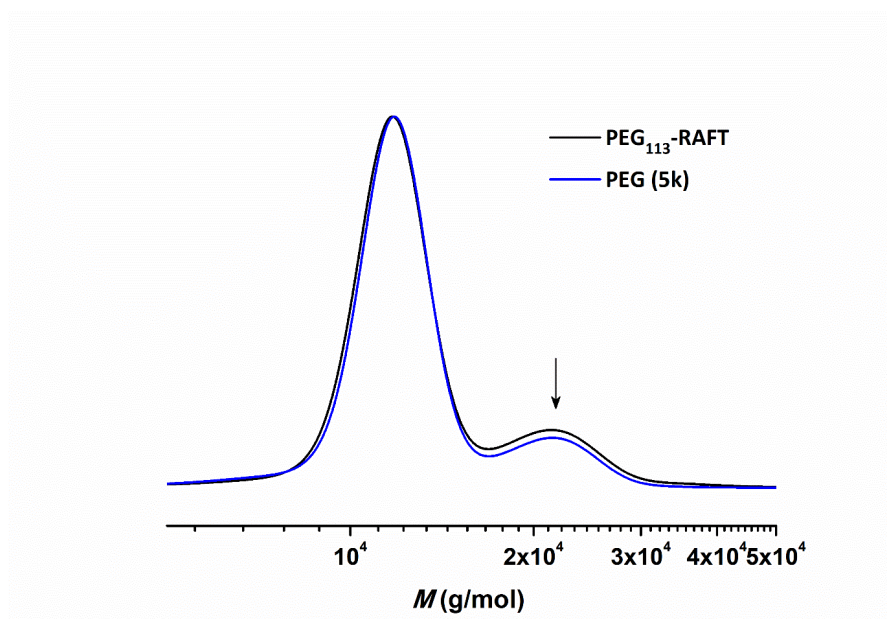
Figure 3.7 GPC traces of poly(ethylene glycol) methyl ether (PEG (5k), average M_n 5,000) and synthesised PEG$_{113}$-RAFT.
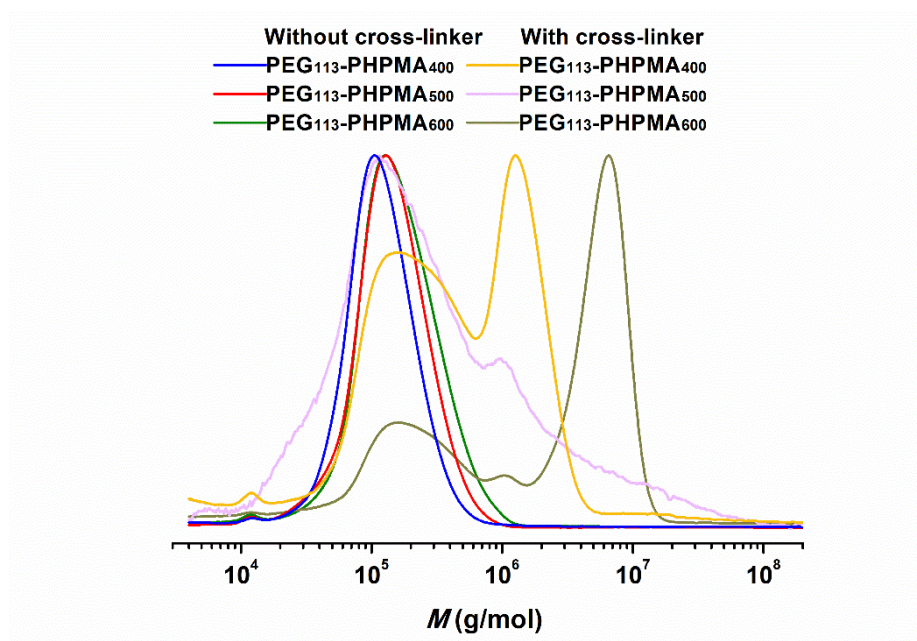
Figure 3.8 GPC traces of a series of PEG$_{113}$-PHPMA$_x$ block copolymers with or without crosslinker (dimethacrylate impurity).

Table 3.1 Characterisation data of PEG$_{113}$-PHPMA$_x$ copolymer nano-objects by sono-PISA and thermal-PISA

Entry[a]	Target PHPMA DP	Preparation method[b]	$M_{n,th}$[c] (conv.%)	GPC $M_{n,GPC}$[d]	M_w/M_n	Z_a (nm)	DLS PDI	Morphology[e]	Note
1	104	US	18,900 (90.0)	31,500	1.24	28.7 ± 1.4	0.11 ± 0.09	S	[f]
2	174	US	30,000 (98.0)	63,000	1.35	45.3 ± 0.6	0.07 ± 0.01	S	[f]
3	200	US	34,200 (>99.0)	44,100	1.13	44.9 ± 0.3	0.08 ± 0.01	S	
4	400	US	60,700 (95.9)	98,400	1.34	61.1 ± 0.8	0.06 ± 0.01	S	
5	500	US	75,800 (97.6)	109,600	1.47	72.0 ± 0.6	0.13 ± 0.01	S	
6	600	US	90,200 (98.0)	124,800	1.50	111.4 ± 1.5	0.11 ± 0.07	S/V	
7	800	US	116,100 (96.0)	158,500	1.61	126.6 ± 1.1	0.05 ± 0.03	V	
8	400	US	62,200 (99.2)	1,200,000; 148,300	1.15; 1.48	77.8 ± 0.4	0.09 ± 0.01	S/C	[f]
9	500	US	74,500 (95.9)	1,222,500; 86,900	1.24; 1.99	94.2 ± 1.0	0.10 ± 0.01	S/W/V	[f]
10	600	US	90,700 (99.0)	5,331,900; 160,300	1.16; 1.47	126.7 ± 1.0	0.11 ± 0.02	V	[f]
11	800	US	118,000 (98.0)	5,193,100; 181,900	1.07; 1.43	153.5 ± 2.8	0.09 ± 0.03	V	[f]
12	100	T	19,800 (>99.0)	33,100	1.10	31.8 ± 0.8	0.13 ± 0.02	S	
13	150	T	27,000 (>99.0)	46,500	1.08	90.5 ± 0.8	0.20 ± 0.02	W	
14	200	T	34,200 (>99.0)	51,300	1.15	593.9 ± 29.6	0.33 ± 0.01	W/V	
15	300	T	48,600 (>99.0)	74,000	1.17	359.2 ± 6.6	0.25 ± 0.02	W/V	
16	400	T	63,000 (>99.0)	84,100	1.19	587.2 ± 22.8	0.19 ± 0.05	V	
17	600	T	91,900 (>99.0)	118,400	1.20	142.8 ± 2.3	0.18 ± 0.01	S	
18	800	T	120,700 (>99.0)	205,100	1.47	581.6 ± 26.2	0.19 ± 0.03	S	

[a] All entries conducted at 10 % w/w solid content. [b] Preparation method: US: sono-PISA, T: thermal-PISA. [c] Monomer conversion calculated based on ^{1}H NMR spectra. $M_{n,th}$ = conversion × target HPMA DP × MM(HPMA)+MM(PEG$_{113}$-RAFT). [d] DMF eluent, PEG standards. [e] S=spheres, V= vesicles, W=worms, C=cylinders. [f] Bimodal or broad GPC chromatography resulted by the cross-linking due to dimethacrylate impurity in HPMA monomer.

3.3.3 Morphology of PEG$_{113}$-PHPMA$_x$ nano-objects

Nano-objects were also constructed utilising same macro-CTA and HPMA but *via* thermal-PISA for comparison purpose. The hydrodynamic diameters and morphologies for nano-objects constructed by sono-PISA and thermal-PISA were significantly different (Table 3.1). For thermal-PISA, similar to many other studies, PEG$_{113}$-PHPMA$_{100}$ copolymer formed spherical micelles at 10% solid content with an average diameter of 20 ± 4 nm (error is the standard deviations as calculated by measuring 60 particles) were measured by TEM (Figure 3.9c), and 31.8 ± 0.8 nm (PDI = 0.13 ± 0.02) by DLS (Table 3.1). The mean diameters measured from the TEM images were smaller than those measured by DLS. This can be attributed to particles being dry rather than hydrated state; and DLS could oversize since the scattering from larger particles can increase the overall particle diameter derived by DLS.[54] A mixture of worms and spheres were generated in the case of PEG$_{113}$-PHPMA$_{150}$ (Figure 3.9d). TEM images of PHPMA at DPs of 200 (Figure 3.10e) and 300 (Figure 3.9e) indicate the mixture of worms and vesicles (including "jellyfish"-like), and the dispersion formed is soft and free-standing gel (Figure 3.9a.b). A pure vesicle phase was obtained when the DP of PHPMA is 400 (Figure 3.10f).
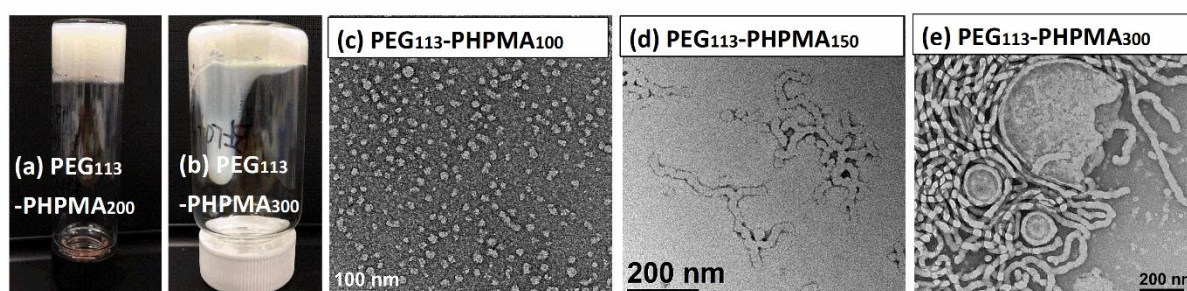
Figure 3.9 Digital photos of standing-free gel dispersion of (a) PEG$_{113}$-PHPMA$_{200}$ and (b) PEG$_{113}$-PHPMA$_{300}$ prepared by thermal-PISA and (c-e) TEM images of nano-objects prepared by thermal-PISA.
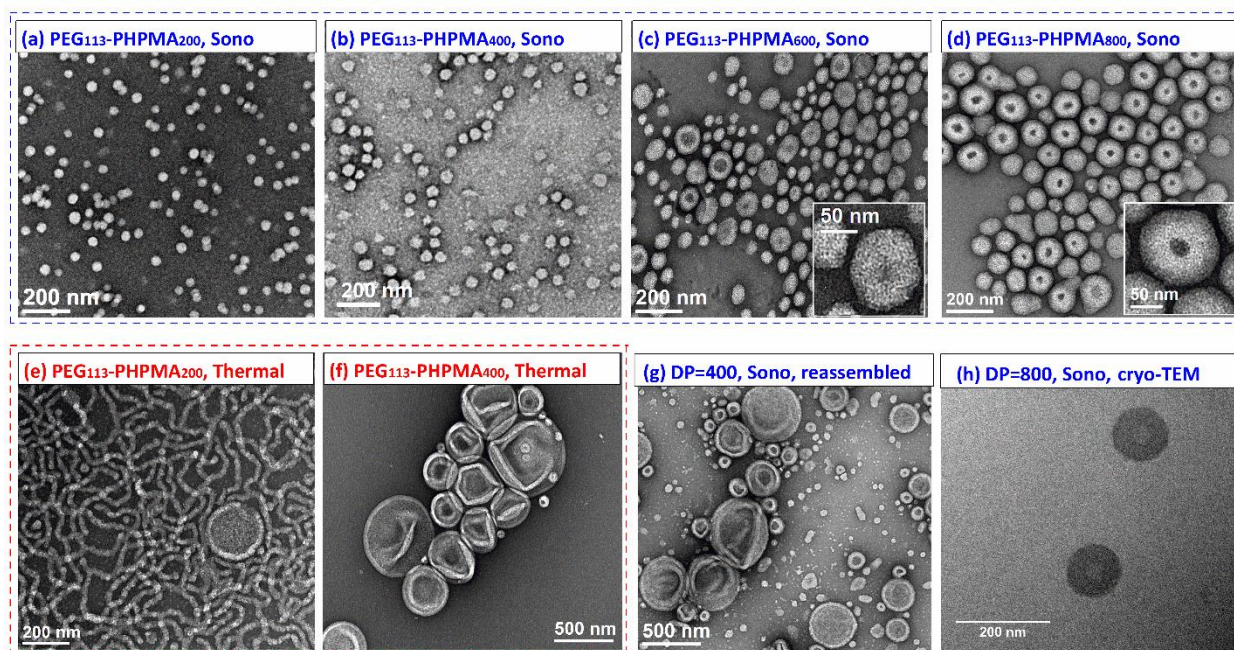
Figure 3.10 Representative TEM images monitored for PEG$_{113}$-PHPMA$_X$ copolymers nano-objects synthesised *via* (a-d) sono-PISA at room temperature and (e, f) thermal-PISA at 50 °C. (g) TEM image of PEG$_{113}$-PHPMA$_{400}$ after reassembly and (h) cryo-TEM image of PEG$_{113}$-PHPMA$_{800}$ vesicles (all prepared at 10 % w/w solid content).

On the other hand, for sono-PISA, when the DP of PHPMA ranges from 104 to 500, only monodisperse spherical micelles were obtained with hydrodynamic diameter from 28.7 to 72.0 nm and PDI 0.06-0.13 as measured by DLS and confirmed by TEM and SEM. At the DP of 600, TEM image (Figure 3.10c) combining with SEM image (Figure 3.11a) confirmed the morphology is a mixture of 46 ± 9 nm spherical particles and 102 ± 13 nm vesicles, DLS indicates an Z-average diameter of 111.4 ± 1.5 nm (PDI = 0.11 ± 0.07). As for higher DP of 800, small vesicles with size of 114 ± 12 nm were obtained (Figure 3.10d), and the wall thickness of the vesicles are around 45 nm. SEM images (Figure 3.11b) confirm the overall morphology of vesicles, which are hollow vesicular rather than donut-like. The morphology of vesicle was further disclosed by cryo-TEM (Figure 3.10h and Figure 3.12).
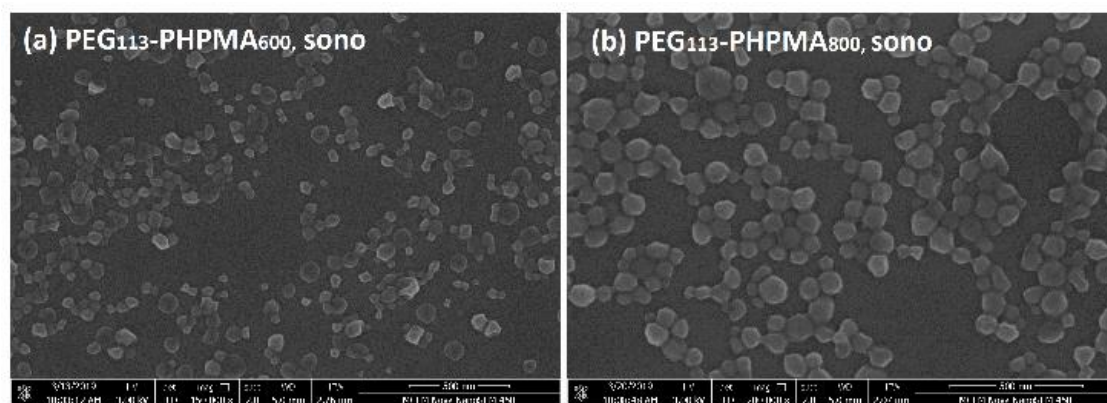
Figure 3.11 Representative SEM images of (a) PEG$_{113}$-PHPMA$_{600}$ and (b) PEG$_{113}$-PHPMA$_{800}$ synthesised by sono-RAFT-PISA (10.0 % w/w solid content).
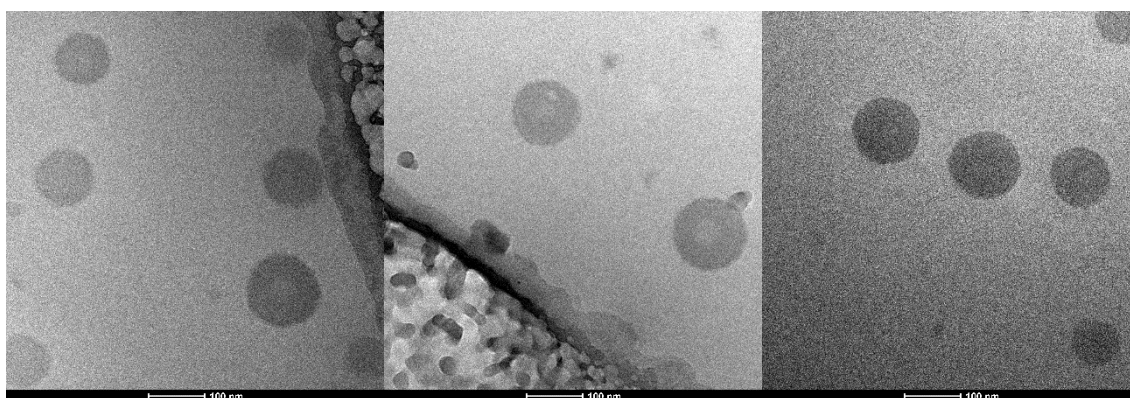
Figure 3.12 Cyro-TEM images of PEG$_{113}$-PHPMA$_{800}$ vesicles synthesised by sono-PISA.

Moreover, by comparing the DLS results of vesicles constructed by these two processes (Figure 3.13), apart from the size of the sonochemically produced vesicles is much smaller (126.2 nm vs 599.2 nm), the PDI is also narrower (0.02 vs 0.23), which indicates the vesicles are monodisperse. These results indicate that for same DP of PHPMA, the morphologies of nano-objects obtained from sono-PISA were distinct from those obtained from thermal-PISA.
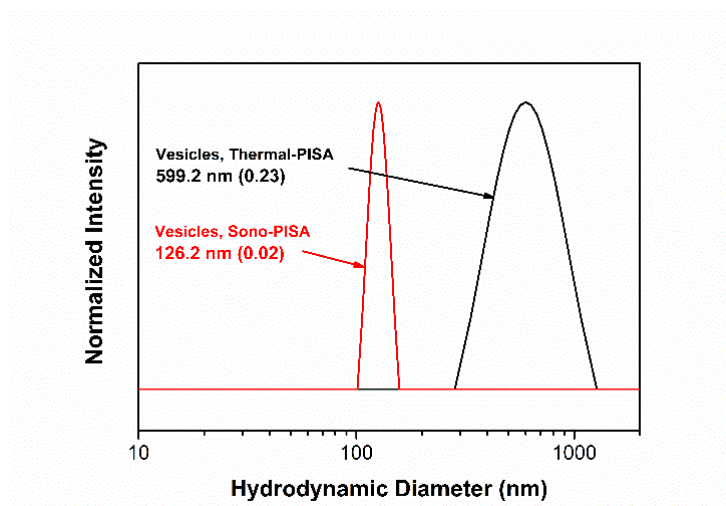
Figure 3.13 DLS size distributions recorded for samples with the target composition of PEG$_{113}$-PHPMA$_{400}$ (prepared *via* thermal-PISA) and PEG$_{113}$-PHPMA$_{800}$ (prepared *via* sono-PISA).
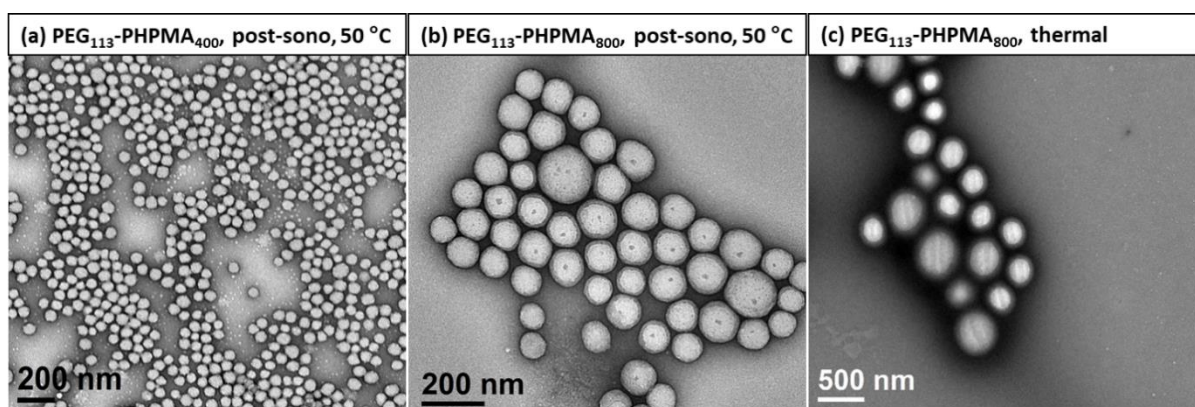
Figure 3.14 Representative TEM images of (a) PEG$_{113}$-PHPMA$_{400}$, (b) PEG$_{113}$-PHPMA$_{800}$ synthesised by sono-RAFT-PISA and warmed up to 50 °C for 24 hr. (c) PEG$_{113}$-PHPMA$_{800}$ synthesised by thermal-PISA (10.0 % w/w solid content). TEM sample preparation protocol was modified in order to investigate the effect of temperature change on morphology. The warmed sample was diluted to 0.10 % w/v using DI water pre-warmed to 50 °C. The TEM sample was prepared immediately after dilution by proceeding the normal procedure.

It was surprising that higher DP of polymerisation was required for the sonochemical morphology transition compared to the thermal-PISA system. The high critical DP is also described above in kinetic studies. Tan *et al.* [55] reported only spheres at DP=350 formed by photo-PISA at room temperature (10% w/w solid content), which is similar to the results in this chapter. However, different morphologies

were formed at 37 °C as in previous report.[56] The effect of reaction temperature difference should be considered. Due to the operating temperature limit of the ultrasonic transducer, sono-PISA cannot be carried out at 50 °C. Hence the control experiment was conducted by heating the nano-objects suspension (10% w/w) after sono-PISA reaction to 50 °C for 24 hr. By comparing TEM images of Figure 3.10b and Figure 3.14a, temperature rise has limited effect on morphology transition of PEG_{113}-$PHPMA_{400}$ since it remains as spheres. However, for PEG_{113}-$PHPMA_{800}$, the lumen of vesicles diminished after heating (Figure 3.14b), and overall size remains around 110 nm. The structure is similar to thermal-PISA synthesised nano-objects (Figure 3.14c), but much smaller in particle size. These demonstrate that temperature could influence the morphology transformation but in a limited extent. In addition, we disassembled the PEG_{113}-$PHPMA_{400}$ spheres prepared *via* sono-PISA by dissolving the dried polymer in tetrahydrofuran (THF), and reassembled *via* solution self-assembly by adding water to polymer solution. As shown in Figure 3.10g, PEG_{113}-$PHPMA_{400}$ reassembled into vesicles with structure very similar to those prepared *via* thermal-PISA, which demonstrates that without ultrasound effect, sono-prepared polymers have the same self-assembly behaviour as thermally-prepared polymers. This result indicates that the morphology difference between thermal-PISA and sono-PISA could result from the presence of ultrasound during polymerisation.

There are only limited studies on investigating the effect of ultrasound on polymer nanoparticles and its morphologies. Miki *et al.* reported the self-assemblies of Janus-type polymers with uniform size were affected by ultrasonic frequency.[57] Dang *et al.* observed changes in morphology of vesicle nanoparticles to large complex micelles following the increase of ultrasonic power intensity.[58] However, these studies did not explain the morphology difference between thermal-PISA and sono-PISA. The hypothesised reason is the influence of ultrasonic energy input during polymerisation. As shown in Figure 3.15, for the nano-objects composed of same quantity of PEG_{113}-$PHPMA_{400}$ chains, the total surface area of spheres is larger than vesicles as spherical particle has smaller size than vesicle. Therefore, the larger surface area of spheres renders higher surface free energy than vesicles, hence it requires further external energy, which was provided by ultrasound. From the perspective of packing parameter (P, defined as $P = V/a_0 l_c$, in which V and l_c represent the volume and length of the hydrophobic block, respectively, a_0 stands for the effective area of the hydrophilic headgroup), when $P \leq 1/3$, sphere is the preferred morphology, and when $1/2 < P \leq 1$, vesicle is the preferred morphology. The higher surface free

energy system allows larger surface area, as the number of molecules (N) remains same, resulting in larger head group area (a_0) and smaller P, therefore spherical morphology is preferred under ultrasound. In terms of nano-objects stability, we examined the morphology and size of sono-PISA prepared nano-objects by TEM and DLS (Figure 3.16). After 3 months standing at room temperature, all suspension remains stable with negligible change in size and morphology, which indicates the nano-objects prepared by sono-PISA are relatively stable at room temperature.

$$P = \frac{V}{a_0 l_c}$$

$$Area = N a_0$$

PEG$_{113}$-PHPMA$_{400}$, Sono-PISA, spheres
Larger a_0, smaller P
Higher free energy, requires external energy

$$P \le \frac{1}{3}$$

PEG$_{113}$-PHPMA$_{400}$, thermal-PISA, vesicles
Smaller a_0, larger P
Lower free energy

$$\frac{1}{2} < P \le 1$$
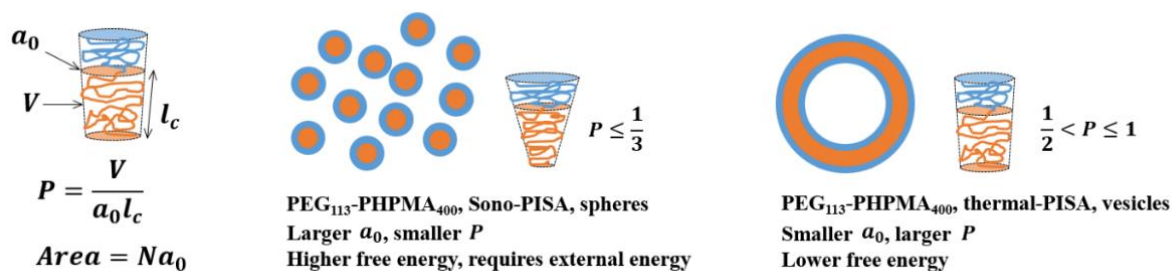
Figure 3.15 Schematic of PEG$_{113}$-PHPMA$_{400}$ nano-objects synthesised *via* sono-PISA and thermal-PISA.
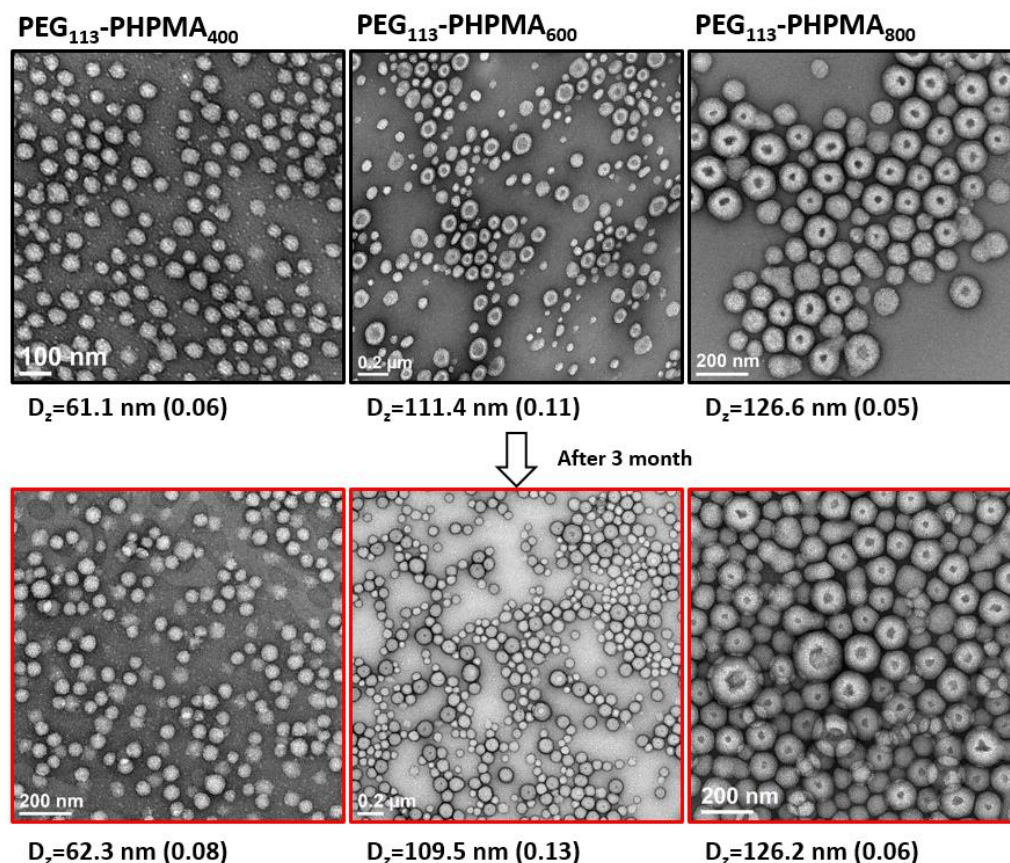
Figure 3.16 DLS size distribution data and representative TEM images of PEG$_{113}$-PHPMA$_{800}$ synthesised by sono-PISA and after 3 months standing at room temperature.

No worm-like micelles were observed for sono-PISA nano-objects when using purified HPMA whether changing the target DP or sampling during polymerisation (Figure 3.17). This could be because the worm region is very narrow in some cases,[59] and thus might exist but have not been found. The other highly possible reason is that although the physical effects generated by the high ultrasonic frequency is limited, acoustic streaming effect is still present in the system and could limit the formation of worm and rod-like micelles. Acoustic streaming is a streaming flow of fluid around an oscillating bubble induced by acoustic field,[60] and has been used to manipulate particles in fluid.[61] This was further demonstrated by applying ultrasound wave on worms suspension generated by thermal-PISA process, the morphology converted from worms to shorter worm fragments and spheres (Figure 3.18b-e), the hydrodynamic diameter also decreased with the increasing sonication time (Figure 3.18a).
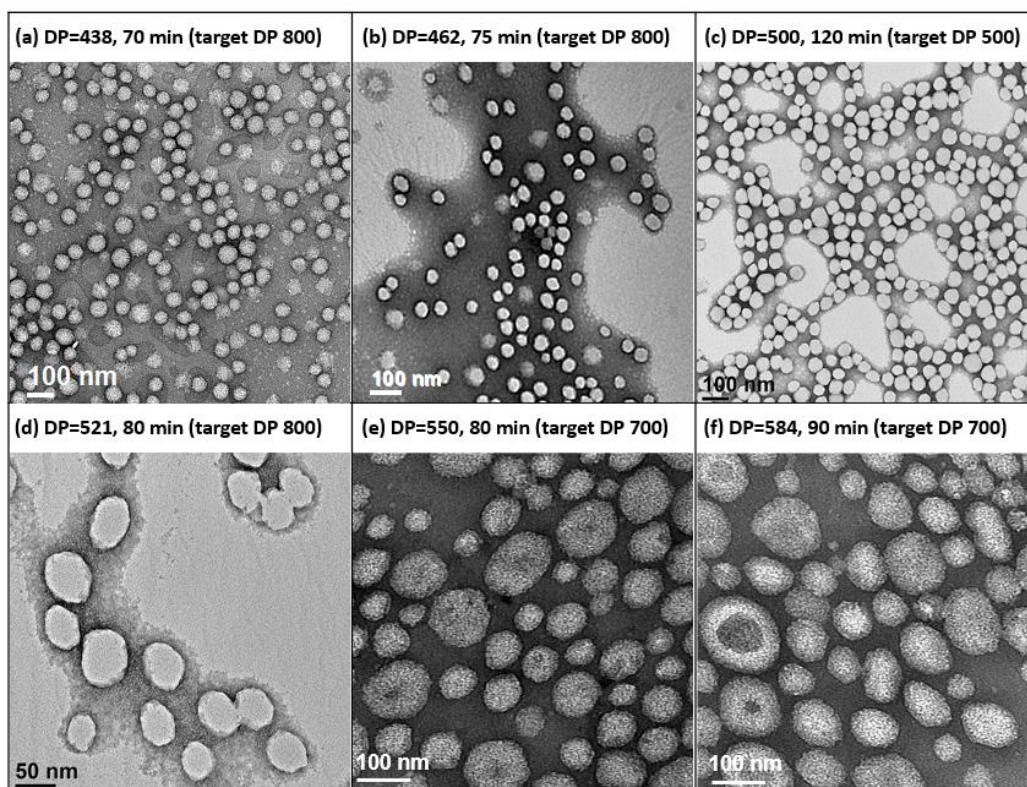
Figure 3.17 TEM images of PEG$_{113}$-PHPMA$_X$ prepared *via* sono-PISA by varying target DP and sampling at certain time points during polymerisation (focused on DP 400~600).
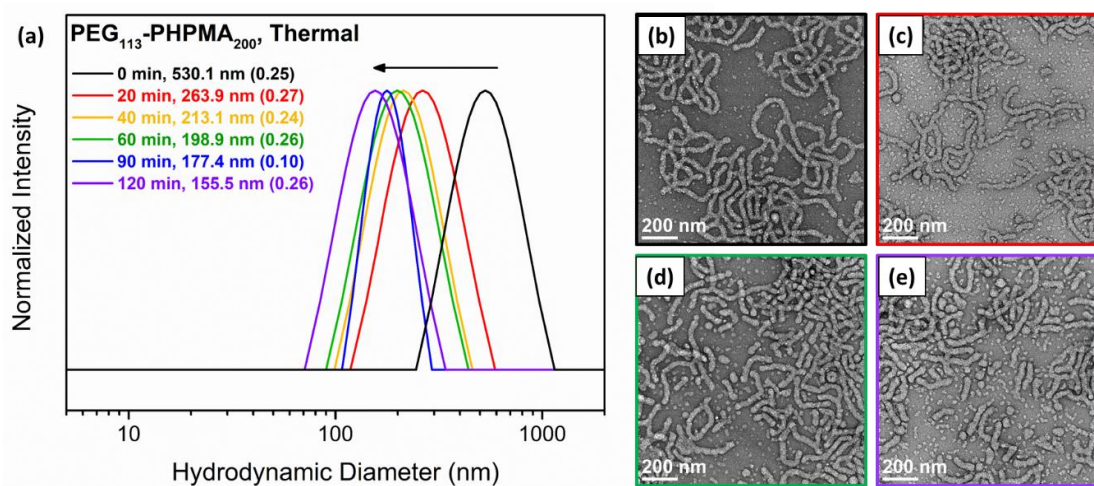
Figure 3.18 (a) DLS size distribution data recorded for thermal-PISA prepared PEG$_{113}$-PHPMA$_{200}$ worms after ultrasound irradiation (990 kHz) for 0, 20, 40, 60, 90 and 120 min. Representative TEM images of ultrasound irradiated PEG$_{113}$-PHPMA$_{200}$ worms for (b) 0 min, (c) 20 min, (d) 60 min, (e) 120 min.

Therefore, for sono-PISA, a strategy to overcome the influence of acoustic streaming effect is required in order to obtain worm-like micelle. Many chemistries have been utilised to prepare covalently stabilised block copolymer nano-objects,[62] and most examples focus on core cross-linking (CCL), because conducting shell cross-linking at high copolymer concentrations usually results in interparticle cross-linking and hence irreversible loss of colloidal stability. Therefore, we have performed sono-RAFT-PISA of unpurified HPMA that contains trace of dimethacrylate crosslinker. Short worms and larger size vesicles were obtained from PEG$_{113}$-PHPMA$_{500}$ (Figure 3.19). Thus, CCL renders nano-objects more streaming-resistant to form elongated morphologies.
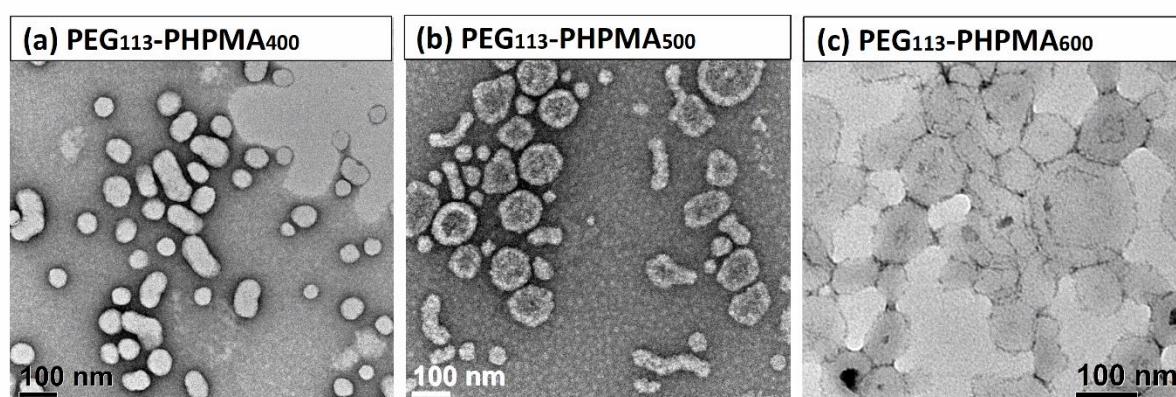
Figure 3.19 Representative TEM images of (a) PEG$_{113}$-PHPMA$_{400}$, (b) PEG$_{113}$-PHPMA$_{500}$ and (c) PEG$_{113}$-PHPMA$_{600}$ synthesised by sono-RAFT-PISA using unpurified monomer HPMA (10.0 % w/w solid content).

In order to further investigate the influence of CCL on morphology of block copolymer nanoparticles, ethylene glycol dimethacrylate (EGDMA) was employed as comonomer (component C) with purified HPMA (component B) in the presence of PEG$_{113}$-RAFT (component A). As shown in Table 3.2, different amount of dimethacrylate was mixed with the purified HPMA as binary comonomer. When the HPMA degree of polymerisation is 400, the hydrodynamic diameter was 61.1 ± 0.8 nm and the morphology is spheres (Table 3.1). However, for the group with same HPMA DP and additional 0.5% molar statistically copolymerised with EGDMA, Z-average size (Z$_a$) increased to 102.4 ± 3.0 nm, and the morphology is a mixture of short worms and micelle dimers (Figure 3.20a) instead of spheres. By increasing the molar ratio of EGDMA to 1.0%, Z$_a$ increased to 195.6 ± 1.5 nm, the length of worms is increased as well (Figure 3.20b). The core-cross-linking enhances the stability of the polymer chains when exposed to the

ultrasonic sonication, while the core-cross-linking between the particles will promote the fusion of the particle cores, resulting in the morphological transformation of spheres to short worms. By further increase the DP of HPMA to 800, the morphology became aggregated small vesicles (Figure 3.20d). Similar trend was found for Z_a by adding higher amount of EGDMA. Because the hydrophobicity of EGDMA is higher than HPMA, the hydrophobicity of the block copolymer increased by chain extended with even a small amount of EGDMA. Whether the change in morphology is due to the variation in hydrophobicity of core-forming block or the effect of cross-linking is unknown. In order to investigate that, there are two strategies: i) replacing the EGDMA with butyl methacrylate (BMA) which has a similar hydrophobicity but not divinyl cross-linker; ii) replacing the EGDMA with hydrophilic divinyl cross-linker poly ethylene glycol dimethacrylate (PEGDMA, M_n 500). The constructed nano-objects (Table 3.2 entry 6, 7) with 0.5 % BMA as comonomer have very close Z_a and morphology to the group (Table 3.1 entry 4, 6) without comonomer. These results suggest that the increase in hydrophobicity, at least with such a subtle change, will not give significant effect on morphology of nano-objects. The Z_a of entry 9 is 28 nm larger than entry 4, this might due to the hydrophilic cross-linker made nanoparticles swelled up in water, leading a slightly larger hydrodynamic diameter. Short worms obtained from entry 9 were very similar with those obtained from entry 4. These results indicate that the sphere-to-short-worm transformation in morphology is due to cross-linking. *In situ* CCL offers a facile approach for the synthesis of short worms *via* sono-PISA process. The mean length of the worms tends to increase with the increasing amount of added cross linker. This could potentially provide with a methodology to control over the length of worms, which would be a breakthrough for current technique because almost all PISA syntheses exhibit a relatively broad distribution of worm lengths.[5]

Table 3.2 Characterisation data of PEG$_{113}$-b-P(HPMA$_X$-co-C$_Y$) nano-objects by sono-PISA

Entry	Component C	Molar ratio of A:B:C[a]	C/B[b] (%)	Z$_{a,DLS}$ (nm)	Morphology[c]
1	EGDMA	1:400:2	0.5	102.4 ± 3.0	s/w
2	EGDMA	1:400:4	1.0	195.6 ± 1.5	s/w
3	EGDMA	1:600:3	0.5	970.1 ± 212.0	w
4	EGDMA	1:800:1	0.125	388.3 ± 9.3	w/v
5	EGDMA	1:800:4	0.5	422.7 ± 10.2	w/v
6	BMA	1:400:2	0.5	65.4 ± 1.5	s
7	BMA	1:600:3	0.5	105.3 ± 2.9	s/w/v
8	PEGDMA	1:400:1	0.25	73.9 ± 1.9	s/w
9	PEGDMA	1:400:2	0.5	130.8 ± 3.6	s/w

[a] A: PEG$_{113}$-RAFT, B: HPMA monomer, C: comonomer. [b] Molar percentage of C/B. [c] S=spheres, V= vesicles, W=worms.

Figure 3.20 Representative TEM images of nano-objects obtained from Table 3.2 entry 1-9 (a-i respectively).

3.4 Conclusions

Overall, it was demonstrated for the first time that various morphologies of block copolymer nano-objects, including spherical micelle, worm, and vesicle can be prepared by sono-RAFT-PISA at ambient temperature. The use of water as both solvent and initiator source in sono-RAFT-PISA exhibits the "green" synthesis feature of this technique. This will allow the fabrication of nano-objects in a system that is sensitive to external initiators or additives. It was also shown that vesicle with uniform and smaller size (~110 nm) compared to conventional thermal-PISA could be easily prepared by this methodology. Furthermore, it was found that the worm-like micelle structure was challenging to achieve due to the presence of acoustic streaming effect in this system. However, the introduction of core-cross-linking components offer a feasible approach for the synthesis of worm-like micelle *via* sono-RAFT-PISA. In addition, with several examples of reactors with uniformly delivered ultrasonic irradiation,[63] sono-PISA is easily scalable and externally-regulated, thus preventing the problems of poor heat transfer or UV intensity decay along reactor geometry in conventional processes. These features may open many new prospects for the field of polymeric nano-objects synthesis.

3.5 Supporting Information

3.5.1 Thermal initiator radical species concentration

Radical species generated from decomposition of azo compound initiator. Thus,

$$\frac{d[R]}{dt} = -2f\frac{d[I]}{dt} = 2fk_d[I], k_d = ln2/t_{1/2}$$

$$[R] = 2f([I]_0 - [I]) = 2f[I]_0(1 - e^{-k_d t})$$

$[R]$ = radical concentration, $[I]$ = initiator concentration, k_d = decomposition rate constant, $t_{1/2}$ = half-life of initiator, f = initiator efficiency.

For this study, take PEG$_{113}$-PHPMA$_{400}$ thermal-PISA as example, initial initiator concentration $[I]_0$ = 0.5 mM. At 50 °C, $t_{1/2}$ of VA-044 = 250 min, $k_d = 2.772 \times 10^{-3} min^{-1}$. Initiator efficiency is not considered when estimating radical species concentration during ultrasound irradiation, thus thermal

initiator f is ignored for comparison. For maximum radical generation, f =1. At end of thermal-PISA

(4 h), t = 240 min, $[R]$ =0.49 mM.

3.6 References

1. N. J. Warren and S. P. Armes, *J. Am. Chem. Soc.*, 2014, **136**, 10174-10185.
2. B. Charleux, G. Delaittre, J. Rieger and F. D'Agosto, *Macromolecules*, 2012, **45**, 6753-6765.
3. B. Karagoz, L. Esser, H. T. Duong, J. S. Basuki, C. Boyer and T. P. Davis, *Polym. Chem.*, 2014, **5**, 350-355.
4. W.-M. Wan and C.-Y. Pan, *Polym. Chem.*, 2010, **1**, 1475-1484.
5. S. L. Canning, G. N. Smith and S. P. Armes, *Macromolecules*, 2016, **49**, 1985-2001.
6. J. Tan, H. Sun, M. Yu, B. S. Sumerlin and L. Zhang, *ACS Macro Lett.*, 2015, **4**, 1249-1253.
7. C. A. Figg, A. Simula, K. A. Gebre, B. S. Tucker, D. M. Haddleton and B. S. Sumerlin, *Chem. Sci.*, 2015, **6**, 1230-1236.
8. A. Blanazs, A. J. Ryan and S. P. Armes, *Macromolecules*, 2012, **45**, 5099-5107.
9. B. Fan and E. R. Gillies, *Mol. Pharmaceutics*, 2017, **14**, 2548-2559.
10. M. Huo, Q. Ye, H. Che, X. Wang, Y. Wei and J. Yuan, *Macromolecules*, 2017, **50**, 1126-1133.
11. J. Huang, H. Zhu, H. Liang and J. Lu, *Polym. Chem.*, 2016, **7**, 4761-4770.
12. B. Fan, J. F. Trant, A. D. Wong and E. R. Gillies, *J. Am. Chem. Soc.*, 2014, **136**, 10116-10123.
13. B. Fan, R. E. Yardley, J. F. Trant, A. Borecki and E. R. Gillies, *Polym. Chem.*, 2018, **9**, 2601-2610.
14. C. J. Mable, K. L. Thompson, M. J. Derry, O. O. Mykhaylyk, B. P. Binks and S. P. Armes, *Macromolecules*, 2016, **49**, 7897-7907.
15. F. D'Agosto, J. Rieger and M. Lansalot, *Angew. Chem. Int. Ed.*, 2020, **59**, 8368-8392.
16. X. Liu and W. Gao, *ACS Appl. Mater. Interfaces*, 2017, **9**, 2023-2028.
17. S. Sugihara, K. Sugihara, S. P. Armes, H. Ahmad and A. L. Lewis, *Macromolecules*, 2010, **43**, 6321-6329.
18. W.-M. Wan and C.-Y. Pan, *Macromolecules*, 2007, **40**, 8897-8905.
19. G. Delaittre, M. Save and B. Charleux, *Macromol. Rapid Commun.*, 2007, **28**, 1528-1533.
20. X. G. Qiao, P. Y. Dugas, B. Charleux, M. Lansalot and E. Bourgeat-Lami, *Macromolecules*, 2015, **48**, 545-556.
21. X. G. Qiao, M. Lansalot, E. Bourgeat-Lami and B. Charleux, *Macromolecules*, 2013, **46**, 4285-4295.
22. L. Zhang, C. Song, J. Yu, D. Yang and M. Xie, *J. Polym. Sci., Part A: Polym. Chem.*, 2010, **48**, 5231-5238.
23. K.-Y. Yoon, S. Shin, Y.-J. Kim, I. Kim, E. Lee and T.-L. Choi, *Macromol. Rapid Commun.*, 2015, **36**, 1069-1074.
24. D. B. Wright, M. A. Touve, L. Adamiak and N. C. Gianneschi, *ACS Macro Lett.*, 2017, **6**, 925-929.
25. K.-Y. Yoon, I.-H. Lee, K. O. Kim, J. Jang, E. Lee and T.-L. Choi, *J. Am. Chem. Soc.*, 2012, **134**, 14291-14294.
26. J. Chiefari, Y. K. Chong, F. Ercole, J. Krstina, J. Jeffery, T. P. T. Le, R. T. A. Mayadunne, G. F. Meijs, C. L. Moad, G. Moad, E. Rizzardo and S. H. Thang, *Macromolecules*, 1998, **31**, 5559-5562.
27. Y. Chong, T. P. Le, G. Moad, E. Rizzardo and S. H. Thang, *Macromolecules*, 1999, **32**, 2071-2074.
28. G. Moad, E. Rizzardo and S. H. Thang, *Polymer*, 2008, **49**, 1079-1131.
29. G. Moad, E. Rizzardo and S. H. Thang, *Aust. J. Chem.*, 2005, **58**, 379-410.
30. G. Moad, E. Rizzardo and S. H. Thang, *Acc. Chem. Res.*, 2008, **41**, 1133-1142.
31. N. J. W. Penfold, J. Yeow, C. Boyer and S. P. Armes, *ACS Macro Lett.*, 2019, **8**, 1029-1054.
32. B. Karagoz, C. Boyer and T. P. Davis, *Macromol. Rapid Commun.*, 2014, **35**, 417-421.
33. W.-M. Wan, C.-Y. Hong and C.-Y. Pan, *Chem. Commun.*, 2009, 5883-5885.

34. L. P. D. Ratcliffe, A. J. Ryan and S. P. Armes, *Macromolecules*, 2013, **46**, 769-777.
35. N. J. Warren, O. O. Mykhaylyk, D. Mahmood, A. J. Ryan and S. P. Armes, *J. Am. Chem. Soc.*, 2014, **136**, 1023-1033.
36. J. Tan, Y. Bai, X. Zhang and L. Zhang, *Polym. Chem.*, 2016, **7**, 2372-2380.
37. J. He, Q. Xu, J. Tan and L. Zhang, *Macromol. Rapid Commun.*, 2019, **40**, 1800296.
38. J. Yeow, O. R. Sugita and C. Boyer, *ACS Macro Lett.*, 2016, **5**, 558-564.
39. S. Piogé, T. N. Tran, T. G. McKenzie, S. Pascual, M. Ashokkumar, L. Fontaine and G. Qiao, *Macromolecules*, 2018, **51**, 8862-8869.
40. P. Pignoli, E. Tremoli, A. Poli, P. Oreste and R. Paoletti, *Circulation*, 1986, **74**, 1399-1406.
41. R. A. Caruso, M. Ashokkumar and F. Grieser, *Langmuir*, 2002, **18**, 7831-7836.
42. A. L. Klibanov, *Investigative radiology*, 2006, **41**, 354-362.
43. B. M. Teo, S. W. Prescott, M. Ashokkumar and F. Grieser, *Ultrason. Sonochem.*, 2008, **15**, 89-94.
44. B. M. Teo, M. Ashokkumar and F. Grieser, *J. Phys. Chem. B*, 2008, **112**, 5265-5267.
45. S. K. Bhangu and M. Ashokkumar, in *Sonochemistry: From Basic Principles to Innovative Applications*, eds. J. C. Colmenares and G. Chatel, Springer International Publishing, Cham, 2017.
46. S. Xu, J. Yeow and C. Boyer, *ACS Macro Lett.*, 2018, **7**, 1376-1382.
47. A. Blanazs, J. Madsen, G. Battaglia, A. J. Ryan and S. P. Armes, *J. Am. Chem. Soc.*, 2011, **133**, 16581-16587.
48. C. Hochanadel, *J. Phys. Chem.*, 1952, **56**, 587-594.
49. J. Tan, X. Zhang, D. Liu, Y. Bai, C. Huang, X. Li and L. Zhang, *Macromol. Rapid Commun.*, 2017, **38**, 1600508.
50. A. Blanazs, R. Verber, O. O. Mykhaylyk, A. J. Ryan, J. Z. Heath, C. W. I. Douglas and S. P. Armes, *J. Am. Chem. Soc.*, 2012, **134**, 9741-9748.
51. L. P. D. Ratcliffe, M. J. Derry, A. Ianiro, R. Tuinier and S. P. Armes, *Angew. Chem. Int. Ed.*, 2019, **58**, 18964-18970.
52. G. Moad, E. Rizzardo and S. H. Thang, *Aust. J. Chem.*, 2009, **62**, 1402-1472.
53. E. Rizzardo, J. Chiefari, B. Y. K. Chong, F. Ercole, J. Krstina, J. Jeffery, T. P. T. Le, R. T. A. Mayadunne, G. F. Meijs, C. L. Moad, G. Moad and S. H. Thang, *Macromol. Symp.*, 1999, **143**, 291-307.
54. D. J. Tobler, S. Shaw and L. G. Benning, *Geochim. Cosmochim. Acta*, 2009, **73**, 5377-5393.
55. J. Tan, Q. Xu, Y. Zhang, C. Huang, X. Li, J. He and L. Zhang, *Macromolecules*, 2018, **51**, 7396-7406.
56. L. D. Blackman, K. E. Doncom, M. I. Gibson and R. K. O'Reilly, *Polym. Chem.*, 2017, **8**, 2860-2871.
57. K. Miki, H. Hashimoto, T. Inoue, H. Matsuoka, H. Harada, M. Hiraoka and K. Ohe, *Small*, 2014, **10**, 3119-3130.
58. L. H. Dang, M. T. Vu, J. Chen, C. K. Nguyen, L. G. Bach, N. Q. Tran and V. T. Le, *ACS Omega*, 2019, **4**, 4540-4552.
59. N. J. Warren, M. J. Derry, O. O. Mykhaylyk, J. R. Lovett, L. P. D. Ratcliffe, V. Ladmiral, A. Blanazs, L. A. Fielding and S. P. Armes, *Macromolecules*, 2018, **51**, 8357-8371.
60. J. Jalal and T. S. Leong, *Fluids*, 2018, **3**, 93.
61. Y. K. Suh and S. Kang, in *Encyclopedia of Microfluidics and Nanofluidics*, ed. D. Li, Springer US, Boston, MA, 2008, pp. 25-33.
62. W.-J. Zhang, C.-Y. Hong and C.-Y. Pan, *Macromol. Rapid Commun.*, 2019, **40**, 1800279.
63. Y. Son, M. Lim and J. Khim, *Ultrason. Sonochem.*, 2009, **16**, 552-556.

Chapter 4

Preparation of Polymer–Metal Nanocomposites with Functional Properties

4.1 Introduction

In recent years, there has been an increasing interest in the synthesis of hybrid nanoparticles or nanocomposites, especially polymer-metal nanocomposites, due to their potential applications in a broad range of areas, including biotechnology, optoelectronics, therapeutics, and catalysis.[1-4] In catalytic applications, polymeric nanoparticles have been used as scaffolds for supporting metal nanocatalysts, such as gold nanoparticles (AuNPs) and palladium nanoparticles (PdNPs), because of the tunability in polymer particle size and well-studied interactions between polymer functional groups and metal atoms.[5-7] More importantly, researchers found that the stabilising/capping agents (*e.g.* citrate) in conventional metal nanoparticles often act as a physical barrier, which blocks the access of reactants during the reaction and adversely affects the overall catalytic performance.[8, 9] By replacing the stabilising/capping agents with polymeric nanoparticles, the surface of the metal nanoparticles is free from any capping agent barrier, thus it can serve as highly active catalysts. For polymer-metal nanocomposite, the metal nanoparticles are usually prepared *in situ* by reduction of a metal salt and immobilised on polymer based on the interaction between one of the polymer blocks and the metal ion. For instance, McCormic and co-workers reported the synthesis of gold-"decorated" vesicles using *in situ* reduction of sodium tetrachloroaurate in the presence of polymers containing tertiary amine groups.[10] Kim *et al.*[8] reported the preparation of poly(*N*-isopropylacrylamide) particles embedded with *in situ* formed AuNPs *via* light irradiation and studied their atypical quasi-homogeneous catalytic functions for homocoupling reactions.

The polymeric nanoparticles for polymer-metal nanocomposites are usually prepared through either solution self-assembly or polymerisation-induced self-assembly (PISA). Whereas, the drawbacks of solution self-assembly, such as low polymer concentration and complex preparation procedures, have limited its scalable preparation.[11-15] PISA on the other hand, yields block copolymer nano-objects *in situ*

during the polymerisation with high polymer solid content (10-40%), promising its large-scale application. Meanwhile, the morphology and size of the nano-objects can be easily tuned by controlling the degree of polymerisation (DP) and solid content.[16, 17] Thus far, several studies have reported the preparation of polymer-metal nanocomposites using PISA nano-objects as the scaffold.[17-20] Davis and Boyer reported the *in situ* reduction of chloroauric acid using $NaBH_4$ in the presence of tertiary amine-containing polymer nano-objects synthesised *via* PISA approach.[20] Pietrasik *et al.* demonstrated the preparation of poly(acrylic acid)-*block*-polystyrene (PAA-*b*-PS) nano-spheres *via* PISA, this polymer nano-sphere was then immobilised with silver nanoparticles and used as surface-enhanced Raman spectroscopy (SERS) substrate for adenine detection and catalyst for reduction of 4-nitrophenol.[18] More recently, our group synthesised a series of cyclodextrin-decorated nano-objects *via* PISA and demonstrated the "guest-host" complexation with AuNPs which are modified with polymer ligands containing adamantane moieties.[17] This provides a new pathway for the fast preparation of polymer-based nanocomposites.

Meanwhile, with the increasing interest in PISA, research devoted to initiation methods of PISA has become a new trend in recent years. Our previous study (Chapter 3 of this thesis) has demonstrated a room-temperature ultrasound-initiated PISA process without the addition of any thermo-/photo-initiators.[21] The sonolysis of H_2O and generation of H˙ and ˙OH to initiate RAFT polymerisation in PISA provide a "green" alternative compared to the conventional thermo-/photo- process. Furthermore, ultrasound allows the preparation of gold colloids and palladium colloids without the addition of any reducing agents,[22-26] as the H˙ generated during sonolysis can also reduce metal ions to form metal nanoparticles. However, to our best knowledge, there is no research yet devoted to the preparation of polymer-metal nanocomposites using ultrasound as both initiation and reducing sources. By combining the ability of ultrasound on initiating polymerisation and producing metal nanoparticles, we demonstrate here not only a 'green' alternative without the addition of initiator or reducing agent, but also a facile synthesis strategy for quick preparation of polymer-metal nanocomposites. Specifically, a tertiary amine-containing polymeric nanoparticle was firstly synthesised by ultrasound-PISA (Scheme 4.1), it was then used as the scaffold for *in situ* generation of metal nanoparticles by sonication. The formed polymer-Au nanocomposite with stepwise-grown AuNPs can be applied as surface-enhanced Raman scattering (SERS) substrate for 4-aminothiophenol (4-ATP) detection. Meanwhile, the prepared

polymer-Au and polymer-Pd nanocomposites were examined for catalytic applications and showed high catalytic efficiency in aerobic alcohol oxidation and Suzuki-Miyaura cross-coupling reaction, respectively.
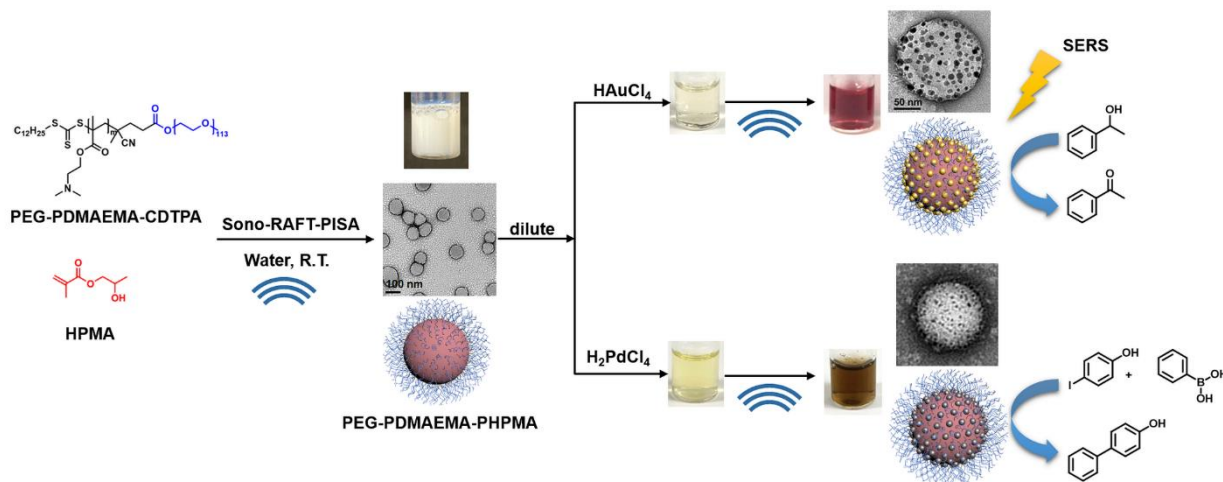
Scheme 4.1 Synthesis of PEG_{113}-*b*-PDMAEMA-*b*-PHPMA copolymers *via* sono-RAFT-PISA process, and *in situ* formation of Au and Pd nanocomposite by ultrasound.

4.2 Materials and Methods

4.2.1 Materials

Diisopropyl carbodiimide (DIC; >99%) was purchased from Oakwood Chemical (USA). 4-Dimethylaminopyridine (DMAP; 99%) was purchased from Alfa Aesar. 4-Cyano-4 (((dodecylthio) carbonothioyl) thio) pentanoic acid (CDTPA; 97%) was purchased from Boron Molecular (Australia). Poly(ethylene glycol) methyl ether ($mPEG_{113}$, average M_n 5,000 g/mol), 2-(dimethylamino)ethyl methacrylate (DMAEMA), hydroxypropyl methacrylate (HPMA, mixture of 2-hydroxypropyl and 2-hydroxyisopropyl methacrylate; 97%), poly(*N*-vinylpyrrolidone) (PVP, average M_n 40,000 g/mol) and palladium on carbon (Pd/C, 5 % w/w loading) were purchased from Sigma Aldrich (Australia). 2,2'-Azobis(isobutyronitrile) (AIBN) was purchased from Wako Pure Chemical Industries, Ltd. All the other solvents were obtained from commercial source and were used as received unless noted otherwise.

4.2.2 Methods

4.2.2.1 Preparation of PEG₁₁₃-b-PDMAEMA block copolymer via RAFT polymerisation

The following representative protocol was used for the preparation of PEG$_{113}$-b-PDMAEMA block copolymer. First, the PEG$_{113}$-CDTPA macro-chain transfer (macro-CTA) agent was synthesised using the method described elsewhere.[21] PEG$_{113}$-CDTPA (0.5 g, 92.6 μmol, 1.0 equiv.), DMAEMA (0.44 g, 2.8 mmol, 30.0 equiv.) and AIBN (3.0 mg, 18.5 μmol, 0.2 equiv.) were dissolved in 3 mL 1,4-dioxane and transferred to a Schlenk flask. The flask was deoxygenated by 3 cycles of freeze-pump-thaw. It was then immersed in an oil bath at 60 °C for 12 h. The block copolymer was purified by precipitation in *n*-hexane and dried in the vacuum oven at 40 °C until constant weight to yield a yellow solid (0.76 g, 80.8% yield) of PEG$_{113}$-b-PDMAEMA$_{24}$ (Figure 4.1). ^{1}H NMR (400 MHz, CDCl$_3$): δ 3.98-4.27 (b, 48H), 3.56-3.72 (b, 445H), 3.37 (s, 3H), 2.39-2.63 (b, 49H), 2.21-2.38 (b, 142H), 1.77-1.94 (b, 78H), 1.21-1.32 (b, 19H), 0.82-1.10 (b, 69H). GPC (DMF, PMMA standards): M_n =13,400 g/mol, Đ = 1.09. Similarly, block copolymers of PEG$_{113}$-b-PDMAEMA$_9$ and PEG$_{113}$-b-PDMAEMA$_{46}$ were successfully synthesised (Figure 4.2 and 4.3 respectively).
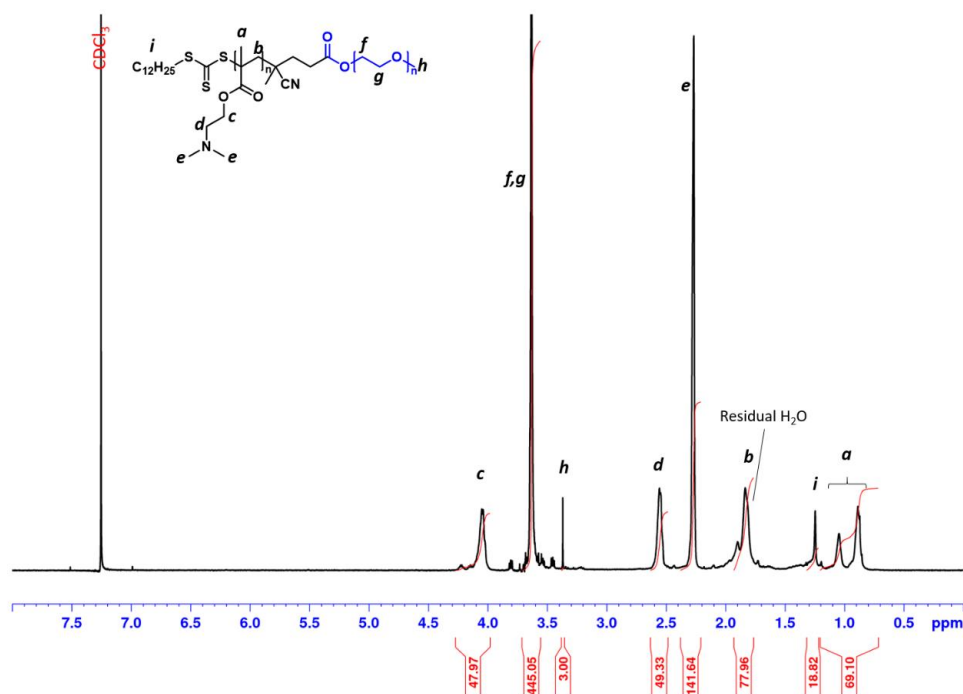
Figure 4.1 ^{1}H NMR spectrum (400 MHz, CDCl$_3$) of PEG$_{113}$-b-PDMAEMA$_{24}$.
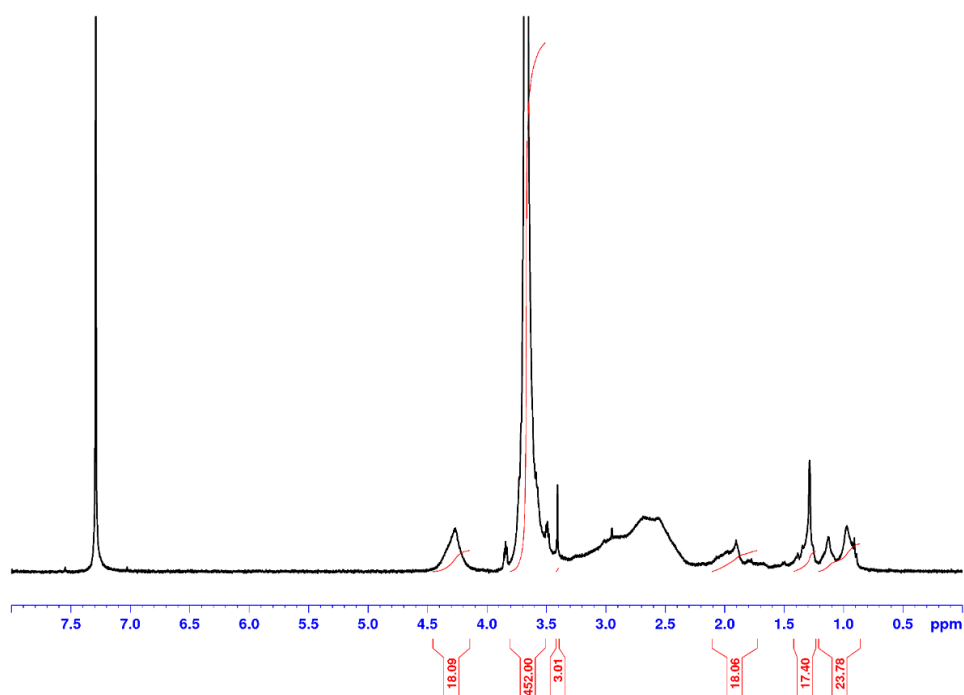
Figure 4.2 ^{1}H NMR spectrum (400 MHz, CDCl$_3$) of PEG$_{113}$-*b*-PDMAEMA$_9$.
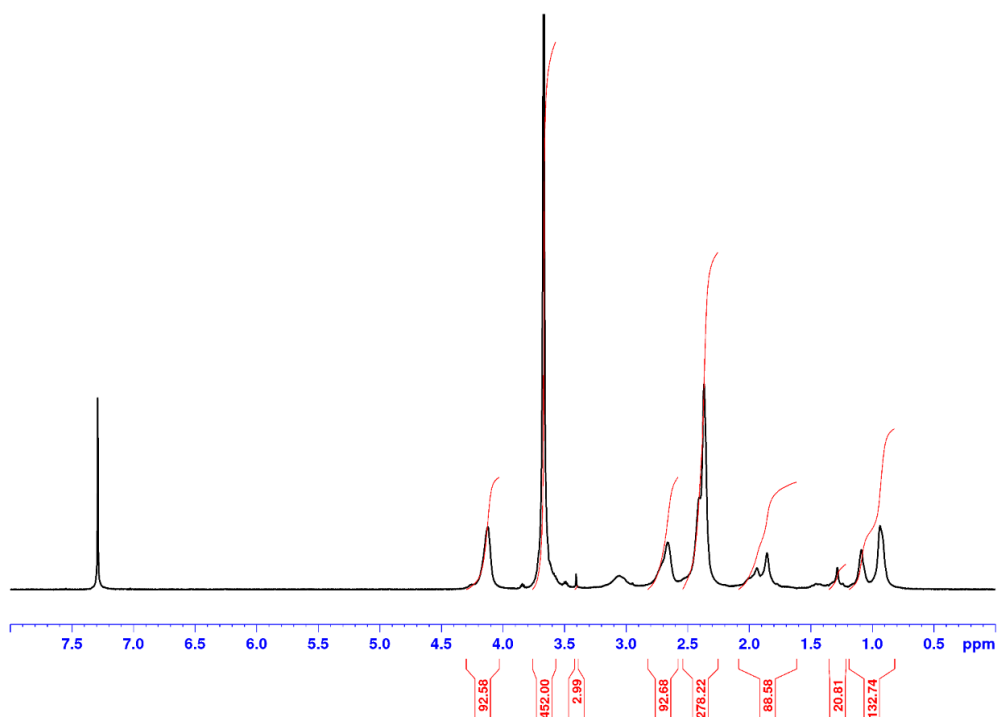
Figure 4.3 ^{1}H NMR spectrum (400 MHz, CDCl$_3$) of PEG$_{113}$-*b*-PDMAEMA$_{46}$.

117

4.2.2.2 The synthesis of polymeric colloids by sono-PISA

The following representative protocol was used for the ultrasound-initiated RAFT dispersion polymerisation-induced self-assembly (sono-RAFT-PISA) process for the synthesis of PEG_{113}-b-$PDMAEMA_{24}$-b-$PHPMA_{300}$. HPMA monomer was disinhibited by passing through a column of basic alumina, it was further purified by passing through a silica gel column (n-hexane: diethyl ether = 1:1 as eluent) to remove dimethacrylate impurity. PEG_{113}-b-$PDMAEMA_{24}$-CDTPA macro-CTA (35.0 mg, 3.8 μmol, equiv. 1.0) and HPMA monomer (165.0 mg, 1.14 mmol, equiv. 300.0) were weighed in a 12 mL glass test tube with socket and dissolved in DI water (1.80 mL, 10 % w/w). The test tube was sealed using a rubber septum and deoxygenated by purging with argon using needles through the liquid for 30 min. The test tube was then sealed properly and immersed in the ultrasonic water bath with circulated cooling water jacket (Figure 4.4a) maintained at room temperature (~23 °C) during the reaction. The distance between the bottom of the test tube and the transducer plate was kept at ~5 cm. The ultrasonic generator (Meinhardt Ultrasonics, model M11-010, output power 250 W) was then switched on (990 kHz, 80% intensity). The reaction was stopped after 2 hr of sonication by switching off the ultrasonic generator and exposure to air.
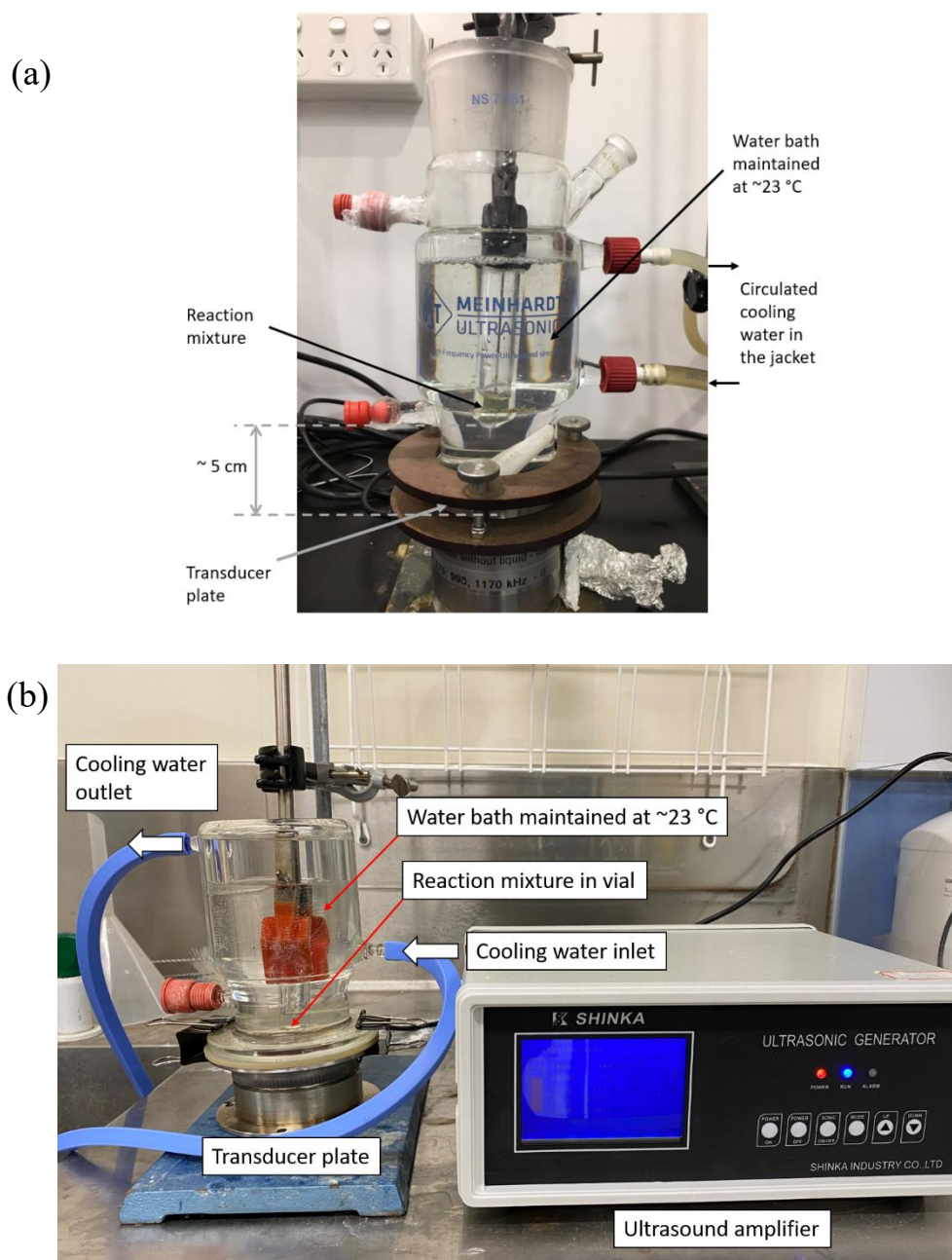
Figure 4.4 Experimental setup of (a) ultrasound transducer (990 kHz, Meinhardt) and reaction vessel for sono-RAFT-PISA experiment at room temperature, water batch temperature measured 23.8 °C at the end of polymerisation (ultrasound amplifier and water circulation pump not shown). (b) ultrasound amplifier (400 kHz, Shinka) and reaction vessel for *in situ* synthesis of polymer-metal nanocomposite.

4.2.2.3 The in situ synthesis of polymer-metal nanocomposite using ultrasound

A typical procedure for the preparation of polymer-Au nanocomposite. 8 μL 25 mM HAuCl$_4$ solution, 2-propanol (20 mM) and PVP (0.2 mg/mL) were mixed with 1.0 mL of the above diluted triblock copolymer dispersion (0.2 mg polymer/mL with 2.8×10^{-2} mM tertiary amine group) in a 6 mL glass *vial*. The *vial* was purged with argon for 5 min and properly sealed. The *vial* was then immersed in an ultrasonic water bath (Figure 4.4b) which was maintained at room temperature (~23 °C) during the reaction. The ultrasonic generator (Shinka, SF-400) was operated at 400 kHz, 100 W for 2 h to reduce Au(III) to Au(0). For stepwise growth, 8 μL 25 mM HAuCl$_4$ solution was added to pre-synthesised polymer-Au nanocomposite, then reduced by the addition of NH$_2$OH (24 μL, 25 mM, allow 5 min in between each step). For the formation of PVP-stabilised AuNPs, 8 μL 25 mM HAuCl$_4$ solution, 2-propanol (20 mM) and PVP (1.0 mg/mL) were mixed with Milli-Q water to make 1.0 mL solution, it was then purged with argon and sonicated in the same way as polymer-Au nanocomposite. For the preparation of polymer-Pd nanocomposite and PVP-stabilised PdNPs, all procedures used were the same except the HAuCl$_4$ solution was replaced by 20 μL of 10 mM H$_2$PdCl$_4$ solution.

4.2.2.4 SERs experiment

For the Raman test, the silicon wafer-supported polymer-Au nanocomposite sample was sealed in a plastic tube together with 5 mg of 4-ATP powder at room temperature. The 4-ATP powder was sublimated, and the 4-ATP molecules gradually diffused towards and bound to the AuNP surface. The SERS measurements were conducted before, after 1-min and 48-h contacting with 4-ATP.

4.2.2.5 Typical procedure for aerobic alcohol oxidation using polymer-Au nanocomposite

The aqueous dispersion of polymer-Au nanocomposite (1.0 mM Au-containing solution, 0.5 mL), 1-phenylethanol (122.2 mg, 1.0 mmol, 1.0 equiv.), *tert*-butyl hydroperoxide (225.3 mg, 2.5 mmol, 2.5 equiv.), KOH (168.3 mg, 3.0 mmol, 3.0 equiv.) and solvent (H$_2$O, 4.5 mL) were added into a round bottom flask equipped with a magnetic stirring bar (washed with aqua regia). The flask was then sealed properly with a rubber septum and the mixture was stirred at 80 °C for 2 h. 0.5 mL of the reaction mixture was withdrawn from the flask and extracted with CDCl$_3$ to determine the yield of acetophenone by ^{1}H NMR analysis (Figure 4.17). After reaction, the reaction mixture was centrifuged at 4000 rpm for

10 min. The sediment polymer-Au nanocomposite was redispersed in water by sonication for reusability test.

4.2.2.6 Typical procedure for Suzuki-Miyaura coupling reaction using polymer-Pd nanocomposite

4-Iodophenol (55 mg, 0.25 mmol, 1.0 equiv.), phenylboronic acid (30.5 mg, 0.25 mmol, 1.0 equiv.), K_2CO_3 (103.7 mg, 0.75 mmol, 3.0 equiv.), solvent (H_2O, 5mL) and polymer-Pd nanocomposite (1.0 mM Pd-containing solution, 25 μL) were added to a 50 mL screw cap *vial* equipped with a magnetic stirring bar (washed with aqua regia). The *vial* was then sealed properly with a cap and the mixture was stirred at 70 °C for 1 h. 5.0 mL methanol was then added to the reaction mixture to dissolve the product and any unreacted starting materials. 1.0 mL solution was collected and dried, the solid was dissolved in $CDCl_3$ and ${}^1H$ NMR spectrum was taken for yield determination. For kinetic studies, 0.5 mL of the reaction mixture was collected every 10 min for a total reaction period of 1 hr. The mixture was dissolved in 0.5 mL methanol and dried for ${}^1H$ NMR analysis to determine the NMR yield. After reaction, the mixture was centrifuged at 600 rpm for 1 min to separate 4-phenylphenol solid and polymer-Pd nanocomposite suspension. The supernatant suspension was collected and reused for another batch of reaction.

4.2.3 Characterisation

Dynamic light scattering (DLS) measurements were performed at 20 °C using Malvern Zetasizer Nano ZS. The aqueous dispersions containing the diblock copolymer nano-objects were diluted to 0.10 % w/v by DI water. Light scattering was detected at 173° and hydrodynamic diameters were determined by assuming spherical, non-interacting, perfectly monodisperse particles. ${}^1H$ Nuclear magnetic resonance spectroscopy (NMR) spectra were recorded on a Bruker Avance 400 NMR spectrometer at frequencies of 400 MHz. NMR chemical shifts (δ) are reported in ppm and were calibrated against residual solvent signals of $CDCl_3$ (δ 7.26), DMSO-d_6 (δ 2.50). Samples were dissolved in $CDCl_3$, or DMSO-d_6 at 5-10 mg mL^{-1}. The data are reported as chemical shift (δ). Gel permeation chromatography (GPC) was performed on a system comprising a Shimadzu LC-20AT pump, Shimadzu RID-20A refractive index detector, and SPD-20A UV–visible detector. The GPC is equipped with a guard column (WAT054415)

and 3×Waters GPC columns (WAT044238, WAT044226, WAT044235, 300 mm×7.8 mm). The eluent is DMF with 10 mM LiBr and eluted at 1 mL/min for 45 min in total. The samples were dissolved in DMF with 10 mM LiBr, filtered through 0.20 μm syringe filters. A calibration curve was obtained from poly(methyl methacrylate) (PMMA) standards (Agilent) ranging from 960 to 1,568,000 g mol^{-1}. Transmission electron microscopy (TEM): Copper grids (formvar/carbon-coated, 400 mesh) were plasma glow-discharged for 10 seconds to create a hydrophilic surface. After glow discharge, 0.10 % w/v aqueous dispersion was dropped on the grid and then negatively stained by uranyl acetate solution (2.0 % w/v). The grid was blotted again to remove excess stain and dried using a gentle nitrogen blow. Imaging was performed using a FEI Tecnai G2 T20 TWIN TEM instrument equipped with Orius SCD200D wide-angle CCD camera operating at 200 kV. High-resolution TEM was performed with Orius SC600 camera. Scanning transmission electron microscopy (STEM): Same sample preparation method as TEM. Imaging was performed using a FEI Magellan 400 FEGSEM instrument equipped with STEM and HADDF detectors. Raman spectra were collected by a Renishaw RM 2000 Confocal micro-Raman System with excitation laser wavelengths of 633 nm; the laser spot size was 1 m. Thermogravimetric analysis (TGA): TGA measurements were performed on a Shimadzu DTG-60H TGA under nitrogen flow with a ramp of 10 °C / min from 20 to 600 °C. The polymer-metal nanocomposites samples were purified by centrifugation at 4000 rpm for 10 min to separate nanocomposites and free metal nanoparticles.

4.3 Results and Discussion

4.3.1 Synthesis of PEG$_{113}$-*b*-PDMAEMA-*b*-PHPMA triblock copolymer nanoparticles

First, macro-chain transfer agent (Macro-CTA) PEG$_{113}$-CDTPA was synthesised through Steglich esterification according to a previously procedure (section 3.2.2, Figure 3.4).[21] The PEG$_{113}$-CDTPA was then chain extended with monomer DMAEMA in 1,4-dioxane (Scheme 4.2) *via* RAFT polymerisation,[27, 28] yielding a diblock copolymer PEG$_{113}$-*b*-PDMAEMA-CDTPA. To study the influence of the chain lengths of PDMAEMA on the formation of polymer nanoparticle and polymer-metal nanocomposites, three different batches were synthesised (Table 4.1). The theoretical molecular weights ($M_{n,theo.}$) of these hydrophilic block copolymers were matched with the molecular weight calculated *via* ^{1}H NMR spectra ($M_{n,NMR}$). Meanwhile, the GPC data (Table 4.1) reveal these block copolymers have low dispersities (*Đ,*

1.06-1.11), which indicates the well-controlled synthesis of the second blocks. It should be noted that the GPC traces of PEG$_{113}$-b-PDMAEMA-CDTPA display bimodal distributions (Figure 4.5). The presence of side peak results from the purchased PEG$_{113}$ because a similar side peak appears on the GPC trace of PEG$_{113}$ (Figure 3.7).
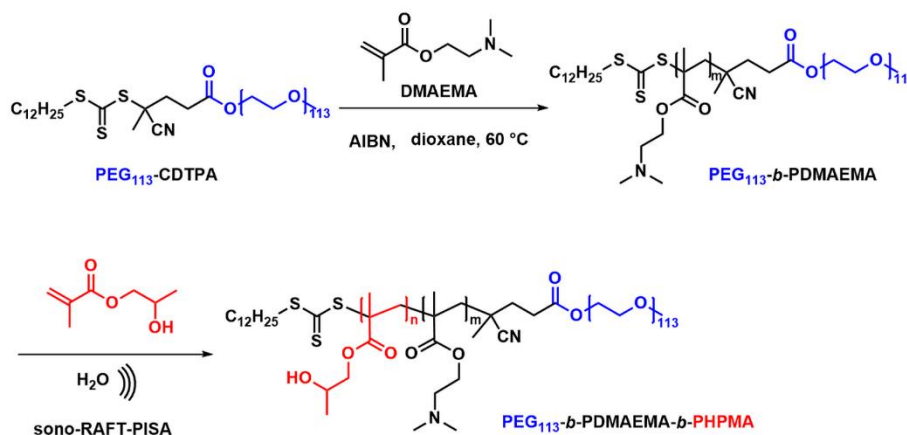
Scheme 4.2 Synthesis of PEG$_{113}$-b-PDMAEMA and PEG$_{113}$-b-PDMAEMA-b-PHPMA copolymers *via* sono-RAFT-PISA process.

Table 4.1 Characterisation data of PEG$_{113}$-CDTPA macro-CTA and the corresponding block copolymers PEG$_{113}$-b-PDMAEMA$_m$-CDTPA.

Entry	Polymer[a]	M_n (g/mol)			$Đ$
		$M_{n,NMR}$[b]	$M_{n,theo}$[c]	$M_{n,GPC}$	
	PEG$_{113}$-CDTPA	5,400	-	11,400	1.02
A	PEG$_{113}$-PDMAEMA$_9$-CDTPA	6,800	6,900	13,000	1.10
B	PEG$_{113}$-PDMAEMA$_{24}$-CDTPA	9,200	9,400	13,400	1.09
C	PEG$_{113}$-PDMAEMA$_{46}$-CDTPA	12,600	13,200	40,300	1.13

[a] DP and conversion determined by ^{1}H NMR (Figure 4.1-4.3). DP of DMAEMA was calculated by following the integral ratio of the N,N'-dimethyl protons against the methyl protons of the PEG adjacent to ether linkage at 3.3 ppm. [b]$M_{n,NMR}=M_{n,DMAEMA}\times$(Integration of N,N'-dimethyl protons/6)+$M_{PEG113-CDTPA}$ [c]$M_{n,theo}=M_{n,DMAEMA}\times conversion\times100\times$([DMAEMA]/[PEG$_{113}$-CDTPA]) +$M_{PEG113-CDTPA}$

Meanwhile, it was also found the molecular weights determined by GPC were higher than the theoretical molecular weights (Table 4.1). The primary reason for this variation is the structural difference between PEG and the PMMA standards used for GPC calibration. In the next study, it was found the shorter block of PDMAEMA (Table 4.1, entry A, PEG$_{113}$-b-PDMAEMA$_9$-CDTPA) was not able

to provide sufficient accessible tertiary amine site for metal nanoparticles (Figure 4.6a, b). However, a longer block (Table 4.1, entry C, PEG$_{113}$-*b*-PDMAEMA$_{46}$-CDTPA) provided enough tertiary amine but generated a long hydrophilic chain in the meantime, which required higher DP of HPMA to form core-shell micelles (Figure 4.6c, d). The medium-length PEG$_{113}$-*b*-PDMAEMA$_{24}$-CDTPA was found to meet both conditions. Therefore, the medium-length PEG$_{113}$-*b*-PDMAEMA$_{24}$-CDTPA was selected for the subsequent studies.
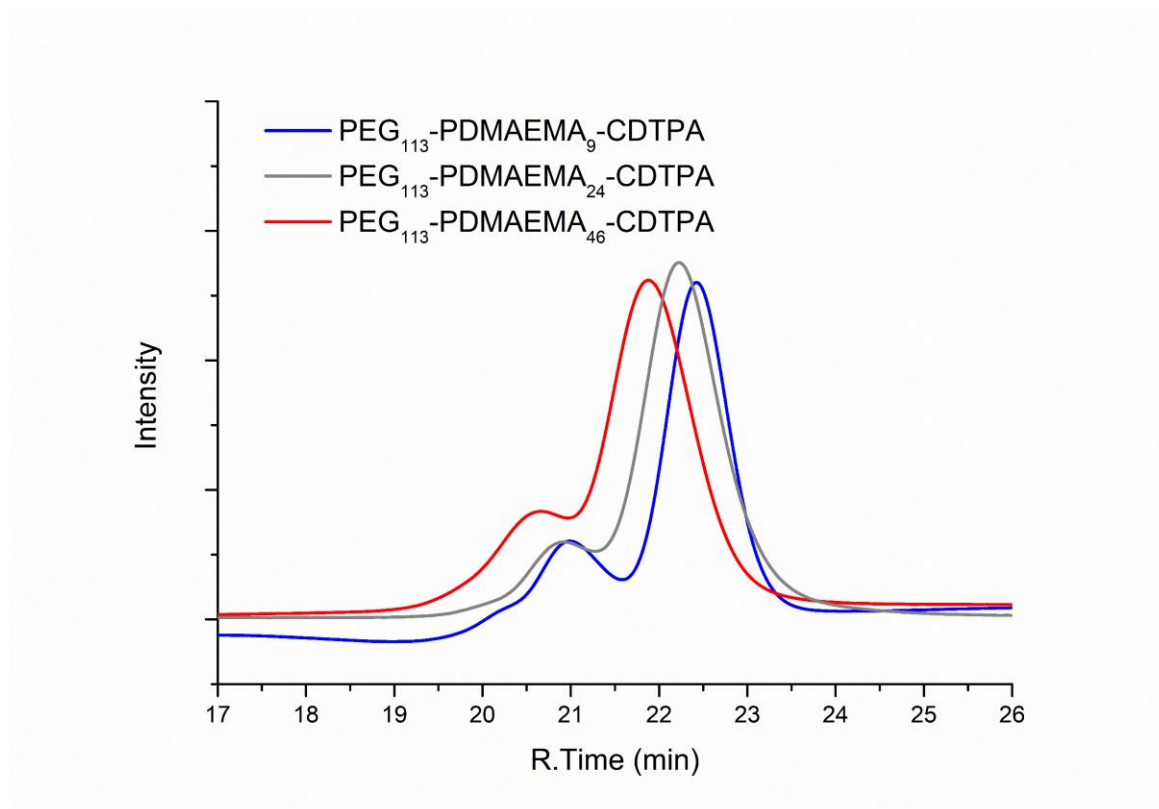
Figure 4.5 Gel permeation chromatography traces (PMMA standards) that obtained for PEG$_{113}$-*b*-PDMAEMA-CDTPA.
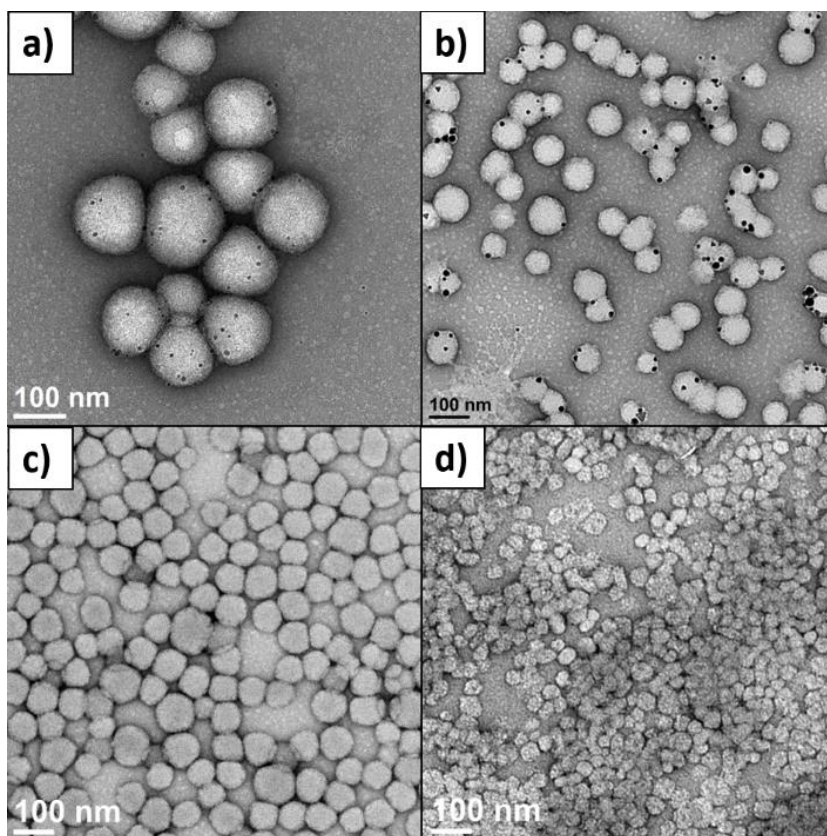
Figure 4.6 TEM images of (a) PEG$_{113}$-b-PDMAEMA$_9$-PHPMA$_{800}$, TA: Au=1:7, (b) PEG$_{113}$-b-PDMAEMA$_9$-PHPMA$_{600}$, TA: Au=1:20, (c) PEG$_{113}$-b-PDMAEMA$_{24}$-PHPMA$_{635}$, (d) PEG$_{113}$-b-PDMAEMA$_{49}$-PHPMA$_{640}$.

Next, PEG$_{113}$-b-PDMAEMA$_{24}$-CDTPA was used as the stabiliser block and HPMA as the monomer for sono-PISA at room temperature and 10% w/w solid content (Scheme 4.2). The PISA was conducted using the 990 kHz ultrasonic reactor, which can split water molecules to generate hydroxyl radicals and initiate polymerisation. Different batches of PEG$_{113}$-PDMAEMA$_{24}$-PHPMA$_n$ with various PHPMA lengths were achieved by changing the targeting DP. As shown in Figure 4.7c, with the increase of the DP of PHPMA block, the cloudiness of the dispersions increased gradually, which indicates the formation of polymer nanoparticles. The dispersions synthesised *via* PISA process were further analysed by ^{1}H NMR spectroscopy and GPC. The ^{1}H NMR spectra (Figure 4.8) confirm that almost all monomers had converted to polymers in this PISA process. The GPC curves (Figure 4.7a) exhibit clear shifting towards higher retention time with the increase of targeting DP. Meanwhile, it was noted that the Đ of these block copolymers increased from 1.21 at DP of 290 to 1.68 at DP of 1170 (Table 4.2). The broadening of the Đ could result from the impurities of PEG$_{113}$ itself, another possible reason is the branching of the

PHPMA blocks caused by the side reaction of hydroxyl radical with polymer chains. This phenomenon was observed in a previous study as well.[21] Despite the relatively broad *Đ*, the subsequent characterisations indicate that it did not adversely affect the formation of uniform polymer nanoparticles.
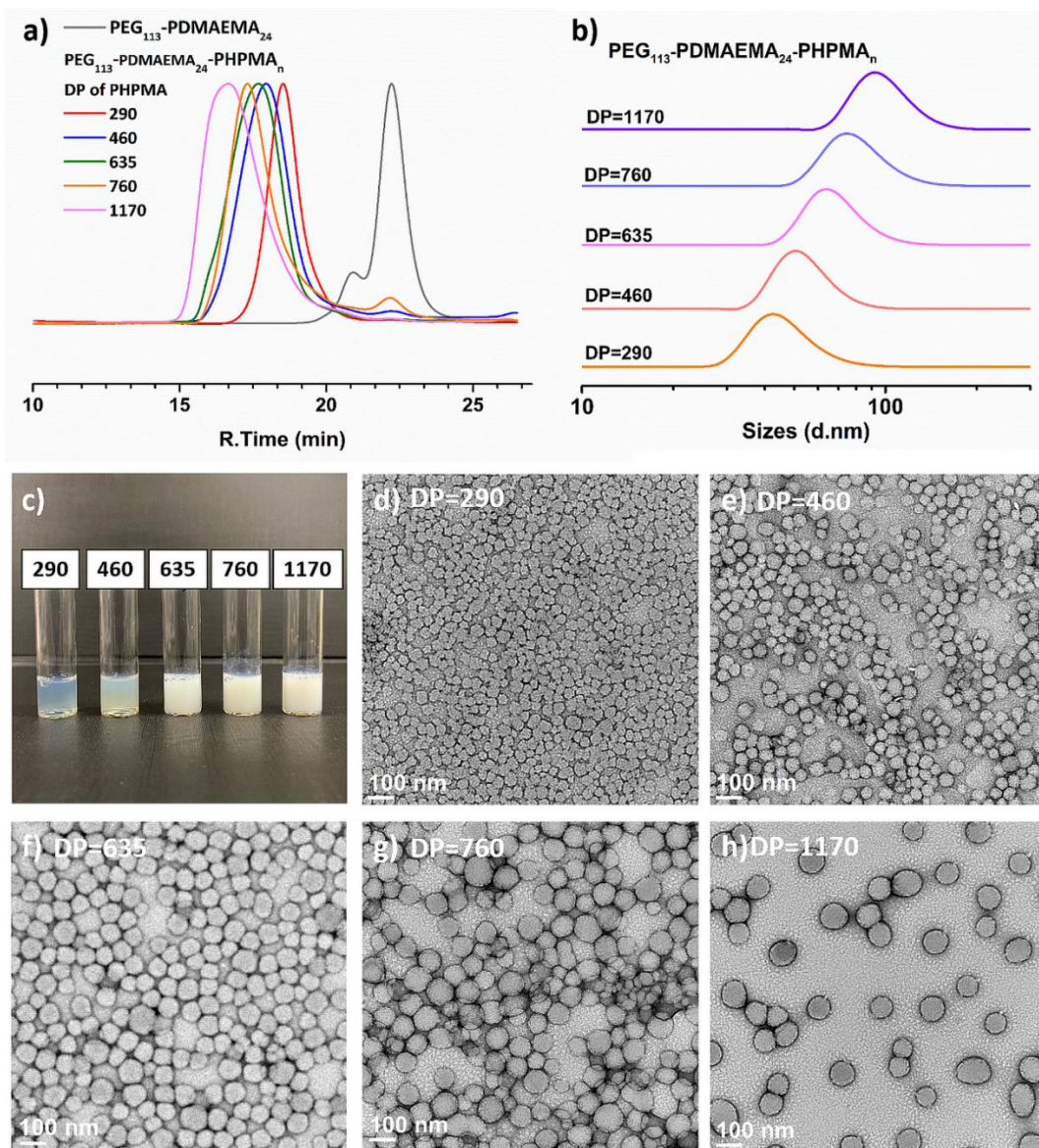
Figure 4.7 (a) GPC traces and (b) DLS traces of PEG_{113}-*b*-$PDMAEMA_{24}$-*b*-$PHPMA_n$ (DP n=290-1170) copolymers synthesised *via* sono-PISA. (c) Photographs and (d-h) TEM images of PEG_{113}-*b*-$PDMAEMA_{24}$-*b*-$PHPMA_n$ prepared *via* sono-PISA, the numbers represent the DP of PHPMA blocks (Table 4.2 entry 1-5 respectively).
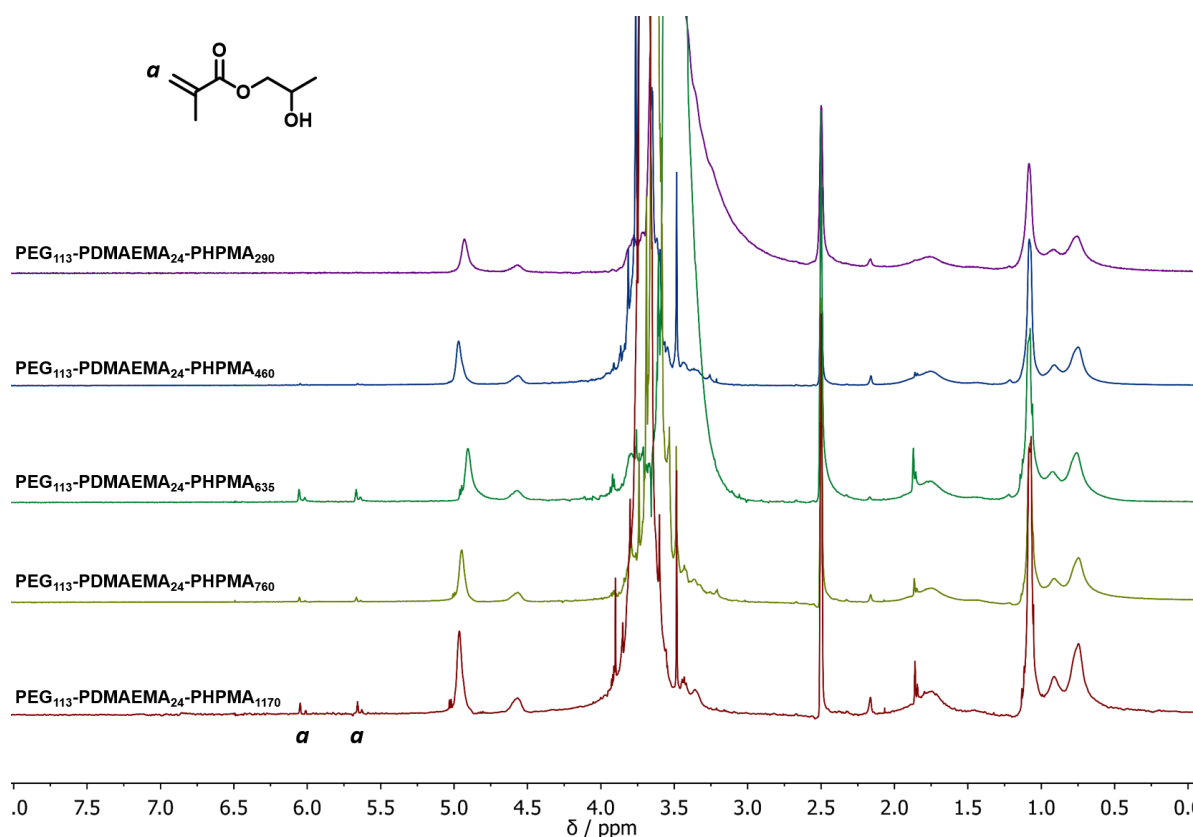
Figure 4.8 ^{1}H NMR spectra of reaction mixture of PEG$_{113}$-b-PDMAEMA$_{24}$-b-PHPMA$_n$ (DP n=290-1170) copolymers synthesised via sono-PISA.

The triblock copolymer dispersions were further analysed by DLS and TEM. The DLS curves (Figure 4.7b) show an apparent shifting of the particle sizes with the increase of PHPMA chain lengths; the average hydrodynamic size increased from 56.0 ± 0.9 nm at the DP of 290 to 115.9 ± 1.2 nm at the DP of 1170 (Table 4.2). Meanwhile, the polydispersity index (PDI) kept around 0.08-0.14, which indicated the narrow size distributions of synthesised nano-objects. The TEM images (Figure 4.7d-h) reveal the structures of the triblock copolymer nano-objects were spherical particles for all entries. No morphological transition to worms or vesicles was observed. Likewise, the TEM images revealed the particle size growth with the increase of the DP, these images also confirmed the uniform size of these polymer nanoparticles. It should be noted that the particle size as measured from the TEM images were slightly smaller than those measured by DLS. This can be attributed to particles being in the dry state under TEM, and DLS could oversize the particles since the scattering from larger particles can increase the overall particle diameter.[29] In this specific PISA process, no worm or vesicle but only spheres were

formed even the DP had increased to 1170. This is due to the use of a relatively long stabiliser block (PEG$_{113}$-*b*-PDMAEMA$_{24}$-CDTPA), which could produce kinetically trapped spheres due to the steric repulsions between long stabilising chains, preventing the fusion and reorganisation of nanoparticles.[30] The polymeric nanoparticles (Table 4.2, entry 5) with relatively large size were then used for *in situ* nanocomposite formation with Au and Pd ions.

Table 4.2 Characterisation data of PEG$_{113}$-*b*-PDMAEMA$_{24}$-*b*-PHPMA$_n$ nanoparticles by sono-PISA.

Entry	DP of HPMA[a]	$M_{n,theo}$ (g/mol)[b]	$M_{n,GPC}$ (g/mol)	Đ	z-average (DLS) (nm)	PDI (DLS)	Diameter by TEM (nm)[c]
1	290	51,000	94,200	1.21	56.0 ± 0.9	0.14 ± 0.01	36.6 ± 7.4
2	460	75,500	143,400	1.52	76.8 ± 0.8	0.14 ± 0.01	54.5 ± 8.3
3	635	100,700	191,300	1.55	88.0 ± 1.9	0.13 ± 0.02	74.8 ± 11.1
4	760	118,700	225,100	1.61	101.2 ± 1.8	0.08 ± 0.01	83.5 ± 12.6
5	1170	177,900	341,700	1.68	115.9 ± 1.2	0.10 ± 0.01	97.8 ± 15.2

[a] *DP was determined by* ^1H *NMR spectrum (Figure 4.8).* [b] $M_{n,theo}= M_{n,HPMA}×conversion×100×([HPMA]/[PEG_{113}$-*b*-PDMAEMA$_{24}$-CDTPA$])$ *+$M_{n,PEG113$-*b*-PDMAEMA24-CDTPA}$* [c] *Average diameter and standard deviation calculated by measuring of 60 random particles.*

4.3.2 *In situ* synthesis of polymer-Au nanocomposite

The tertiary amine group in the PEG$_{113}$-*b*-PDMAEMA$_{24}$-*b*-PHPMA$_n$ can effectively bind with Au ions due to the chemisorption effect (Figure 4.9).[31-33] It was reported that the PDMAEMA block will be partially protonated with the addition of HAuCl$_4$, and the remaining unprotonated tertiary amine groups can reduce the AuCl$_4^-$ counterion to zero-valent Au *in situ via* coordination–reduction mechanism without the addition of external reductants.[34] McCormick *et al.* reported that when PDMAEMA: NaAuCl$_4$ = 10:1, the reduction of AuCl$_4^-$ to AuNPs was achieved *via* coordination–reduction mechanism without the addition of external reductants.[10] Zhao *et al.* also reported Au^{3+} could be reduced by hydroxyl group under alkaline condition, and thus achieving the green synthesis of AuNPs without any harsh reductive substance.[35, 36] The presence of hydroxyl group in PHPMA and alkaline condition from tertiary amine could potentially provide reducing condition for Au^{3+}. However, in our study, when the molar feed ratio of tertiary amine group (TA): HAuCl$_4$=1:7, we did not observe self-reduction after 1 day at room temperature. This was also noticed in a previous report by Boyer and Davis.[20] The slow self-reduction was because the majority of the TA was protonated with the addition of HAuCl$_4$, and no additional TA

is available to provide alkaline condition to reduce $AuCl_4^-$. Thus, an external reductant is required to form AuNPs, commonly, reducing agents, such as citrate and $NaBH_4$ are added to reduce Au precursor ions. Nevertheless, the ultrasound can provide a "green" alternative method to reduce metal ions to
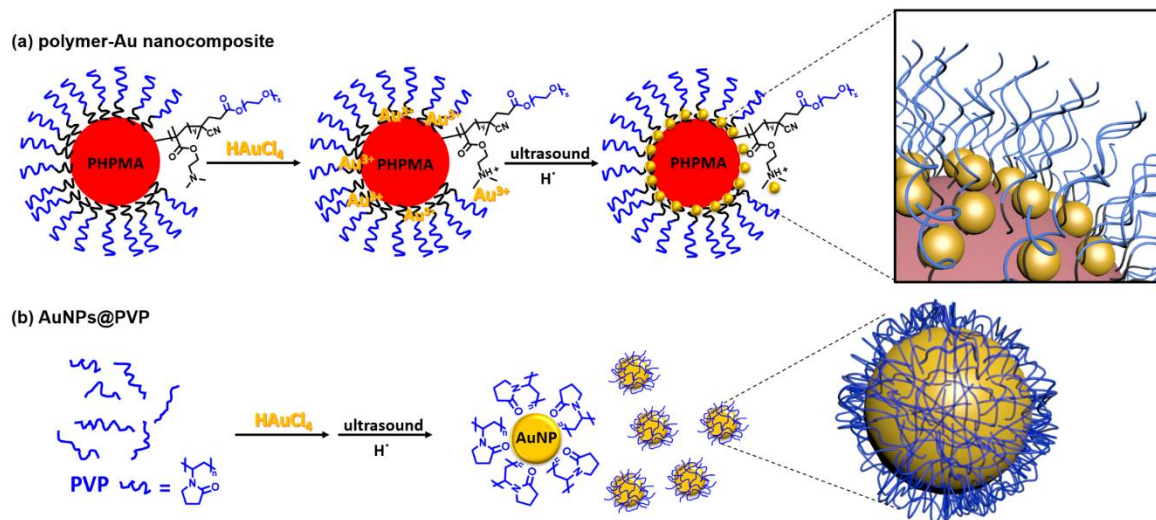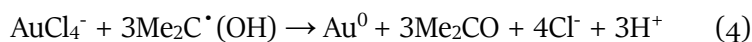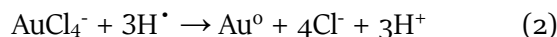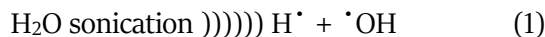

Figure 4.9 Schematic illustration of the preparation of (a) polymer-Au nanocomposite and (b) PVP-stabilised AuNPs (AuNPs@PVP) *via* ultrasound sonication.

metal nanoparticles without the addition of any reducing agents. Since ultrasound at lower frequency has a higher rate of reduction,[23] 400 kHz ultrasound was selected for the formation of metal nanoparticles instead of the 990 kHz ultrasound used in sono-PISA process. The sonolysis of H_2O generates $H\cdot$ and $\cdot OH$, the Au(III) is expected to be reduced by primary reducing species $H\cdot$ as shown in Equations (1)-(2).[22, 25] Alcohols such as 2-propanol can be added to act as a radical scavenger,[22, 25] which leads to additional reduction reaction (Equations (3)-(5)). These reactions combined could result in the formation of AuNPs. Meanwhile, a small quantity of poly(*N*-vinylpyrrolidone) (PVP) was added to improve the stability of nanocomposite as it can attach to the AuNPs, however, it could also compete with amino groups to form PVP-stabilised free AuNPs. Therefore, a low PVP concentration (0.2 mg/mL) was selected after a few attempts.

$$H_2O \text{ sonication }))))))) H^{\bullet} + {}^{\bullet}OH \qquad (1)$$

$$AuCl_4^- + 3H^{\bullet} \rightarrow Au^o + 4Cl^- + 3H^+ \qquad (2)$$

$$H^{\bullet}({}^{\bullet}OH) + Me_2CHOH \rightarrow Me_2C^{\bullet}(OH) + H_2(H_2O) \qquad (3)$$

$$AuCl_4^- + 3Me_2C^{\bullet}(OH) \rightarrow Au^0 + 3Me_2CO + 4Cl^- + 3H^+ \qquad (4)$$

$$nAu^0 \rightarrow Au_n \qquad (5)$$

The immobilisation of AuNPs on polymeric nanoparticles is confirmed by TEM, UV-Vis and high-angle annular dark-field imaging (HAADF). As shown in TEM images (Figure 4.10b, c) of polymer-Au nanocomposites ($Au@PEG_{113}$-b-$PDMAEMA_{24}$-b-$PHPMA_{1170}$) (TA: Au=1:7 and 1:20), the spherical AuNPs were uniformly dispersed on the shell layer of the polymeric nanoparticles. Thermal gravimetric analysis (TGA) of purified nanocomposite was conducted to determine the Au mass loading on the polymer colloidal matrix. The determined mass loading of Au present in the nanocomposites is approximately equal to the theoretical Au content (Table 4.3, Figure 4.11). The size of AuNPs was dependent on the TA: Au ratio; the size of AuNPs was measured as 4-6 nm when TA: Au = 1:7, and 7-14 nm when TA: Au = 1:20. In UV-Vis analysis (Figure 4.10a), the absorption spectra exhibited a surface plasmon resonance (SPR) band shifting from λ_{max} = 529 nm to 542 nm when the TA: Au ratio changed from 1:7 to 1:20. This also reflects the size increment of AuNPs, which is in good agreement with the result measured by TEM. The formation of AuNPs was further confirmed by High-angle annular dark-field (HADDF) microscopy. HAADF is a STEM technique that is highly sensitive to variations of atomic number in the sample. For elements with a higher atomic number, the HAADF detector senses a stronger signal, causing them to appear brighter in the resulting image. Due to the high atomic number of Au compared to the polymer matrix, the AuNPs appeared brighter under HAADF (Figure 4.10d). Meanwhile, this study evidently demonstrated the uniform distribution of AuNPs on the surface of the polymer nanoparticles. Figure 4.10e shows the selected area electron diffraction (SAED) obtained from polymer-Au composite, which exhibits concentric rings with intermittent bright spots corresponding to (111), (200), (220), (311), (222), (400), and (331). High-resolution TEM (HRTEM) image (Figure 4.10f) of a gold nanoparticle shows the lattice spacing for the (111) planes is measured to be 2.35 Å

(measurement in Figure 4.12a). This reflects the polycrystalline and face-centred-cubic nature of the AuNP and provides direct evidence for the presence of AuNPs in the nanocomposite.
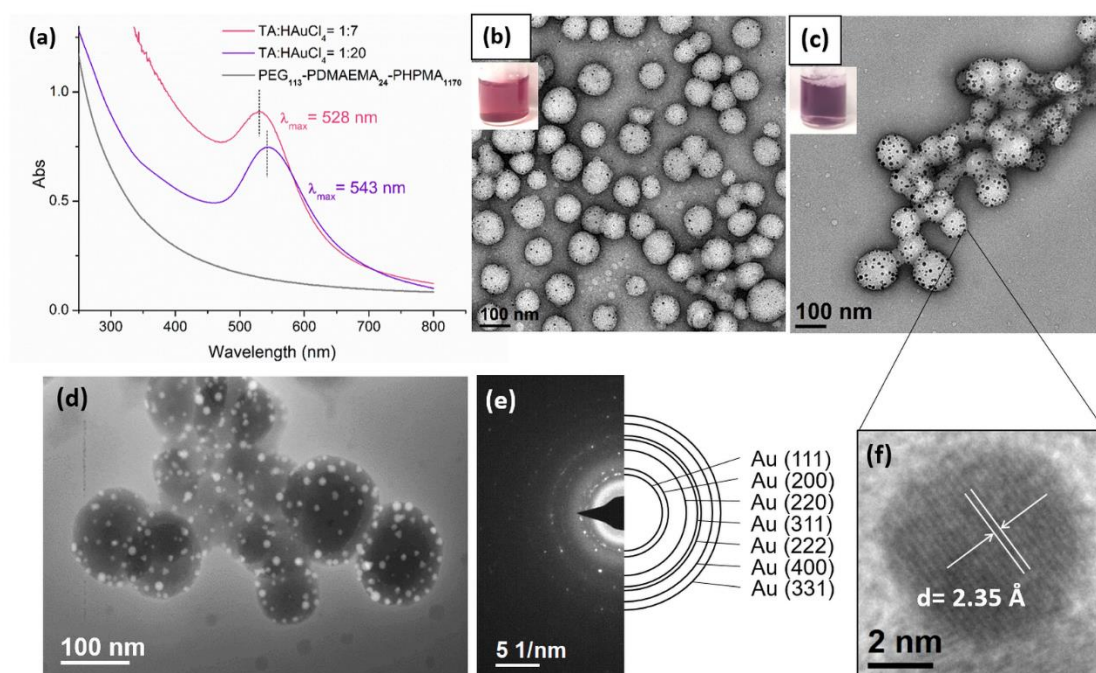

Figure 4.10 (a) UV-Vis spectra of polymer-Au nanocomposites. Digital photos and TEM images of polymer-Au composites with (b) TA: Au = 1:7 and (c) TA: Au = 1:20. (d) STEM HADDF image and (e) SAED pattern of polymer-Au nanocomposite (TA: Au = 1:20). (f) High resolution TEM image of a gold nanoparticle. (All composites were attached with small amount of PVP for stability enhancement.)
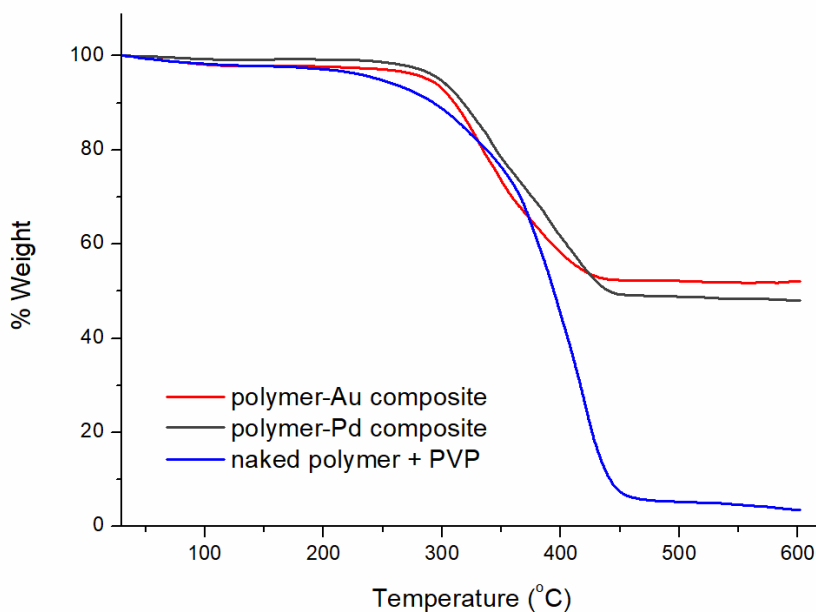
Figure 4.11 Typical TGA thermograms of polymer-Au/polymer-Pd and naked polymer +PVP.

Table 4.3 Typical polymer-Au/polymer-Pd nanocomposites formation in polymer colloids dispersion.

Polymer/water (mg/mL)	TA:metal ratio	TA (mM)	Metal (mM)	Metal NP[a] (%)	Metal NP[b] theo. (%)
Polymer-Au nanocomposite (PEG$_{113}$-*b*-PDMAEMA$_{24}$-*b*-PHPMA$_{1170}$)					
0.2	1:37	0.027	1.0	48.6	49.6
Polymer-Pd nanocomposite (PEG$_{113}$-*b*-PDMAEMA$_{24}$-*b*-PHPMA$_{1170}$)					
0.2	1:37	0.027	1.0	44.5	34.7

[a]Metal NP content determined by thermal gravimetric analysis after purification.

[b] Theoretical metal NP content calculated using the following equation: AuNPs (%) = [molar concentration of Au × sample volume × Mw of Au]/ [molar concentration × sample volume × Mw of Au + 0.2 mg/ml × sample volume]. PdNPs content can be obtained in the same way.
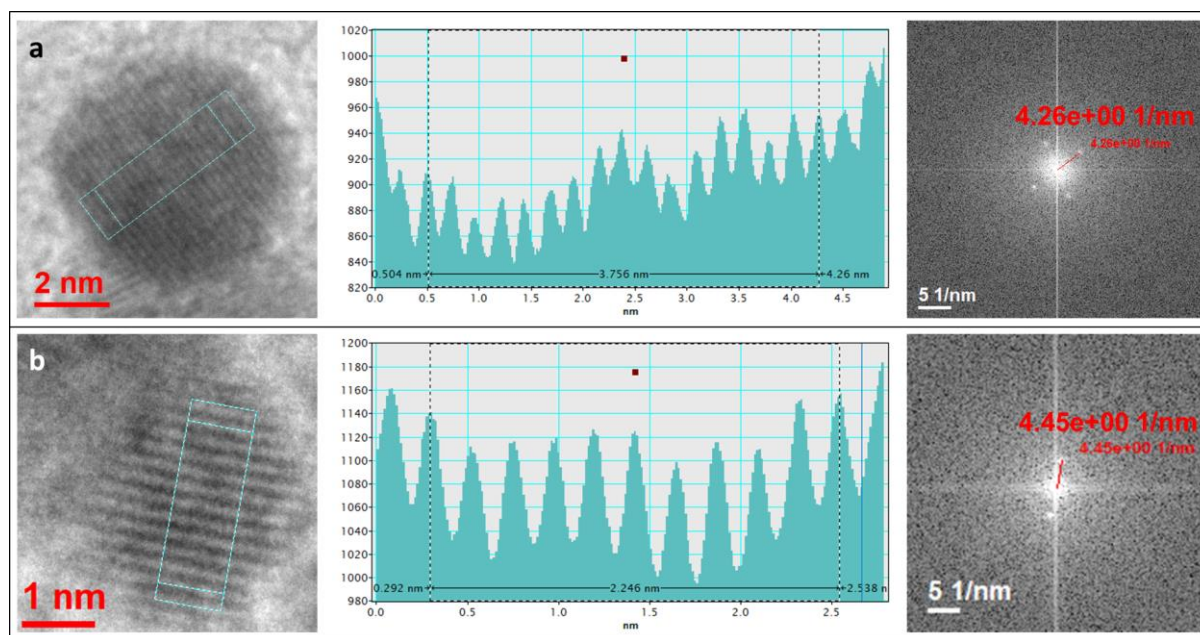
Figure 4.12 HRTEM image with intensity profile diagram and fast Fourier transformation (FFT) of selected area of the (a) AuNP and (b) PdNP on polymer-metal composite. The lattice spacing was calculated by measuring the total distance between n spaces, *e.g.* distance of AuNP=3.756 nm/16= 0.23475 nm. FFT was employed to confirm the distance result by measuring distance from centre to bright point, d=1/(4.26 1/nm)= 0.23474 nm.

Next, the further size evolution of AuNPs was attempted by adjusting the molar ratio of TA: Au. However, by simply adjusting the initial TA: Au ratio from 1:7 or 1:20 to 1:100, the generated AuNPs were not uniform in size nor were they uniformly dispersed on the shell layer of the polymer nanoparticles (Figure 4.13). Thus, the originally prepared polymer-Au nanocomposite was used as seeds for further growth of AuNPs by stepwise growth methodology. Specifically, the initial prepared AuNPs in a lower TA: Au ratio (1:7) was used as seeds and a certain amount of $HAuCl_4$ solution was added. In the next, reducing agent NH_2OH was added to reduce the Au precursor and to form larger AuNPs. This step was repeated up to 7-9 times until the nanocomposites became unstable and formed precipitates. Meanwhile, UV-Vis spectroscopy and TEM were applied to monitor the growth of AuNPs. The UV-Vis spectra (Figure 4.14a) showed the λ_{max} of the SPR band red-shifted about 4-6 nm per step and totally shifted up to 53 nm (from ~530 nm to 583 nm) upon the growth of 7 steps. This result indicated the size increasing of the AuNPs with each growth step, because the SPR absorption of small

AuNPs increases with their diameters.[37] Furthermore, TEM analysis evidently revealed the AuNPs size evolution; the size grew from ~5 nm at the beginning to 20-30 nm at the final step (Figure 4.14b-f). It was observed that the overall quantity of the AuNPs on each polymeric nanoparticle remained approximately constant, suggesting that the Au precursors were primarily consumed in the production of larger AuNPs and no new particle nucleation occurred.[38, 39]
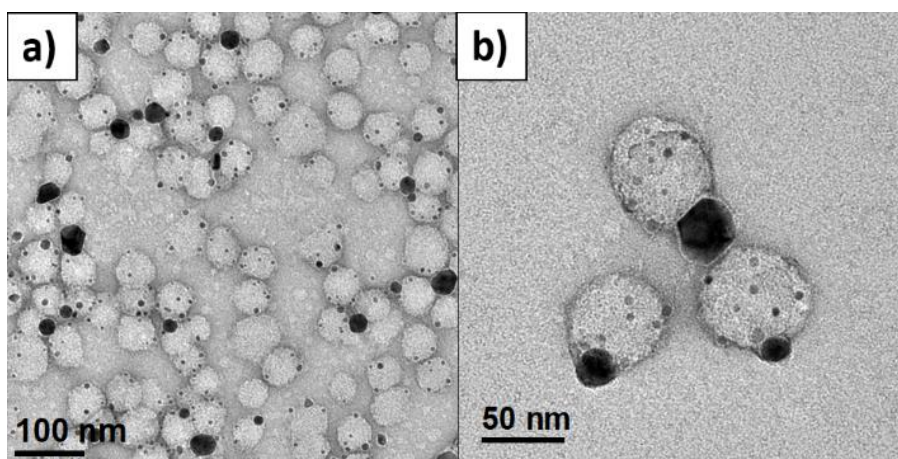

Figure 4.13 TEM images of Au@PEG$_{113}$-*b*-PDMAEMA$_{24}$-*b*-PHPMA$_{1170}$, TA: Au=1:100, AuNPs *in situ* formed by sonication.
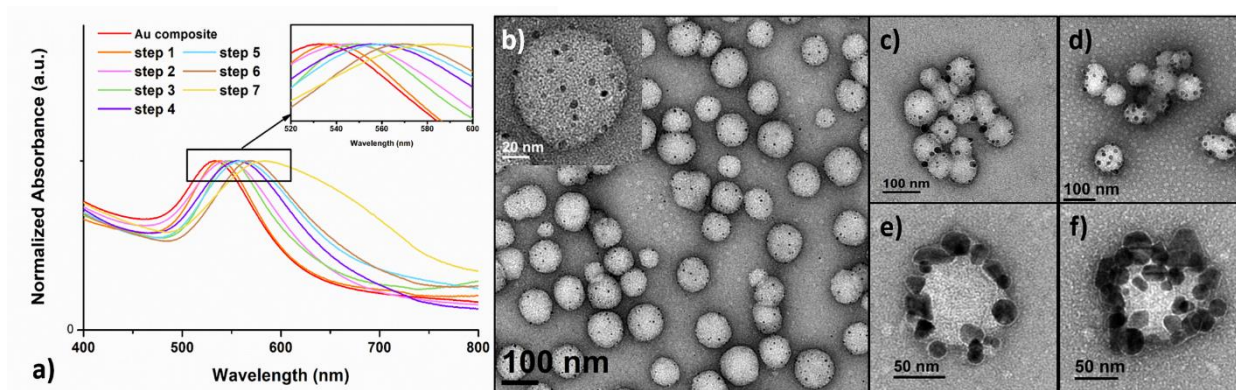
Figure 4.14 (a) UV-Vis absorption spectra of plasmonic Au nanocomposites prepared by the stepwise growth. TEM images of the (b) initial polymer-Au nanocomposites and after (c) step 1, (d) step 2, (e) step 6 and (f) step 7.

The densely clustered AuNPs on the surface of polymer-Au nanocomposites are expected to generate electromagnetic hot spots between the AuNPs, making the nanocomposite a potential surface-enhanced Raman scattering (SERS) substrate candidate for localised probe molecules. Therefore,

SERS effect of polymer-Au nanocomposite after step 7 was further analysed. We performed the SERS measurement on the drop-casted polymer-Au nanocomposite using 4-aminothiophenol (4-ATP) as the probe molecule.
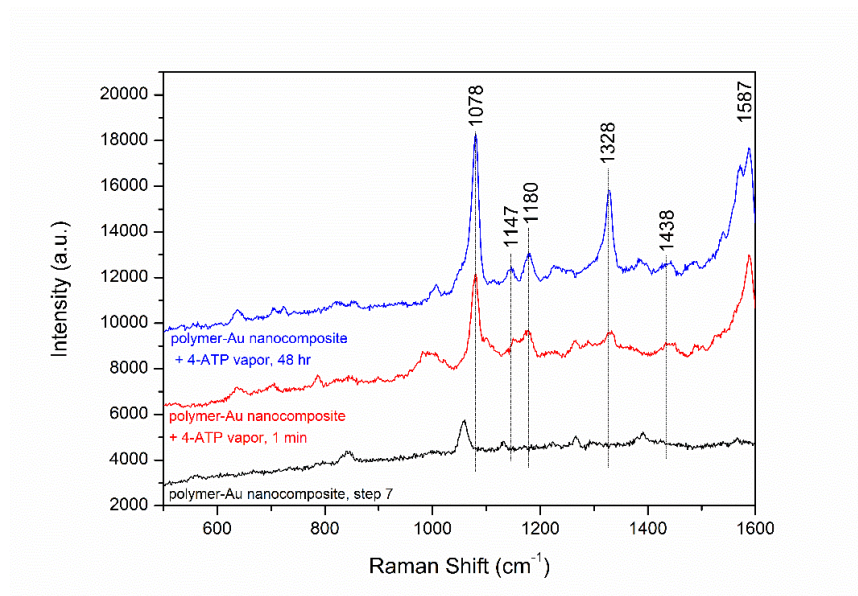
Figure 4.15 SERS spectra of 4-ATP vapor from the polymer-Au nanocomposite substrate and original polymer-Au nanocomposite.

As shown in Figure 4.15, two dominant peaks at 1078 and 1587 cm^{-1} were observed from the SERS spectra of polymer-Au nanocomposite diffused by 4-ATP vapor for 1 min and 48 hr. These correspond to the a_1 vibrational modes of v(C-S) and v(C-C).[40] The weaker enhancement of b_2 modes at 1147, 1180, 1328 and 1438 cm^{-1} were also observed from the SERS spectra.[40] This preliminary SERS measurement confirmed the application of polymer-Au nanocomposite as SERS substrate.

The oxidation of alcohols to aldehydes or ketones is a pivotal functional group transformation in organic chemistry. Previous study has found AuNPs with smaller size exhibit higher catalytic activity.[41] Thus, the catalytic ability of polymer-Au nanocomposite with smaller AuNPs (Au@PEG$_{113}$-b-PDMAEMA$_{24}$-b-PHPMA$_{1170}$, TA: Au=1:7) was testified through the oxidation reaction of 1-phenylethanol to acetophenone (Figure 4.16). The reactions were conducted in water at 80 °C by fixing the reaction time to 2 hr and varying the catalyst quantities. The yield of acetophenone was calculated by the analysis of the ^{1}H NMR spectra (Figure 4.16).

135
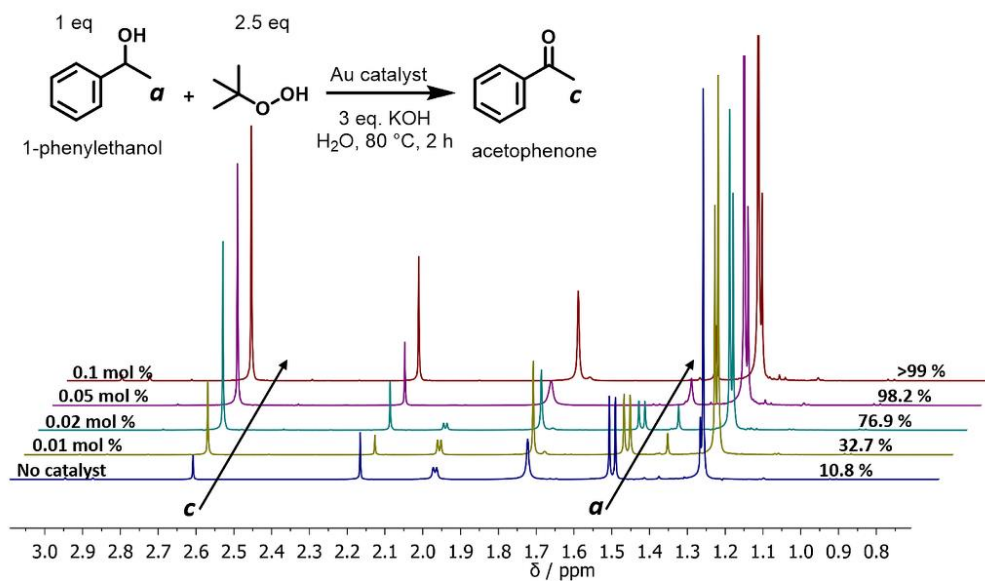
Figure 4.16 ^{1}H NMR spectra of 1-phenylethanol oxidation. (2.63 ppm: methyl group of acetophenone; 1.51 ppm: methyl group of 1-phenylethanol). (The full spectrum and NMR yield calculation equation are available in Figure 4.17.)
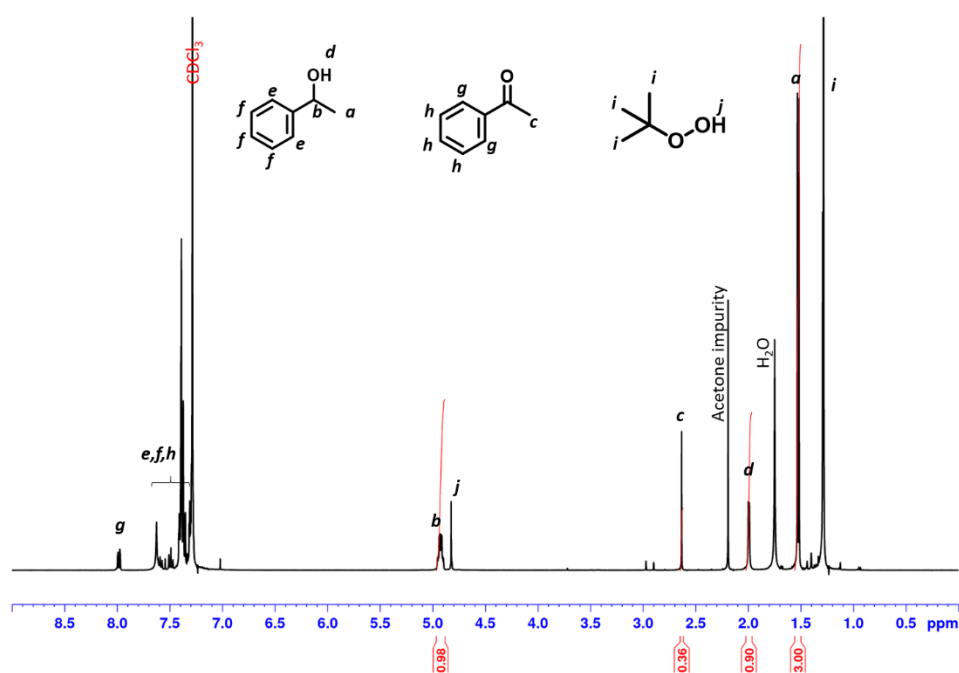

Figure 4.17 ^{1}H NMR spectrum (400 MHz, CDCl$_3$) of 1-phenylethanol oxidation. (NMR yield = Integration of c/(Integration of c + Integration of a)).

136

It was found that the doublet located at 1.52 ppm, which corresponds to the methyl group of 1-phenylethanol, gradually decreased in intensity with the increase of catalyst amount. Meanwhile, a new singlet located at 2.62 ppm, which corresponds to the methyl group of acetophenone, increased gradually in intensity. Without the presence of catalyst, the reaction could only proceed with 10.8% yield (Table 4.4, entry 1), however, with the presence of 0.05 mol% polymer-Au nanocomposites the reaction proceeded with 98.2% yield in 2 hr (Table 4.4, entry 5). In addition, the catalytic efficiency of polymer-Au nanocomposite was compared with that of PVP-stabilised AuNPs (Au@PVP) having the same average AuNPs size (Figure 4.18b). Both catalysts could achieve full conversion within 2 h at 0.1 mol % of catalysts (Table 4.4, entry 2 and 3). However, by decreasing the catalyst concentrations, Au@PVP exhibited lower catalytic efficiency compared to polymer-Au nanocomposite. When the catalyst equivalent was 0.01 mol%, the yields were 21.0% for Au@PVP and 32.7% for polymer-Au nanocomposite (Table 4.4, entry 8 and 9). The polymer-Au nanocomposite affords a higher turnover frequency (TOF) value of $1.64 \times 10^3 \, h^{-1}$, compared to $1.05 \times 10^3 \, h^{-1}$ of Au@PVP (calculated by the 0.01 mol% total Au atoms at 2 h). Generally, the catalytic efficiency of polymer-Au nanocomposite is higher than AuNPs. The reason for this phenomenon is that PVP can dampen the catalytic activity by blocking active sites (*e.g.*, edges, corners, and terraces) (Figure 4.9b).[9, 42] For polymer-Au nanocomposite (Figure 4.9a), only a very small amount of PVP was added, and the AuNPs were embedded on the hydrophilic block of polymeric nano-spheres, leaving the relatively larger area of "naked" Au surface thus more accessible active sites. The immobilisation of AuNPs on the hydrophilic chains also allows good contact with reactants in the aqueous medium.

Table 4.4 Aerial oxidation reaction of 1-phenylethanol to acetophenone using Au catalyst

Entry	Catalyst	Catalyst eq. (mol %)[a]	NMR yield (%)
1	Non	-	10.8
2	Au@PVP	0.1	>99
3	Polymer-Au nanocomposite	0.1	>99
4	Au@PVP	0.05	92.6
5	Polymer-Au nanocomposite	0.05	98.2
6	Au@PVP	0.02	71.4
7	Polymer-Au nanocomposite	0.02	76.9
8	Au@PVP	0.01	21.0
9	Polymer-Au nanocomposite	0.01	32.7

[a] Catalyst eq. (mol %) = [catalyst]/[1-phenylethanol] × 100%

Figure 4.18 TEM images of (a) polymer-Au nanocomposite and (b) Au@PVP with approximate same AuNPs size; (c) polymer-Pd nanocomposite and (d) Pd@PVP with approximate same PdNPs size.

Another significant aspect of the nanocomposite catalyst is the reusability. Therefore, the performance of reused nanocomposite was also studied, and the data is presented in Figure 4.19, the polymer-Au composite maintained its well stability and dispersity after separation. In addition, the composite was reused without a notable loss of catalytic activity with near full conversion in the first four batches and good yield in the fifth batch (Figure 4.19, 4.20).
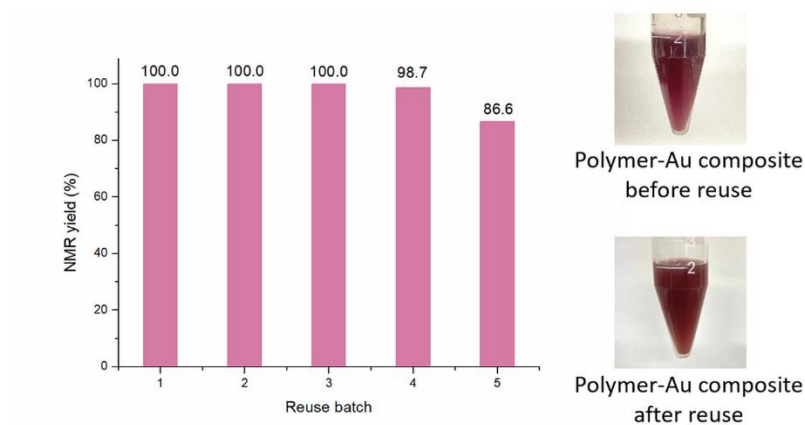
Figure 4.19 Reusability of polymer-Au nanocomposite in aerobic oxidation of 1-phenylethanol and digital photo of polymer-Au nanocomposite before and after reuse.
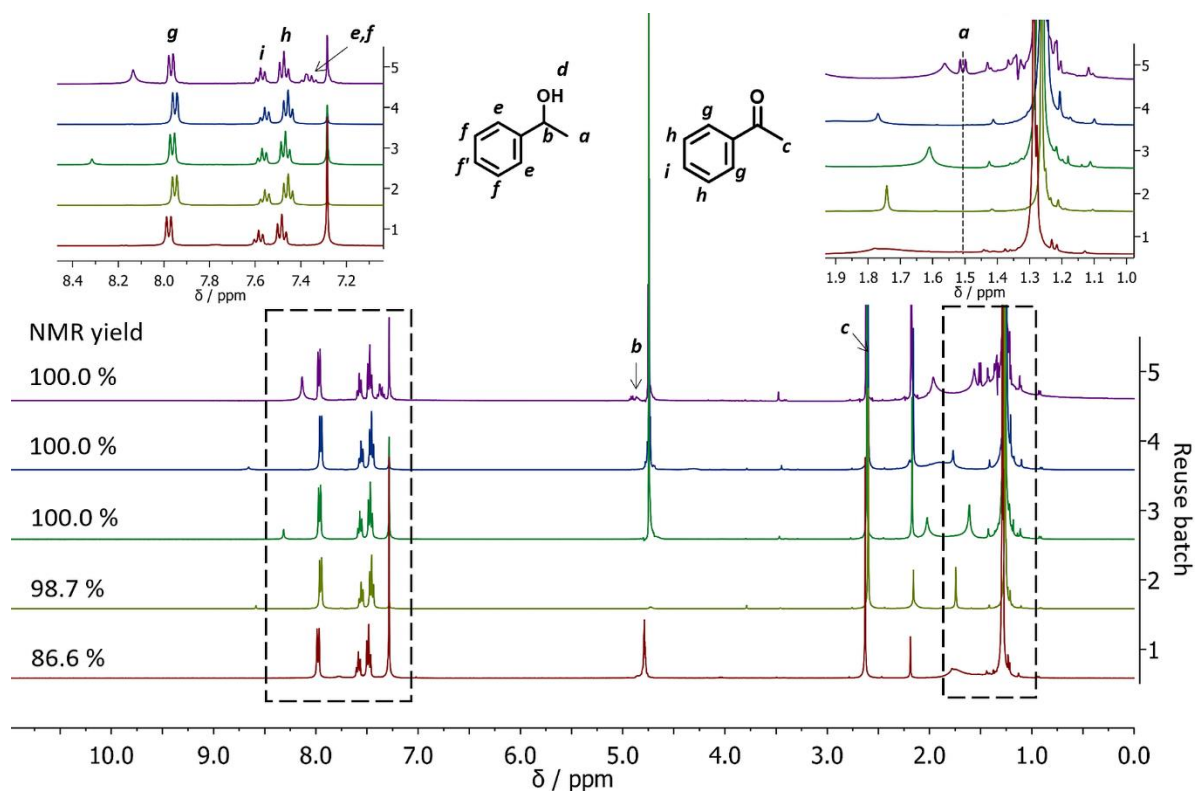
Figure 4.20 ¹H NMR spectra of five reuse batches of aerobic oxidation.

4.3.3 *In situ* synthesis of polymer-Pd nanocomposite

The presence of tertiary amine (TA) groups in the shell of polymer nanoparticles also allows the immobilisation of Pd nanoparticles (PdNPs) through the coordination between the amino groups with Pd ions and subsequent reduction by ultrasound generated reducing species. The successful immobilisation of PdNPs on polymer matrix was confirmed by TEM, UV-Vis spectroscopy and SAED. Specifically, the TEM images (Figure 4.21a, b) reveal that PdNPs with size of 1-4 nm (TA: Pd =1:7) and 3-5 nm (TA: Pd =1:20) were uniformly dispersed on the shell layer of the polymeric nanoparticles. In addition, the UV-Vis spectra (Figure 4.21c) show the absorption band at 420 nm corresponding to Pd^{+2} ions disappeared after sonication, indicating that Pd(II) has been completely reduced to Pd(0). Furthermore, HRTEM image (Figure 4.21b inset) of a PdNP shows the lattice spacing for the (111) planes is measured to be 2.25 Å (measurement in Figure 4.12b). The SAED pattern (Figure 4.21d) of the nanocomposites exhibits concentric rings, corresponding to the (111), (200), (220), and (311) crystal planes of the face-centred-cubic structure of Pd, which further demonstrate the presence of PdNPs.
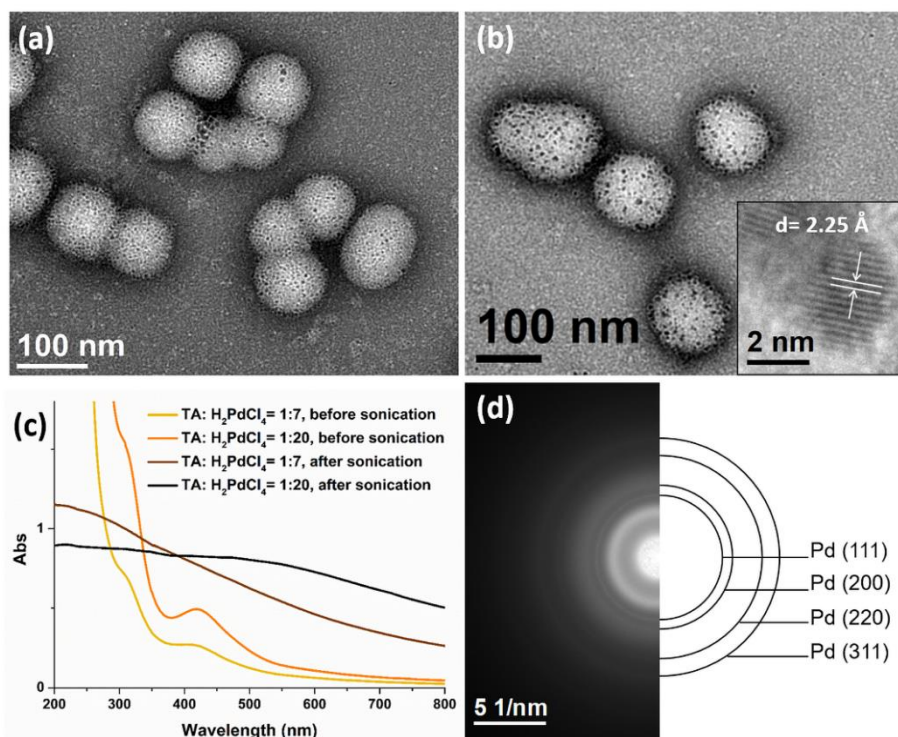
Figure 4.21 TEM images of Pd@PEG$_{113}$-*b*-PDMAEMA$_{24}$-*b*-PHPMA$_{1170}$ nanocomposites with TA: Pd ratio of (a) 1:7 and (b) 1:20 (c) UV-vis spectra of palladium nanocomposite before and after sonication. (d) The selected area electron diffraction pattern of the nanocomposites.

Pd(0) catalysts have been broadly utilised in Suzuki–Miyaura cross-coupling reaction, which is the C–C bond formation between aryl halides and aryl boronic acids, and is a powerful tool in organic syntheses.[43] Recently, many studies have synthesised new types of Pd catalysts, including Pd with different ligands, Pd immobilised on MOFs and other new matrices, which received good catalytic efficiency.[44-47] Herein, the polymer-Pd nanocomposite (Pd@PEG$_{113}$-*b*-PDMAEMA$_{24}$-*b*-PHPMA$_{1170}$, TA: Pd = 1:7) catalysed Suzuki-Miyaura cross-coupling of 4-iodophenol and phenylboronic acid was examined and compared with commercial palladium on activated carbon (Pd/C) and Pd@PVP (Figure 4.18d). In the absence of any Pd catalysts, the coupling reaction could only proceed with 8.5% yield (Table 4.5, entry 1) in 1 hr. All Pd catalysts were found to exhibit excellent efficiency, with almost complete conversions achieved at catalyst concentrations above 0.18 mol% (Table 4.5, entry 2-4). Because of the high efficiency of Pd catalysts, the concentration of catalysts was reduced step by step to compare their catalytic efficiency at a lower dosage. As shown in Table 4.5, the efficiency of Pd@PVP

and polymer-Pd nanocomposite remained at excellent levels, achieving a nearly complete conversion even when the concentration was reduced to 0.04 mol% (Table 4.5, entry 6, 7, 9, 10). In contrast, the yield decreased to 44.8% for Pd/C at the catalyst concentration of 0.09 mol% (Table 4.5, entry 5), and it further reduced to 12.5% (Table 4.5, entry 8), which is close to the control group without any Pd catalyst, at the catalyst concentration of 0.04 mol%.

Polymer-Pd nanocomposite and Pd@PVP could achieve high conversions even at catalyst concentration as low as 0.01 mol% (100 ppm, Table 4.5, entry 13, 14). Therefore, to compare the catalytic efficiency of polymer-Pd nanocomposite and Pd@PVP at extremely low concentrations, the reactions were conducted with 100 ppm and 40 ppm of corresponding catalysts, and the kinetics were monitored by NMR analysis with periodic sampling. As shown in Figure 4.22, the efficiency performances of both catalysts were very close at the concentration of 100 ppm. Nevertheless, polymer-Pd nanocomposite was more efficient than Pd@PVP at the concentration of 40 ppm, it has a higher TOF value of 4.3×10^4 h^{-1}, compared to 2.5×10^4 h^{-1} of Pd@PVP (calculated by the 0.004 mol% total Pd atoms at 10 min). Notably, the polymer-Pd nanocomposite still achieved a yield of 33.6 % within 1h at 20 ppm (Table 4.5, entry 18) compared to the 21.5% yield of Pd@PVP at the same condition (Table 4.5, entry 17). Overall, the catalytic efficiency of the immobilised Pd nanocatalyst was verified to be higher than Pd/C and Pd@PVP in this 4-iodophenol and phenylboronic acid Suzuki-Miyaura cross-coupling reaction. This can be explained by the same rationales as discussed for polymer-Au nanocomposite. On the other hand, the catalytic activity of polymer-Pd nanocomposite gradually decreased after several reuse tests (Figure 4.23, 4.24). The yield decreased from 98.8 to 82.1 % after 5 times, however, the yields is still within acceptable range for practical application.

Table 4.5 Summary of Suzuki–Miyaura Cross Coupling Reaction Using different types of Pd catalysts.
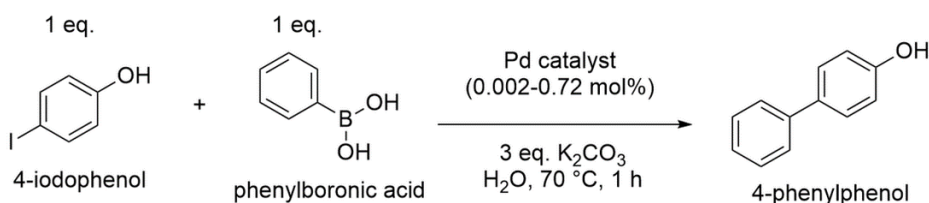
Entry	Catalyst	Catalyst eq. (mol %)[a]	NMR yield (%)[b]
1	Non	-	8.5
2	Pd/C	0.18-0.72	>99
3	Pd@PVP	0.18-0.72	>99
4	polymer-Pd nanocomposite	0.18-0.72	>99
5	Pd/C	0.09	44.8
6	Pd@PVP	0.09	>99
7	polymer-Pd nanocomposite	0.09	>99
8	Pd/C	0.04	12.5
9	Pd@PVP	0.04	>99
10	polymer-Pd nanocomposite	0.04	>99
11	Pd@PVP	0.02	96.8
12	polymer-Pd nanocomposite	0.02	97.4
13	Pd@PVP	0.01	92.6
14	polymer-Pd nanocomposite	0.01	93.8
15	Pd@PVP	0.004 (40 ppm)	51.5
16	polymer-Pd nanocomposite	0.004 (40 ppm)	65.8
17	Pd@PVP	0.002 (20 ppm)	21.5
18	polymer-Pd nanocomposite	0.002 (20 ppm)	33.6

[a] Catalyst eq. (mol %) = [catalyst]/[4-iodophenol] × 100%, [b] Yield was calculated by comparing the NMR spectrum of reaction, detailed calculation equation was listed in Figure 4.25.
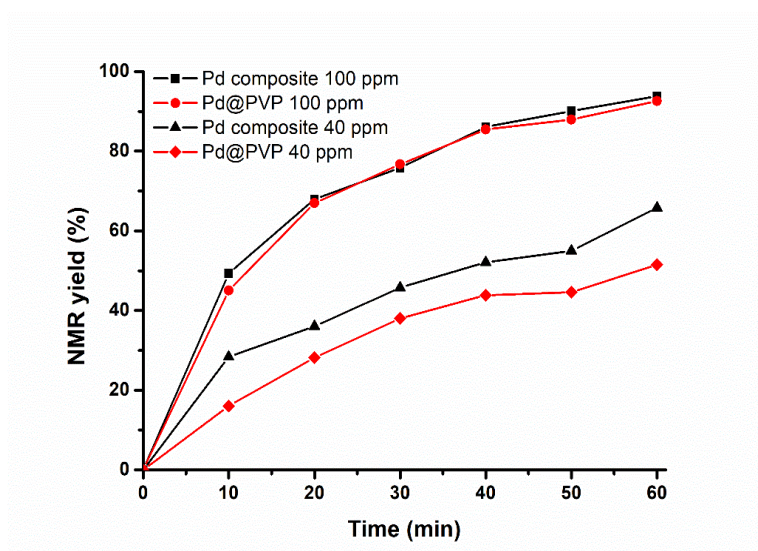
Figure 4.22 Time-dependent NMR yield of 4-phenylphenol in the Suzuki–Miyaura Coupling catalysed by polymer-Pd nanocomposite and Pd@PVP.
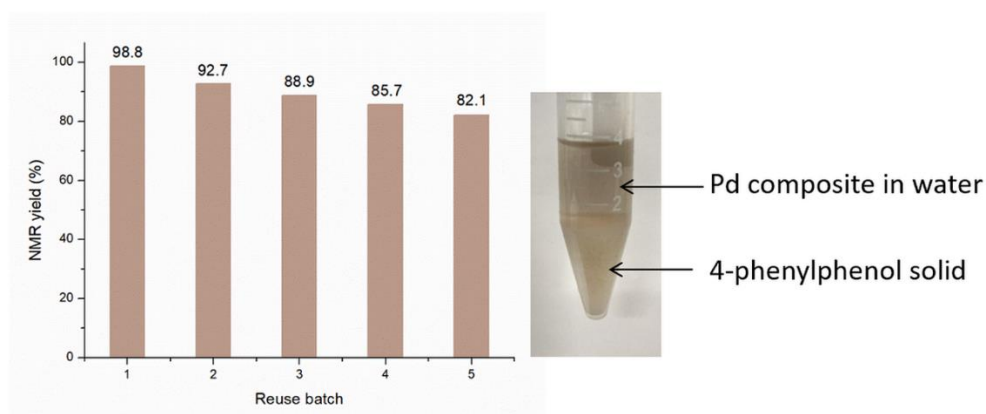
Figure 4.23 Reusability of polymer-Pd nanocomposite in Suzuki coupling reaction and digital photo of separation of polymer-Pd nanocomposite from reaction.
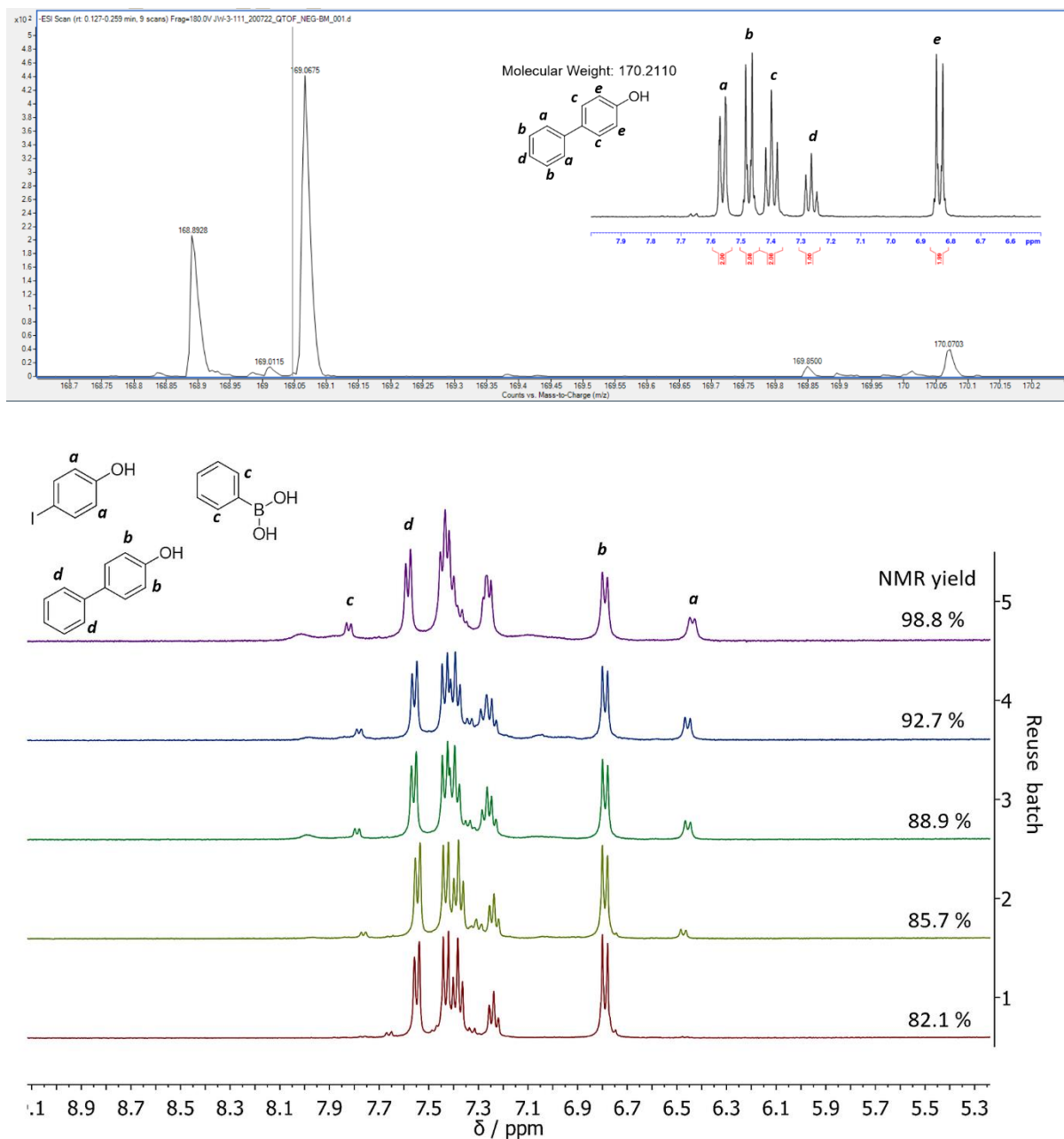
144

Figure 4.24 (top) Mass spectrum and ^{1}H NMR spectrum (400 MHz, CDCl$_3$) of 4-phenylphenol.

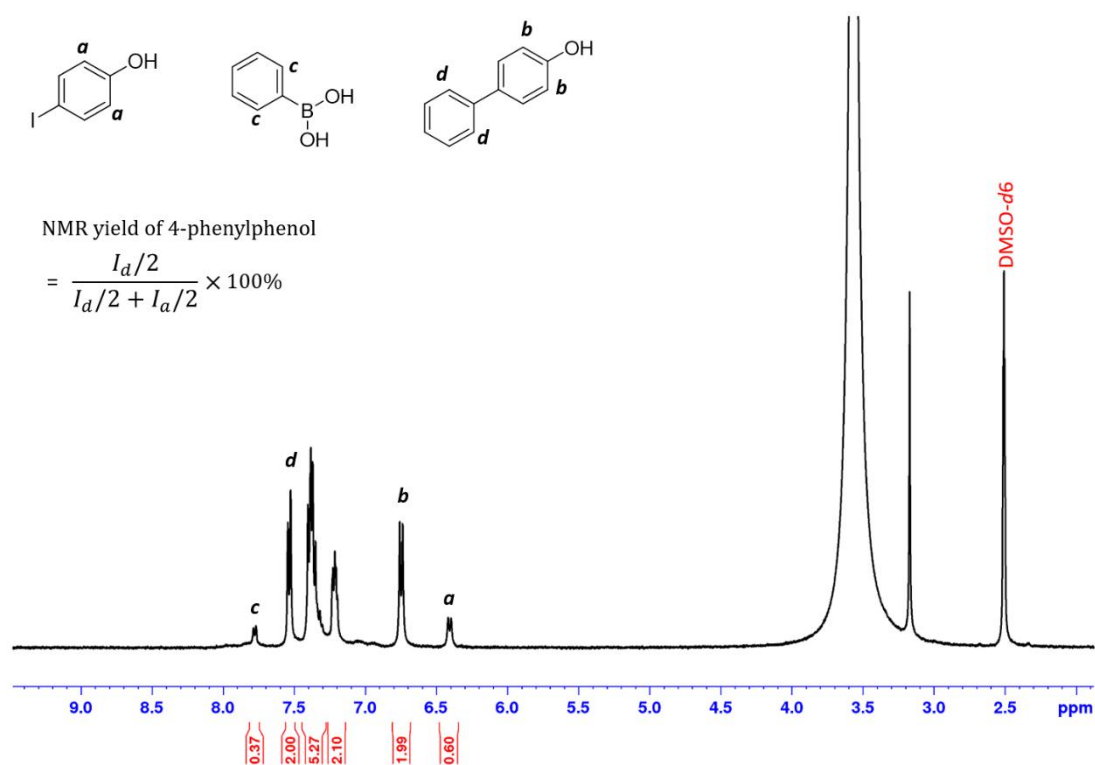(bottom)^{1}H NMR spectra of five reuse batches of Suzuki coupling reaction.

Figure 4.25 ^{1}H NMR spectrum (400 MHz, CDCl$_3$) of Suzuki coupling solution and calculation of NMR yield.

4.4 Conclusions

It was demonstrated that polymer-metal nanocomposites could be prepared by utilising ultrasound as initiation and reducing sources for the synthesis of polymer and metal nanoparticles, respectively. The use of sono-PISA provides an effective *in situ* self-assembly strategy for the scalable preparation of copolymer nano-spheres PEG$_{113}$-*b*-PDMAEMA$_{24}$-*b*-PHPMA$_n$. It was also shown that the sizes of the polymeric nano-spheres can be easily modified by increasing the DP of the PHPMA block. In addition, using ultrasound as the reducing source, it is possible to prepare polymer-Au and polymer-Pd nanocomposites with AuNPs and PdNPs being immobilised on the hydrophilic shell of the polymer matrix. It was found that the size of metal nanoparticles is closely related to the ratio of tertiary amine groups in the polymer matrix to metal atoms. These polymer-metal nanocomposite materials are particularly attractive as nano-catalysts, and the catalytic applications of both polymer-Au and polymer-

Pd nanocomposites were demonstrated for the aerobic oxidation of alcohol and Suzuki-Miyaura cross-coupling reactions, respectively. Meanwhile, these metal nanocomposites exhibit superior catalytic efficiency than PVP-stabilised metal nanoparticles or commercially available Pd/C. Furthermore, it was also demonstrated that the sizes of AuNPs on the polymer matrix could be further grown incrementally to afford potential applications such as SERS substrate. Overall, this study should open many new prospects for the field of polymer-metal nanocomposite due to the "green" nature of sonochemistry and scalable feature of the PISA process. Future work will involve the *in situ* formation of metal nanoparticles on the stabilising macro-RAFT agent by ultrasound followed by sono-PISA process, or even a "one-pot" synthesis of polymer-metal composites by forming metal nanoparticles and sono-PISA in the same reaction flask.

4.5 References

1. O. S. Muddineti, B. Ghosh and S. Biswas, *Int. J. Pharm.*, 2015, **484**, 252-267.
2. M. Han, X. Gao, J. Z. Su and S. Nie, *Nat. Biotechnol.*, 2001, **19**, 631-635.
3. I. V. Kityk, J. Ebothé, I. Fuks-Janczarek, A. A. Umar, K. Kobayashi, M. Oyama and B. Sahraoui, *Nanotechnology*, 2005, **16**, 1687-1692.
4. Y. Liu, B. Fan, Q. Shi, D. Dong, S. Gong, B. Zhu, R. Fu, S. H. Thang and W. Cheng, *ACS Nano*, 2019, **13**, 6760-6769.
5. D. M. Vriezema, M. Comellas Aragonès, J. A. A. W. Elemans, J. J. L. M. Cornelissen, A. E. Rowan and R. J. M. Nolte, *Chem. Rev.*, 2005, **105**, 1445-1490.
6. P. Shi, C. Gao, X. He, P. Sun and W. Zhang, *Macromolecules*, 2015, **48**, 1380-1389.
7. S. Ogasawara and S. Kato, *J. Am. Chem. Soc.*, 2010, **132**, 4608-4613.
8. P. N. Eyimegwu, J. A. Lartey and J.-H. Kim, *ACS Appl. Nano Mater.*, 2019, **2**, 6057-6066.
9. W. Jang, J. Yun, L. Ludwig, S. G. Jang, J. Y. Bae, H. Byun and J.-H. Kim, *Front. Chem.*, 2020, **8**, 834.
10. Y. Li, A. E. Smith, B. S. Lokitz and C. L. McCormick, *Macromolecules*, 2007, **40**, 8524-8526.
11. P. Lim Soo and A. Eisenberg, *J. Polym. Sci., Part B: Polym. Phys.*, 2004, **42**, 923-938.
12. Z. Deng and S. Liu, *Polymer*, 2020, **207**, 122914.
13. B. Fan, R. E. Yardley, J. F. Trant, A. Borecki and E. R. Gillies, *Polym. Chem.*, 2018, **9**, 2601-2610.
14. B. Fan, J. F. Trant, G. Hemery, O. Sandre and E. R. Gillies, *Chem. Commun.*, 2017, **53**, 12068-12071.
15. J. F. Trant, N. Jain, D. M. Mazzuca, J. T. McIntosh, B. Fan, S. M. Haeryfar, S. Lecommandoux and E. R. Gillies, *Nanoscale*, 2016, **8**, 17694-17704.
16. B. Fan, J. Wan, J. Zhai, X. Chen and S. H. Thang, *ACS Nano*, 2021, **15**, 4688-4698.
17. B. Fan, Y. Liu, J. Wan, S. Crawford and S. H. Thang, *ACS Mater. Lett.*, 2020, **2**, 492-498.
18. Y. Zhang, P. Filipczak, G. He, G. Nowaczyk, L. Witczak, W. Raj, M. Kozanecki, K. Matyjaszewski and J. Pietrasik, *Polymer*, 2017, **129**, 144-150.
19. Y. Zhang, Z. Wang, K. Matyjaszewski and J. Pietrasik, *Eur. Polym. J.*, 2019, **110**, 49-55.
20. R. Bleach, B. Karagoz, S. M. Prakash, T. P. Davis and C. Boyer, *ACS Macro Lett.*, 2014, **3**, 591-596.
21. J. Wan, B. Fan, Y. Liu, T. Hsia, K. Qin, T. Junkers, B. M. Teo and S. H. Thang, *Polym. Chem.*, 2020, **11**, 3564-3572.

22. R. A. Caruso, M. Ashokkumar and F. Grieser, *Langmuir*, 2002, **18**, 7831-7836.
23. K. Okitsu, M. Ashokkumar and F. Grieser, *J. Phys. Chem. B*, 2005, **109**, 20673-20675.
24. K. Okitsu, A. Yue, S. Tanabe, H. Matsumoto and Y. Yobiko, *Langmuir*, 2001, **17**, 7717-7720.
25. S. A. Yeung, R. Hobson, S. Biggs and F. Grieser, *J. Chem. Soc., Chem. Commun.*, 1993, **4**, 378-379.
26. Y. Mizukoshi, K. Okitsu, Y. Maeda, T. A. Yamamoto, R. Oshima and Y. Nagata, *J. Phys. Chem. B*, 1997, **101**, 7033-7037.
27. B. Fan, J. Wan, A. McKay, Z. Qu and S. H. Thang, *Polym. Chem.*, 2020, **11**, 5649-5658.
28. J. Chiefari, Y. K. Chong, F. Ercole, J. Krstina, J. Jeffery, T. P. T. Le, R. T. A. Mayadunne, G. F. Meijs, C. L. Moad, G. Moad, E. Rizzardo and S. H. Thang, *Macromolecules*, 1998, **31**, 5559-5562.
29. B. Fan and E. R. Gillies, *Mol. Pharmaceutics*, 2017, **14**, 2548-2559.
30. N. J. W. Penfold, J. Yeow, C. Boyer and S. P. Armes, *ACS Macro Lett.*, 2019, **8**, 1029-1054.
31. J. D. S. Newman and G. J. Blanchard, *Langmuir*, 2006, **22**, 5882-5887.
32. J. Hu, G. Zhang, Z. Ge and S. Liu, *Prog. Polym. Sci.*, 2014, **39**, 1096-1143.
33. S. Luo, J. Xu, Y. Zhang, S. Liu and C. Wu, *J. Phys. Chem. B*, 2005, **109**, 22159-22166.
34. J.-J. Yuan, A. Schmid, S. P. Armes and A. L. Lewis, *Langmuir*, 2006, **22**, 11022-11027.
35. G. Zhao, X. Ran, X. Zhou, X. Tan, H. Lei, X. Xie, L. Yang and G. Du, *ACS Sustainable Chem. Eng.*, 2018, **6**, 3938-3947.
36. X. Tan, Y. Fan, S. Wang, Y. Wu, W. Shi, T. Huang and G. Zhao, *Electrochim. Acta*, 2020, **335**, 135706.
37. W. Haiss, N. T. K. Thanh, J. Aveyard and D. G. Fernig, *Anal. Chem.*, 2007, **79**, 4215-4221.
38. K. R. Brown and M. J. Natan, *Langmuir*, 1998, **14**, 726-728.
39. K. R. Brown, D. G. Walter and M. J. Natan, *Chem. Mater.*, 2000, **12**, 306-313.
40. K. J. Si, D. Sikdar, L. W. Yap, J. K. K. Foo, P. Guo, Q. Shi, M. Premaratne and W. Cheng, *Adv. Opt. Mater.*, 2015, **3**, 1710-1717.
41. H. Tsunoyama, H. Sakurai, Y. Negishi and T. Tsukuda, *J. Am. Chem. Soc.*, 2005, **127**, 9374-9375.
42. K. M. Koczkur, S. Mourdikoudis, L. Polavarapu and S. E. Skrabalak, *Dalton Trans.*, 2015, **44**, 17883-17905.
43. S. E. Hooshmand, B. Heidari, R. Sedghi and R. S. Varma, *Green Chem.*, 2019, **21**, 381-405.
44. R. Martin and S. L. Buchwald, *Acc. Chem. Res.*, 2008, **41**, 1461-1473.
45. B. Yuan, Y. Pan, Y. Li, B. Yin and H. Jiang, *Angew. Chem. Int. Ed.*, 2010, **49**, 4054-4058.
46. W. Dong, L. Zhang, C. Wang, C. Feng, N. Shang, S. Gao and C. Wang, *RSC Adv.*, 2016, **6**, 37118-37123.
47. M. W. Easson, J. H. Jordan, J. M. Bland, D. J. Hinchliffe and B. D. Condon, *ACS Appl. Nano Mater.*, 2020, **3**, 6304-6309.

Chapter 5

Polymerisation-Induced Hierarchical Self-Assembly: From Monomer to Complex Colloidal Molecules and Beyond

5.1 Introduction

Biological systems feature sophisticated levels of hierarchical structures, as exemplified by proteins, enzymes and DNA, which govern the precise functions of life. This phenomenon has inspired researchers to design and fabricate artificial nanomaterials with complex structures through bottom-up hierarchical self-assembly for the applications of electronics, photonics and sensors.[1-9] In the past decade, a myriad of hierarchical nanostructures composed of various building blocks, both organic and inorganic ones, have been achieved through the interactions, such as electrostatic attraction,[10] DNA hybridisation,[11] ligand reaction,[4, 12] hydrogen bonding[13] and hydrophobic interactions.[14-17] Polymer assemblies represent one class of soft colloidal particles. Currently, a series of polymer nanostructures,[18, 19] including micelle,[20, 21] worm, vesicle,[22] lamellae,[23] tecto(dendrimers),[24, 25] cubosome[26-28] and hexosome[29] have been realised *via* solution self-assembly of diblock copolymers. However, for more complex nanostructures, such as hierarchical polymer colloids, requires the rational design of polymer structures contain three or more blocks with distinct physical properties.[30-32] For example, Müller and co-workers showed that by synthesising linear triblock terpolymers with properly designed length ratios of the blocks, a wide range of compartmentalised morphologies could be achieved, such as spheres, cylinders, sheets, and vesicles, all equipped with a variety of patch morphologies.[33-35] In addition, they demonstrated the application of these nanoscale structures to be soft colloidal building blocks that can be further self-assembled on a higher-level complexity. Nevertheless, conventional self-assembly of block copolymers involves synthesis and self-assembly in separate steps, and the latter step is usually achieved under low concentration (*e.g.* 0.1-1.0 wt %), which poses difficulties for large-scale applications.[36]

Polymerisation-induced self-assembly (PISA) has been exploited as a robust and scalable technique for the preparation of diblock copolymers nanomaterials with different morphologies at high solid contents (up to 40-50 wt %).[37-49] More importantly, PISA technique can achieve the chemical synthesis and self-assembly in one step without further purification, especially for these prepared in the aqueous environment. However, it has been demonstrated that the utilisation of PISA for the fabrication of complex patchy particles composed of triblock terpolymers was extremely challenging in the aqueous medium, mainly because of the limited monomers that are suitable for this process.[50, 51] The existing examples all require the utilisation of PISA-suitable monomers, which are soluble in water, whereas the formed polymer should be hydrophobic for *in situ* self-assembly.[52, 53] Water-immiscible monomers like styrene[54] and *tert*-butyl acrylate[55] commonly generate kinetically trapped spheres. This tremendously limits the diversity of formulations involving water-immiscible monomers when preparing anisotropic or hierarchical colloids *via* the PISA process.

Fortunately, some seminal works have demonstrated the possibility of utilising cyclodextrin (CD) to convert hydrophobic monomers into water-soluble complexes over the past decades. For example, Ritter *et al.* conducted an extensive investigation on the polymerisation of CD/monomer "guest-host" complexes,[56-62] and reported the synthesis of amphiphilic block copolymer by reversible addition-fragmentation chain-transfer (RAFT) polymerisation of CD/monomer complex in water.[63] Yuan *et al.* reported the direct dispersion polymerisation of CD/styrene complex to form different nano-objects including nanotubes and dumbbell-like micelles.[50] However, no effort has been devoted to synthesise triblock terpolymer-based hierarchical structures by PISA through the formation of CD complex. The achievement of this research will not only solve the problems such as multi-step synthesises and low particle concentration of conventional solution self-assembly process, but also provide various soft colloidal building blocks for further self-assembly into higher-order nanostructures.

Herein, we demonstrate a promising strategy for the scalable preparation of ABC linear triblock terpolymer-based nanomaterials through RAFT-PISA of CD/hydrophobic monomer complex in the aqueous environment. Methylated-β-cyclodextrin (MβCD) was complexed with hydrophobic monomer to make a homogeneous aqueous solution by "host-guest" inclusion. The RAFT dispersion polymerisation of the MβCD/monomer complex was performed with a poly(ethylene glycol) (PEG)

macromolecular chain transfer agent (macro-CTA) to form colloidal seeds. The diblock colloidal seeds were further chain extended by dispersion polymerisation of another MβCD/monomer complex to produce triblock colloids *in situ*. With the rational selection of monomers, including styrene (st), *tert*-butyl acrylate (*t*BA), *tert*-butyl methacrylate (*t*BMA), a series of triblock terpolymers, such as poly(ethylene glycol)-*b*-polystyrene-*b*-poly(*tert*-butyl acrylate) (PEG-*b*-PS-*b*-P*t*BA), poly(ethylene glycol)-*b*-poly(*tert*-butyl acrylate)-*b*-polystyrene (PEG-*b*-P*t*BA-*b*-PS) and poly(ethylene glycol)-*b*-poly(*tert*-butyl methacrylate)-*b*-polystyrene (PEG-*b*-P*t*BMA-*b*-PS) were successfully synthesised. Because of the distinct physical compatibilities, interfacial tensions and glass transition temperatures (T_g) of each block, the aqueous PISAs resulted in diverse particle morphologies, including anisotropic "Janus" particles and corresponding colloidal molecules (CMs) with different valence bonds, core-shell-corona micelles and raspberry-like micelles. This facile strategy realised a sequential one-pot synthesis of anisotropic colloids by PISA utilising water-immiscible monomers, which provides the possibility for large-scale production of CMs or other hierarchical structures. As a result, it can be readily applied to different block copolymer formulations to enrich the complexity in morphologies and functions of *in situ* hierarchically self-assembled nano-objects.

5.2 Materials and Methods

5.2.1 Materials

Diisopropyl carbodiimide (DIC; >99%) was purchased from Oakwood Chemical (USA). 4-Dimethylaminopyridine (DMAP; 99%) was purchased from Alfa Aesar. 4-Cyano-4 (((dodecylthio) carbonothioyl) thio) pentanoic acid (CDTPA; 97%) was purchased from Boron Molecular (Australia). Randomly methylated-β-cyclodextrin (MβCD, M_n ~1300 g/mol, average degree of substitution = 11.8, 98%, Zhiyuan Biotech, China) was used as received. Poly(ethylene glycol) methyl ether (mPEG$_{113}$, average M_n 5,000 g/mol; mPEG$_{45}$, average M_n 2,000 g/mol), *tert*-butyl methacrylate (*t*BMA), *tert*-butyl acrylate (*t*BA) and styrene (st) were purchased from Sigma Aldrich (Australia). 4,4'-Azobis(4-cyanopentanoic acid) (ACVA) was purchased from Wako Pure Chemical Industries, Ltd. Deionised (DI) water was obtained from Milli-Q system (Millipore). All the other solvents were obtained from commercial sources and were used as received unless noted otherwise.

5.2.2 Methods

5.2.2.1 Preparation of PEG_{113}-CDTPA and PEG_{45}-CDTPA macro-CTA agents

The synthesis of PEG$_{113}$-RAFT (PEG$_{113}$-CDTPA) was performed using the same procedure described in section 3.2.2.[38] The esterification reaction between mPEG$_{113}$ and CDTPA resulted in pale-yellow polymer (PEG$_{113}$-RAFT) was analysed by ^{1}H NMR spectroscopy and GPC. ^{1}H NMR (400 MHz, CDCl$_3$): δ 4.25 (t, 2H), 3.45-3.81 (m, 452H), 3.37 (s, 3H), 3.31 (t, 2H), 2.37-2.65 (m, 4H), 1.86 (s, 3H), 1.68 (m, 2H), 1.25-1.38 (b, 18H), 0.87 (t, 3H). ^{13}C NMR (150 MHz, CDCl$_3$): δ 216.8, 171.3, 118.9, 71.8, 70.4, 68.8, 64.0, 58.9, 46.2, 33.7, 31.8, 29.2, 24.7, 22.6, 14.0.

For the synthesis of PEG$_{45}$-CDTPA, same synthesis procedure was used only by replacing mPEG$_{113}$ with mPEG$_{45}$. The polymer was purified by dialysis against acetone: methanol co-solvent (1:1 v/v) using 1 kDa MWCO membrane. ^{1}H NMR (400 MHz, CDCl$_3$): δ 4.25 (t, 2H), 3.45-3.81 (m, 180H), 3.37 (s, 3H), 3.32 (t, 2H), 2.37-2.65 (m, 4H), 1.87 (s, 3H), 1.69 (m, 2H), 1.25-1.39 (b, 18H), 0.88 (t, 3H).

5.2.2.2 Typical synthesis of PEG-b-PS colloidal atoms

A typical protocol for the preparation of PEG$_{113}$-*b*-PS (targeting DP = 100): PEG$_{113}$-CDTPA (102.4 mg, 0.0190 mmol) and MβCD (2470 mg, 1.90 mmol) were dissolved in 7.23 mL DI H$_2$O, then st (197.6 mg, 1.90 mmol) was added, the solid content was maintained at 3 wt %. The mixture was then sonicated for 10 min and stirred vigorously for 30 min at room temperature to obtain a homogeneous MβCD/st solution. ACVA (1.6 mg, 0.0057 mmol, ACVA/CTA=0.3) was then added. The solution was deoxygenated by 3 cycles of freeze-vacuum-thaw and immersed into a 70 °C oil bath for 16 h. The solution was then cooled to room temperature and exposed to air. For kinetic study, the solution was purged with argon for 15 min, sealed and immersed into a 70 °C oil bath. Aliquots of solution were collected at specific time point for analysis. ^{1}H NMR spectra of the dried crude suspension was obtained using CDCl$_3$ as solvent. PEG-*b*-P*t*BA, PEG-*b*-P*t*BMA diblock copolymers were synthesised using the same procedure.

5.2.2.3 Typical synthesis of PEG -b-PS-b-PtBA colloidal molecules

A typical protocol for the preparation of PEG$_{113}$-b-PS$_{100}$-b-PtBA (targeting DP=250): 991.4 mg of PEG$_{113}$-b-PS$_{100}$ suspension (3 wt %, containing 1.88×10^{-3} mmol of PEG$_{113}$-b-PS$_{100}$ and 0.188 mmol MβCD), tBA (60.3 mg, 0.470 mmol) and MβCD (366.6 mg, 0.282 mmol) were mixed with 1.58 mL DI H$_2$O to make a 3 wt % solid content suspension. The mixture was then sonicated for 10 min and stirred for 30 min to obtain a homogeneous suspension, and ACVA (26 μL of 6 mg ACVA/mL methanol solution, ACVA/CTA=0.3) was added. The suspension was deoxygenated by 3 cycles of freeze-vacuum-thaw, and immersed into a 70 °C oil bath for 16h. The suspension was then cooled to room temperature and exposed to air. Kinetic study was conducted using the same procedure as PEG-b-PS. PEG-b-PtBA-b-PS, PEG-b-PtBMA-b-PS triblock terpolymers were synthesised using the same procedure.

5.2.2.4 Synthesis of PEG-b-PS-b-PtBA from PEG-b-PS seeds via emulsion polymerisation

The preparation of PEG$_{113}$-b-PS$_{100}$-b-PtBA (targeting DP=200): 2 mL of PEG$_{113}$-b-PS$_{100}$ suspension (3 wt %) was dialysed against DI H$_2$O using 3.5 kDa MWCO membrane for two days to remove MβCD, 5 mL (1.2 wt %) suspension was obtained after dialysis. ^{1}H NMR results confirmed almost all MβCD was removed. Then, 1908.3 mg of dialysed PEG$_{113}$-b-PS$_{100}$ suspension (1.2 wt %, containing 22.9 mg, 1.45×10^{-3} mmol of PEG$_{113}$-b-PS$_{100}$), tBA (37.1 mg, 0.29 mmol) were mixed with 54.6 μL DI H$_2$O to make a 3 wt % solid content suspension. The mixture was then sonicated for 10 min and stirred for 30 min to obtain a cloudy homogeneous suspension that no tBA droplets were visible, and ACVA (25 μL of 6 mg ACVA/mL methanol solution, ACVA/CTA=0.3) was added. The suspension was deoxygenated by 3 cycles of freeze-vacuum-thaw, and immersed into a 70 °C oil bath for 16 h. The suspension was then cooled to room temperature and exposed to air.

5.2.2.5 Synthesis of PEG-b-PtBMA via PISA of MβCD/tBMA complex with various ratio

Synthesis of PEG$_{113}$-b-PtBMA (targeting DP = 100): PEG$_{113}$-CDTPA (24.8 mg, 4.6×10^{-3} mmol) and various amount of MβCD (0 mg for 0:1 MβCD/tBMA ratio, 119.2 mg – 1:5, 298 mg – 1:2, 596 mg – 1:1) were dissolved in 2.91 mL DI H$_2$O (amount varying with MβCD to maintain polymer solid content at 3 wt %), then tBMA (65.2 mg, 0.46 mmol) was added. The mixture was then sonicated for 10 min and stirred vigorously for 30 min at room temperature to obtain homogeneous MβCD/tBMA solution and

turbid tBMA emulsions. ACVA (0.4 mg, 1.4×10^{-3} mmol, ACVA/CTA=0.3, 67 μL of 6 mg/mL methanol solution) was then added. The solution was deoxygenated by 3 cycles of freeze-vacuum-thaw and immersed into a 70 °C oil bath for 16 h. The solution was then cooled to room temperature and exposed to air. Synthesis of PEG$_{45}$-b-PtBMA (targeting DP = 50) were conducted using the same procedure by replacing PEG$_{45}$-CDTPA and adjusting the amount of reagents accordingly. The groups with 1:1 MβCD/tBMA were dialysed against DI H$_2$O using 3.5 kDa MWCO membrane for two days to remove MβCD. All suspensions were analysed by ^{1}H NMR, GPC, DLS and TEM (summarised in Figure 5.5-5.7 and Table 5.1).

5.2.3 Characterisation

Transmission electron microscopy (TEM). The images were taken using an FEI Tecnai G2 T20 TWIN TEM instrument equipped with Orius SCD200D wide-angle CCD camera operating at 200 keV. Copper grids (formvar/carbon coated, 400 mesh) were plasma glow-discharged for 10 seconds to create a hydrophilic surface. After glow discharge, the grid was contacted with a drop (about 15 μL) of 0.10 % w/v aqueous dispersions containing the diblock copolymer nano-objects for 3 min. Excess sample solution was removed by blotting, and the residual was left on the grid to dry completely. The negative staining process was done by allowing 3 μL of uranyl acetate solution (2.0 % w/v) to stay on the grid for 1 min, then blotted and dried. Ruthenium tetroxide vapor staining: mix freshly prepared 25 μL RuCl$_3$ solution ($\sim$ 4 % w/v) and 25 μL NaClO solution (10-15 % w/v), place the solution and grids in a sealed container at ambient temperature for overnight.

Scanning electron microscopy (SEM). The SEM sample was prepared by casting a drop (about 10 μL) of 0.10% w/v aqueous dispersions containing the diblock copolymer nano-objects on a silicon wafer. The dispersion was then dried using a gentle nitrogen blow. The sample was then coated with a thin layer ($\sim$2 nm) of iridium to make it conductive. Imaging was performed using an FEI Magellan 400 FEGSEM instrument operating at 5.0 kV.

Atomic force microscopy-infrared spectroscopy (AFM-IR). The AFM-IR sample was prepared by casting a drop (about 10 μL) of 0.10% w/v aqueous dispersions on a silicon wafer, and studied using Bruker NanoIR3 system. AFM scanning was performed at 0.3 Hz line scan rate with 100-150 pixel

density on each edge using the non-contact tapping mode probes capable of IR mapping (Model: PR-EX-TnIR-A-10). IR spectra within the range of 790-1850 cm^{-1} were taken on the nanoparticles with 100 % laser power, 3 % duty cycle, and 2429 pt IR focus spot.

Dynamic light scattering (DLS) measurements were performed at 25 °C using Malvern Zetasizer Nano ZS. The aqueous dispersions containing the diblock copolymer nano-objects were diluted to 0.10 % w/v by DI water. Light scattering was detected at 90° and hydrodynamic diameters were determined by assuming spherical, non-interacting, perfectly monodisperse particles.

^{1}H Nuclear magnetic resonance (NMR) spectra were recorded on a Bruker Avance 400 NMR spectrometer at frequencies of 400 MHz. NMR chemical shifts (δ) are reported in ppm and were calibrated against residual solvent signals of CDCl$_3$ (δ 7.26) and D$_2$O (δ 4.79). Samples were dissolved in CDCl$_3$ or D$_2$O at 5-10 mg mL^{-1}. The data are reported as chemical shift (δ).

Gel permeation chromatography (GPC) was performed on a system comprising a Shimadzu LC-20AT pump, Shimadzu RID-20A refractive index detector, and SPD-20A UV–visible detector. The GPC is equipped with a guard column (WAT054415) and 3×Waters GPC columns (WAT044238, WAT044226, WAT044235, 300 mm×7.8 mm). The eluent is DMF with 10 mM LiBr and eluted at 1 mL/min for 45 min in total, the column was maintained at 40 °C during elution. The samples were dissolved in DMF with 10 mM LiBr, filtered through 0.20 μm syringe filters. A calibration curve was obtained from poly(methyl methacrylate) (PMMA) standards (Agilent) ranging from 960 to 1,568,000 g mol^{-1}.

Turbidity was performed using Thermo Scientific Orion AQ4500 turbidimeter.

5.3 Results and Discussion

5.3.1 The rational selection of monomers

The hierarchical self-assembly of ABC triblock terpolymers are governed by several factors, including physical compatibility, interfacial energy, T_g, composition orders, *etc.* Therefore, the selection of monomers is extremely important for achieving target morphologies. PEG was chosen as block A as it renders excellent hydrophilicity to stabilising hydrophobic blocks in the aqueous medium. To access

hierarchical structures, the phase separation between block B and C is required. Moreover, the interfacial energies of block B and C with the water molecules also play critical roles in the self-assembly process. When the interfacial tension between block B and solution is higher than that between block C and solution ($\gamma_{BS} > \gamma_{CS}$), CM can be achieved; conversely, raspberry-like micelles will likely be formed.[52] In addition, the T_g of core-forming blocks could impact the chain mobility and thus the morphology transition.[64] By carefully reviewing these factors, st, tBA and tBMA were selected as core-forming monomers. The phase separations between PS (S) and PtBA (T),[65] PS and PtBMA (M)[66] were reported previously (PEG, PS, PtBA, PtBMA are abbreviated to E, S, T, M in next discussion, respectively). The interfacial tension and T_g of these blocks are distinct as well (Figure 5.1), the calculation of interfacial tension was showed in section 5.5.1, Table 5.3).
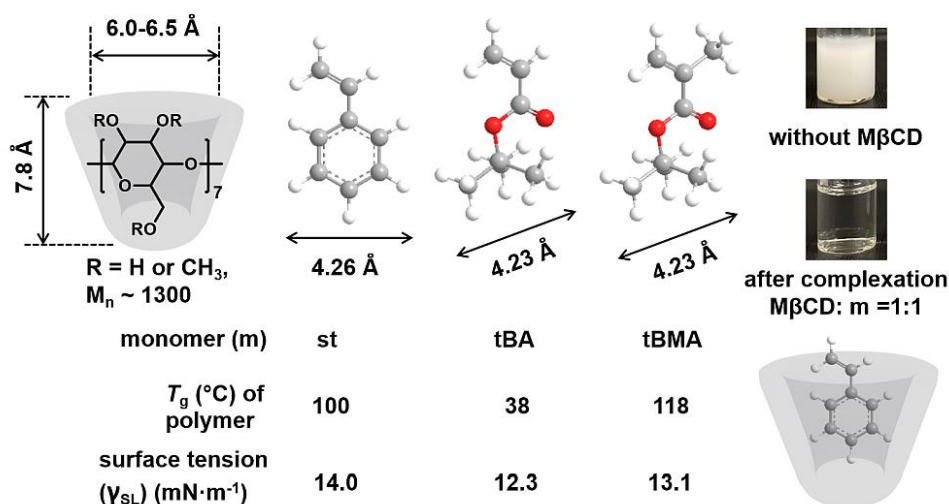
Figure 5.1 Structure of methylated-β-cyclodextrin (MβCD) and chosen monomers forming inclusion complexes with MβCD host.

5.3.2 The "host-guest" complexation between MβCD and monomers

More importantly, due to the proper molecular size and hydrophobic nature of these monomers (Figure 5.1), they can form "host-guest" complexes with MβCD.[50, 67] The complexation between MβCD and tBMA was previously reported by Madison and Long[67] for the purpose of free radical polymerisation in aqueous phase. However, different to the method of direct complexation in water in this study, their complex was prepared by dissolving the tBMA and MβCD in chloroform and the evaporation of solvent.

In this chapter, the complexation between MβCD and *t*BMA was examined by visual appearance and ^{1}H NMR. MβCD and *t*BMA were mixed in D_2O with molar ratio of 1:1, 1:2, 1:5 and 0:1, turbidity and ^{1}H NMR spectrum were obtained after 10 min-sonication. As shown in Figure 5.2, the turbidity of the solution decreased with higher added amount of MβCD, indicated the better solubility of *t*BMA in D_2O. The turbidity of suspension with 1:1 ratio of MβCD: *t*BMA was only 1.06 NTU, which is distinct from the other groups. The ^{1}H NMR spectra (Figure 5.2) support this observation, for the unstable *t*BMA in D_2O emulsion (0:1), most *t*BMA presented in the oil phase. With increased amount of added MβCD, the integration of peaks of *t*BMA in oil phase decreased, whereas those in aqueous phase increased. For MβCD: *t*BMA =1:1, only aqueous *t*BMA peaks were observed. Same experiments were conducted to confirm the complexation between MβCD /st and MβCD/*t*BA as shown in Figure 5.3 and Figure 5.4. It was found the ratio of MβCD: monomer =1:1 is required to make optimum water-soluble complexes
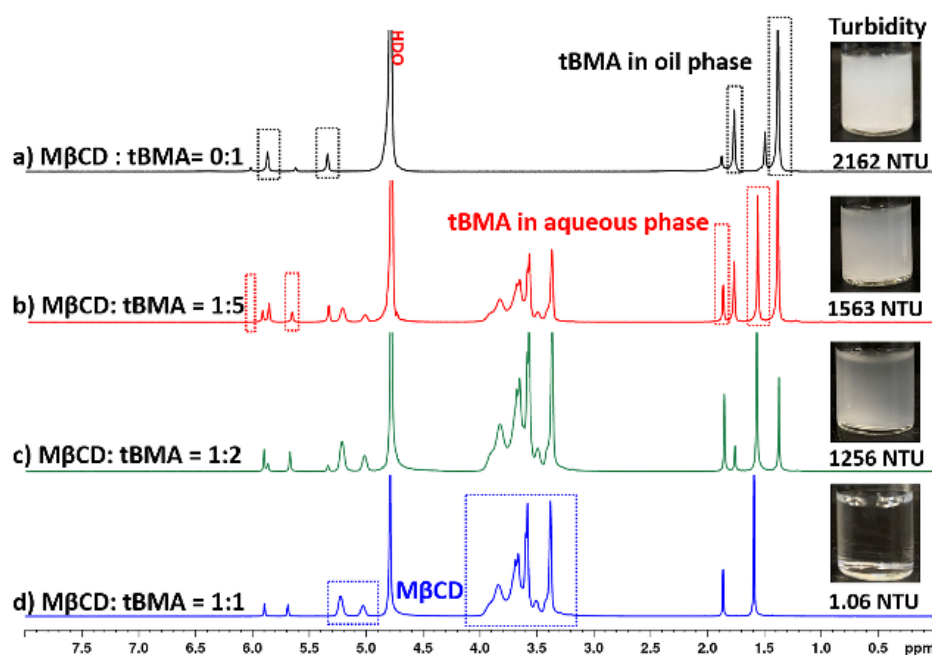
Figure 5.2 ^{1}H NMR spectra (400 MHz, D_2O) and digital photo of MβCD/tBMA in D_2O with MβCD: tBMA molar ratio of (a) 0:1, (b) 1:5, (c) 1:2 and (d) 1:1, the concentrations of tBMA were maintained at 5 mg/mL in D_2O for all analyses.
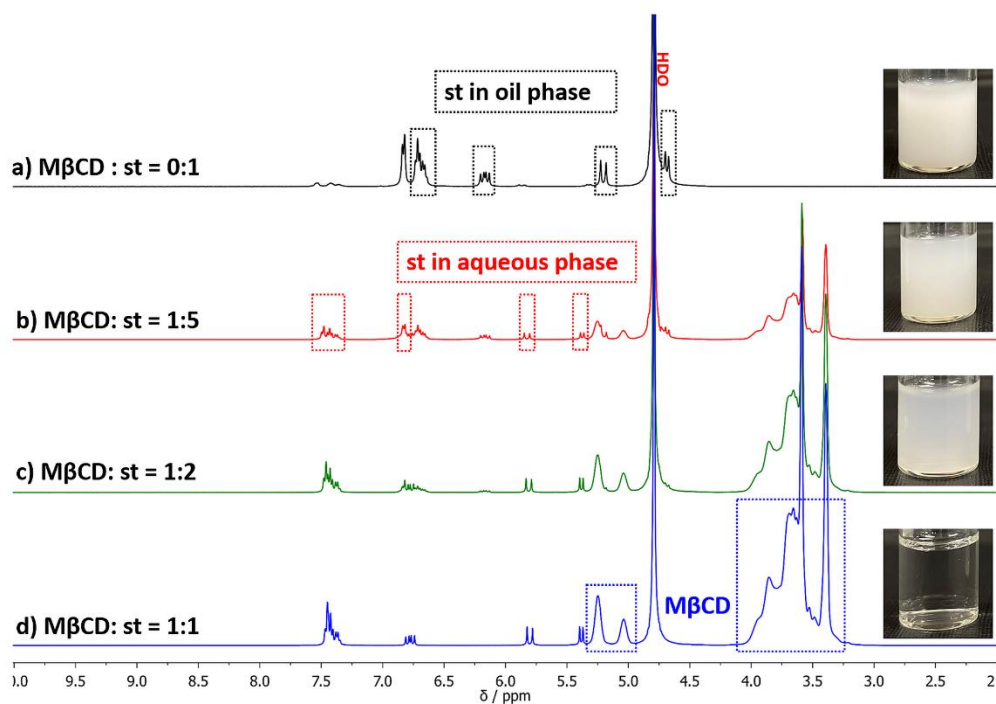
Figure 5.3 ^{1}H NMR spectra (400 MHz, D$_2$O) and digital photo of MβCD/st in D$_2$O with MβCD: st molar ratio of (a) 0:1, (b) 1:5, (c) 1:2 and (d) 1:1 (5 mg st/mL D$_2$O).
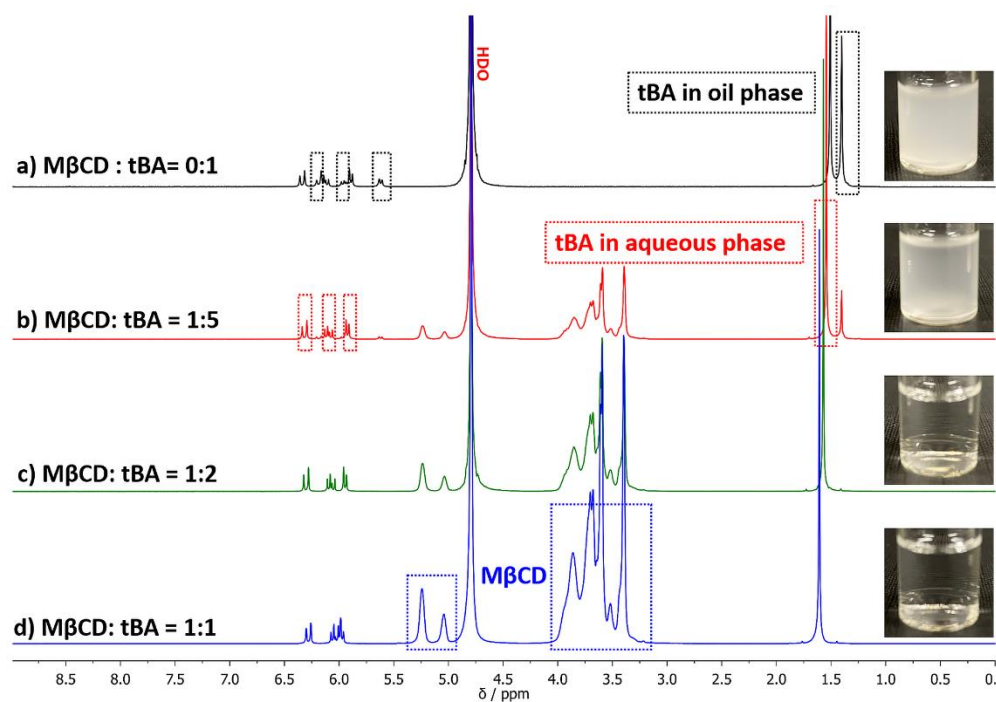
Figure 5.4 ^{1}H NMR spectra (400 MHz, D$_2$O) and digital photo of MβCD/tBA in D$_2$O with MβCD: tBA molar ratio of (a) 0:1, (b) 1:5, (c) 1:2 and (d) 1:1 (5 mg tBA/mL D$_2$O).

In addition, the impact of MβCD: monomer ratio on the PISA process was also systematically studied. This was investigated by dispersion polymerisation of PEG$_{45}$-CDTPA and PEG$_{113}$-CDTPA with tBMA at different ratio of MβCD: tBMA = 0:1, 1:5, 1:2 and 1:1 (target DP 50 and 100 respectively). The suspensions at the end of 16 h were analysed (Table 5.1). The various ratio of MβCD: tBMA did not have obvious impact on the degree of polymerisation and the molecular weight (Figure 5.5). However, the stability of nanoparticles suspension decreased with the reduced amount of MβCD, as judged by observation and DLS (Figure 5.6). For the groups with MβCD: tBMA ratio less than 1:1 (Table 5.1, entry 1-3 and 5-7), PDI is higher than 0.1, which indicated broad size distributions of the suspensions. Some peculiarly large Z$_a$ diameters (Table 5.1, entry 1,2) were obtained due to poor sample quality, which were generated from the agglomeration of the unstable polymer particles in water. The reason for particle instability is that when MβCD is added at a ratio of less than 1:1, tBMA is presented as a water-immiscible monomer instead of a water-soluble complex and undergoes emulsion polymerisation in water. In the early stage of polymerisation, the chemical potential of the monomer droplets is higher than that of the monomer in the first nucleated particles formed by oligomers. As a result, a large amount of the monomer would transfer from the droplets to these particles, leading to a large increase in size and colloidal instability. This phenomenon is known as the superswelling effect.[68] For the group with 1:1 ratio of MβCD: tBMA (Table 5.1, entry 4,8), the majority of tBMA is complexed with MβCD, and thus suppress the transfer of tBMA into particles and result in stable nanoparticles with low PDI. TEM analysis strongly demonstrated the distinct difference between the morphologies of copolymer nanoparticles with different ratio of MβCD: tBMA. The ones with MβCD: tBMA =1:1 were uniform and monodispersed nano-objects as shown in Figure 5.7d and 5.7i, whereas the group with MβCD: tBMA =1:2 (Figure 5.7c, 5.7h), a mixture of different morphologies was found. Mixture and agglomerates were observed for groups with MβCD: tBMA =1:5 and 0:1 (Figure 5.7a, b, f, g). These results demonstrate that MβCD: monomer ratio has an impact on the monomer solubility, which determines whether the process undergoes emulsion or dispersion polymerisation. In order to synthesise stable nanoparticles by dispersion polymerisation, the ratio of MβCD: monomer was maintained at 1:1.

Table 5.1 Characterisation data of PEG-*b*-PtBMA with various molar ratio of MβCD: tBMA.

Entry	MβCD: *t*BMA	DP[a]	$M_{n,NMR}$[b] (kg/mol)	$M_{n,GPC}$ (kg/mol)	Đ	$Z_{a,DLS}$ (nm)	PDI$_{DLS}$
Targeting PEG$_{45}$-*b*-PtBMA$_{50}$							
1	0:1	44	8.7	6.9	1.07	2906	0.23
2	1:5	46	8.9	7.3	1.11	9239	0.78
3	1:2	45	8.8	7.2	1.10	561.8	0.71
4	1:1	46	8.9	7.8	1.12	159.7	0.01
4a	1:1 MβCD dialysed	46	8.9	7.3	1.10	159.8	0.07
Targeting PEG$_{113}$-*b*-PtBMA$_{100}$							
5	0:1	87	17.8	16.2	1.15	109.0	0.40
6	1:5	95	18.9	17.7	1.24	66.7	0.26
7	1:2	94	18.8	17.3	1.17	89.8	0.10
8	1:1	97	19.2	18.0	1.20	93.6	0.02
8a	1:1 MβCD dialysed	97	19.2	17.3	1.21	93.3	0.01

[a] DP of P*t*BMA calculated by ^{1}H NMR.

[b] $M_{n,NMR} = M_{n,\text{ macro-RAFT}} + DP_{PtBMA} \times M_{n,tBMA}$
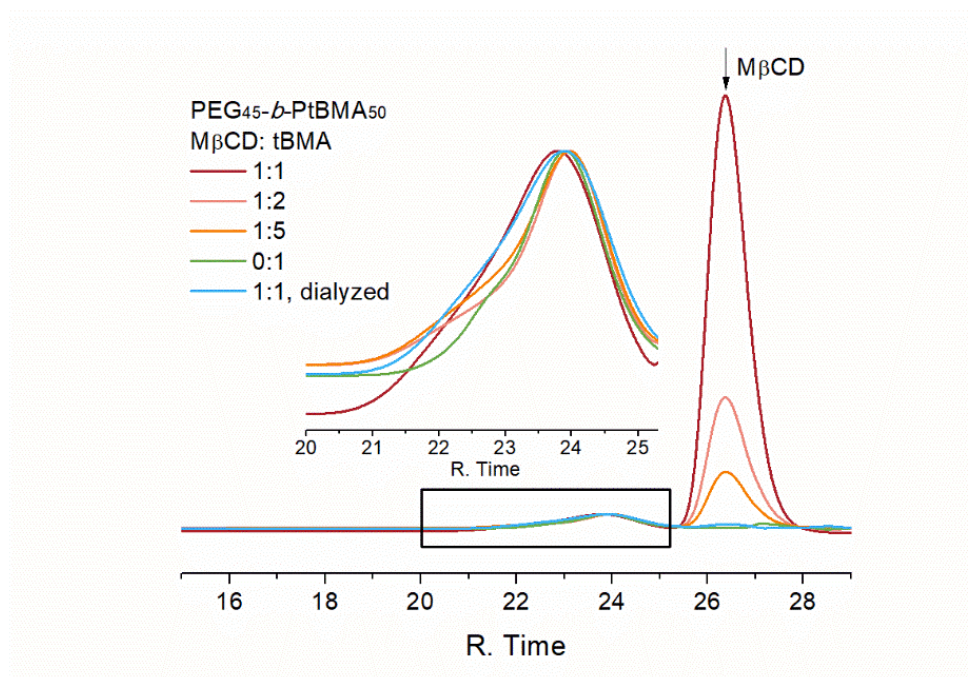
Figure 5.5 GPC traces of synthesised PEG$_{45}$-*b*-PtBMA$_{n}$ (n=44-46) suspension with MβCD: tBMA molar ratio of 0:1, 1:5, 1:2 and 1:1, and 1:1 with MβCD being removed by dialysis (DMF as eluent, PMMA standards).

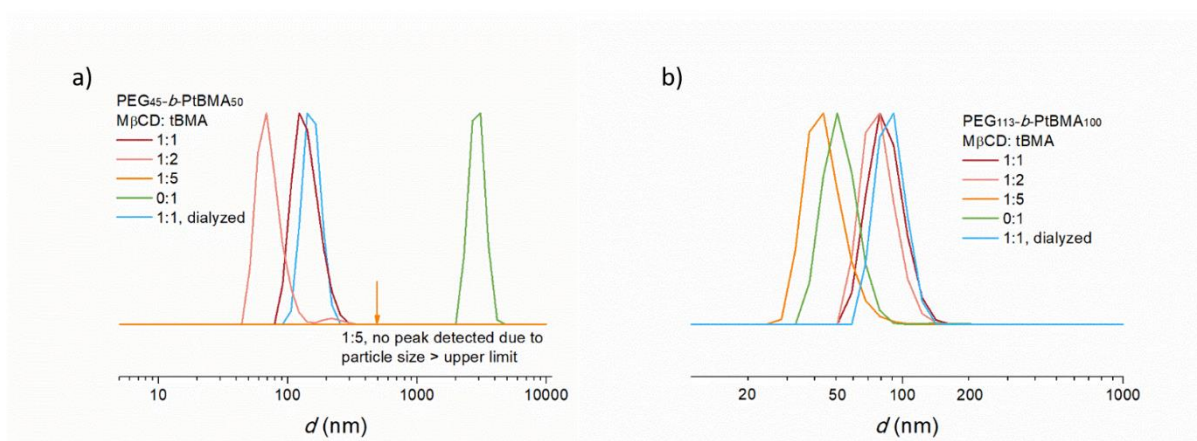Figure 5.6 DLS curves of (a) PEG$_{45}$-*b*-PtBMA$_{50}$ and (b) PEG$_{113}$-*b*-PtBMA$_{100}$ suspension with MβCD: tBMA molar ratio of 0:1, 1:5, 1:2 and 1:1, and 1:1 with MβCD being removed by dialysis.
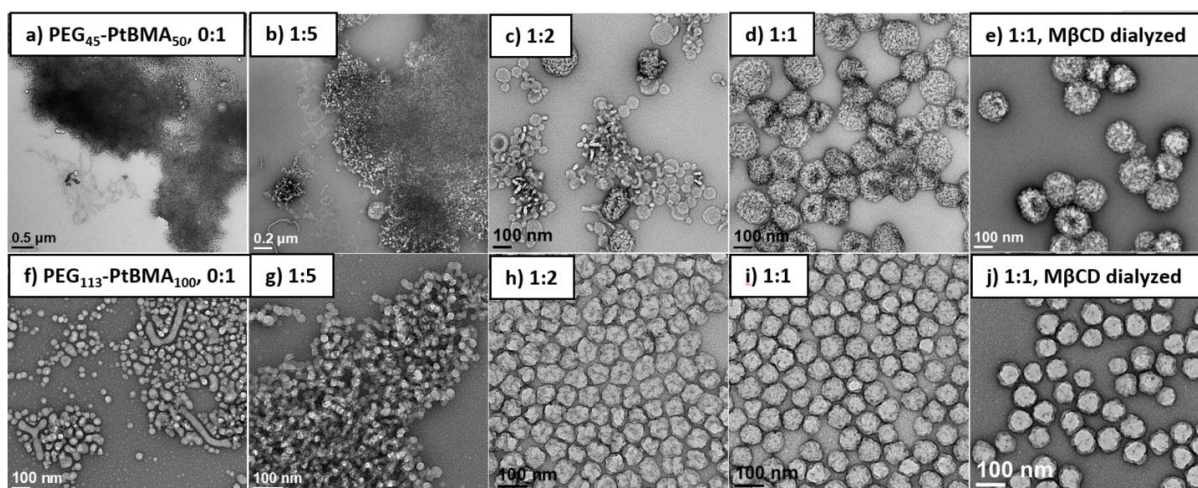

Figure 5.7 Representative TEM images of synthesised (a-e) PEG$_{45}$-*b*-PtBMA$_{50}$ and (f-j) PEG$_{113}$-*b*-PtBMA$_{100}$ with various molar ratio of MβCD: tBMA and after removal of MβCD by dialysis.

After forming polymers, the increased steric hindrance and the strong hydrophobic interaction of neighboring repeating units (*e.g.* aromatic rings and *tert*-butyl moieties) will compete with the interaction of MβCD,[69] which results in the dissociation between MβCD and polymer. The MβCD unthreaded from polymer chains is freely soluble in water and can be removed without changing the morphology of particles (Figure 5.7e and 5.7j). This was examined by removing MβCD from PEG$_{45}$-P*t*BMA$_{46}$ and PEG$_{113}$-P*t*BMA$_{97}$ suspension by dialysis against DI H$_2$O for two days. Almost all MβCD was removed according to ^{1}H NMR spectra (Figure 5.8, 5.9). The DP of PEG-*b*-P*t*BMA polymers remained

the same after dialysis as calculated by NMR, and the molecular weights measured by GPC (Figure 5.5) were almost unchanged as well. As judged by DLS (Table 5.1, entry 4a and 8a), the particles also remained stable after dialysis and were close in size to the particles before dialysis. The morphology of particles remained unchanged as judged by TEM (Figure 5.7e and 5.7j). These results agree with the findings of Yuan *et al.*'s study, in which CD unthreaded from resulted PS chains during polymerisation.[50] The MβCD unthreaded from polymer chains is freely soluble in water and can be removed for reuse. A simpler approach would be to complex free MβCD directly with the monomer of the third block for further polymerisation without removing it, as in this study.
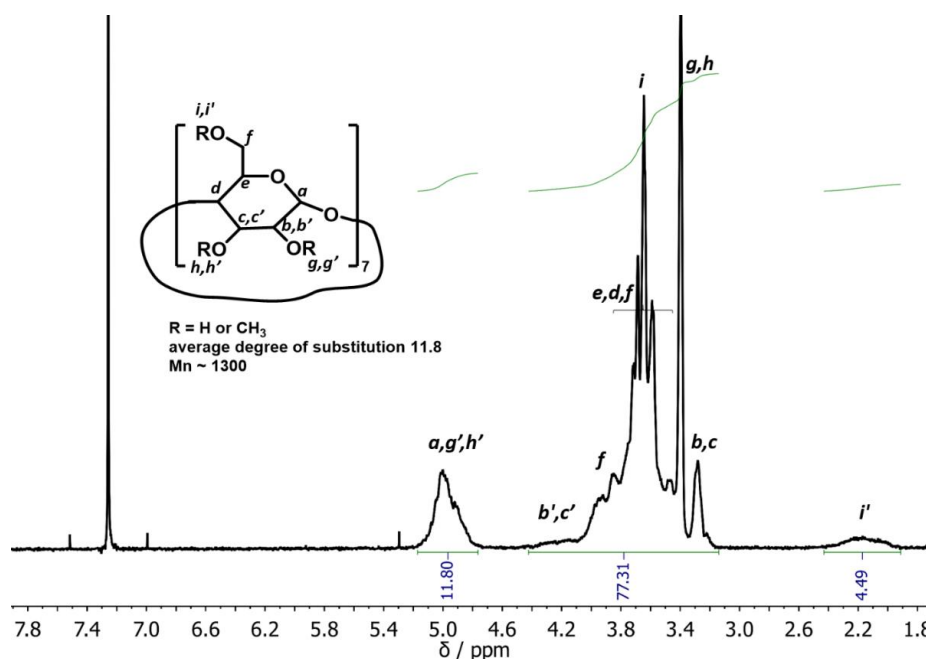
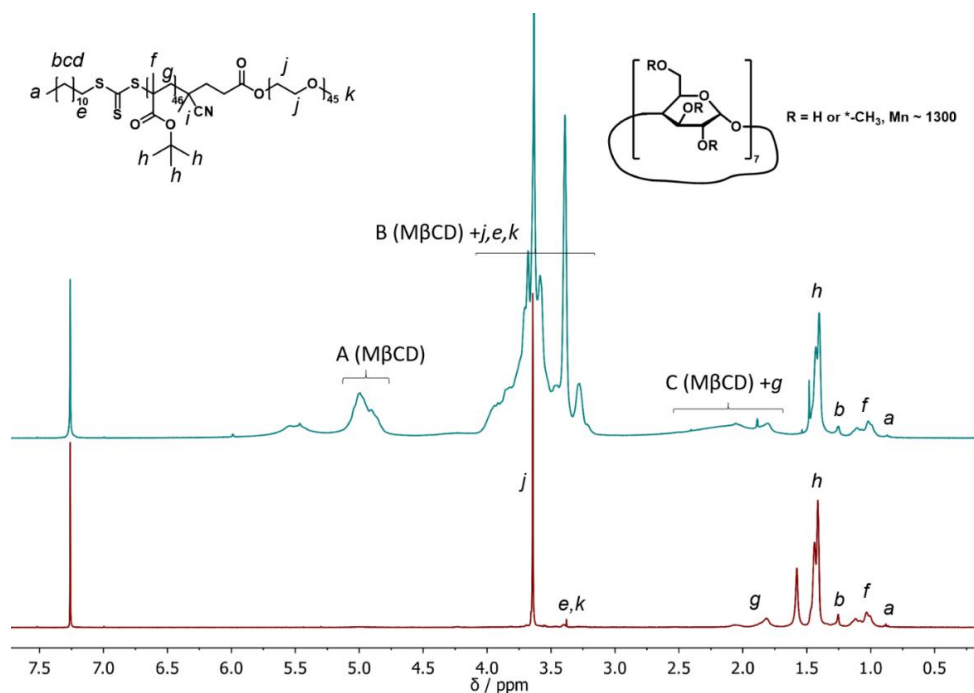Figure 5.8 ^{1}H NMR spectrum (400 MHz, CDCl$_3$) of randomly methylated-β-cyclodextrin.

Figure 5.9 ^{1}H NMR spectra (400 MHz, CDCl$_3$) of PEG$_{45}$-*b*-PtBMA$_{46}$ suspension before (above) and after (below) dialysis. Almost all MβCD were removed after dialysis. Similar result was obtained for the suspension of PEG$_{113}$-*b*-PtBMA$_{97}$ before and after dialysis. DP of PtBMA calculated form crude suspension = (integration of f)/ (integration of A) × [MβCD]/[macro-RAFT] ×11.8 / 3 DP of PtBMA calculated from suspension after dialysis = (integration of f)/ (integration of j) × repeating unit of PEG ×4 /3.

5.3.3 Synthesis of AX$_n$-type colloidal molecules (CMs) comprised of triblock terpolymer PEG-*b*-PS-*b*-P*t*BA (EST)

First, macro-RAFT agent comprised of PEG$_{113}$ and widely used RAFT agent 4-cyano-4-((((dodecylthio)carbonothioyl)thio)pentanoic acid (CDTPA)[70, 71] was synthesised through Steglich esterification. The PEG$_{113}$-CDTPA was then chain-extended with st by dispersion polymerisation of MβCD/st complex (1:1) in water (Scheme 5.1) at 70 °C with 4,4'-azobis(4-cyanopentanoic acid) (ACVA) as initiator. The reaction temperature was selected as it is relatively high to allow good mobility and still below the lower critical solution temperature (LCST) of PEG (LCST > 100 °C).[72] Figure 5.10 shows

the kinetics data of PEG$_{113}$-CDTPA mediated polymerisation of MβCD/st (targeting DP 100, conversion determined by ^{1}H NMR as shown in Figure 5.12), the plot of ln([M]$_0$/[M]) *vs.* time depicts two regimes,
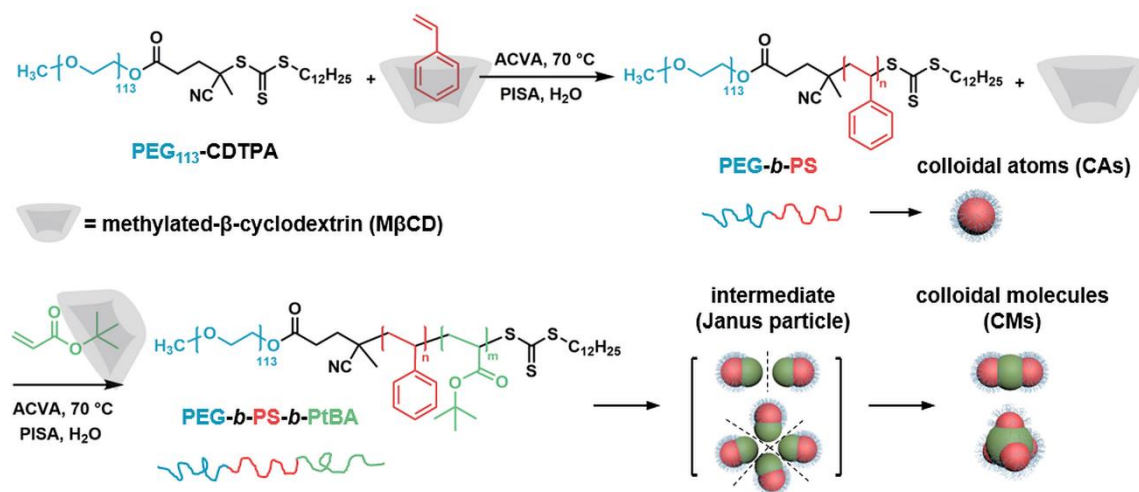
Scheme 5.1 Synthesis of PEG-*b*-PS colloidal atoms and PEG-*b*-PS-*b*-P*t*BA colloidal molecules using MβCD/monomer complex *via* PISA.

which are in agreement with the typical kinetics of PISA process reported previously.[38] The intersection of two kinetics lines indicates the micellar nucleation, at which point the unreacted monomer enters into the core to solvate the hydrophobic polymer chains.[73, 74] The cloudiness of suspension and hydrodynamic diameter as measured by dynamic light scattering (DLS) increased with the conversion (Figure 5.11). The gel permeation chromatography (GPC) traces (Figure 5.13) progressively shifted towards higher retention time, which indicates the increase of molecular weight of the PEG-*b*-PS with the increment of reaction time, and showed a linear relationship with the monomer conversion (Figure 5.10b). Meanwhile, the dispersity (*Đ*) increased slightly with the chain length of polymer (Figure 5.10b), however, remained relatively low (*Đ* <1.2). These characteristics indicate that the dispersion polymerisation proceeded in a well-controlled manner.
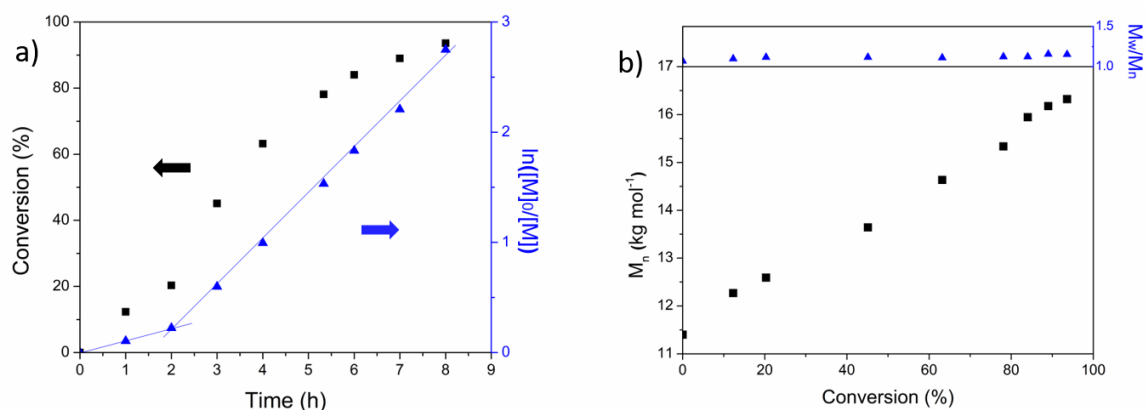
Figure 5.10 (a) ln([M]$_0$/[M]) and conversion *vs.* time and (b) molecular weight and Đ *vs.* conversion plots for the polymerisation of MβCD/st in water at 70 ˚C. (Solid content = 3 wt %, [ACVA]:[PEG$_{113}$-CDTPA]:[st]:[MβCD] = 0.3: 1: 100: 100.)
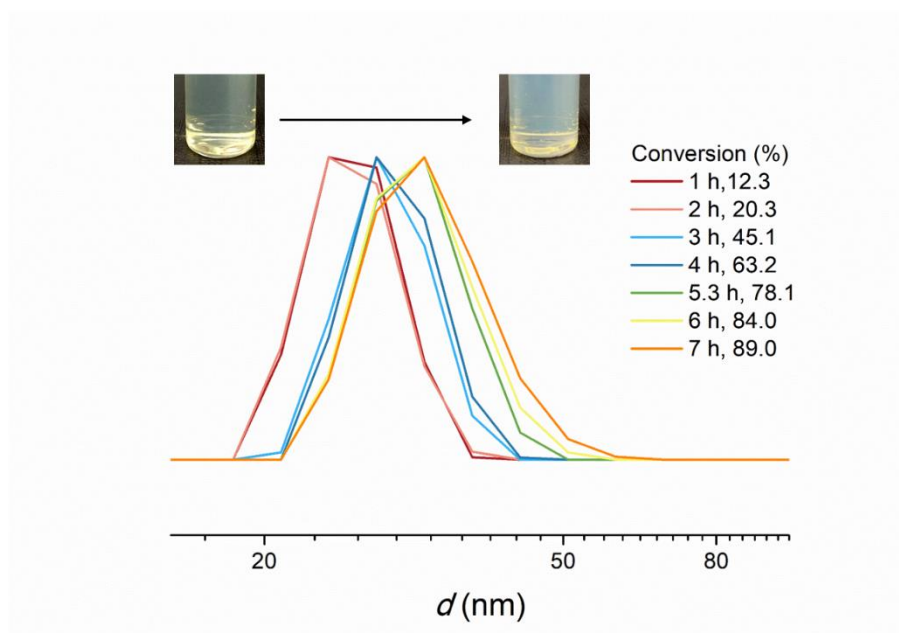

Figure 5.11 DLS curves of suspensions collected at specific time points during dispersion polymerisation of MβCD/st (targeting PEG$_{113}$-*b*-PS$_{100}$) with increasing conversion. Inset photos show the comparison of cloudiness before and after PISA.
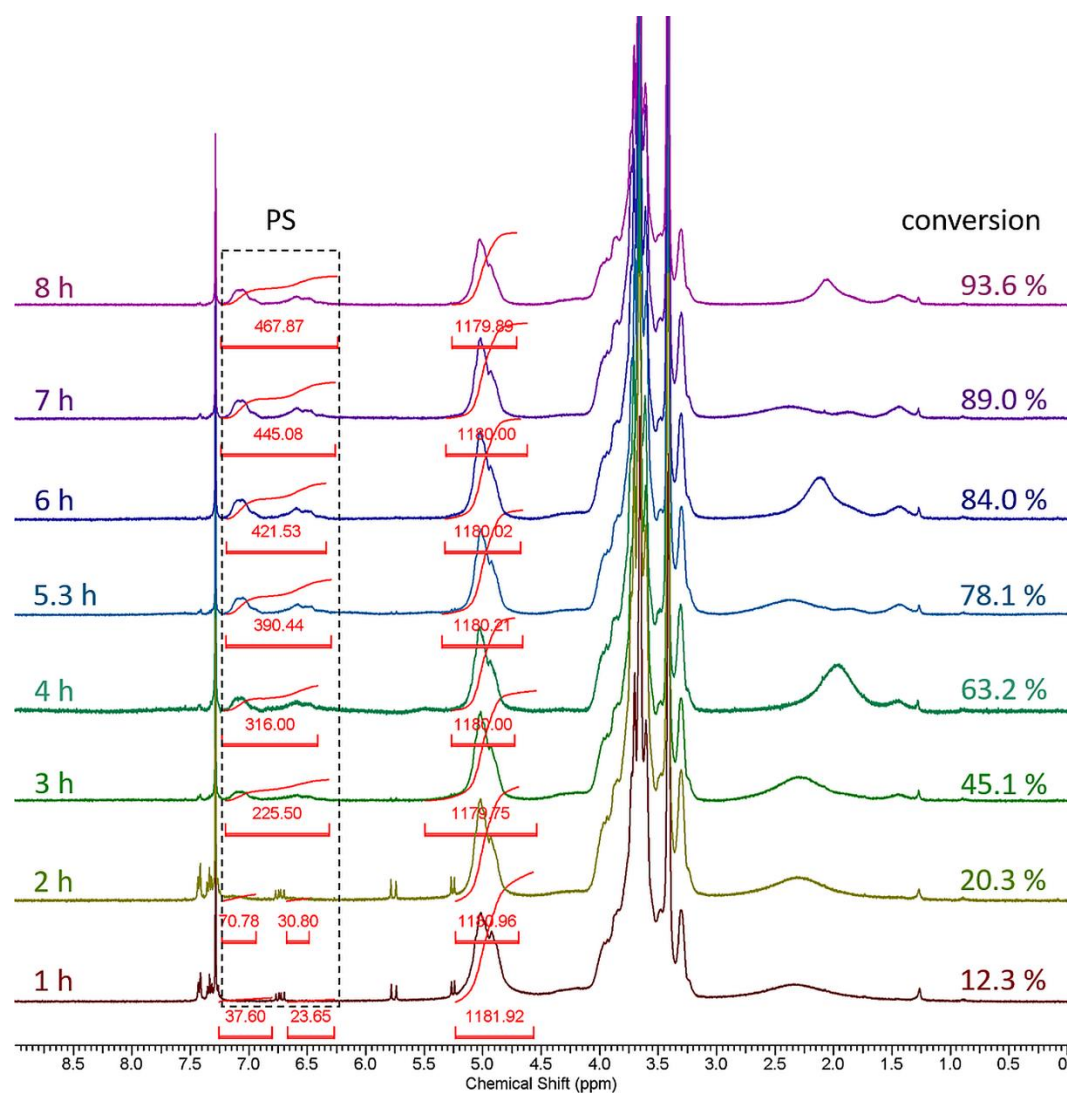
Figure 5.12 ^{1}H NMR spectra (400 MHz, CDCl$_3$) of suspensions collected at specific time points during dispersion polymerisation of MβCD/st (targeting PEG$_{113}$-*b*-PS$_{100}$). DP of PS = [1/5 × integration of PS (7.2-6.3 ppm)]/ [1/(11.8×100) × integration of MβCD (5.3-4.7 ppm)]. Conversion estimated by DP of PS/100×100%.
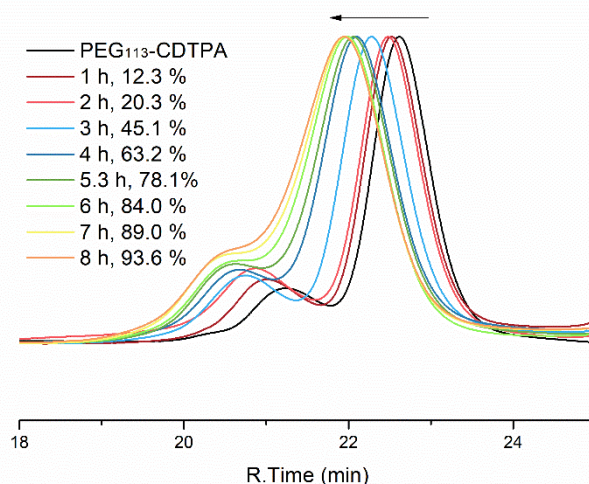
Figure 5.13 GPC traces of PEG$_{113}$-CDTPA and PEG$_{113}$-b-PS$_x$ collected at specific time points during dispersion polymerisation of MβCD/st (targeting PEG$_{113}$-b-PS$_{100}$) (DMF as eluent, PMMA standards). *The bimodal curves are because of the impurity from the commercial PEG$_{113}$.*

For the synthesised colloidal atoms (CAs), TEM image (Figure 5.14a) shows the morphology of PEG$_{113}$-b-PS$_{100}$ (E$_{113}$S$_{100}$) is spherical with an average diameter of 26.4 nm. Next, the further chain extension with PtBA as the third block leads to the increase in hydrodynamic diameter (Figure 5.14b) and transformation of CAs from 26.4 nm spheres to 50~55 nm cylinder-like clusters (Figure 5.14c). The TEM image of PEG$_{113}$-b-PS$_{100}$-b-PtBA$_{80}$ (E$_{113}$S$_{100}$T$_{80}$) (Figure 5.14c) shows three-segment cylinder-like particles with two dark grey segments on each end and a light grey domain in the central part, suggesting the PS domain in both ends and PtBA domain in the core, because PS with aromatic rings appears darker than PtBA under TEM. The width of PS segments (w~ 27 nm) also matching with the average particle diameter of E$_{113}$S$_{100}$ CAs (d ~26.4 nm). To further study this morphology and confirm the composition of E$_{113}$S$_{100}$T$_{80}$ particles, the sample was stained with uranyl acetate (UA) and then ruthenium tetroxide (RuO$_4$). The UA negative staining can reveal the overall morphology, whereas RuO$_4$ can react with PS to enhance electron absorption. The stained TEM image (Figure 5.14d) substantiates that PS domain appears in the peripheral region and PtBA in the central region (UA staining: a 'halo' of stain forms around the particle; RuO$_4$ staining: PS dark grey, PtBA white, PEG not visible). This rarely achieved hierarchical structure was coined as colloidal molecule (CM),[75] and this

specific one resembles the molecular structure of CO_2 with a formulation of X-A-X (or AX_2) (valence number N=2) and a bond angle of 180°. CMs are clusters of particles or CAs that mimic the symmetry of molecular structures and have attracted extensive interest due to their specific properties.[1, 76-78] These CMs could potentially function as building blocks for the direct assembly of complex hierarchically organised materials.[79-81]
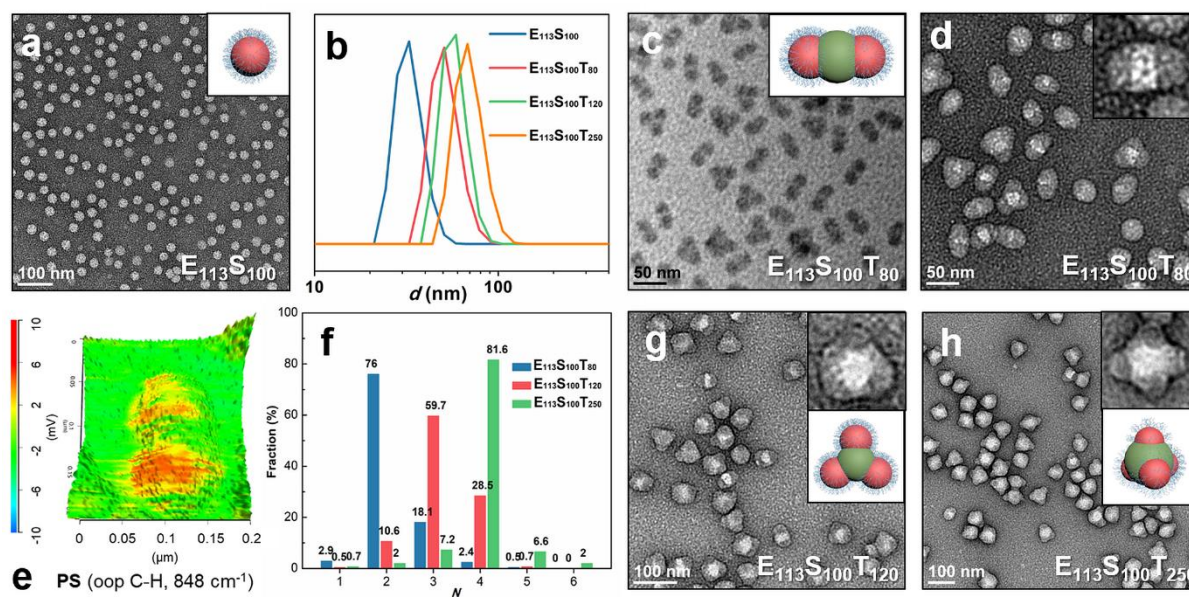

Figure 5.14 Representative TEM images and 3D structures (E-blue, S-red, T-green) of (a) $E_{113}S_{100}$ (UA stained), (c) $E_{113}S_{100}T_{80}$ (unstained), (d, g, h) $E_{113}S_{100}T_x$ (x= 80, 120, 250) (UA-RuO$_4$ stained). (b) DLS profiles of $E_{113}S_{100}T_x$ (x= 0, 80, 120, 250) colloids. (e) AFM-IR 3D overlay of topography and IR maps of $E_{113}S_{100}T_{80}$ obtained at 848 cm^{-1} wavenumbers. (f) Valence number (N) distribution of AX_n-type CMs of $E_{113}S_{100}T_x$ (x= 80, 120, 250), obtained by analysing > 500 random particles by UA-RuO$_4$ stained TEM.

To further confirm the composition of the CMs, atomic force microscopy-infrared spectroscopy (AFM-IR) was employed as an advanced technique to map the nanoparticle component distribution. The AFM-IR spectra of background and nanoparticles were recorded in the range between 1850 and 800 cm^{-1} (Figure 5.15a). Two specific IR regions were selected as fingerprints for PS and PEG/PtBA. The ester and ether C-O stretching at 1044 cm^{-1} resulted from both PtBA and PEG. The out-of-plane (oop) bending of the aromatic C-H bond at 848 cm^{-1} is typical of PS. Subsequently, IR chemical mappings of CM were recorded at the selected 1044 and 848 cm^{-1} wavenumbers, making the distribution of polymer

domains easily distinguishable (Figure 5.14e and Figure 5.15b). The green colour in the 3D topographies indicates no IR absorption and the colour shifts from yellow to red with the increasing of signal. It was found that PS signal (848 cm^{-1}) was detectable on both peripheral sides of CM (Figure 5.14e), which is consistent with the TEM results. Noteworthily, the dimension of the CM estimated by AFM topography is larger than that by TEM because of the lateral broadening of surface protrusions, which results from the AFM imaging artefact due to the tip convolution effect.[82, 83] Overall, the combined TEM images and AFM-IR results verified the successful preparation of AX$_2$-type CMs in analogy to CO$_2$.
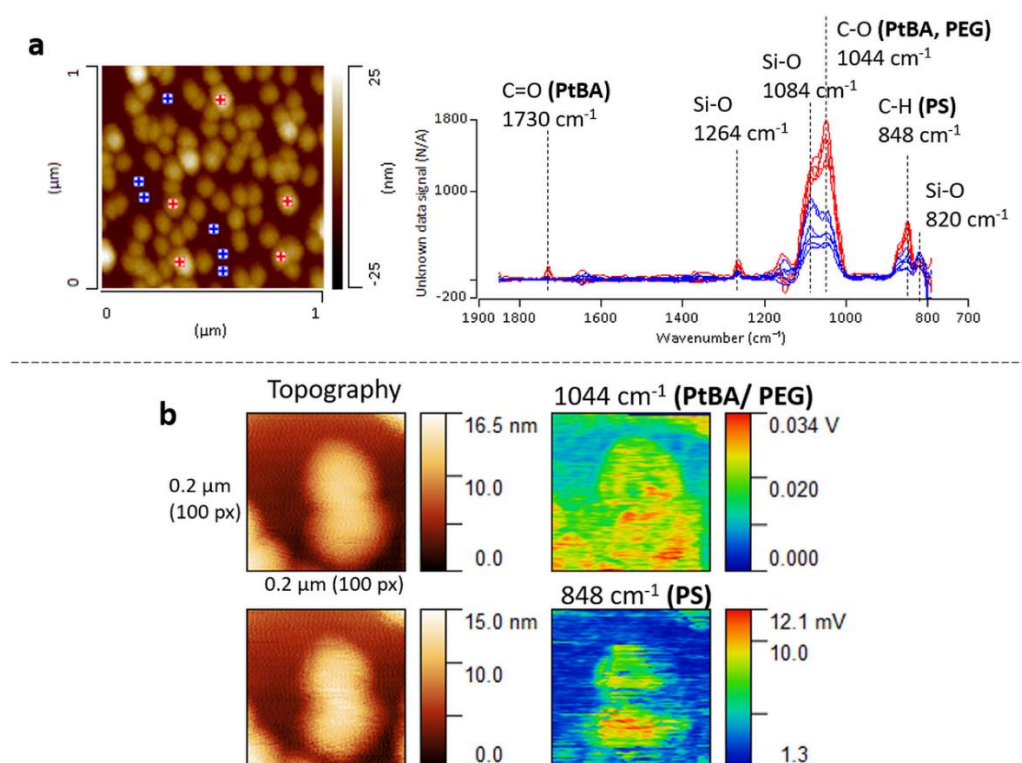

Figure 5.15 (a) IR spectra collected from background and particles of E$_{113}$S$_{100}$T$_{80}$ colloids. (No signal detected between the 1600-1400 cm^{-1} wavenumber due to IR chip fault. Other wavenumbers were not affected.) (b) Topography maps and IR signal maps of E$_{113}$S$_{100}$T$_{80}$ colloids obtained at 1044 cm^{-1} and 848 cm^{-1} wavenumbers.

The E$_{113}$S$_{100}$T$_{80}$ mainly produced AX$_2$ CMs (76 %), with small portion of CM intermediate (N=1, 2.9 %), AX$_3$ (N=3, 18.1 %) and AX$_4$ (N=4, 2.4 %) CMs (distribution shown in Figure 5.14f). With the further growth of the third block (PtBA, DP=120), significantly more AX$_3$ and AX$_4$ were observed in the TEM image (Figure 5.14g); the fraction of AX$_2$ (10.6 %) decreased drastically along with the increase of AX$_3$

(59.7 %) and AX_4 (28.5 %) portions. When the degree of polymerisation (DP) of PtBA increased to 250, AX_4 became the dominant structure (81.6 %) (Figure 5.14f, h). Considering the polymer solid content (3 wt %) and the fraction of each type of CMs, the $E_{113}S_{100}T_{80}$ and $E_{113}S_{100}T_{250}$ suspensions yielded 22.8 g/L AX_2 and 24.5 g/L AX_4, respectively. These values are much higher than previously reported methodology through the solution self-assembly process (typically <1 g/L).[35, 84] More importantly, in the colloids of $E_{113}S_{100}T_x$ (x= 80-250), CMs with different valences ranging from 2 to 6 (linear, triangular, tetrahedral, trigonal bipyramidal, square pyramidal, octahedral) were successfully captured by both TEM and SEM (Figure 5.16a). These artificial CMs are analogues of molecules such as CO_2, BCl_3, CH_4, PCl_5, BrF_5 and SF_6, which further demonstrates the potential of this technique in the preparation of CMs with high diversity. Meanwhile, it has been demonstrated that MβCD plays a critical role in the formation of AX_n-type CMs, as the control group ($E_{113}S_{100}$) with MβCD being removed by dialysis, the synthesised $E_{113}S_{100}T_{200}$ in water only resulted in kinetically trapped spherical nanoparticles without obvious patches (Figure 5.17).
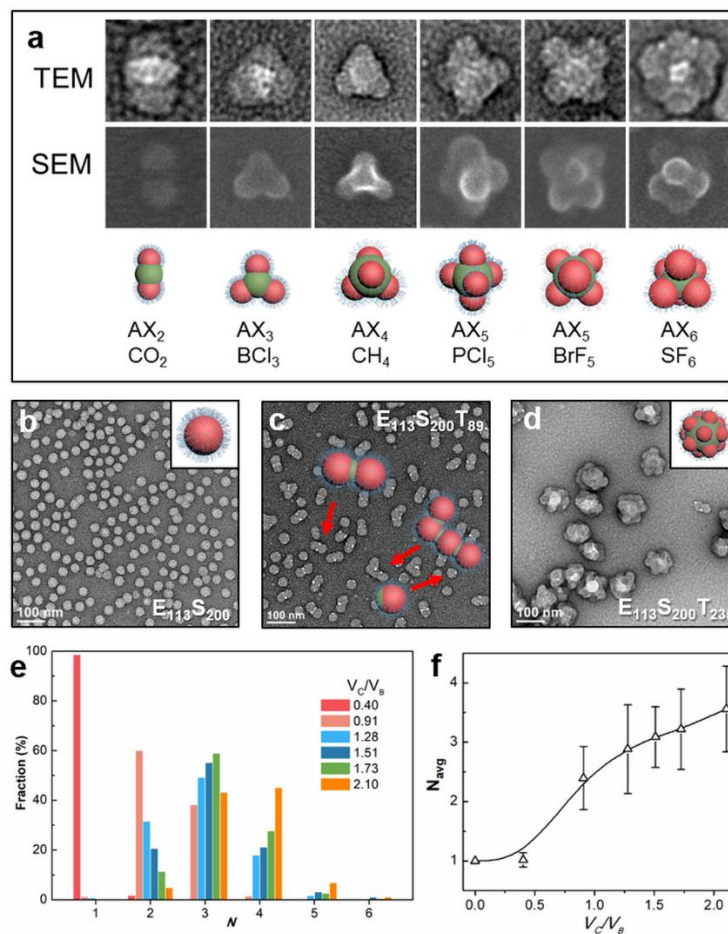
Figure 5.16 (a) Representative TEM and SEM images of AX_n-type (n=2-6) CMs observed from $E_{113}S_{100}T_x$ (x= 80-250) colloids. (b-d) TEM images of $E_{113}S_{200}$, $E_{113}S_{200}T_{89}$ and $E_{113}S_{200}T_{235}$. (e) Valence number (*N*) distribution of CMs with various V_C/V_B ratio (0.40-2.10) during PISA (targeting $E_{113}S_{100}T_{200}$). (f) Plot of mean average valence number (N_{avg}) against V_C/V_B. Error bars are standard deviation of population σ (calculation of N_{avg} and σ showed in Section 5.5.2).

Figure 5.17 TEM images of $E_{113}S_{100}T_{200}$ synthesised in water without MβCD.

Using the same approach, CMs composed of $E_{113}S_{200}T_x$ with $E_{113}S_{200}$ as CAs (d ~32.9 nm, Figure 5.16b) were fabricated as well. Colloidal intermediate (AX, "Janus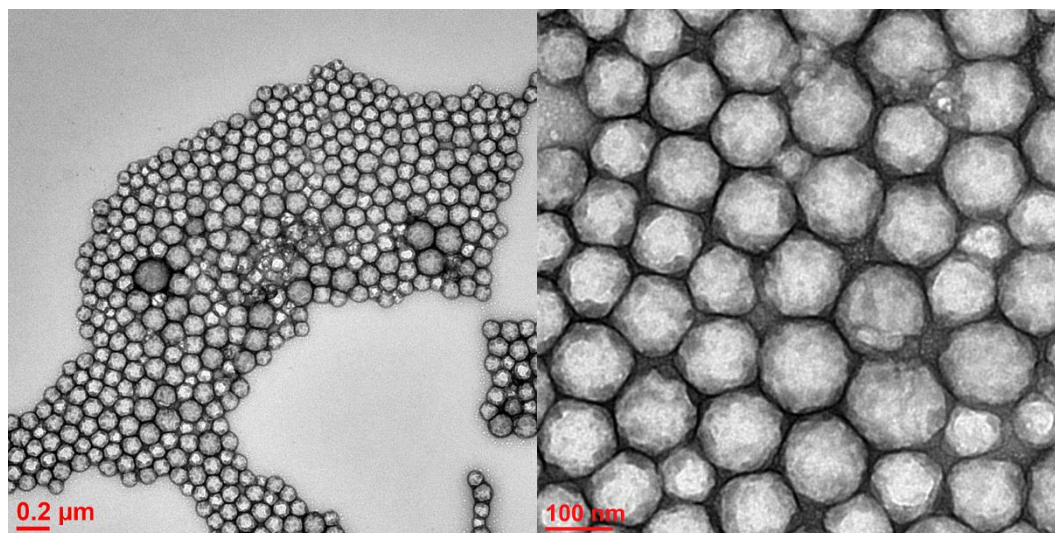" particle) and AX_2 were observed (Figure 5.16c) as the major products for $E_{113}S_{200}T_{89}$. The width of the dark grey PS domain (w~32-35 nm) matches the average diameter of $E_{113}S_{200}$ CAs. Meanwhile, some short chain-like clusters containing 3-4 CAs in a row were observed (Figure 5.16c). For $E_{113}S_{200}T_{235}$, with longer PtBA, CMs with high valence numbers (N>6) were identified as the dominant morphology (Figure 5.16d). By verifying the valence number distribution of $E_{113}S_{100}T_x$ and $E_{113}S_{200}T_x$, there is a general trend that the average valence number (N_{avg}) of CMs increases with the DP of PtBA, which is directly related to the volume ratio of PtBA to PS (V_C/V_B) (calculation of V_C/V_B showed in Section 5.5.2 and Table 5.4). However, even for CMs with the very close V_C/V_B, $e.g.$ $E_{113}S_{100}T_{120}$ (V_C/V_B = 1.55) and $E_{113}S_{200}T_{235}$ (V_C/V_B = 1.52), the morphology and N_{avg} could be distinct due to different CAs (Figure 5.14a and 5.16b) were employed. The particular reason for this circumstance is that the packing number of $E_{113}S_{200}$ CA is larger than $E_{113}S_{100}$, thus the number of diblock polymer chains in a single CA is different for $E_{113}S_{100}$ and $E_{113}S_{200}$, leading to different CM intermediates and different clustering in the seeded dispersion polymerisation. Thus, the influence of volume ratio V_C/V_B can only be discussed for the CMs prepared from CAs with the same length of PS block.

Next, to understand the morphological evolution, aliquots were collected at specific time points of seeded dispersion polymerisation ($E_{113}S_{100}$ to $E_{113}S_{100}T_x$, targeting x=200), and a series of $E_{113}S_{100}T_x$ (x=31-163) samples were obtained (Table 5.2 and Figure 5.18). The kinetic study depicts a linear

Table 5.2 Kinetic study of seeded dispersion polymerisation of MβCD/tBA complex ($E_{113}S_{100}$ to $E_{113}S_{100}T_x$, targeting X=200).

Entry	Time (h)	Polymer[a]	V_C/V_B	Conv. (%)[b]	$M_{n,NMR}$ (kg/mol)	$M_{n,GPC}$ (kg/mol)	Đ	$Z_{a,DLS}$ (nm)	PDI_{DLS}	N_{avg}
1	1	$E_{113}S_{100}T_{31}$	0.40	15.6	19.8	18.9	1.19	36.2	0.10	1.02 ± 0.12
2	2	$E_{113}S_{100}T_{52}$	0.67	26.0	22.5	19.9	1.21	46.2	0.16	-[*]
3	3	$E_{113}S_{100}T_{70}$	0.91	35.1	24.8	20.2	1.25	56.9	0.20	2.39 ± 0.53
4	4	$E_{113}S_{100}T_{88}$	1.14	44.2	27.1	20.9	1.26	58.5	0.18	-[*]
5	5	$E_{113}S_{100}T_{99}$	1.28	49.5	28.5	21.5	1.28	60.4	0.11	2.88 ± 0.75
6	6	$E_{113}S_{100}T_{107}$	1.39	53.6	29.6	21.9	1.31	61.0	0.20	-[*]
7	7	$E_{113}S_{100}T_{117}$	1.51	58.5	30.8	22.1	1.28	63.7	0.11	3.09 ± 0.51
8	8	$E_{113}S_{100}T_{127}$	1.65	63.7	32.1	22.4	1.30	62.4	0.08	-[*]
9	9	$E_{113}S_{100}T_{134}$	1.73	66.8	32.9	22.6	1.31	62.9	0.17	3.22 ± 0.68
10	10	$E_{113}S_{100}T_{143}$	1.85	71.6	34.2	22.9	1.30	62.4	0.05	-[*]
11	16	$E_{113}S_{100}T_{163}$	2.10	81.4	36.7	23.3	1.33	64.8	0.07	3.56 ± 0.72

[a]DP of polymers were calculated from ^{1}H NMR (Figure 5.18).
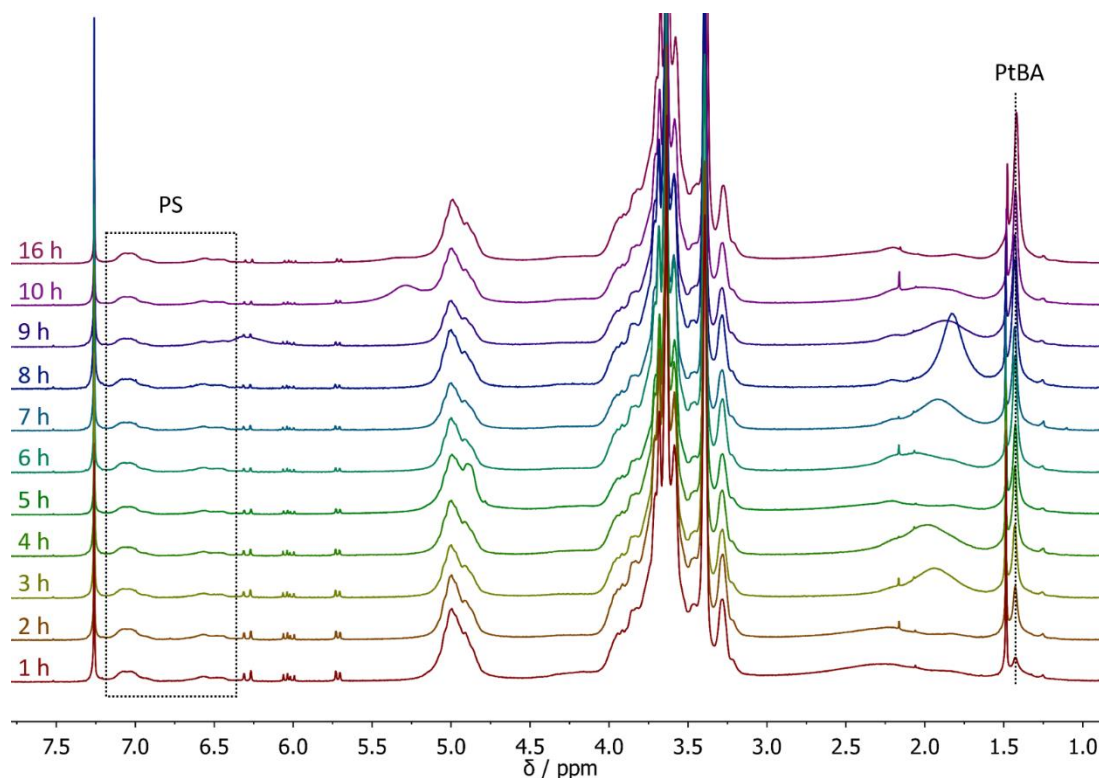[b]Conversion = repeating unit of PtBA/([tBA]/[PEG$_{113}$-b-PS$_{100}$]) × 100 %
[*]Not measured.

Figure 5.18 ^{1}H NMR spectra (400 MHz, CDCl$_3$) of suspensions collected at specific time points during dispersion polymerisation of MβCD/*t*BA (targeting PEG$_{113}$-*b*-PS$_{100}$-*b*-PtBA$_{200}$). DP of P*t*BA = [1/9 × integration of P*t*BA(1.42 ppm)]/ [1/500 × integration of PS(7.2-6.4 ppm)].

pseudo-first-order rate plot, indicating a constant propagating radical concentration during the polymerisation (Figure 5.19a). As expected, no micellar nucleation state was found because the micelle formation has been achieved in the synthesis of CAs. The GPC traces exhibited small shoulders (Figure 5.20), which might be due to the presence of impurity from commercial PEG$_{113}$ and high molecular weight polymers produced by recombination termination or chian transfer reactions. This phenomenon is well-documented and constantly observed for the RAFT polymerisation of acrylate monomers.[85] However, the progress of GPC curves with reaction time, the liner increase of molecular weight with conversion as well as the low *Đ* indicate the living characteristics and the good control of the seeded dispersion polymerisation (Figure 5.19b). The growth of P*t*BA blocks leads to an increase in the hydrodynamic diameter (Figure 5.21) and the transformation of morphology (Figure 5.22).
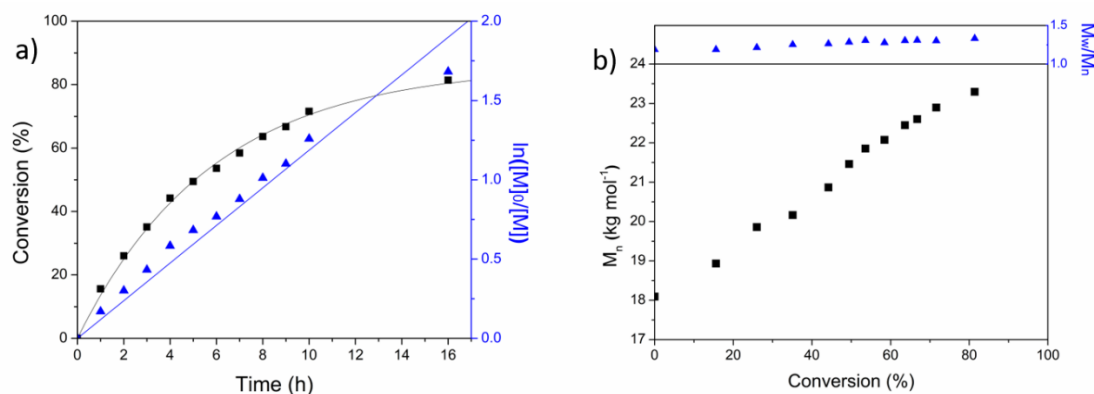
174

Figure 5.19 (a) ln($[M]_0/[M]$) and conversion *vs.* time and (b) molecular weight and *Đ vs.* conversion plots for the polymerisation of MβCD/*t*BA in water at 70 ˚C. Solid content = 3 wt %. [ACVA]/[PEG$_{113}$-*b*-PS$_{100}$]/[*t*BA]/[MβCD] = 0.3/1/200/200.
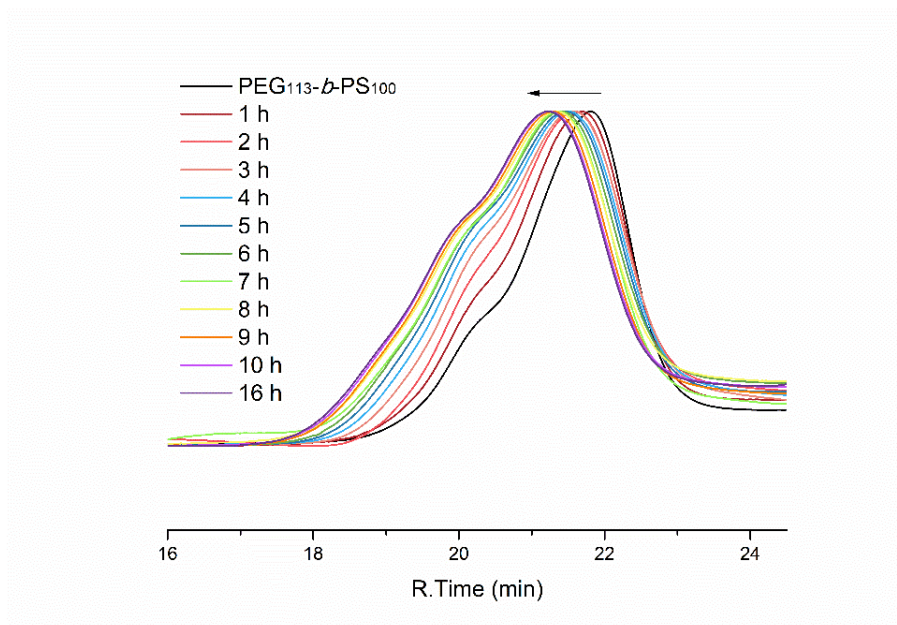
Figure 5.20 GPC traces of PEG$_{113}$-*b*-PS$_{100}$ and PEG$_{113}$-*b*-PS$_{100}$-*b*-P*t*BA$_x$ collected at specific time points during dispersion polymerisation of MβCD/*t*BA (targeting PEG$_{113}$-*b*-PS$_{100}$-*b*-P*t*BA$_{200}$) (DMF as eluent, PMMA standards).

Figure 5.21 DLS curves of suspensions collected at specific time points during dispersion polymerisation of MβCD/*t*BA (targeting PEG$_{113}$-*b*-PS$_{100}$-*b*-P*t*BA$_{200}$). Inset photos show the comparison of cloudiness before and after polymerisation.

Figure 5.22 Representative TEM images of $E_{113}S_{100}T_x$ AX_n-type CMs collected at specific time points during dispersion polymerisation of MβCD/tBA (targeting PEG$_{113}$-b-PS$_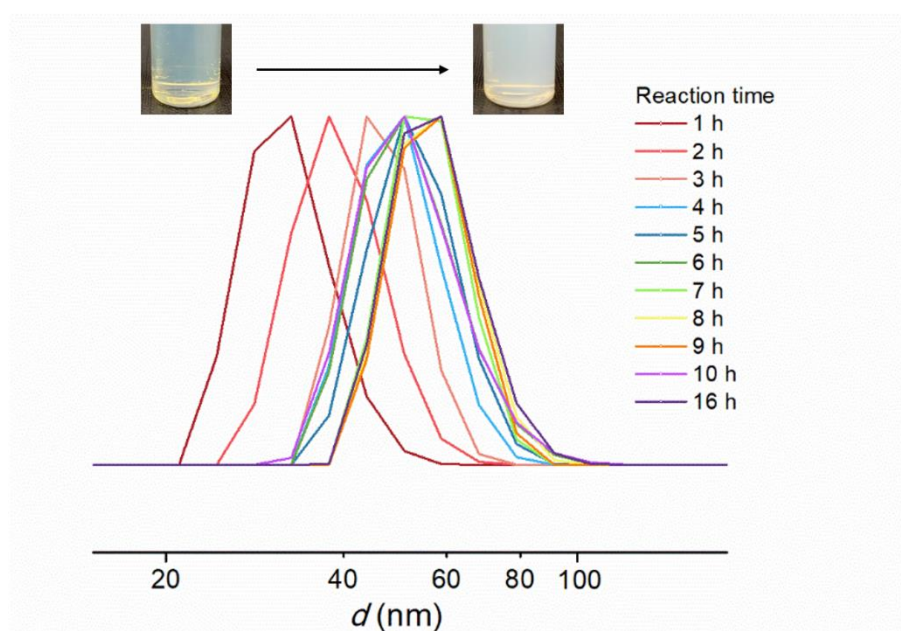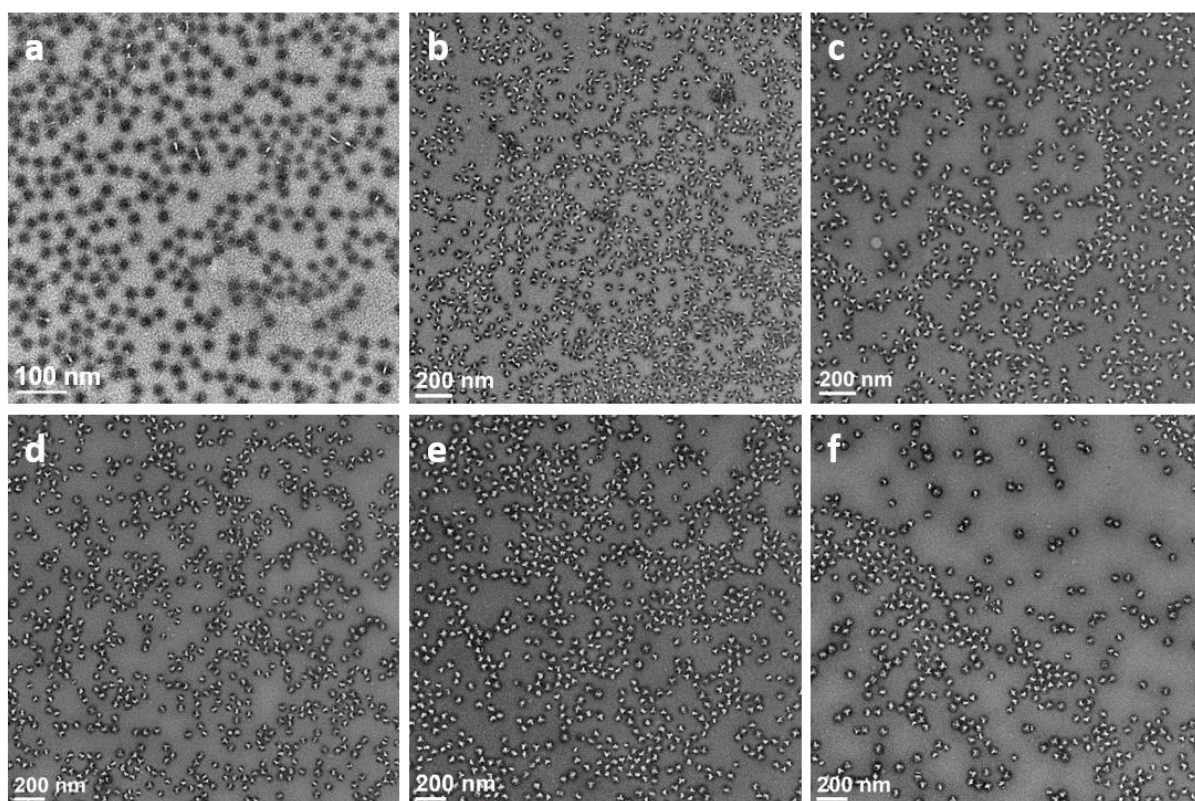{100}$-$b$-P$tBA_{200}$). (a) x=31, V_C/V_B=0.40, (b) x=70, V_C/V_B=0.91, (c) x=99, V_C/V_B=0.1.28, (d) x=117, V_C/V_B=1.51, (e) x=134, V_C/V_B=1.73, (f) x=163, V_C/V_B=2.10.

Figure 5.16e shows the distribution of CMs valence number (N) shifts toward higher N value with the increasing of V_C/V_B. Specifically, $E_{113}S_{100}T_{31}$ remained as spheres with only 1.5% of AX_2 CMs because PtBA is too short to form domains that lead to clustering. For $E_{113}S_{100}T_{70}$ with a longer PtBA chain (higher V_C/V_B), the intermediate "Janus" particles were no longer stable and further assembled into 59.8% AX_2, 38.0% AX_3, and only 1.2% spheres were observed. The relationship between the average valence (N_{avg}) and V_C/V_B was further revealed in Figure 5.16f; as V_C/V_B increase from 0.4 to 2.1, the N_{avg} gradually increase from 1.02 to 3.6. This finding is in good agreement with the principle of solvent-based preparation of multicompartment micelles (MCMs) by Müller et $al.$,[84] as well as the mechanism of CMs formation proposed by Yuan and coworkers.[52] For an ABC triblock terpolymer, when the ratio between block C and block B is higher than 1 (V_C/V_B >1), the unstable monovalent Janus intermediates assembly into AX_n-type colloidal molecules or cluster-like MCMs, the valence N of CMs is determined

by V_C/V_B. When the $V_C/V_B \leqslant 1$, divalent intermediates with two attractive patches could form colloidal chains (Figure 5.16c). Different from previous studies, the CM morphology in this chapter was implemented based on an EST formulation in aqueous medium. In addition, the present study outperformed previous methods in terms of facilitation and efficiency. Unlike previous methods involving multi-step synthesis/purification and solvent exchange or low monomer conversion, this study achieved a one-pot synthesis of high-purity CM with almost complete monomer conversion using water as the only solvent, making it perfectly suitable for large-scale production.

5.3.4 Synthesis of core-shell-corona micelles comprised of triblock terpolymer PEG-*b*-P*t*BA-*b*-PS (ETS)

Another advantage of this MβCD/monomer complex PISA system is that all complexed monomers with different properties are soluble in water, thus the composition of block B and block C can be readily switched, achieving a different type of hierarchical structures. Therefore, PEG-*b*-P*t*BA ($E_{113}T_x$) diblock copolymer nanoparticles were also synthesised by dispersion polymerisation of the MβCD/*t*BA complex. $E_{113}T_{85}$ and $E_{113}T_{180}$ are nanospheres with size around 25 nm and 40 nm, respectively (Figure 5.23a, b). Next, both nanospheres were employed as seeds for polymerisation of MβCD/st complex to form PEG-*b*-P*t*BA-*b*-PS ($E_{113}T_xS_y$) triblock terpolymers nanoparticles in water. With the increasing of PS block length(Figure 5.24), only spheres were observed, and no evident phase separation was observed in the unstained and UA stained particles (Figure 5.23c, d). Nevertheless, with the staining of RuO$_4$ vapor, the multicompartment nature of particles was unambiguously visualised in TEM images, revealing the presence of PS composition within the core of the nanospheres (Figure 5.25a). The phase separation between PS and P*t*BA blocks inside the spheres resulting in the formation of the core-shell-corona micelles (PS-core black, P*t*BA-shell white, PEG-corona not visible). This confirms that PS block grew inside the P*t*BA shell rather than between the interface of P*t*BA and water. The shell thickness of $E_{113}T_{85}S_{100}$ is around 5 nm (Figure 5.25a), and it increased to ~9 nm for $E_{113}T_{180}S_{103}$ (Figure 5.25b). However, the core size for $E_{113}T_{85}S_{100}$ and $E_{113}T_{180}S_{103}$ are both around 20 nm (Figure 5.25a, b), as they have approximately the same length of PS. Since P*t*BA has a low T_g (38 °C), the shell can be easily expanded with the increasing of the core size. This is reflected in $E_{113}T_{85}S_{200}$, which has a core size of ~25 nm and a thin shell layer (Figure 5.25c). Meanwhile, due to the good mobility of P*t*BA block, the

shell layer of some of these particles had merged, resulting in the formation of multi-core spheres and peapod-like structures (Figure 5.25a, c).
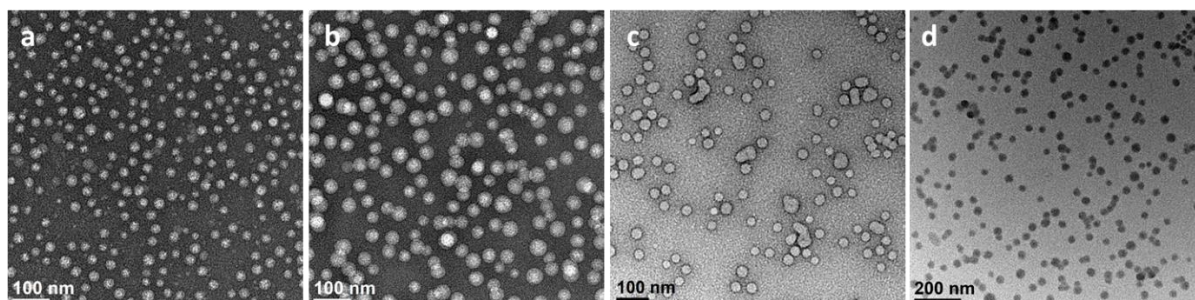

Figure 5.23 TEM images of (a) $E_{113}T_{85}$, (b) $E_{113}T_{180}$ and (c) $E_{113}T_{85}S_{100}$ (UA stained) (d) $E_{113}T_{85}S_{100}$ (unstained).
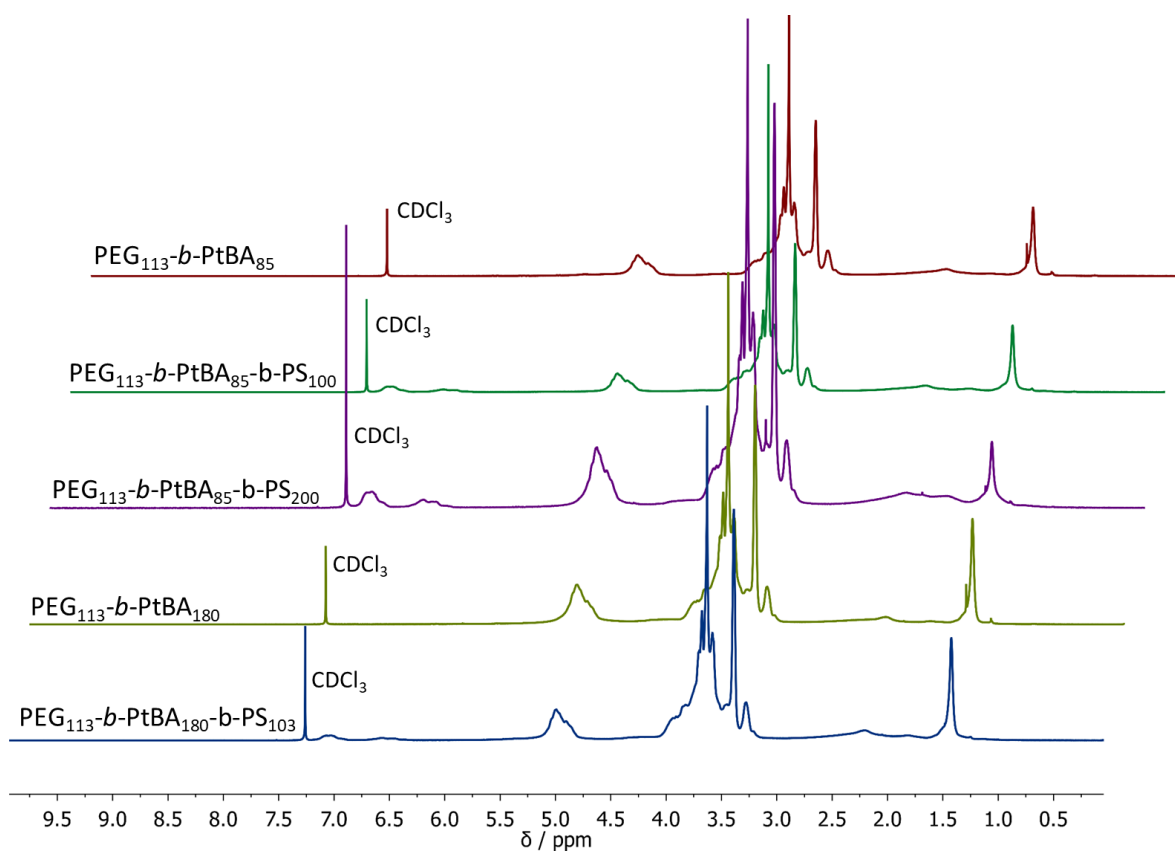

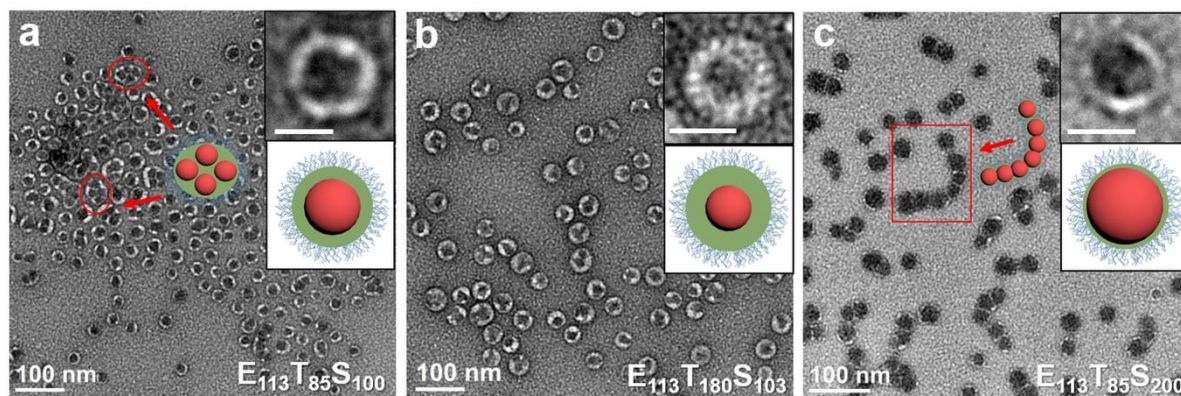Figure 5.24 ^1H NMR spectra (400 MHz, CDCl$_3$) of $E_{113}T_{85}$, $E_{113}T_{180}$ and $E_{113}T_mS_x$.

Figure 5.25 Representative TEM images and 3D structures (E-blue, T-green, S-red) of (a) $E_{113}T_{85}S_{100}$, (b) $E_{113}T_{180}S_{103}$, (c) $E_{113}T_{85}S_{200}$ (UA-RuO$_4$ stained). Scale bars are 20 nm in the insets.

The substantial morphological differences between PEG-*b*-PS-*b*-P*t*BA CMs and PEG-*b*-P*t*BA-*b*-PS core-shell-corona micelles indicate that the sequence of the second and third block would significantly impact the obtained particles in the PISA process. A similar conclusion was drawn in the solution self-assembly of triblock terpolymers. Laschewsky *et al.* reported the self-assembly of ABC, ACB and BAC types of triblock terpolymers and discovered the formation of different types of particles, including core-shell-corona micelles and double patched nanoparticles.[14, 15] In this work, the solid-water surface tension and T_g of PS and P*t*BA are both different, thus altering the sequence will impact the eventual self-assembly results. The influence of these factors will be further discussed in section 5.3.6.

5.3.5 Synthesis of raspberry-like nanoparticles comprised of triblock terpolymer PEG-*b*-PtBMA-*b*-PS (EMS)

The polymer chain mobility is greatly decreased at a temperature below T_g, which prevents the transformation from spherical micelles to higher order morphology.[86-89] P*t*BMA has a relatively high T_g (118 °C) and is too stiff to fuse with other particles at the reaction temperature (70 °C). Therefore, by replacing block B (P*t*BA) with P*t*BMA, which is also incompatible with PS, block C (PS) would likely protrude from the P*t*BMA shell. To verify this hypothesis, ABC block terpolymers composed of PEG-*b*-P*t*BMA-*b*-PS were synthesised *via* PISA as well. First, the seed suspension composed of PEG-*b*-P*t*BMA ($E_{113}M_{97}$) was prepared. The diblock copolymer formed spheres with a rough surface and diameter ~

80 nm (Figure 5.26a). Next, a series of PEG-*b*-P*t*BMA-*b*-PS (with targeting DP of PS from 30 to 300, Figure 5.26) were synthesised using $E_{113}M_{97}$ as seed and MβCD/st complex as chain extended monomer.
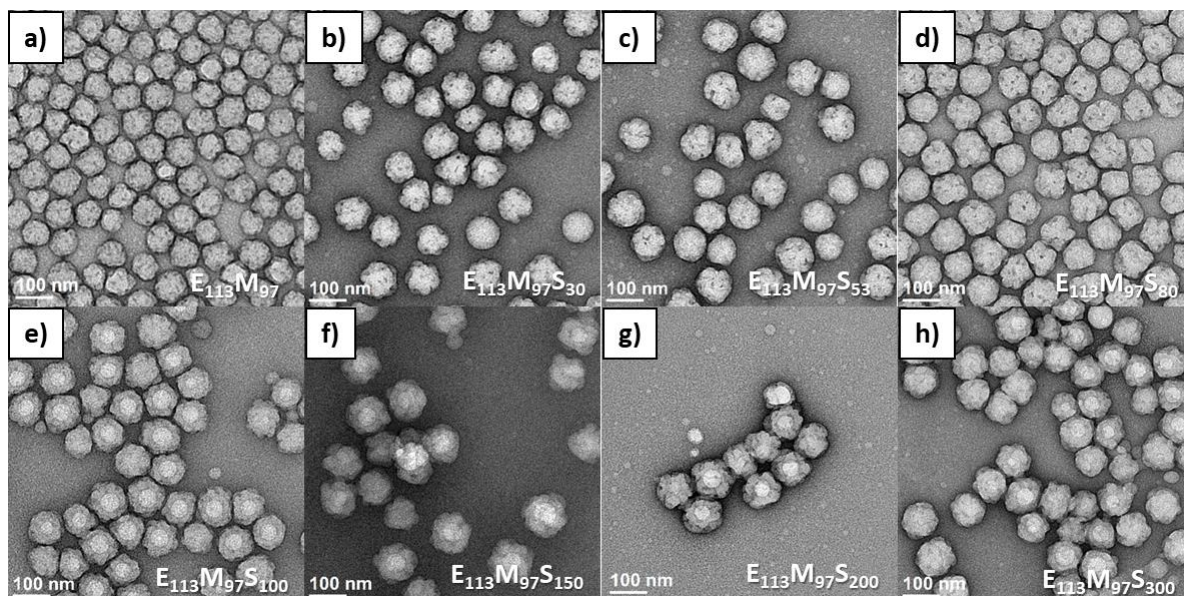
Figure 5.26 TEM images of synthesised $E_{113}M_{97}S_x$ (x=0-300) terpolymer nanoparticles (UA stained).

When the DP of block C reached 100 (Figure 5.27a), the PS domains was observed as dark grey patches on the particle, which results in the formation of raspberry-like structure. This phenomenon was resulted from the microphase separation between P*t*BMA and PS and also because of the high T_g of P*t*BMA. At the beginning of polymerisation, PS micro-domains aggregate inside the P*t*BMA core. With the growth of PS chain length and volume, the P*t*BMA core is not sufficient to conceal the PS domain, and it is too rigid to expand or fuse with other particles (forming multi-core micelles as ETS), PS domain will crack the P*t*BMA shell and protrude to form small patches at the interface between P*t*BMA and water. To further verify this raspberry-like structure, AFM-IR analysis (Figure 5.27b) was conducted. It was found the PS signal was detected over scattered regions on the sphere, suggesting that PS dispersed as micro-domains on the particle. With the further growth of PS block ($E_{113}M_{97}S_{200}$), a similar raspberry-like structure with more PS domains on each particle was found due to increased PS volume (Figure 5.28b).
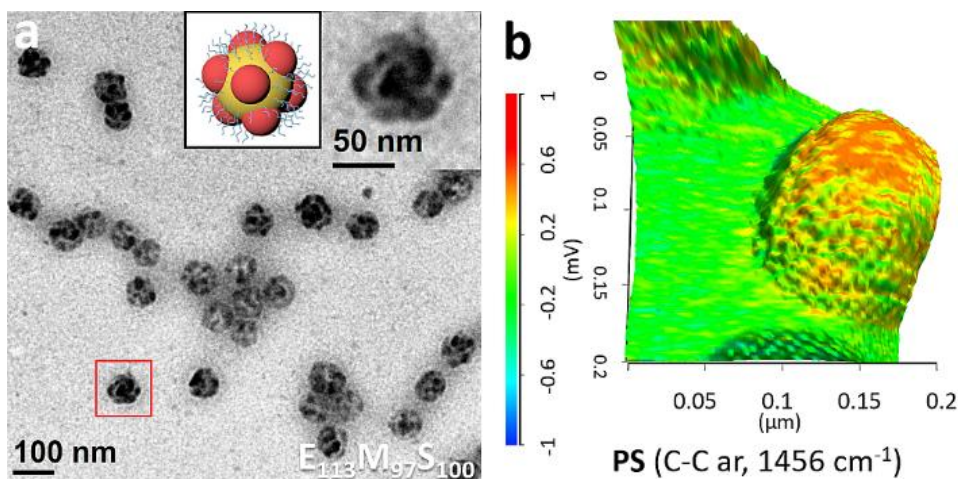
Figure 5.27 (a) TEM images of $E_{113}M_{97}S_{100}$ raspberry-like particles (unstained). (b) AFM-IR 3D overlay of topography and IR maps of $E_{113}M_{97}S_{100}$ obtained at 1456 cm^{-1} wavenumbers.
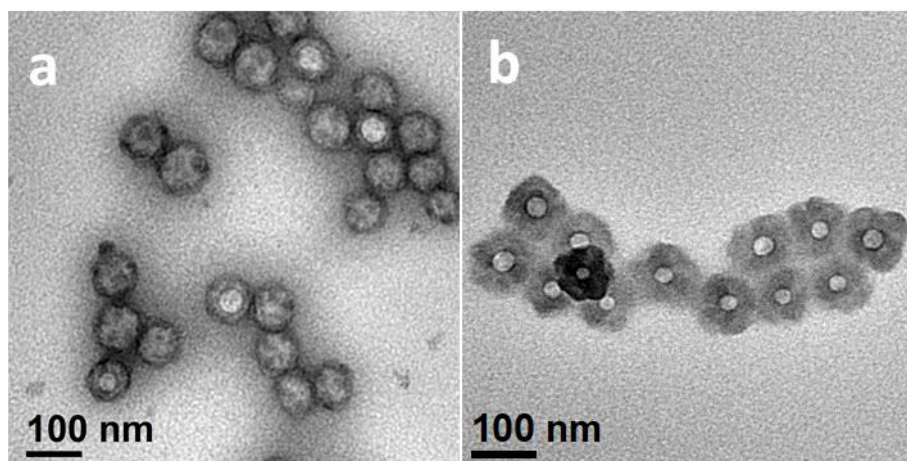
Figure 5.28 TEM images of synthesised (a) $E_{113}M_{97}S_{100}$ (UA-RuO$_4$ stained) and (b) $E_{113}M_{97}S_{100}$ (unstained) raspberry-like particles.

5.3.6 Assembly mechanism of ABC triblock copolymer during PISA

The universal self-assembly driving force is to reach thermodynamic equilibrium by minimisation of the free energy,[34] including the circumstance in this chapter. The free energy can be presented as

$$F = F_{corona} + F_{core} + F_{interface}$$

where F_{corona} describes repulsive interactions between coronal chains A, whereas F_{core} accounts for the conformational entropy losses in the collapsed core-forming segments.[84] In this chapter, all triblock

copolymers contain the same coronal block A, and F_{core} is negligibly small, thus the interfacial energy $F_{interface}$ determines the morphology of ABC linear triblock terpolymers. It can be presented as

$$F_{interface} = \gamma_{BS}S_{BS} + \gamma_{CS}S_{CS} + \gamma_{BC}S_{BC}$$

Where γ_{BS}, γ_{CS}, γ_{BC} are the surface tension and S_{BS}, S_{CS}, S_{BC} are the interfacial areas at the B-solvent, C-solvent, B-C interfaces, respectively. As shown in Figure 5.29, for ABC linear triblock terpolymer, if the interfacial tension $\gamma_{BS} > \gamma_{CS}$, the block C tends to aggregate at the interface between the block B solvent interface to minimise S_{BS} and the total $F_{interface}$. As a result, it forms CM intermediates and hierarchically self-assembles into AX_n-type CMs. In the PISA of EST, as the surface tension at PS and water interface is higher than that at PtBA and water interface ($\gamma_{S-W} > \gamma_{B-W}$), P$t$BA aggregates in the interface of PS and water to minimise unfavourable PS/water interface (the surface tensions were calculated from Girifalco-Good equation as shown in Section 5.5.1, Table 5.3). On the contrary, if $\gamma_{BS} < \gamma_{CS}$, block C tends to grow inside the core of block B, forming the core-shell-corona micelles first. With the further growth of block C, and for the case with block B that has a relatively low T_g, the good mobility of B allows the fusion of particle shells to form multi-core and peapod-like MCMs; for the case with block B that has a high T_g, the fusion between B is limited, and block C will protrude from the core to form raspberry-like MCMs. This explains the morphological evolutions for ETS and EMS (Figure 5.25a and 5.27a).
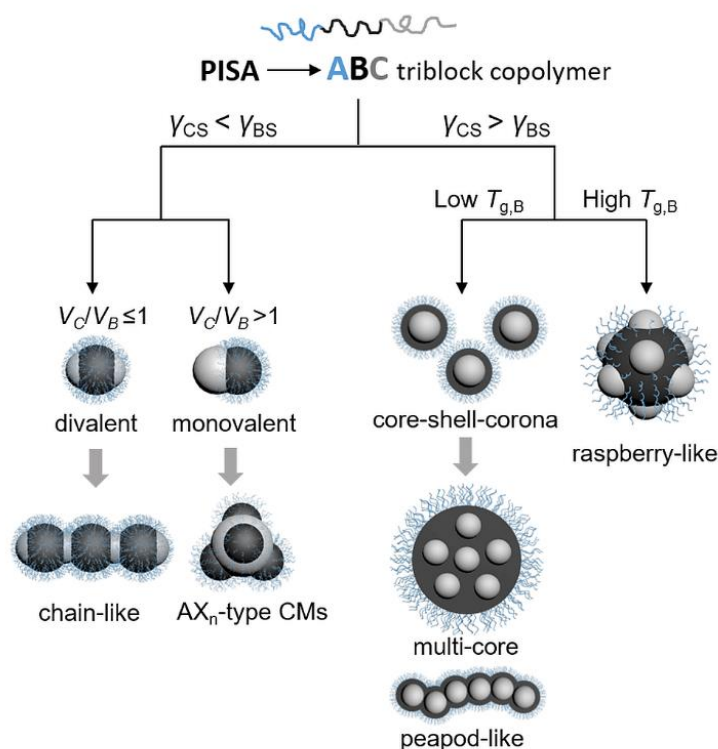
Figure 5.29 The ABC triblock terpolymer hierarchically self-assembly mechanisms under the current PISA condition.

This chapter not only introduced a facile methodology for the preparation of hierarchical polymer nanostructures with diverse morphologies, but also systematically studied various factors, including surface tension, polymer composition order and the glass transition temperature of polymers, that could affect the morphologies of triblock terpolymers. Therefore, the proposed mechanism derived from this chapter could serve as a guideline of triblock terpolymer self-assembly to predict the morphologies of different formulations. Meanwhile, it is conceivable that many other hydrophobic monomers with specific functional groups that are capable of complexing with β-CD can also be applied to conduct dispersion polymerisation in water. Beyond β-CD, it is well-known that α- and γ-CD with different inner hydrophobic cavity sizes can also complex with a variety of guest molecules and monomers. For instance, the complex between aliphatic groups and α-CD,[90] and two pyrenyl groups with one γ-CD[91] were reported previously. It is foreseeable that monomers with these functional groups could also be applied in the aqueous PISA process to furnish the library of polymer self-assembly.

5.4 Conclusions

It was demonstrated that through the formation of MβCD/monomer complex, well-defined ABC triblock terpolymer colloids with diverse morphologies could be conveniently prepared *via* aqueous PISA. The water-immiscible monomers could be readily converted into water-soluble complexes at 1:1 molar ratio of monomer: MβCD, and therefore providing a series of additional monomer options for aqueous PISA. Furthermore, the kinetic study confirmed the dispersion polymerisation process of st (1:1 to MβCD) with PEG-CDTPA as chain transfer agent. A series of ABC triblock copolymer nanoparticles are achieved by the addition of a third monomer (1:1 to MβCD) in the seeded dispersion polymerisation process. Depends on the polymer component and order, a series of different particle morphologies have been achieved. Specifically, EST self-assembled into rarely achieved AX_n-type colloidal molecules *in situ* with high purity and concentration (*e.g.* 81.6 % AX_4, 24.5 g/L), which provides a scalable possibility for the synthesis of CMs. ETS and EMS form core-shell-corona micelles and raspberry-like micelles, respectively. In addition, the particle formation mechanism driven by minimisation of interfacial energy was summarised, which provides a guideline for the rational design of ABC triblock terpolymer nanoparticles. Overall, the robust, scalable nature of this aqueous formulation is expected to provide opportunities in the growing field of block copolymer self-assembly, since they allow access to diverse particle morphologies at relatively high solid contents.

5.5 Supporting Information

5.5.1 Calculation of surface and interfacial tension

Contact angles of liquids on solids are often described with the Young's equation:

$$\gamma_{SV} = \gamma_{SL} + \gamma_{LV} \cos \theta$$, equation (1)
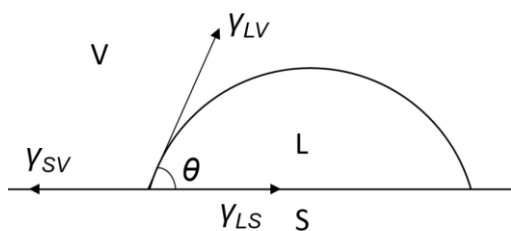
Where $\gamma_{SV}, \gamma_{SL}, \gamma_{LV}$ are the solid/vapor, solid/liquid and liquid/vapor interface tensions. θ: the contact angle. The surface tension can also be calculated from the Girifalco and Good equation[92]:

$$\gamma_{SL} = \gamma_{SV} + \gamma_{LV} - 2 \cdot \Phi \cdot (\gamma_{SV}\gamma_{LV})^{1/2} \text{ , equation (2)}$$

In many cases, Φ is of the order of unity, which is the case for aliphatic compounds where only dispersion forces are present:
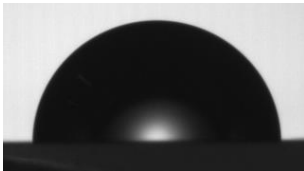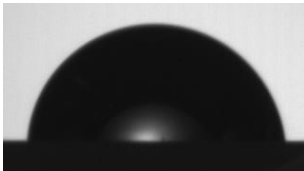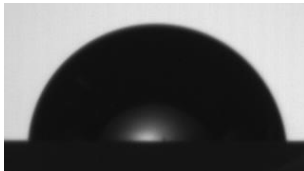
$$\gamma_{SL} \approx \gamma_{SV} + \gamma_{LV} - 2(\gamma_{SV}\gamma_{LV})^{1/2} \text{ , equation (3)}$$

Combining equation (3) with equation (1), gives:

$$\gamma_{SV} = \gamma_{LV} \, (1 + \cos\theta)^2 / 4\Phi^2 \approx \gamma_{LV} \, (1 + \cos\theta)^2 / 4$$

In this study, γ_{LV} is water/air surface tension, which is 72.8 mN·m^{-1} at 20 °C.

Table 5.3 Summary of surface and interfacial tension of polymers.

	PS	PtBA	PtBMA
$M_{n,GPC}$ (kg·mol^{-1})	57.5	21.3	17.4
Contact angle θ (°)	83.0 ± 0.2	79.8 ± 0.4	81.2 ± 0.6
γ_{SV} (mN·m^{-1})	22.9 ± 0.1	25.2 ± 0.3	24.2 ± 0.5
γ_{SL} (mN·m^{-1})	14.0 ± 0.1	12.3 ± 0.2	13.1 ± 0.3

5.5.2 Calculation and summary of N_{avg} and σ

Table 5.4 Summary of ES colloidal atoms and EST colloidal molecules.

Entry	Polymer[a]	V_C/V_B [b]	$M_{n,NMR}$ [c] (kg/mol)	$M_{n,GPC}$ (kg/mol)	Đ	$Z_{a,DLS}$ (nm)	PDI_{DLS}	N_{avg} [d]
I	$E_{113}S_{100}$	0	15.8	18.1	1.19	37.7	0.04	1
II	$E_{113}S_{200}$	0	26.2	23.0	1.31	43.7	0.10	1
III	$E_{113}S_{100}T_{80}$	1.03	26.0	20.8	1.26	59.1	0.07	2.22 ± 0.55
IV	$E_{113}S_{100}T_{120}$	1.55	31.2	19.6	1.31	62.4	0.08	3.18 ± 0.64
V	$E_{113}S_{100}T_{250}$	3.23	47.9	20.7	1.39	76.6	0.04	3.97 ± 0.60
VI	$E_{113}S_{200}T_{89}$	0.58	37.6	24.0	1.31	66.4	0.14	1.67 ± 0.61
VII	$E_{113}S_{200}T_{235}$	1.52	56.3	25.9	1.39	108.5	0.04	>6

[a]DP of polymers were calculated from ^{1}H NMR.

[b]V_C/V_B is the volume ratio of block C and B of the ABC triblock terpolymer, which is PtBA/PS in this case.

$$\frac{V_C}{V_B} = \frac{M_C/\rho_C}{M_B/\rho_B} = \frac{DP_C M_{monomer\ C} \times \rho_B}{DP_B M_{monomer\ B} \times \rho_C}$$

where ρ_B is the density of PS (1.05 g/cm^3) and ρ_C is the density of PtBA (1.00 g/cm^3). $M_{monomer\ B}$ and $M_{monomer\ C}$ are the molecular weights of styrene and tert-butyl acrylate.

[c]$M_{n,NMR} = M_{n,\ macro\text{-}RAFT} + DP_{PS} \times M_{n,st} + DP_{PtBA} \times M_{n,tBA}$

[d]Average valence (N_{avg}) of EST CMs is measured by counting > 500 particles in a TEM image.

$$N_{avg} = \sum_{i=1}^{n} N_i/n, \qquad \sigma = \sqrt{\frac{\sum_{i=1}^{n}\left(N_i - N_{avg}\right)^2}{n}}$$

where n is the total number of counted particles, σ is the standard deviation of the counted particles, N_i is the valence number of the ith particle.

5.6 References

1.   C. Zeng, Y. Chen, K. Kirschbaum, K. J. Lambright and R. Jin, *Science*, 2016, **354**, 1580-1584.
2.   G. von Freymann, V. Kitaev, B. V. Lotsch and G. A. Ozin, *Chem. Soc. Rev.*, 2013, **42**, 2528-2554.
3.   H. Inan, M. Poyraz, F. Inci, M. A. Lifson, M. Baday, B. T. Cunningham and U. Demirci, *Chem. Soc. Rev.*, 2017, **46**, 366-388.
4.   C. Yi, H. Liu, S. Zhang, Y. Yang, Y. Zhang, Z. Lu, E. Kumacheva and Z. Nie, *Science*, 2020, **369**, 1369-1374.
5.   D. A. Tomalia and S. N. Khanna, *Chem. Rev.*, 2016, **116**, 2705-2774.
6.   W. Wen, W. Ouyang, S. Guan and A. Chen, *Polym. Chem.*, 2021, **12**, 458-465.
7.   S. Guan, C. Zhang, W. Wen, T. Qu, X. Zheng, Y. Zhao and A. Chen, *ACS Macro Lett.*, 2018, **7**, 358-363.
8.   Q. Xu, T. Huang, S. Li, K. Li, C. Li, Y. Liu, Y. Wang, C. Yu and Y. Zhou, *Angew. Chem. Int. Ed.*, 2018, **57**, 8043-8047.
9.   T. S. Skelhon, Y. Chen and S. A. F. Bon, *Soft Matter*, 2014, **10**, 7730-7735.
10.   L. Hong, A. Cacciuto, E. Luijten and S. Granick, *Nano Lett.*, 2006, **6**, 2510-2514.
11.   Y. Wang, Y. Wang, D. R. Breed, V. N. Manoharan, L. Feng, A. D. Hollingsworth, M. Weck and D. J. Pine, *Nature*, 2012, **491**, 51-55.
12.   M. A. van Dongen, S. Vaidyanathan and M. M. Banaszak Holl, *Soft Matter*, 2013, **9**, 11188-11196.
13.   J. Hu and G. Liu, *Macromolecules*, 2005, **38**, 8058-8065.
14.   K. Skrabania, H. v. Berlepsch, C. Böttcher and A. Laschewsky, *Macromolecules*, 2010, **43**, 271-281.
15.   J.-N. Marsat, M. Heydenreich, E. Kleinpeter, H. v. Berlepsch, C. Böttcher and A. Laschewsky, *Macromolecules*, 2011, **44**, 2092-2105.
16.   P. Shi, Q. Li, X. He, S. Li, P. Sun and W. Zhang, *Macromolecules*, 2014, **47**, 7442-7452.
17.   X. He, Y. Qu, C. Gao and W. Zhang, *Polym. Chem.*, 2015, **6**, 6386-6393.
18.   Z. Deng and S. Liu, *Polymer*, 2020, **207**, 122914.
19.   J. Xiao and J. Du, *J. Am. Chem. Soc.*, 2020, **142**, 6569-6577.
20.   B. Fan, R. E. Yardley, J. F. Trant, A. Borecki and E. R. Gillies, *Polym. Chem.*, 2018, **9**, 2601-2610.
21.   B. Fan and E. R. Gillies, *Mol. Pharmaceutics*, 2017, **14**, 2548-2559.
22.   Y. Mai and A. Eisenberg, *Chem. Soc. Rev.*, 2012, **41**, 5969-5985.
23.   T. Gädt, N. S. Ieong, G. Cambridge, M. A. Winnik and I. Manners, *Nat. Mater.*, 2009, **8**, 144-150.
24.   D. A. Tomalia, H. M. Brothers, L. T. Piehler, H. D. Durst and D. R. Swanson, *Proc. Natl. Acad. Sci. U. S. A.*, 2002, **99**, 5081-5087.
25.   S. Uppuluri, D. R. Swanson, L. T. Piehler, J. Li, G. L. Hagnauer and D. A. Tomalia, *Adv. Mater.*, 2000, **12**, 796-800.
26.   Y. La, C. Park, T. J. Shin, S. H. Joo, S. Kang and K. T. Kim, *Nat. Chem.*, 2014, **6**, 534-541.
27.   Z. Lin, J. Zhou, C. Cortez-Jugo, Y. Han, Y. Ma, S. Pan, E. Hanssen, J. J. Richardson and F. Caruso, *J. Am. Chem. Soc.*, 2020, **142**, 335-341.
28.   S. Ha, Y. La and K. T. Kim, *Acc. Chem. Res.*, 2020, **53**, 620-631.
29.   X. Lyu, A. Xiao, W. Zhang, P. Hou, K. Gu, Z. Tang, H. Pan, F. Wu, Z. Shen and X.-H. Fan, *Angew. Chem. Int. Ed.*, 2018, **57**, 10132-10136.
30.   Y. Lu, J. Lin, L. Wang, L. Zhang and C. Cai, *Chem. Rev.*, 2020, **120**, 4111-4140.
31.   K. Zhang, H. Miao and D. Chen, *J. Am. Chem. Soc.*, 2014, **136**, 15933-15941.
32.   L. Cheng, G. Zhang, L. Zhu, D. Chen and M. Jiang, *Angew. Chem. Int. Ed.*, 2008, **47**, 10171-10174.
33.   A. H. Gröschel, A. Walther, T. I. Löbling, F. H. Schacher, H. Schmalz and A. H. E. Müller, *Nature*, 2013, **503**, 247-251.
34.   A. H. Gröschel and A. H. E. Müller, *Nanoscale*, 2015, **7**, 11841-11876.
35.   T. I. Löbling, O. Borisov, J. S. Haataja, O. Ikkala, A. H. Gröschel and A. H. E. Müller, *Nat. Commun.*, 2016, **7**, 12097.

36.   M. A. Rahman, Y. Cha, L. Yuan, P. Pageni, T. Zhu, M. S. Jui and C. Tang, *J. Polym. Sci.*, 2020, **58**, 77-83.
37.   B. Fan, Y. Liu, J. Wan, S. Crawford and S. H. Thang, *ACS Mater. Lett.*, 2020, **2**, 492-498.
38.   J. Wan, B. Fan, Y. Liu, T. Hsia, K. Qin, T. Junkers, B. M. Teo and S. H. Thang, *Polym. Chem.*, 2020, **11**, 3564-3572.
39.   B. Fan, J. Wan, J. Zhai, X. Chen and S. H. Thang, *ACS Nano*, 2021, **15**, 4688-4698.
40.   J. Wan, B. Fan and S. H. Thang, *Nanoscale Adv.*, 2021, **3**, 3306-3315.
41.   C. Liu, C.-Y. Hong and C.-Y. Pan, *Polym. Chem.*, 2020, **11**, 3673-3689.
42.   W.-J. Zhang, C.-Y. Hong and C.-Y. Pan, *Macromol. Rapid Commun.*, 2015, **36**, 1428-1436.
43.   X. Dai, Y. Zhang, L. Yu, X. Li, L. Zhang and J. Tan, *ACS Macro Lett.*, 2019, **8**, 955-961.
44.   M. Huo, M. Zeng, D. Li, L. Liu, Y. Wei and J. Yuan, *Macromolecules*, 2017, **50**, 8212-8220.
45.   F. Lv, Z. An and P. Wu, *Nat. Commun.*, 2019, **10**, 1397.
46.   S. Xu, J. Yeow and C. Boyer, *ACS Macro Lett.*, 2018, **7**, 1376-1382.
47.   B. Charleux, G. Delaittre, J. Rieger and F. D'Agosto, *Macromolecules*, 2012, **45**, 6753-6765.
48.   P. Shi, C. Gao, X. He, P. Sun and W. Zhang, *Macromolecules*, 2015, **48**, 1380-1389.
49.   N. J. W. Penfold, J. R. Whatley and S. P. Armes, *Macromolecules*, 2019, **52**, 1653-1662.
50.   X. Chen, L. Liu, M. Huo, M. Zeng, L. Peng, A. Feng, X. Wang and J. Yuan, *Angew. Chem. Int. Ed.*, 2017, **56**, 16541-16545.
51.   N. J. Warren and S. P. Armes, *J. Am. Chem. Soc.*, 2014, **136**, 10174-10185.
52.   D. Li, X. Chen, M. Zeng, J. Ji, Y. Wang, Z. Yang and J. Yuan, *Chem. Sci.*, 2020, **11**, 2855-2860.
53.   P. Chambon, A. Blanazs, G. Battaglia and S. P. Armes, *Macromolecules*, 2012, **45**, 5081-5090.
54.   W. Zhang, F. D'Agosto, O. Boyron, J. Rieger and B. Charleux, *Macromolecules*, 2011, **44**, 7584-7593.
55.   P. Gurnani, C. Sanchez-Cano, K. Abraham, H. Xandri-Monje, A. B. Cook, M. Hartlieb, F. Lévi, R. Dallmann and S. Perrier, *Macromol. Biosci.*, 2018, **18**, 1800213.
56.   J. Jeromin and H. Ritter, *Macromol. Rapid Commun.*, 1998, **19**, 377-379.
57.   H. Cinar, O. Kretschmann and H. Ritter, *Macromolecules*, 2005, **38**, 5078-5082.
58.   H. Köllisch, C. Barner-Kowollik and H. Ritter, *Macromol. Rapid Commun.*, 2006, **27**, 848-853.
59.   O. Kretschmann, S. W. Choi, M. Miyauchi, I. Tomatsu, A. Harada and H. Ritter, *Angew. Chem. Int. Ed.*, 2006, **45**, 4361-4365.
60.   O. Kretschmann, C. Steffens and H. Ritter, *Angew. Chem. Int. Ed.*, 2007, **46**, 2708-2711.
61.   B. V. K. J. Schmidt, M. Hetzer, H. Ritter and C. Barner-Kowollik, *Macromolecules*, 2011, **44**, 7220-7232.
62.   B. V. K. J. Schmidt, M. Hetzer, H. Ritter and C. Barner-Kowollik, *Macromol. Rapid Commun.*, 2013, **34**, 1306-1311.
63.   H. S. Köllisch, C. Barner-Kowollik and H. Ritter, *Chem. Commun.*, 2009, 1097-1099.
64.   N. J. W. Penfold, J. Yeow, C. Boyer and S. P. Armes, *ACS Macro Lett.*, 2019, **8**, 1029-1054.
65.   Y. Hirai, T. Wakiya and H. Yabu, *Polym. Chem.*, 2017, **8**, 1754-1759.
66.   D. Yao, K. Zhang and Y. Chen, *Polymer*, 2016, **94**, 1-7.
67.   P. H. Madison and T. E. Long, *Biomacromolecules*, 2000, **1**, 615-621.
68.   Y. Luo, J. Tsavalas and F. J. Schork, *Macromolecules*, 2001, **34**, 5501-5507.
69.   D. Taura, Y. Taniguchi, A. Hashidzume and A. Harada, *Macromol. Rapid Commun.*, 2009, **30**, 1741-1744.
70.   B. Fan, J. Wan, Y. Liu, W. W. Tian and S. H. Thang, *Polym. Chem.*, 2021, **12**, 3015-3025.
71.   B. Fan, J. Wan, A. McKay, Z. Qu and S. H. Thang, *Polym. Chem.*, 2020, **11**, 5649-5658.
72.   S. Saeki, N. Kuwahara, M. Nakata and M. Kaneko, *Polymer*, 1976, **17**, 685-689.
73.   N. J. Warren, O. O. Mykhaylyk, D. Mahmood, A. J. Ryan and S. P. Armes, *J. Am. Chem. Soc.*, 2014, **136**, 1023-1033.
74.   J. Tan, X. Zhang, D. Liu, Y. Bai, C. Huang, X. Li and L. Zhang, *Macromol. Rapid Commun.*, 2017, **38**, 1600508.
75.   A. van Blaaderen, *Science*, 2003, **301**, 470-471.
76.   R. Colorado, R. J. Villazana and T. R. Lee, *Langmuir*, 1998, **14**, 6337-6340.

77. J. A. Fan, C. Wu, K. Bao, J. Bao, R. Bardhan, N. J. Halas, V. N. Manoharan, P. Nordlander, G. Shvets and F. Capasso, *Science*, 2010, **328**, 1135-1138.

78. S. J. Barrow, X. Wei, J. S. Baldauf, A. M. Funston and P. Mulvaney, *Nat. Commun.*, 2012, **3**, 1-9.

79. Zhang, A. S. Keys, T. Chen and S. C. Glotzer, *Langmuir*, 2005, **21**, 11547-11551.

80. I. D. Hosein, M. Ghebrebrhan, J. D. Joannopoulos and C. M. Liddell, *Langmuir*, 2010, **26**, 2151-2159.

81. S. Sacanna and D. J. Pine, *Curr. Opin. Colloid Interface Sci.*, 2011, **16**, 96-105.

82. T. A. Betley, M. M. Banaszak Holl, B. G. Orr, D. R. Swanson, D. A. Tomalia and J. R. Baker, *Langmuir*, 2001, **17**, 2768-2773.

83. U. Schwarz, H. Haefke, P. Reimann and H. J. Güntherodt, *J. Microsc.*, 1994, **173**, 183-197.

84. A. H. Gröschel, F. H. Schacher, H. Schmalz, O. V. Borisov, E. B. Zhulina, A. Walther and A. H. E. Müller, *Nat. Commun.*, 2012, **3**, 710.

85. J. Chiefari, J. Jeffery, R. T. Mayadunne, G. Moad, E. Rizzardo and S. H. Thang, *Macromolecules*, 1999, **32**, 7700-7702.

86. J. Zhou, W. Zhang, C. Hong and C. Pan, *Polym. Chem.*, 2016, **7**, 3259-3267.

87. C. A. Figg, R. N. Carmean, K. C. Bentz, S. Mukherjee, D. A. Savin and B. S. Sumerlin, *Macromolecules*, 2017, **50**, 935-943.

88. J. Yeow, R. Chapman, J. Xu and C. Boyer, *Polym. Chem.*, 2017, **8**, 5012-5022.

89. W. Wen and A. Chen, *Polym. Chem.*, 2021, **12**, 2743-2751.

90. L. Barrientos, E. Lang, G. Zapata-Torres, C. Celis-Barros, C. Orellana, P. Jara and N. Yutronic, *J. Mol. Model.*, 2013, **19**, 2119-2126.

91. N. Li, L. Qi, J. Qiao and Y. Chen, *Anal. Chem.*, 2016, **88**, 1821-1826.

92. L. Girifalco and R. J. Good, *J. Phys. Chem.*, 1957, **61**, 904-909.

Chapter 6

Conclusions and Future Directions

6.1 Overall Conclusions

Polymerisation-induced self-assembly (PISA) is a significant step forward from conventional solution self-assembly by providing *in situ* synthesis of nano-objects with a relatively high solid content. PISA is based on the extension of a second block from a macro-CTA to form amphiphilic self-assemblies *via* either dispersion or emulsion polymerisation (depending on the monomer solubility in solvent). The morphology of the *in situ* formed self-assemblies could be controlled by varying the degree of polymerisation (DP), and the ratio of solvophilic and solvophobic blocks. The synthesis of block copolymers in PISA usually requires the use of RDRP techniques, especially RAFT polymerisation. In recent years, PISA has been extensively utilised to perform convenient and relatively large-scale synthesis of functional nano-objects with higher-order of complexity. Recent progress in the emerging trends of RAFT-mediated PISA were summarised in Chapter 2. Different non-thermal initiation processes were discussed, including photo-, enzyme-, redox- and ultrasound-initiation. These initiation processes proceed at lower reaction temperature thus allowing the PISA to be combined with temperature-sensitive biomolecules, which may open up new scopes of research for PISA formulations. Nano-objects with higher-order of complexity, conjugated with organic/inorganic materials, and with stimuli-responsiveness were also summarised, demonstrating that PISA has the ability to realise a diverse range of functional materials. Some examples of high throughput PISA such as continuous flow and oxygen tolerant processes were summarised, showing the efforts in the realisation of upscale production. Finally, Chapter 2 also provides an overview of the current applications of PISA-derived nano-objects in the fields of biomedicine, catalysts, Pickering emulsifiers, imaging agents, lubricants, templating agents, pigments, etc.

In this thesis, new scope of PISA *via* ultrasound initiation and hierarchical self-assembly has been explored. Chapter 3 demonstrates the first example of an ultrasound-initiation of PISA process at room temperature that achieved PEG_{113}-*b*-$PHPMA_x$ block copolymer nano-objects in various morphologies.

The use of water as both solvent and initiator source in sono-RAFT-PISA exhibits the "green" synthesis feature of this technique. This allows the fabrication of nano-objects in a system that is sensitive to heat and external initiators or additives. The morphologies of the same block copolymer were different between thermal-PISA and sono-PISA. Vesicles with uniform and smaller size (~110 nm) which are rarely achieved by thermal-PISA can be easily prepared by this methodology. Furthermore, due to the acoustic streaming effect in an ultrasound system, worm-like micelles were challenging to be achieved. However, the introduction of core-cross-linking components offers a feasible approach for the synthesis of worm-like micelle via sono-RAFT-PISA.

In Chapter 4, ultrasound has been used to generate both initiators for PISA and reducing species for the *in situ* formation of metal nanoparticles, thus achieving nanocomposites of polymeric nanoparticles embedded with metal nanoparticles. The use of sono-PISA provides an effective *in situ* self-assembly strategy for the scalable preparation of copolymer nano-spheres PEG$_{113}$-*b*-PDMAEMA$_{24}$-*b*-PHPMA$_n$. It was also shown that the sizes of the polymeric nano-spheres can be easily modified by increasing the DP of the PHPMA block. In addition, using ultrasound as the reducing source, it is possible to prepare polymer-Au and polymer-Pd nanocomposites with AuNPs and PdNPs being immobilised on the PDMAEMA block. It was found that the size of metal nanoparticles is closely related to the ratio of tertiary amine groups in the polymer matrix to metal atoms. These polymer-metal nanocomposite materials are particularly attractive as nano-catalysts, and the catalytic applications of both polymer-Au and polymer-Pd nanocomposites were demonstrated for the aerobic oxidation of alcohol and Suzuki-Miyaura cross-coupling reactions, respectively. Meanwhile, these metal nanocomposites exhibit superior catalytic efficiency than PVP-stabilised metal nanoparticles due to the larger exposed metal area. Furthermore, it was also demonstrated that the sizes of AuNPs on the polymer matrix could be further grown incrementally to afford potential applications such as SERS substrate.

Chapter 5 demonstrates a promising strategy of polymerisation-induced hierarchical self-assembly resulting in complex morphologies. Through the "host-guest" complexation between MβCD and monomers, water-immiscible monomers (st, *t*BMA, *t*BA) could be readily converted into water-soluble complexes at 1:1 molar ratio of monomer: MβCD, therefore providing a series of additional monomer options for aqueous dispersion polymerisation. A series of ABC linear triblock copolymer nanoparticles

(EST, ETS, EMS) were achieved by the addition of a third monomer (1:1 to MβCD) in the seeded dispersion polymerisation process. Specifically, EST self-assembled into rarely achieved AX_n-type colloidal molecules *in situ* with high purity and concentration (e.g. 81.6 % AX_4, 24.5 g/L), which provides a scalable possibility for the synthesis of CMs. ETS and EMS form core-shell-corona micelles and raspberry-like micelles, respectively. The proposed particle formation mechanism suggests that different morphologies were formed due to the interfacial energy.

6.2 Recommended Future Investigations

In this thesis, RAFT-mediated PISA with high versatility and compatibility has evolved into a more powerful tool than it was a decade ago. Here, some recommended future investigations are provided based on current limitations found in this field.

To date, many morphologies observed in conventional solution self-assembly have been realised by PISA, however, there are still some complex structures that have yet to be realised, for example, Janus cylinder,[1] ellipsoidal particle stacked internal lamellae,[2] oblate ellipsoids[3] and so forth. Besides, whether there are any "PISA-exclusive" structures that cannot be accessed by conventional solution self-assembly. More efforts to achieve complex structures by PISA are expected, where hierarchical self-assembly will attract more attention to achieve 2D and 3D hierarchical structures, eventually leading to higher-level architecture by PISA. It is foreseen that the exploration in morphology and the expansion of the library of PISA-derived nanostructures will attract more interest.

RAFT-PISA has been applied to a variety of monomers in diverse solvent systems, including water, polar solvents (*e.g.* alcohols), non-polar solvents (*e.g.* *n*-alkanes[4, 5]) and other media including ionic liquids,[6, 7] supercritical CO_2[8-10] and silicone oil,[11] except for strong nucleophilic solvents that may degrade the thiocarbonylthio group. In the future, aqueous formulations will be the focus, as "green" solvents benefit the most in industrial applications. Nano-object produced in aqueous systems also have fewer issues in residual solvents and organic volatile impurities.

Aqueous PISA typically forms kinetically trapped spheres when using water-immiscible monomers. Although some efforts have been made,[12] including our strategy in Chapter 5, to overcome kinetic

trapping, a simpler and more universal strategy is needed. It is recommended that more attention should be paid to overcoming kinetic trapping with fewer additives and higher solids content.

Good mechanical properties are usually reliant on the high molecular weight of the polymer. Fabricating nano-objects with ultra-high molecular weights is a challenge and often requires cross-linking. Increased research is needed to achieve nano-objects with good mechanical properties, which can be combined with the cargo encapsulation capabilities of PISA to produce functional hybrid materials such as films and hydrogels efficiently.

Another big trend for the future is the automated or even the artificial intelligence controlled PISA process. There are already initial attempts by researchers in this area. It is even possible to develop a user-oriented platform, which can be self-controlled according to the desired properties or morphology of the user, thus freeing the hands from experienced chemists. The realisation of this goal will be based on big data of PISA processes and the properties of nano-objects. We believe that as the demand from industry increases, more funds and interdisciplinary talents will join the area of study to help it move to broader applications.

6.3 References

1. A. Wolf, A. Walther and A. H. E. Müller, *Macromolecules*, 2011, **44**, 9221-9229.
2. D. Klinger, C. X. Wang, L. A. Connal, D. J. Audus, S. G. Jang, S. Kraemer, K. L. Killops, G. H. Fredrickson, E. J. Kramer and C. J. Hawker, *Angew. Chem. Int. Ed.*, 2014, **53**, 7018-7022.
3. S.-J. Jeon, G.-R. Yi and S.-M. Yang, *Adv. Mater.*, 2008, **20**, 4103-4108.
4. L. A. Fielding, M. J. Derry, V. Ladmiral, J. Rosselgong, A. M. Rodrigues, L. P. D. Ratcliffe, S. Sugihara and S. P. Armes, *Chem. Sci.*, 2013, **4**, 2081-2087.
5. B. Darmau, M. J. Rymaruk, N. J. Warren, R. Bening and S. P. Armes, *Polym. Chem.*, 2020, **11**, 7533-7541.
6. Q. Zhang and S. Zhu, *ACS Macro Lett.*, 2015, **4**, 755-758.
7. H. Zhou, C. Liu, C. Gao, Y. Qu, K. Shi and W. Zhang, *J. Polym. Sci., Part A: Polym. Chem.*, 2016, **54**, 1517-1525.
8. X. Wang, L. Shen and Z. An, *Prog. Polym. Sci.*, 2018, **83**, 1-27.
9. A. Xu, Q. Lu, Z. Huo, J. Ma, B. Geng, U. Azhar, L. Zhang and S. Zhang, *RSC Adv.*, 2017, **7**, 51612-51620.
10. J. Jennings, M. Beija, A. P. Richez, S. D. Cooper, P. E. Mignot, K. J. Thurecht, K. S. Jack and S. M. Howdle, *J. Am. Chem. Soc.*, 2012, **134**, 4772-4781.
11. M. J. Rymaruk, S. J. Hunter, C. T. O'Brien, S. L. Brown, C. N. Williams and S. P. Armes, *Macromolecules*, 2019, **52**, 2822-2832.
12. D. Li, M. Huo, L. Liu, M. Zeng, X. Chen, X. Wang and J. Yuan, *Macromol. Rapid Commun.*, 2019, **40**, 1900202.

Appendix

Published papers included in the main body of this thesis

Polymer Chemistry

rsc.li/polymers

ROYAL SOCIETY OF CHEMISTRY
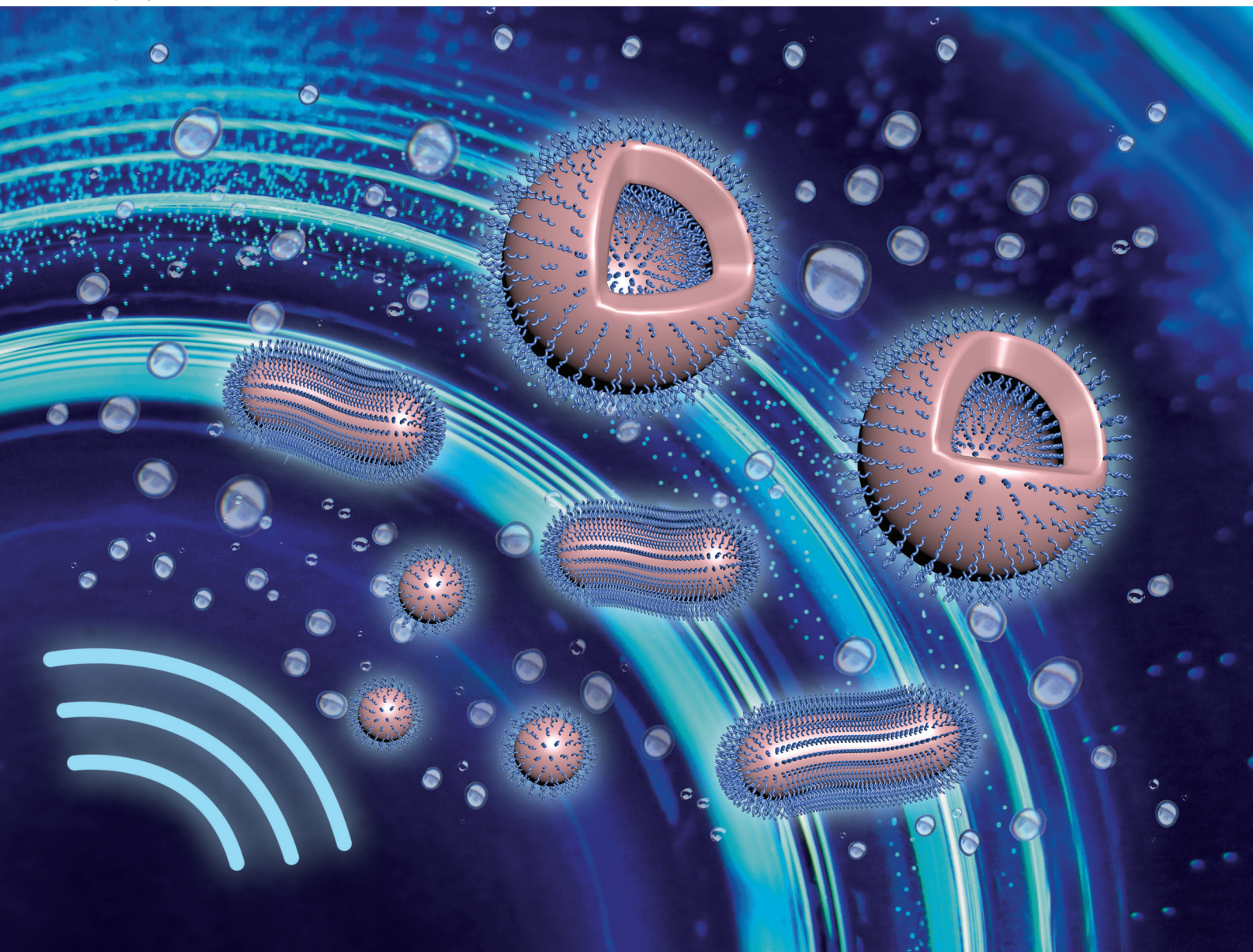
PAPER
Boon M. Teo, San H. Thang *et al.*
Room temperature synthesis of block copolymer nano-objects with different morphologies *via* ultrasound initiated RAFT polymerization-induced self-assembly (sono-RAFT-PISA)

Check for updates

Room temperature synthesis of block copolymer nano-objects with different morphologies *via* ultrasound initiated RAFT polymerization-induced self-assembly (sono-RAFT-PISA)†

Jing Wan,[a] Bo Fan,[a] Yiyi Liu,[b] Tina Hsia,[a] Kaiyuan Qin,[a] Tanja Junkers, [ID] [a] Boon M. Teo [ID] *[a] and San H. Thang [ID] *[a]

Polymerization-induced self-assembly (PISA), which allows scalable synthesis of nano-objects, has drawn significant research attention in the past decade. However, the initiation methods in most of the current reported PISA are still restricted to thermal or photo processes. Sonolysis of a water molecule by high frequency ultrasound to generate a hydroxyl radical and to initiate polymerization has the potential to be a new "initiator-free" synthesis technique. Despite ultrasound-initiated polymerization-induced self-assembly (sono-PISA) being reported, only spherical micelle morphology was achieved. We demonstrate here the first room temperature synthesis of diblock copolymer nano-objects with different morphologies using ultrasound (990 kHz) initiated reversible addition–fragmentation chain transfer PISA (sono-RAFT-PISA) in an aqueous system. It was found that the morphologies of the block copolymer nano-objects prepared by sono-RAFT-PISA were different from those prepared by conventional thermal-PISA. Furthermore, the impacts of ultrasound and presence of a cross-linker on the nano-object morphology were investigated. It was observed that the stability of worm-like micelles will be affected by ultrasound but could be strengthened *via* core-cross-linking (CCL). Overall, the externally-regulatable, easily scalable and sustainable "green" features of ultrasound have the potential to promote the application of sono-PISA for the fabrication of nano-objects.

Introduction

Polymerization-induced self-assembly (PISA), which has drawn significant research attention in the past decade,[1–4] is a relatively new and powerful methodology for *in situ* fabrication of nano-objects during polymerization. In a typical PISA process, a solvophilic macromolecule (macro-CTA; block A) is chain-extended using a second monomer in a suitable solvent *via* either dispersion or emulsion polymerization (depending on the monomer solubility in the solvent).[5] The growth of the second block (B), which is insoluble in the solvent, leads to the *in situ* self-assembly of the AB diblock copolymer into nano-objects. By varying the degree of polymerization (DP), and the volume fraction of A and B blocks, nano-objects with various morphologies such as spheres, worms, vesicles and even oligo-lamellar vesicles can be obtained at different solid contents (10 to up to 40–50% w/w).[5–8] The self-assembled nano-objects have a broad range of applications, such as drug delivery,[3,9] bio-imaging agents,[10,11] stimuli-responsive smart nanomaterials,[12,13] Pickering emulsifiers[14] and so forth.

The synthesis of block copolymers in PISA usually requires the use of living/controlled polymerization techniques.[15] The common controlled polymerization technique for PISA reported in the literature is the reversible deactivation radical polymerization (RDRP) technique, including reversible addition–fragmentation chain transfer (RAFT) polymerization, atom transfer radical polymerization (ATRP)[16–18] and nitroxide-mediated polymerization (NMP).[19–21] Recently, the Xie and Choi groups reported ring-opening metathesis polymerization (ROMP) induced self-assembly (ROMP-PISA), which further expanded the polymerization techniques for PISA.[22–25] Nevertheless, for practical applications, the most widely used technique for PISA is RAFT polymerization, which is versatile for a broad range of monomers and solvents.[26–30]

Thermal initiation and photo-initiation are the most widely employed methods for generating radicals required for RAFT polymerization in the PISA process. However, in the past few

[a]*School of Chemistry, Monash University, Clayton, VIC 3800, Australia.*
E-mail: san.thang@monash.edu, boonmian.teo@monash.edu
[b]*Department of Chemical Engineering, Monash University, Clayton, VIC 3800, Australia*

†Electronic supplementary information (ESI) available: NMR, GPC, and DLS data; TEM, cryo-TEM and SEM images. See DOI: 10.1039/d0py00461h

years, there has been growing interest in new initiation mechanisms that provide alternative approaches for PISA. This trend and new initiation mechanisms were thoroughly reviewed by Armes and Boyer recently.[31] Thermally initiated RAFT-PISA is usually conducted at elevated temperature (usually ≥50 °C) with the utilization of a water-soluble azo-compound initiator regarding aqueous dispersion polymerization.[32–35] Photo-initiated RAFT-PISA[36,37] provides a successful strategy for low temperature and room temperature reactions; Boyer's group reported the iniferter approach to perform the PISA process without the addition of an external initiator or catalyst,[38] however, it still involves the addition of photo-initiators in most photo-PISA processes.

The promising strategy of RAFT-PISA initiated by ultrasound without the addition of external initiators or additives has not been explored until recently by Qiao and Ashokkumar.[39] Ultrasound is a sound wave with a frequency higher than 20 kHz which has been applied in the fields of imaging,[40] chemical synthesis[41] and guided drug delivery.[42] In polymer synthesis, emulsion polymerization of hydrophobic monomers has been achieved using low frequency (20–100 kHz) ultrasound.[43,44] In this sono-polymerization process, ultrasound was used as a source of external energy and to initiate radical generation for the preparation of a mini-emulsion or a microemulsion. Compared to low-frequency ultrasound, high-frequency (>200 kHz) ultrasound creates a larger number of cavitation bubbles with a smaller size, and it leads to a notable increase of radical generation and a decrease in the shear forces so that no polymer degradation occurs.[45] In a recent study by Qiao and Ashokkumar,[39] high frequency ultrasound was employed for the synthesis of poly(poly(ethylene glycol) methyl ether acrylate)-*block*-poly[(*N*-isopropyl acrylamide)-*co*-(*N*,*N*'-methylenebisacrylamide)] (PPEGA-*b*-P(NIPAM-*co*-MBA)) thermosensitive nanogel *via* dispersion polymerization at 45 °C. MBA was employed as a crosslinker in order to maintain the PNIPAM-based copolymer micelles at a temperature below the lower critical solution temperature (LCST). However, only spherical micelles were prepared *via* this strategy at elevated temperature. The possibility of performing sono-RAFT-PISA at room temperature and the formation of polymeric nano-objects in other morphologies are worth investigating.

In this study, we describe the first room temperature sono-RAFT-PISA to obtain PEG-based nano-objects with various morphologies (Scheme 1). First, the PEG macro-CTA (PEG$_{113}$-RAFT) was synthesized using a modified procedure from the literature.[46] In the next step, 2-hydroxypropyl methacrylate (HPMA) was employed as a core-forming monomer (B), which has been reported to generate a range of morphologies including spheres, worms and vesicles in thermal and photo-initiated PISA.[35,47] High frequency ultrasound (990 kHz) was applied to generate hydroxyl radicals by sonolysis of water molecules, and induce the polymerization reaction. *Via* this strategy, we successfully achieved the room temperature sono-RAFT-PISA and obtained not only spherical micelles but also worm-like micelles and small vesicles for the first time.

## Experimental section

Materials

Diisopropyl carbodiimide (DIC; >99%) was purchased from Oakwood Chemical (USA). 4-Dimethylaminopyridine (DMAP; 99%) was purchased from Alfa Aesar. 4-Cyano-4-(((dodecylthio)carbonothioyl)thio)pentanoic acid (CDTPA; 97%) was purchased from Boron Molecular (Australia). Poly(ethylene glycol) methyl ether (mPEG$_{113}$, average M_n 5000) and hydroxypropyl methacrylate (HPMA, a mixture of 2-hydroxypropyl and 2-hydroxyisopropyl methacrylate; 97%) were purchased from Sigma-Aldrich (Australia). 2,2'-Azobis[2-(2-imidazolin-2-yl)propane]dihydrochloride (AIPD, VA-044) was purchased from Wako Pure Chemical Industries, Ltd. All the other solvents were obtained from a commercial source and were used as received unless noted otherwise.

Synthesis of the poly(ethylene glycol) trithiocarbonate (PEG$_{113}$-CDTPA) macro-CTA

mPEG$_{113}$ (6.0 g, 1.2 mmol) was dissolved in 30 mL toluene in a round bottom flask to remove water azeotropically that associated with PEG by rotary evaporation (repeated 3 times). Dichloromethane (30 mL) was then added to the flask containing mPEG$_{113}$ (6.0 g, 1.2 mmol). CDTPA (970.0 mg, 2.4 mmol), DIC (0.3 g, 2.4 mmol) and DMAP (29.0 mg, 0.24 mmol) were added to the flask in order. The flask was sealed with a rubber septum. The esterification reaction was allowed to proceed with stirring at room temperature for 24 hours. The polymer was collected by precipitation of the reaction mixture in cold diethyl ether 3 times. PEG$_{113}$-RAFT was obtained as a pale yellow solid after drying under reduced pressure (76% yield). ^{1}H NMR (400 MHz, CDCl$_3$): δ 4.25 (t, 3H), 3.45–3.81 (m, 452H), 3.37 (s, 3H), 3.31 (t, 3H), 2.37–2.65 (m, 4H), 1.86 (s, 3H), 1.68 (m, 2H), 1.25–1.38 (b, 18H), 0.87 (t, 3H). ^{13}C NMR (150 MHz, CDCl$_3$): δ 216.8, 171.3, 118.9, 71.8, 70.4, 68.8, 64.0, 58.9, 46.2, 33.7, 31.8, 29.2, 24.7, 22.6, 14.0.

RAFT dispersion polymerization of HPMA *via* ultrasound initiation

The following representative protocol was used for the ultrasound-initiated RAFT dispersion polymerization-induced self-assembly (sono-RAFT-PISA) process for the synthesis of PEG$_{113}$-PHPMA$_{600}$ at 10% w/w solid content at room temperature (~23 °C). The HPMA monomer was disinhibited by
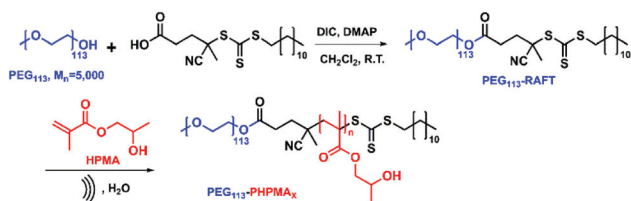
Scheme 1 Synthesis of PEG$_{113}$-RAFT and PEG$_{113}$-PHPMA$_X$ copolymers *via* the sono-RAFT-PISA process.

passing through a column of basic alumina, and then passing through a silica gel column (*n*-hexane : diethyl ether = 1 : 1 eluent) to remove the dimethacrylate impurity. PEG$_{113}$-CDTPA macro-CTA (11.7 mg, 2.2 μmol) and HPMA monomer (188.3 mg, 1.32 mmol, target DP = 600) were weighed in a 12 mL glass test tube with a socket and dissolved in DI water (1.80 mL, 10% w/w). The test tube was sealed using a rubber septum and deoxygenated by purging with argon using needles through the liquid for 30 minutes. The test tube was then immersed in an ultrasonic water bath with a circulated cooling water jacket maintained at room temperature (~23 °C) during the reaction. The distance between the bottom of the test tube and the transducer plate was kept as 5 cm (as shown in Fig. S3†). The ultrasonic generator (Meinhardt Ultrasonics, model M11-010, output power 250 W) was then switched on (990 kHz, 80% intensity). For kinetic studies, aliquots were removed periodically for analyses by ^{1}H NMR spectroscopy (Fig. S1c†) and GPC. The reaction was stopped by switching off the ultrasonic generator and exposure to air after 1–2 h of irradiation.

RAFT dispersion polymerization of HPMA *via* thermal initiation

The following protocol was used for thermally initiated RAFT dispersion polymerization-induced self-assembly (thermal-PISA) for the synthesis of PEG$_{113}$-PHPMA$_{400}$ at 10% w/w solid content at 50 °C. The HPMA monomer was pre-treated as described above. PEG$_{113}$-CDTPA macro-CTA (17.1 mg, 3.2 μmol), HPMA monomer (182.9 mg, 1.28 mmol, target DP = 400) and VA-044 (32 μL of 10 mg ml^{-1} stock solution, 1.0 μmol) were added in a round-bottom flask containing a stirrer bar and dissolved in DI water (1.80 mL, 10% w/w). The flask was sealed using a rubber septum and deoxygenated by purging with argon using needles through the liquid for 60 minutes. The mixture was stirred at 700 rpm for 30 minutes, followed by immersing the flask in an oil bath at 50 °C. The stirring speed was maintained at 700 rpm throughout the reaction. The reaction was stopped by cooling to 20 °C and exposure to air after 4 h.

Quantification of the generated hydrogen peroxide (H$_2$O$_2$)

By assuming that the produced hydroxyl radicals mostly recombine to form hydrogen peroxide, the quantification of hydrogen peroxide was used to estimate the formation of radicals. The spectroscopic method described by Hochanadel[48] was used, in which I$^-$ is oxidized to I$_3^-$ by H$_2$O$_2$ in a 1 : 1 ratio. In detail, 1 mL of freshly sonicated sample was mixed with 1 mL of solution A (0.4 M KI, 0.1 M NaOH, and 0.02 mM (NH$_4$)$_6$Mo$_7$O$_{24}$·4H$_2$O) and 1 mL of solution B (0.1 M C$_8$H$_5$KO$_4$). The solution was allowed to stand for 5 minutes for the reaction to proceed. The solution was then analyzed by UV/Vis spectrophotometry and the absorption at 353 nm was recorded. The molar extinction coefficient for I$_3^-$ of 26 400 M^{-1} cm^{-1} was used.

Analytical techniques

Dynamic light scattering (DLS) measurements were performed at 20 °C using a Brookhaven Nanobrook Omni Particle Size Analyzer. The aqueous dispersions containing the diblock copolymer nano-objects were diluted to 0.10% w/v using DI water. Light scattering was detected at 90° and hydrodynamic diameters were determined by assuming spherical, non-interacting, perfectly monodisperse particles. ^{1}H Nuclear magnetic resonance spectroscopy (NMR) spectra were recorded on a Bruker Avance 400 NMR spectrometer at frequencies of 400 MHz. NMR chemical shifts (δ) are reported in ppm and were calibrated against residual solvent signals of CDCl$_3$ (δ 7.26) and DMSO-d_6 (δ 2.50). Samples were dissolved in CDCl$_3$ and DMSO-d_6 at 5–10 mg mL^{-1}. The data are reported as chemical shift (δ). Gel permeation chromatography (GPC) was performed on a system comprising a Shimadzu LC-20AT pump, a Shimadzu RID-20A refractive index detector, and an SPD-20A UV–visible detector. The GPC is equipped with a guard column (WAT054415) and 3× Waters GPC columns (WAT044238, WAT044226, WAT044235, 300 mm × 7.8 mm). The eluent is DMF with 10 mM LiBr and eluted at 1 mL min^{-1} for 45 min in total. The samples were dissolved in DMF with 10 mM LiBr, and filtered through 0.20 μm syringe filters. A calibration curve was obtained from poly(methylmethacrylate) (PMMA) standards (Agilent) ranging from 960 to 1 568 000 g mol^{-1}. Transmission electron microscopy (TEM): copper grids (formvar/carbon coated, 400 mesh) were plasma glow-discharged for 10 seconds to create a hydrophilic surface. After glow discharge, the grid was brought into contact with a drop (about 15 μL) of 0.10% w/v aqueous dispersions containing the diblock copolymer nano-objects for 3 minutes. After blotting to remove excess sample dispersion, the grids were negatively stained by bringing them into contact with a drop (about 15 μL) of uranyl acetate solution (2.0% w/v) for 1 minute. The grid was blotted again to remove excess stain and dried using a gentle nitrogen blow. Imaging was performed using an FEI Tecnai G2 T20 TWIN TEM instrument equipped with an Orius SCD200D wide-angle CCD camera operating at 200 kV. Cryogenic transmission electron microscopy (cryo-TEM): the image was taken using an FEI Tecnai Spirit G2 TEM. Briefly, copper grids (200-mesh) coated with a holey carbon film (Quantifoil R2/2) were glow discharged in a Pelco glow discharge unit to render them hydrophilic. 5 μL of sample (0.1 mg mL^{-1}) were applied onto the grids, which were blotted against two filter papers for 3 seconds at a blot force of −3 in a Vitrobot plunge freezer system (FEI). The resulting thin sample film was vitrified in a controlled environment vitrification system at 4 °C and 70% relative humidity by plunging the sample into liquid ethane, which was maintained at its melting point with liquid nitrogen. The vitrified specimens were transferred to a Gatan 626 cryoholder and observed at an operating voltage of 120 kV in a Tecnai Transmission Electron Microscope (FEI) at a temperature of −179 °C. Images were recorded with a Gatan Eagle high-resolution CCD camera (4k × 4k) at magnifications ranging from 15 000× to 110 000× and digitized using the Tecnai Image Acquisition (TIA) program. Scanning electron microscopy (SEM): the SEM sample was prepared by casting a drop (about 10 μL) of 0.10% w/v aqueous dispersions containing the diblock copolymer nano-objects on

a silicon wafer. The dispersion was then dried using a gentle nitrogen blow. The sample was then coated with a thin layer (~2 nm) of iridium to make it conductive. Imaging was performed using an FEI Nova NanoSEM 450 FEGSEM instrument operating at 3.0 or 5.0 kV.

Results and discussion

Before any PISA attempts, we confirmed the formation of radicals using the high-frequency (990 kHz) ultrasound transducer through the quantification of hydrogen peroxide in argon-purged water, with the assumption that the produced hydroxyl radicals mostly recombine to form hydrogen peroxide. It was observed that the generation of H_2O_2 is proportional to ultrasound irradiation time and frequency (Fig. S4†). After 2 hours of irradiation at 990 kHz, the concentration of H_2O_2 increased to ~630 μM, which corresponds to 1.26 mM of hydroxyl radicals (by assuming that one H_2O_2 is formed by two hydroxyl radicals).

The macro-RAFT agent (PEG$_{113}$-CDTPA) was synthesized by coupling of hydrophilic poly(ethylene glycol) methyl ether (PEG$_{113}$, average M_n 5000) with 4-cyano-4-(((dodecylthio)carbonothioyl)thio)pentanoic acid (CDTPA) through Steglich esterification, with diisopropyl carbodiimide (DIC) as a coupling agent and 4-dimethylaminopyridine (DMAP) as a catalyst. The success of coupling and the purity of the macro-RAFT agent were confirmed by ^{1}H NMR and ^{13}C NMR spectroscopy (Fig. S1a and S1b†).

Next, PEG$_{113}$-CDTPA was chain extended with a purified monomer (HPMA) in an aqueous environment under ultrasound irradiation. As shown in the kinetics data (Fig. 1), sono-PISA could be roughly separated into two regimes, which have a very similar pattern to the kinetics of thermal-PISA investigated by the Armes group[35] and photo-PISA reported by Tan *et al.*[36] The first regime, which occurs between 0 to 60 min, has a relatively slow polymerization rate, corresponding to the formation of diblock copolymer chains which are still in a molecularly dissolved state. The point of intersection of two lines indicates that the micellar nucleation occurs at around 70 min, which corresponds to 41.5% conversion of HPMA for this formulation. This conversion corresponds to a mean DP of 250 for the nucleation of the PHPMA block. Beyond this point, the polymerization rate drastically increases. This is due to micelle cores acting as multiple mini-reactors; the unreacted HPMA monomer enters into the core to solvate the hydrophobic PHPMA chains.[35,49] The critical DP of 250 is much higher than the critical DP of 110 previously reported by Tan *et al.* for the PPEGMA$_{14}$-CDPA macro-CTA utilized to polymerize HPMA (target DP = 200) at room temperature,[36] also higher than the critical DP of 135 reported by Warren *et al.* for PEG$_{113}$-PHPMA (target DP = 600) at 50 °C.[35] The temperature of polymerization is one of the factors that leads to different critical DPs, since the degree of hydration for the PHPMA block is temperature-dependent as previously reported.[50,51] The other possible reason is suspected to be the ultrasound effect. This will be discussed in the morphology studies section.

The GPC results show a linear relationship between M_n and PHPMA conversion (Fig. 1 inset), which confirmed the living characteristics of this ultrasound-initiated RAFT polymerization. Meanwhile, the dispersity ($Đ$) increases with the chain length of the polymer (Fig. 1 inset), and the final $Đ$ of PEG$_{113}$-PHPMA$_{600}$ is still relatively low ($M_w/M_n = 1.50$). These characteristics indicate that good control is maintained for dispersion polymerization initiated by ultrasound. The GPC analysis of PEG$_{113}$-PHPMA$_X$ (target DP from 200–800) confirms a systematic increase in M_n and a relatively low $Đ$ of 1.13–1.61 (Fig. 2). It should be noted that the GPC trace of PEG$_{113}$-RAFT is bimodal, and the M_n value of PEG$_{113}$-RAFT is around 11 400 (based on poly(methyl methacrylate) calibration standards) and 21 300 for the side peak. The presence of the side peak impurity is not due to the synthesis of PEG$_{113}$-RAFT but due to

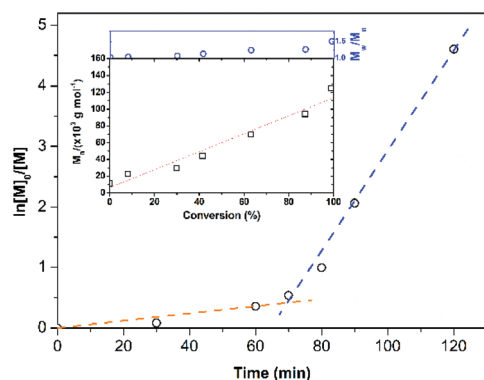**Fig. 1** Polymerization kinetics of HPMA (PEG$_{113}$-PHPMA$_{600}$ targeted) *via* ultrasound (990 kHz, 80%) initiated RAFT aqueous dispersion polymerization at room temperature (~23 °C) and 10% w/w solid content.

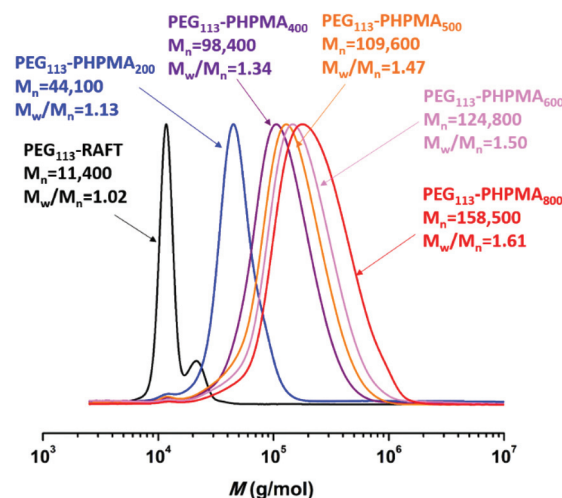**Fig. 2** Gel permeation chromatography traces (PMMA standards) obtained for PEG$_{113}$-PHPMA$_X$ (target DP x = 200–800) copolymers synthesized *via* sono-PISA at room temperature (~23 °C).

the purchased $mPEG_{113}$ because the same side peak appears on the GPC trace of $mPEG_{113}$ (Fig. S5†). Upon comparing the GPC results of the diblock polymer with the same DP but prepared by sono-PISA and thermal-PISA (Table S1†), the M_n values are very close but the $Đ$ values of sono-PISA are not as low as those of thermal-PISA. This could result from the different concentrations of radicals generated through polymerization. Taking PEG_{113}-$PHPMA_{400}$ thermal synthesis as an example, the total radical concentration generated by VA-044 is 0.49 mM (50 °C, 4 h, calculation described in the ESI†), whereas the hydroxyl radical concentration is around 1.26 mM at the end of 2 h of sonication. The relatively high hydroxyl radical concentration during sono-PISA can be considered as a relatively low CTA/initiator ratio and can contribute to the formation of dead chains.[29,52,53] The essentiality of removing the dimethacrylate impurity in HPMA is also shown by GPC studies. The GPC trace with bimodal polymer peaks was obtained from the same experiments using HPMA without the removal of dimethacrylate (Fig. S6†), showing significant elimination of cross-linking *via* the use of purified HPMA.

Nano-objects were also constructed utilizing the same macro-CTA and HPMA but *via* thermal-PISA for comparison purpose. The hydrodynamic diameters and morphologies for nano-objects constructed by sono-PISA and thermal-PISA were significantly different (Table S1†). For thermal-PISA, similar to many other studies, the PEG_{113}-$PHPMA_{100}$ copolymer formed spherical micelles at 10% solid content with an average diameter of 20 ± 4 nm (the error is the standard deviations as calculated by measuring 60 particles) as measured by TEM (Fig. S7c†) and 31.8 ± 0.8 nm (PDI = 0.13 ± 0.02) by DLS (Table S1†). The mean diameters measured from the TEM

images were smaller than those measured by DLS. This can be attributed to particles being dry rather than hydrated, and DLS could overestimate particle size since the scattering from larger particles can increase the overall particle diameter derived by DLS.[54] A mixture of worms and spheres was generated in the case of PEG_{113}-$PHPMA_{150}$ (Fig. S7d†). TEM images of PHPMA at DPs of 200–300 indicate the mixture of worms and vesicles (including "jellyfish"-like) (Fig. 3e and S7e†), and the dispersion formed is soft and free-standing gel (Fig. S7a and b†). A pure vesicle phase was obtained when the DP of PHPMA is 400 (Fig. 3f). On the other hand, for sono-PISA, when the DP of PHPMA ranges from 104 to 500, only monodisperse spherical micelles were obtained with the hydrodynamic diameter from 28.7 to 72.0 nm and PDI of 0.06–0.13 as measured by DLS and confirmed by TEM and SEM. At a DP of 600, the TEM image (Fig. 3c) combined with the SEM image (Fig. S8a†) confirmed that the morphology is a mixture of 46 ± 9 nm spherical particles and 102 ± 13 nm vesicles; DLS indicates a Z-average diameter of 111.4 ± 1.5 nm (PDI = 0.11 ± 0.07). As for a higher DP of 800, small vesicles with a size of 114 ± 12 nm were obtained (Fig. 3d), and the wall thickness of the vesicles is around 45 nm. SEM images (Fig. S8b†) confirm the overall morphology of vesicles, which are hollow vesicular rather than donut-like. The morphology of the vesicle was further disclosed by cryo-TEM (Fig. 3h and Fig. S13†). Moreover, by comparing the DLS results of vesicles constructed by these two processes (Fig. 4), apart from the fact that the size of the sonochemically produced vesicles is much smaller (126.2 nm *vs.* 599.2 nm), the PDI is also narrower (0.02 *vs.* 0.23), which indicates that the vesicles are monodisperse. These results indicate that for the same DP of PHPMA, the
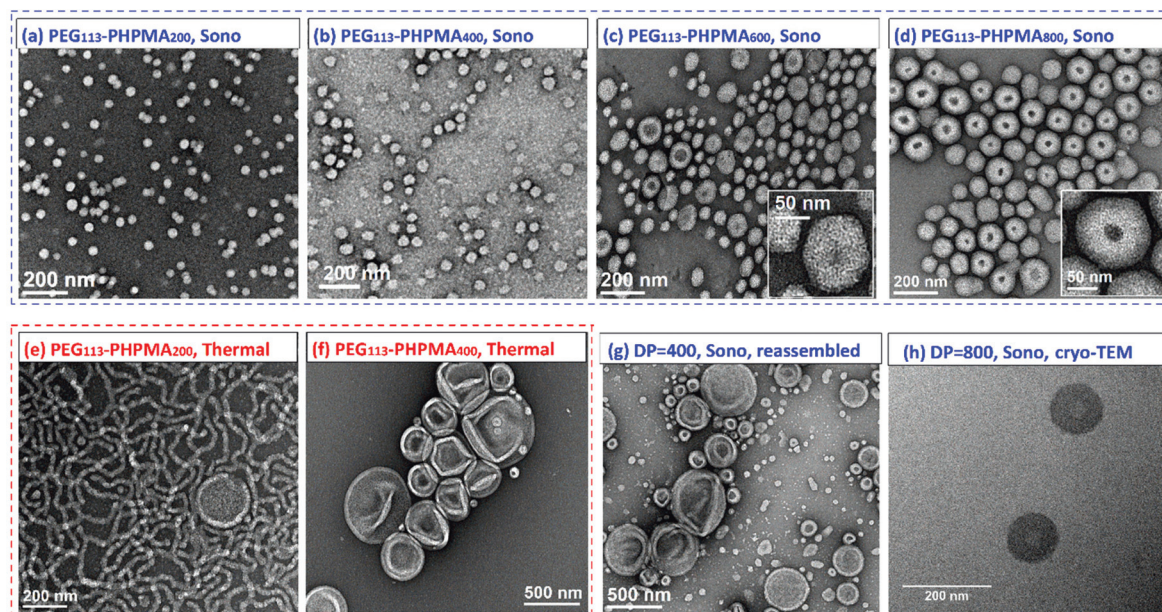

Fig. 3 Representative TEM images monitored for PEG_{113}-$PHPMA_X$ copolymer nano-objects synthesized *via* (a–d) sono-PISA at room temperature and (e and f) thermal-PISA at 50 °C. (g) TEM image of PEG_{113}-$PHPMA_{400}$ after reassembly and (h) cryo-TEM image of PEG_{113}-$PHPMA_{800}$ vesicles (all prepared at 10% w/w solid content).
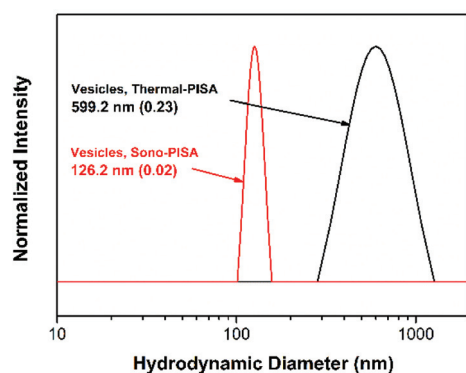
Fig. 4 DLS size distributions recorded for samples with the target composition of PEG_{113}-$PHPMA_{400}$ (prepared *via* thermal-PISA) and PEG_{113}-$PHPMA_{800}$ (prepared *via* sono-PISA).

morphologies of the nano-objects obtained from sono-PISA were distinct from those obtained from thermal-PISA.

It was surprising that a higher DP was required for the sonochemical morphology transition compared to the thermal-PISA system. The high critical DP is also described above in kinetic studies. Tan *et al.*[55] reported that only spheres are at DP = 350 formed by photo-PISA at room temperature (10% w/w solid content), which is similar to the results in this study. However, different morphologies were formed at 37 °C as in the previous report.[56] The effect of the reaction temperature difference should be considered. Due to the upper limit of operating temperature of the ultrasonic transducer, sono-PISA cannot be performed at 50 °C. Hence the control experiment was conducted by heating the nano-object suspension (10% w/w) after the sono-PISA reaction to 50 °C for 24 h. By comparing the TEM images of Fig. 3b and Fig. S9a,† the temperature rise has a limited effect on the morphology transition of PEG_{113}-$PHPMA_{400}$ since it remains as spheres. However, for PEG_{113}-$PHPMA_{800}$, the lumen of vesicles diminished after heating (Fig. S9b†), and the overall size remains around 110 nm. The structure is similar to that of thermal-PISA synthesized nano-objects (Fig. S9c†), but it is much smaller in particle size. These demonstrate that temperature could influence the morphology transformation but to a limited extent. In addition, we disassembled the PEG_{113}-$PHPMA_{400}$ spheres prepared *via* sono-PISA by dissolving the dried polymer in tetrahydrofuran (THF), and reassembled *via* solution self-assembly by adding water to the polymer solution. As shown

in Fig. 3g, PEG_{113}-$PHPMA_{400}$ reassembled into vesicles with a structure very similar to those prepared *via* thermal-PISA, which demonstrates that without an ultrasound effect, sono-prepared polymers have the same self-assembly behavior as thermally-prepared polymers. This result indicates that the morphology difference between thermal-PISA and sono-PISA could result from the presence of ultrasound during the polymerization.

There are only limited studies on investigating the effect of ultrasound on polymer nanoparticles and their morphologies. Miki *et al.* reported that the self-assemblies of Janus-type polymers with a uniform size were affected by ultrasonic frequency.[57] Dang *et al.* observed a change in the morphology of vesicle nanoparticles to large complex micelles following the increase of ultrasonic power intensity.[58] However, these studies did not explain the morphology difference between thermal-PISA and sono-PISA. The hypothesized reason is the influence of ultrasonic energy input during polymerization. As shown in Fig. 5, for the nano-objects composed of the same quantity of PEG_{113}-$PHPMA_{400}$ chains, the total surface area of spheres is larger than that of vesicles as a spherical particle has a smaller size than a vesicle. Therefore, the larger surface area of spheres renders higher surface free energy than vesicles, hence it requires further external energy, which was provided by ultrasound. From the perspective of the packing parameter (P, defined as $P = V/a_0 l_c$, in which V and l_c represent the volume and length of the hydrophobic block, respectively, and a_0 stands for the effective area of the hydrophilic headgroup), when $P \leq 1/3$, sphere is the preferred morphology, and when $1/2 < P \leq 1$, vesicle is the preferred morphology. The higher surface free energy system allows a larger surface area, as the number of molecules (N) remains the same, resulting in a larger head group area (a_0) and a smaller P; therefore spherical morphology is preferred under ultrasound. In terms of nano-object stability, we examined the morphology and size of sono-PISA prepared nano-objects by TEM and DLS (Fig. S10†). After 3 months of standing at room temperature, all suspensions remain stable with a negligible change in size and morphology, which indicates that the nano-objects prepared by sono-PISA are relatively stable at room temperature.

No worm-like micelle was observed for sono-PISA nano-objects when using purified HPMA whether changing the target DP or sampling during polymerization (Fig. S11†). This could be due to the fact that the worm region can be very narrow in some cases,[59] and thus worms might exist but
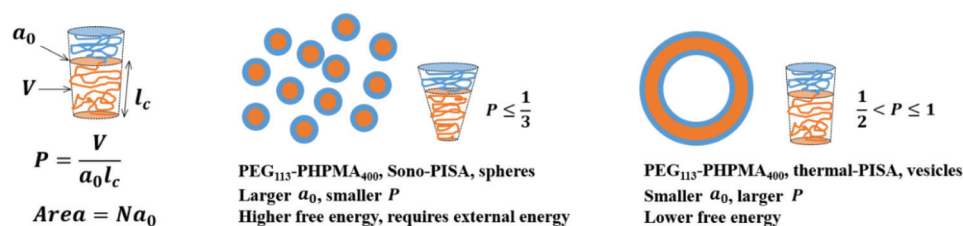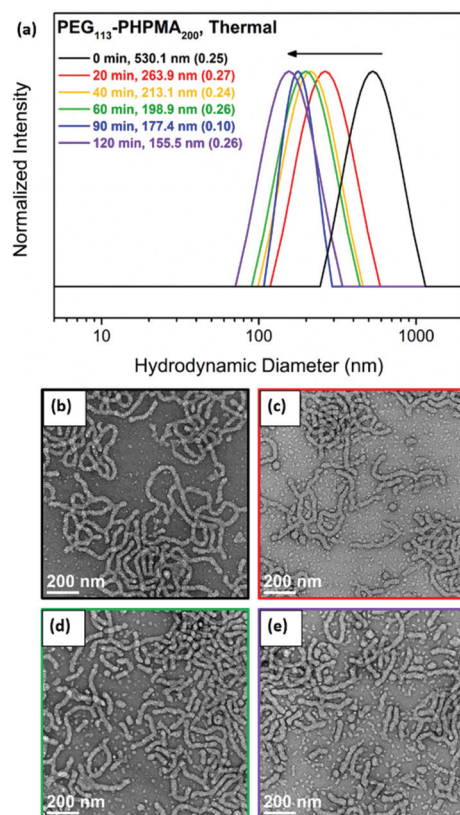

Fig. 5 Schematic of PEG_{113}-$PHPMA_{400}$ nano-objects synthesized *via* sono-PISA and thermal-PISA.

have not been found. The other highly possible reason is that although the physical effects generated by the high ultrasonic frequency are limited, the acoustic streaming effect is still present in the system and could limit the formation of worm and rod-like micelles. Acoustic streaming is a streaming flow of fluid around an oscillating bubble induced by an acoustic field,[60] and has been used to manipulate particles in a fluid.[61] This was further demonstrated by applying an ultrasound wave on a worm suspension generated by a thermal-PISA process; the morphology changed from worms to shorter worm fragments and spheres (Fig. 6b–e), and the hydrodynamic diameter also decreased with increasing sonication time (Fig. 6a). Therefore, for sono-PISA, a strategy to overcome the influence of the acoustic streaming effect is required in order to obtain a worm-like micelle. Many chemistries have been utilized to prepare covalently stabilized block copolymer nano-objects,[62] and most examples focus on core cross-linking (CCL), because conducting shell cross-linking at high copolymer concentrations usually results in interparticle cross-linking and hence irreversible loss of colloidal stability. Therefore, we have performed sono-RAFT-PISA of unpurified HPMA that contains a trace of the dimethacrylate crosslinker. Short worms and larger size vesicles were obtained from PEG_{113}-$PHPMA_{500}$

Table 1 Characterization data of PEG_{113}-b-$P(HPMA_X$-co-$C_Y)$ copolymer nano-objects by sono-PISA

Entry	Component C	Molar ratio of A : B : C[a]	C/B[b] (%)	$Z_{a,DLS}$ (nm)	Morphology[c]
1	EGDMA	1 : 400 : 2	0.5	102.4 ± 3.0	s/w
2	EGDMA	1 : 400 : 4	1.0	195.6 ± 1.5	s/w
3	EGDMA	1 : 600 : 3	0.5	970.1 ± 212.0	w
4	EGDMA	1 : 800 : 1	0.125	388.3 ± 9.3	w/v
5	EGDMA	1 : 800 : 4	0.5	422.7 ± 10.2	w/v
6	BMA	1 : 400 : 2	0.5	65.4 ± 1.5	s
7	BMA	1 : 600 : 3	0.5	105.3 ± 2.9	s/w/v
8	PEGDMA	1 : 400 : 1	0.25	73.9 ± 1.9	s/w
9	PEGDMA	1 : 400 : 2	0.5	130.8 ± 3.6	s/w

[a] A: PEG_{113}-RAFT, B: HPMA monomer, C: comonomer. [b] Molar percentage of C/B. [c] s = spheres, v = vesicles, w = worms.

(Fig. S12†). Thus, CCL renders nano-objects more streaming-resistant to form elongated morphologies.

In order to further investigate the influence of CCL on the morphology of block copolymer nanoparticles, ethylene glycol dimethacrylate (EGDMA) was employed as a comonomer (component C) with purified HPMA (component B) in the presence of PEG_{113}-RAFT (component A). As shown in Table 1, different amounts of dimethacrylate were mixed with the purified HPMA as a binary comonomer. When the HPMA degree of polymerization is 400, the hydrodynamic diameter was 61.1 ± 0.8 nm and the morphology is a sphere (Table S1†). However, for the group with same DP of HPMA and an additional 0.5% molar EGDMA (entry 1), the Z-average size (Z_a) increased to 102.4 ± 3.0 nm, and the morphology is a mixture of short worms and micelle dimers (Fig. 7a) instead of spheres. By increasing the molar ratio of EGDMA to 1.0%, Z_a increased to

Fig. 6 (a) DLS size distribution data recorded for thermal-PISA prepared PEG_{113}-$PHPMA_{200}$ worms after ultrasound irradiation (990 kHz) for 0, 20, 40, 60, 90 and 120 min. Representative TEM images of ultrasound irradiated PEG_{113}-$PHPMA_{200}$ worms for (b) 0 min, (c) 20 min, (d) 60 min, and (e) 120 min.
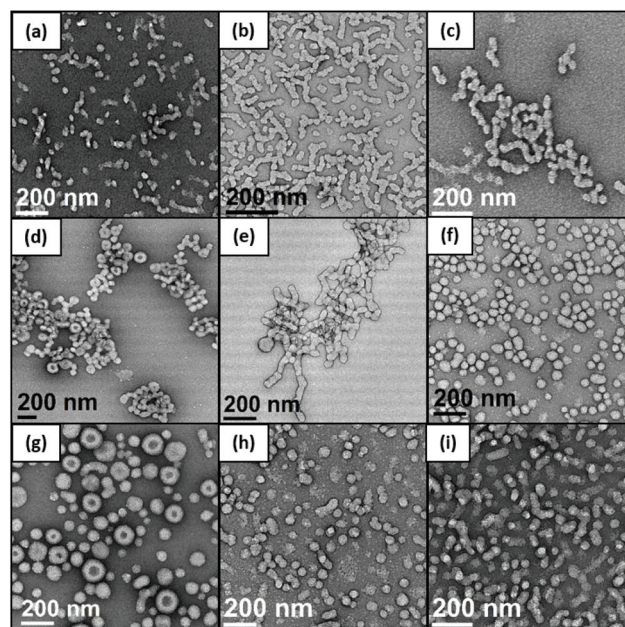

Fig. 7 Representative TEM images of nano-objects obtained from Table 1 entries 1–9 ((a)–(i) respectively).

195.6 ± 1.5 nm and the length of worms increased as well (Fig. 7b). By further increase in the DP of HPMA to 800, the morphology became aggregated small vesicles (Fig. 7d). A similar trend was found for Z_a by adding a higher amount of EGDMA. Because the hydrophobicity of EGDMA is higher than that of HPMA, the hydrophobicity of the block copolymer increased by a chain extended with even a small amount of EGDMA. Whether the change in morphology is due to the variation in hydrophobicity of the core-forming block or the effect of cross-linking is unknown. In order to investigate that, there are two strategies: (i) replacing EGDMA with butyl methacrylate (BMA) which has a similar hydrophobicity but not a divinyl cross-linker and (ii) replacing EGDMA with hydrophilic divinyl cross-linker poly ethylene glycol dimethacrylate (PEGDMA, M_n 500). The constructed nano-objects (Table 1 entries 6 and 7) with 0.5% BMA as a comonomer have very similar Z_a values and morphologies to the group (Table S1† entries 4 and 6) without the comonomer. These results suggest that the increase in hydrophobicity, at least with such a subtle change, will not lead to a significant effect on the morphology of nano-objects. The Z_a value of entry 9 is 28 nm larger than that of entry 4; this might be due to the fact that the hydrophilic cross-linker made nanoparticles swell up in water, leading to a slightly larger hydrodynamic diameter. Short worms obtained from entry 9 were very similar to those obtained from entry 4. These results indicate that the sphere-to-short-worm transformation in morphology is due to cross-linking. *In situ* CCL offers a facile approach for the synthesis of short worms *via* the sono-PISA process. The mean length of the worms tends to increase with increasing amount of the added cross linker. This could potentially lead to a methodology to control the length of worms, which would be a breakthrough for the current technique because almost all PISA syntheses exhibit a relatively broad distribution of worm lengths.[5]

Conclusions

Overall, it was demonstrated for the first time that various morphologies of block copolymer nano-objects, including spherical micelle, worm, and vesicle, can be prepared by sono-RAFT-PISA at ambient temperature. The use of water as both solvent and initiator source in sono-RAFT-PISA exhibits the "green" synthesis feature of this technique. This will allow the fabrication of nano-objects in a system that is sensitive to external initiators or additives. It was also shown that a vesicle with a uniform and smaller size (~110 nm) compared to conventional thermal-PISA can be easily prepared by this methodology. Furthermore, it was found that the worm-like micelle structure was challenging to achieve due to the presence of an acoustic streaming effect in this system. However, the introduction of core-cross-linking components offers a feasible approach for the synthesis of a worm-like micelle *via* sono-RAFT-PISA. In addition, with several examples of reactors with uniformly delivered ultrasonic irradiation,[63] sono-PISA is easily scalable and externally-regulated, thus avoiding the pro-

blems of poor heat transfer or UV intensity decay along the reactor geometry in conventional processes. These features should open many new prospects for the field of polymeric nano-object synthesis.

Conflicts of interest

There are no conflicts to declare.

Acknowledgements

Notes and references

1 N. J. Warren and S. P. Armes, *J. Am. Chem. Soc.*, 2014, **136**, 10174–10185.
2 B. Charleux, G. Delaittre, J. Rieger and F. D'Agosto, *Macromolecules*, 2012, **45**, 6753–6765.
3 B. Karagoz, L. Esser, H. T. Duong, J. S. Basuki, C. Boyer and T. P. Davis, *Polym. Chem.*, 2014, **5**, 350–355.
4 W.-M. Wan and C.-Y. Pan, *Polym. Chem.*, 2010, **1**, 1475–1484.
5 S. L. Canning, G. N. Smith and S. P. Armes, *Macromolecules*, 2016, **49**, 1985–2001.
6 J. Tan, H. Sun, M. Yu, B. S. Sumerlin and L. Zhang, *ACS Macro Lett.*, 2015, **4**, 1249–1253.
7 C. A. Figg, A. Simula, K. A. Gebre, B. S. Tucker, D. M. Haddleton and B. S. Sumerlin, *Chem. Sci.*, 2015, **6**, 1230–1236.
8 A. Blanazs, A. J. Ryan and S. P. Armes, *Macromolecules*, 2012, **45**, 5099–5107.
9 B. Fan and E. R. Gillies, *Mol. Pharmaceutics*, 2017, **14**, 2548–2559.
10 M. Huo, Q. Ye, H. Che, X. Wang, Y. Wei and J. Yuan, *Macromolecules*, 2017, **50**, 1126–1133.
11 J. Huang, H. Zhu, H. Liang and J. Lu, *Polym. Chem.*, 2016, **7**, 4761–4770.
12 B. Fan, J. F. Trant, A. D. Wong and E. R. Gillies, *J. Am. Chem. Soc.*, 2014, **136**, 10116–10123.
13 B. Fan, R. E. Yardley, J. F. Trant, A. Borecki and E. R. Gillies, *Polym. Chem.*, 2018, **9**, 2601–2610.
14 C. J. Mable, K. L. Thompson, M. J. Derry, O. O. Mykhaylyk, B. P. Binks and S. P. Armes, *Macromolecules*, 2016, **49**, 7897–7907.
15 F. D'Agosto, J. Rieger and M. Lansalot, *Angew. Chem., Int. Ed.*, 2020, DOI: 10.1002/anie.201911758.
16 X. Liu and W. Gao, *ACS Appl. Mater. Interfaces*, 2017, **9**, 2023–2028.
17 S. Sugihara, K. Sugihara, S. P. Armes, H. Ahmad and A. L. Lewis, *Macromolecules*, 2010, **43**, 6321–6329.
18 W.-M. Wan and C.-Y. Pan, *Macromolecules*, 2007, **40**, 8897–8905.

19 G. Delaittre, M. Save and B. Charleux, *Macromol. Rapid Commun.*, 2007, **28**, 1528–1533.

20 X. G. Qiao, P. Y. Dugas, B. Charleux, M. Lansalot and E. Bourgeat-Lami, *Macromolecules*, 2015, **48**, 545–556.

21 X. G. Qiao, M. Lansalot, E. Bourgeat-Lami and B. Charleux, *Macromolecules*, 2013, **46**, 4285–4295.

22 L. Zhang, C. Song, J. Yu, D. Yang and M. Xie, *J. Polym. Sci., Part A: Polym. Chem.*, 2010, **48**, 5231–5238.

23 K.-Y. Yoon, S. Shin, Y.-J. Kim, I. Kim, E. Lee and T.-L. Choi, *Macromol. Rapid Commun.*, 2015, **36**, 1069–1074.

24 D. B. Wright, M. A. Touve, L. Adamiak and N. C. Gianneschi, *ACS Macro Lett.*, 2017, **6**, 925–929.

25 K.-Y. Yoon, I.-H. Lee, K. O. Kim, J. Jang, E. Lee and T.-L. Choi, *J. Am. Chem. Soc.*, 2012, **134**, 14291–14294.

26 J. Chiefari, Y. K. Chong, F. Ercole, J. Krstina, J. Jeffery, T. P. T. Le, R. T. A. Mayadunne, G. F. Meijs, C. L. Moad, G. Moad, E. Rizzardo and S. H. Thang, *Macromolecules*, 1998, **31**, 5559–5562.

27 Y. Chong, T. P. Le, G. Moad, E. Rizzardo and S. H. Thang, *Macromolecules*, 1999, **32**, 2071–2074.

28 G. Moad, E. Rizzardo and S. H. Thang, *Polymer*, 2008, **49**, 1079–1131.

29 G. Moad, E. Rizzardo and S. H. Thang, *Aust. J. Chem.*, 2005, **58**, 379–410.

30 G. Moad, E. Rizzardo and S. H. Thang, *Acc. Chem. Res.*, 2008, **41**, 1133–1142.

31 N. J. W. Penfold, J. Yeow, C. Boyer and S. P. Armes, *ACS Macro Lett.*, 2019, **8**, 1029–1054.

32 B. Karagoz, C. Boyer and T. P. Davis, *Macromol. Rapid Commun.*, 2014, **35**, 417–421.

33 W.-M. Wan, C.-Y. Hong and C.-Y. Pan, *Chem. Commun.*, 2009, 5883–5885.

34 L. P. D. Ratcliffe, A. J. Ryan and S. P. Armes, *Macromolecules*, 2013, **46**, 769–777.

35 N. J. Warren, O. O. Mykhaylyk, D. Mahmood, A. J. Ryan and S. P. Armes, *J. Am. Chem. Soc.*, 2014, **136**, 1023–1033.

36 J. Tan, Y. Bai, X. Zhang and L. Zhang, *Polym. Chem.*, 2016, **7**, 2372–2380.

37 J. He, Q. Xu, J. Tan and L. Zhang, *Macromol. Rapid Commun.*, 2019, **40**, 1800296.

38 J. Yeow, O. R. Sugita and C. Boyer, *ACS Macro Lett.*, 2016, **5**, 558–564.

39 S. Piogé, T. N. Tran, T. G. McKenzie, S. Pascual, M. Ashokkumar, L. Fontaine and G. Qiao, *Macromolecules*, 2018, **51**, 8862–8869.

40 P. Pignoli, E. Tremoli, A. Poli, P. Oreste and R. Paoletti, *Circulation*, 1986, **74**, 1399–1406.

41 R. A. Caruso, M. Ashokkumar and F. Grieser, *Langmuir*, 2002, **18**, 7831–7836.

42 A. L. Klibanov, *Invest. Radiol.*, 2006, **41**, 354–362.

43 B. M. Teo, S. W. Prescott, M. Ashokkumar and F. Grieser, *Ultrason. Sonochem.*, 2008, **15**, 89–94.

44 B. M. Teo, M. Ashokkumar and F. Grieser, *J. Phys. Chem. B*, 2008, **112**, 5265–5267.

45 S. K. Bhangu and M. Ashokkumar, in *Sonochemistry: From Basic Principles to Innovative Applications*, ed. J. C. Colmenares and G. Chatel, Springer International Publishing, Cham, 2017, DOI: 10.1007/978-3-319-54271-3_1.

46 S. Xu, J. Yeow and C. Boyer, *ACS Macro Lett.*, 2018, **7**, 1376–1382.

47 A. Blanazs, J. Madsen, G. Battaglia, A. J. Ryan and S. P. Armes, *J. Am. Chem. Soc.*, 2011, **133**, 16581–16587.

48 C. Hochanadel, *J. Phys. Chem.*, 1952, **56**, 587–594.

49 J. Tan, X. Zhang, D. Liu, Y. Bai, C. Huang, X. Li and L. Zhang, *Macromol. Rapid Commun.*, 2017, **38**, 1600508.

50 A. Blanazs, R. Verber, O. O. Mykhaylyk, A. J. Ryan, J. Z. Heath, C. W. I. Douglas and S. P. Armes, *J. Am. Chem. Soc.*, 2012, **134**, 9741–9748.

51 L. P. D. Ratcliffe, M. J. Derry, A. Ianiro, R. Tuinier and S. P. Armes, *Angew. Chem., Int. Ed.*, 2019, **58**, 18964–18970.

52 G. Moad, E. Rizzardo and S. H. Thang, *Aust. J. Chem.*, 2009, **62**, 1402–1472.

53 E. Rizzardo, J. Chiefari, B. Y. K. Chong, F. Ercole, J. Krstina, J. Jeffery, T. P. T. Le, R. T. A. Mayadunne, G. F. Meijs, C. L. Moad, G. Moad and S. H. Thang, *Macromol. Symp.*, 1999, **143**, 291–307.

54 D. J. Tobler, S. Shaw and L. G. Benning, *Geochim. Cosmochim. Acta*, 2009, **73**, 5377–5393.

55 J. Tan, Q. Xu, Y. Zhang, C. Huang, X. Li, J. He and L. Zhang, *Macromolecules*, 2018, **51**, 7396–7406.

56 L. D. Blackman, K. E. Doncom, M. I. Gibson and R. K. O'Reilly, *Polym. Chem.*, 2017, **8**, 2860–2871.

57 K. Miki, H. Hashimoto, T. Inoue, H. Matsuoka, H. Harada, M. Hiraoka and K. Ohe, *Small*, 2014, **10**, 3119–3130.

58 L. H. Dang, M. T. Vu, J. Chen, C. K. Nguyen, L. G. Bach, N. Q. Tran and V. T. Le, *ACS Omega*, 2019, **4**, 4540–4552.

59 N. J. Warren, M. J. Derry, O. O. Mykhaylyk, J. R. Lovett, L. P. D. Ratcliffe, V. Ladmiral, A. Blanazs, L. A. Fielding and S. P. Armes, *Macromolecules*, 2018, **51**, 8357–8371.

60 J. Jalal and T. S. Leong, *Fluids*, 2018, **3**, 93.

61 Y. K. Suh and S. Kang, in *Encyclopedia of Microfluidics and Nanofluidics*, ed. D. Li, Springer US, Boston, MA, 2008, pp. 25–33.

62 W.-J. Zhang, C.-Y. Hong and C.-Y. Pan, *Macromol. Rapid Commun.*, 2019, **40**, 1800279.

63 Y. Son, M. Lim and J. Khim, *Ultrason. Sonochem.*, 2009, **16**, 552–556.

PAPER

Check for updates

Sonochemical preparation of polymer–metal nanocomposites with catalytic and plasmonic properties†

Jing Wan, [ID] Bo Fan [ID] and San H. Thang [ID] *

Polymer–metal nanocomposites are of increasing interest for a wide range of applications; however, the preparation of these nanocomposites often requires the addition of external initiation and reducing agents for the synthesis of polymer and metal nanoparticles, respectively. Herein, we demonstrate the preparation of polymer–metal nanocomposites for improved catalytic performance by utilizing ultrasound as both the initiation and reducing source. Specifically, synthesis of the macro-RAFT agent containing poly[2-(dimethylamino)ethyl methacrylate], followed by ultrasound-initiated polymerization-induced self-assembly (sono-PISA), provides triblock copolymer nanoparticles containing tertiary amine groups. These polymer nanoparticles were further used as the scaffold for the *in situ* reduction of metal ions (Au and Pd ions) by radicals generated *via* sonolysis of water without additional reducing agents. The immobilization of metal nanoparticles has been confirmed by TEM and electron diffraction patterns. Polymer–Au nanocomposites with stepwise-grown AuNPs can be applied as surface-enhanced Raman scattering (SERS) substrates for 4-aminothiophenol (4-ATP) detection. Furthermore, the catalytic performances of these prepared polymer–Au and polymer–Pd nanocomposites were examined for aerobic alcohol oxidation and the Suzuki–Miyaura cross-coupling reaction, respectively. Overall, this strategy is expected to greatly expand the utility of ultrasound in the preparation of polymer–metal nanocomposites and promote the catalytic applications of these nanocomposites.

Introduction

In recent years, there has been an increasing interest in the synthesis of hybrid nanoparticles or nanocomposites, especially polymer–metal nanocomposites, due to their potential applications in a broad range of areas, including biotechnology, optoelectronics, therapeutics, and catalysis.[1–4] In catalytic applications, polymeric nanoparticles have been used as scaffolds for supporting metal nanocatalysts, such as gold nanoparticles (AuNPs) and palladium nanoparticles (PdNPs), because of the tunability in polymer particle size and well-studied interactions between polymer functional groups and metal atoms.[5–7] More importantly, researchers found that stabilizing/capping agents (*e.g.* citrate) used in the preparation of conventional metal nanoparticles often act as a physical barrier, which blocks the access of reactants during the reaction and adversely affects the overall catalytic performance.[8,9] By replacing stabilizing/capping agents with polymeric nanoparticles, the surface of metal nanoparticles is free from any

capping agent barrier, and thus they can serve as highly active catalysts. For polymer–metal nanocomposites, metal nanoparticles are usually prepared *in situ* by reduction of a metal salt and immobilized on a polymer based on the interaction between one of the polymer blocks and the metal ion. For instance, McCormick and co-workers reported the synthesis of gold-"decorated" vesicles using *in situ* reduction of sodium tetrachloroaurate in the presence of polymers containing tertiary amine groups.[10] Kim *et al.*[8] reported the preparation of poly(*N*-isopropylacrylamide) particles embedded with *in situ* formed AuNPs *via* light irradiation and studied their atypical quasi-homogeneous catalytic functions for homocoupling reactions.

Polymeric nanoparticles for polymer–metal nanocomposites are usually prepared through either solution self-assembly or polymerization-induced self-assembly (PISA), whereas the drawbacks of solution self-assembly, such as low polymer concentration and complex preparation procedures, have limited its scalable application.[11–15] PISA, on the other hand, yields block copolymer nano-objects *in situ* during the polymerization with high polymer solid content (10–40%), promising its large-scale application. Meanwhile, the morphology and size of the nano-objects can be easily tuned by controlling the degree of polymerization (DP) and solid content.[16,17] Thus far, several studies have reported the preparation of polymer–

School of Chemistry, Monash University, Clayton, VIC, 3800, Australia. E-mail: san. thang@monash.edu

† Electronic supplementary information (ESI) available: Experimental details, ^{1}H NMR, ^{13}C NMR spectra and MS spectra of RAFT agents and polymers, GPC curves and additional TEM images. See DOI: 10.1039/d1na00120e

metal nanocomposites using PISA nano-objects as the scaffold.[17–20] Davis and Boyer reported the *in situ* reduction of chloroauric acid using NaBH$_4$ in the presence of tertiary amine-containing polymer nano-objects synthesized *via* the PISA approach.[20] Pietrasik *et al.* demonstrated the preparation of poly(acrylic acid)-*block*-polystyrene (PAA-*b*-PS) nano-spheres *via* PISA, and these polymer nano-spheres were then immobilized with silver nanoparticles and used as surface-enhanced Raman spectroscopy (SERS) substrates for adenine detection and catalysts for reduction of 4-nitrophenol.[18] More recently, our group synthesized a series of cyclodextrin-decorated nano-objects *via* PISA and demonstrated the "guest–host" complexation with AuNPs which are modified with polymer ligands containing adamantane moieties.[17] This provides a new pathway for the fast preparation of polymer-based nanocomposites.

Meanwhile, with increasing interest in PISA, research devoted to initiation methods of PISA has become a new trend in recent years. Our previous study has demonstrated a room-temperature ultrasound-initiated PISA process without the addition of any thermo-/photo-initiators.[21] The sonolysis of H$_2$O and generation of H˙ and ˙OH to initiate RAFT polymerization in PISA provide a "green" alternative compared to the conventional thermo-/photo-process. Furthermore, ultrasound allows the preparation of gold colloids and palladium colloids without the addition of any reducing agents,[22–26] as the H˙ generated during sonolysis can also reduce metal ions to form metal nanoparticles. However, to the best of our knowledge, there is no research yet devoted to the preparation of polymer–metal nanocomposites using ultrasound as both initiation and reducing sources. By combining the ability of ultrasound to initiate polymerization and produce metal nanoparticles, we demonstrate here not only a 'green' alternative without the addition of an initiator or reducing agent, but also a facile synthesis strategy for quick preparation of polymer–metal nanocomposites. Specifically, tertiary amine-containing polymeric nanoparticles were firstly synthesized by ultrasound-PISA

(Scheme 1), and then they were used as the scaffold for *in situ* generation of metal nanoparticles by sonication. The formed polymer–Au nanocomposite with stepwise-grown AuNPs can be applied as a surface-enhanced Raman scattering (SERS) substrate for 4-aminothiophenol (4-ATP) detection. Meanwhile, the prepared polymer–Au and polymer–Pd nanocomposites were examined for catalytic applications and showed high catalytic efficiency in aerobic alcohol oxidation and the Suzuki–Miyaura cross-coupling reaction, respectively.

Results and discussion

Synthesis of PEG$_{113}$-*b*-PDMAEMA-*b*-PHPMA triblock copolymer nanoparticles

First, macro-chain transfer agent (macro-CTA) PEG$_{113}$-CDTPA (Fig. S1†) was synthesized through Steglich esterification according to a previously published procedure.[21] The PEG$_{113}$-CDTPA was then chain extended with monomer DMAEMA in 1,4-dioxane (Scheme 2) *via* RAFT polymerization,[27,28] yielding a diblock copolymer PEG$_{113}$-*b*-PDMAEMA-CDTPA. To study the influence of the chain lengths of PDMAEMA on the formation of polymer nanoparticles and polymer–metal nanocomposites, three different batches were synthesized (Table S1†). The theoretical molecular weights ($M_{n,theo}$) of these hydrophilic
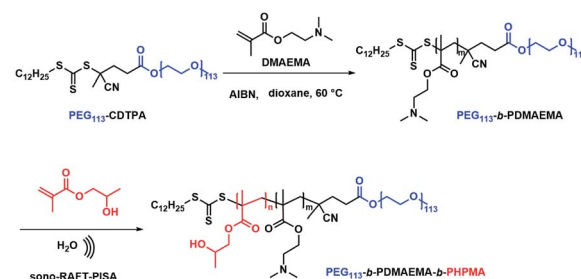
Scheme 2 Synthesis of PEG$_{113}$-*b*-PDMAEMA and PEG$_{113}$-*b*-PDMAEMA-*b*-PHPMA copolymers *via* the sono-RAFT-PISA process.
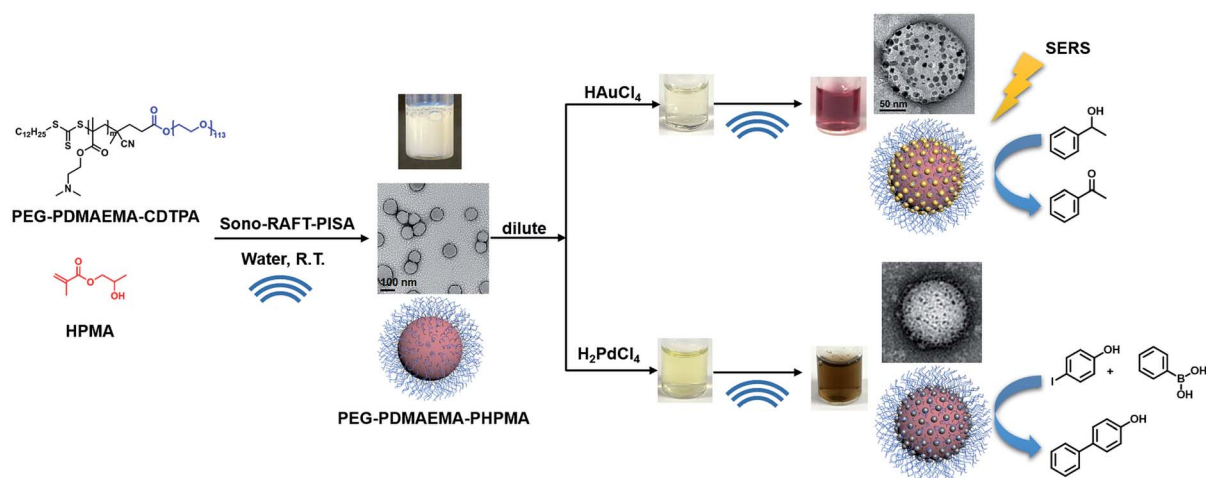
Scheme 1 Synthesis of PEG$_{113}$-*b*-PDMAEMA-*b*-PHPMA copolymers *via* the sono-RAFT-PISA process, and *in situ* formation of the Au and Pd nanocomposite by ultrasound.

block copolymers were matched with the molecular weight calculated *via* ^{1}H NMR spectra ($M_{n,NMR}$). Meanwhile, the GPC data (Table S1†) reveal that these block copolymers have low dispersities (*Đ*, 1.06–1.11), which indicates the well-controlled synthesis of the second blocks. It should be noted that the GPC traces of PEG$_{113}$-*b*-PDMAEMA-CDTPA display bimodal distributions (Fig. S6†). The presence of side peak results from the purchased PEG$_{113}$ because a similar side peak appears on the GPC trace of PEG$_{113}$ (Fig. S7†). Meanwhile, it was also found that the molecular weights determined by GPC were higher than the theoretical molecular weights (Table S1†). The primary reason for this variation is the structural difference between PEG and the PMMA standards used for GPC calibration. In the next study, it was found that the shorter block of PDMAEMA (Table S1,† entry A, PEG$_{113}$-*b*-PDMAEMA$_9$-CDTPA) was not able to provide sufficient accessible tertiary amine sites for metal nanoparticles (Fig. S8a and b†). However, a longer block (Table S1,† entry C, PEG$_{113}$-*b*-PDMAEMA$_{46}$-CDTPA) provided enough tertiary amine but generated a long hydrophilic chain in the meantime, which required higher DP of HPMA to form core–shell micelles (Fig. S8c and d†). The medium-length PEG$_{113}$-*b*-PDMAEMA$_{24}$-CDTPA was found to meet both conditions. Therefore, the medium-length PEG$_{113}$-*b*-PDMAEMA$_{24}$-CDTPA was selected for the next studies.

Next, PEG$_{113}$-*b*-PDMAEMA$_{24}$-CDTPA was used as the stabilizer block and HPMA as the monomer for sono-PISA at room temperature and 10% w/w solid content (Scheme 2). The PISA was conducted using the 990 kHz ultrasonic reactor, which can split water molecules to generate hydroxyl radicals and initiate polymerization. Different batches of PEG$_{113}$-PDMAEMA$_{24}$-PHPMA$_n$ with various PHPMA lengths were achieved by changing the targeting DP. As shown in Fig. 1c, with the increase of the DP of the PHPMA block, the cloudiness of the dispersions increased gradually, which indicates the formation of polymer nanoparticles. The dispersions synthesized *via* the PISA process were further analyzed by ^{1}H NMR spectroscopy and GPC. The ^{1}H NMR spectra (Fig. S9†) confirm that almost all monomers had converted to polymers in this PISA process. The GPC curves (Fig. 1a) exhibit clear shifting towards higher retention time with the increase of targeting DP. Meanwhile, it was noted that the *Đ* of these block copolymers increased from 1.21 at DP of 290 to 1.68 at DP of 1170 (Table 1). The broadening of the *Đ* could result from the impurities of PEG$_{113}$ itself, and another possible reason is the branching of the PHPMA blocks caused by the side reaction of hydroxyl radicals with polymer chains. This phenomenon was observed in a previous study as well.[21] Despite the relatively broad *Đ*, the subsequent characterization studies indicate that it did not adversely affect the formation of uniform polymer nanoparticles.

The triblock copolymer dispersions were further analyzed by DLS and TEM. The DLS curves (Fig. 1b) show an apparent shifting of the particle sizes with the increase of PHPMA chain lengths; the average hydrodynamic size increased from 56.0 ± 0.9 nm at the DP of 290 to 115.9 ± 1.2 nm at the DP of 1170 (Table 1). Meanwhile, the polydispersity index (PDI) kept around 0.08–0.14, which indicated the narrow size distributions of synthesized nano-objects. The TEM images (Fig. 1d–h) reveal
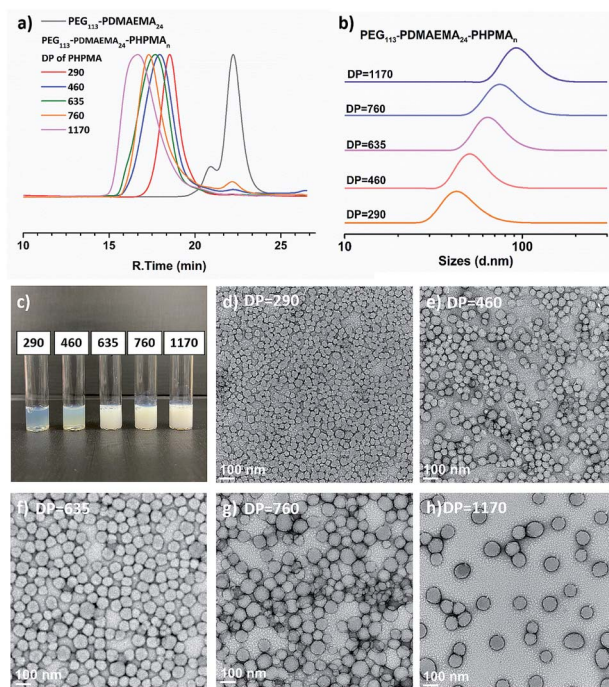

Fig. 1 (a) GPC traces and (b) DLS traces of PEG$_{113}$-*b*-PDMAEMA$_{24}$-*b*-PHPMA$_n$ (DP n = 290–1170) copolymers synthesized *via* sono-PISA. (c) Photographs and (d–h) TEM images of PEG$_{113}$-*b*-PDMAEMA$_{24}$-*b*-PHPMA$_n$ prepared *via* sono-PISA, the numbers represent the DP of PHPMA blocks (Table 1 entries 1–5 respectively).

that the structures of the triblock copolymer nano-objects were spherical particles for all entries. No morphological transition to worms or vesicles was observed. Likewise, the TEM images revealed the particle size growth with the increase of the DP, and these images also confirmed the uniform size of these polymer nanoparticles. It should be noted that the particle sizes as measured from the TEM images were slightly smaller than those measured by DLS. This can be attributed to particles being in the dry state under TEM, and DLS could oversize the particles since the scattering from larger particles can increase the overall particle diameter.[29] In this specific PISA process, no worm or vesicle but only spheres were formed even the DP had increased to 1170. This is due to the use of a relatively long stabilizer block (PEG$_{113}$-*b*-PDMAEMA$_{24}$-CDTPA), which could produce kinetically trapped spheres due to the steric repulsions between long stabilizing chains, preventing the fusion and reorganization of nanoparticles.[30] The polymeric nanoparticles (Table 1, entry 5) with a relatively large size were then used for *in situ* nanocomposite formation with Au and Pd ions.

In situ synthesis of polymer–Au nanocomposites

The tertiary amine group in the PEG$_{113}$-*b*-PDMAEMA$_{24}$-*b*-PHPMA$_n$ can effectively bind with Au ions due to the chemisorption effect (Fig. 2).[31–33] It was reported that the PDMAEMA block will be partially protonated with the addition of HAuCl$_4$, and the remaining unprotonated tertiary amine groups can reduce the AuCl$_4^-$ counterion to zero-valent Au *in situ via* the coordination–reduction mechanism without the addition of
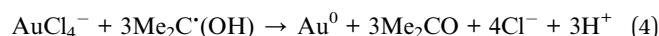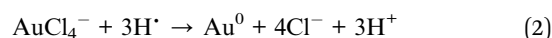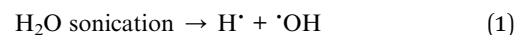
Table 1 Characterization data of PEG_{113}-b-$PDMAEMA_{24}$-b-$PHPMA_n$ nanoparticles by sono-PISA

Entry	DP of HPMA[a]	$M_{n,theo}$[b] (g mol^{-1})	$M_{n,GPC}$ (g mol^{-1})	$Đ$	Z-Average (DLS) (nm)	PDI (DLS)	Diameter by TEM[c] (nm)
1	290	51 000	94 200	1.21	56.0 ± 0.9	0.14 ± 0.01	36.6 ± 7.4
2	460	75 500	143 400	1.52	76.8 ± 0.8	0.14 ± 0.01	54.5 ± 8.3
3	635	100 700	191 300	1.55	88.0 ± 1.9	0.13 ± 0.02	74.8 ± 11.1
4	760	118 700	225 100	1.61	101.2 ± 1.8	0.08 ± 0.01	83.5 ± 12.6
5	1170	177 900	341 700	1.68	115.9 ± 1.2	0.10 ± 0.01	97.8 ± 15.2

[a] DP was determined by the ^1H NMR spectrum (Fig. S9). [b] $M_{n,theo} = M_{n,HPMA} \times conversion \times 100 \times ([HPMA]/[PEG_{113}$-$b$-$PDMAEMA_{24}$-$CDTPA]) + M_{n,PEG_{113}$-$b$-$PDMAEMA_{24}$-$CDTPA}$. [c] Average diameter and standard deviation calculated by measuring 60 random particles.

external reductants.[34] McCormick *et al.* reported that when PDMAEMA : $NaAuCl_4$ = 10 : 1, the reduction of $AuCl_4^-$ to AuNPs was achieved *via* the coordination–reduction mechanism without the addition of external reductants.[10] Zhao *et al.* also reported that Au^{3+} could be reduced by the hydroxyl group under alkaline conditions, thus achieving the green synthesis of AuNPs without any harsh reductive substance.[35,36] The presence of hydroxyl groups in PHPMA and alkaline conditions from tertiary amine could potentially provide reducing conditions for Au^{3+}. However, in our study, when the molar feed ratio of tertiary amine group (TA) : $HAuCl_4$ = 1 : 7, we did not observe self-reduction after 1 day at room temperature. This was also noticed in a previous report by Boyer and Davis.[20] The slow self-reduction was because the majority of the TA was protonated with the addition of $HAuCl_4$, and no additional TA was available to provide alkaline condition to reduce $AuCl_4^-$. Thus, an external reductant is required to form AuNPs, commonly, reducing agents, such as citrate and $NaBH_4$ are added to reduce Au precursor ions. Nevertheless, ultrasound can provide a "green" alternative method to reduce metal ions to metal nanoparticles without the addition of any reducing agents. Since ultrasound at lower frequency has a higher rate of reduction,[23] 400 kHz ultrasound was selected for the formation of metal nanoparticles instead of the 990 kHz ultrasound used in the sono-PISA process. The sonolysis of H_2O generates H' and

'OH, the Au(III) is expected to be reduced by primary reducing species H' as shown in eqn (1) and (2).[22,25] Alcohols such as 2-propanol can be added to act as a radical scavenger,[22,25] which leads to additional reduction reaction (eqn (3)–(5)). These reactions combined could result in the formation of AuNPs. Meanwhile, a small quantity of poly(N-vinylpyrrolidone) (PVP) was added to improve the stability of nanocomposites as they can attach to the AuNPs, however, it could also compete with amino groups to form PVP-stabilized free AuNPs. Therefore, a low PVP concentration (0.2 mg mL^{-1}) was selected after a few attempts.

$$H_2O \text{ sonication} \rightarrow H^• + {}^•OH \quad (1)$$

$$AuCl_4^- + 3H^• \rightarrow Au^0 + 4Cl^- + 3H^+ \quad (2)$$

$$H^•({}^•OH) + Me_2CHOH \rightarrow Me_2C^•(OH) + H_2(H_2O) \quad (3)$$

$$AuCl_4^- + 3Me_2C^•(OH) \rightarrow Au^0 + 3Me_2CO + 4Cl^- + 3H^+ \quad (4)$$

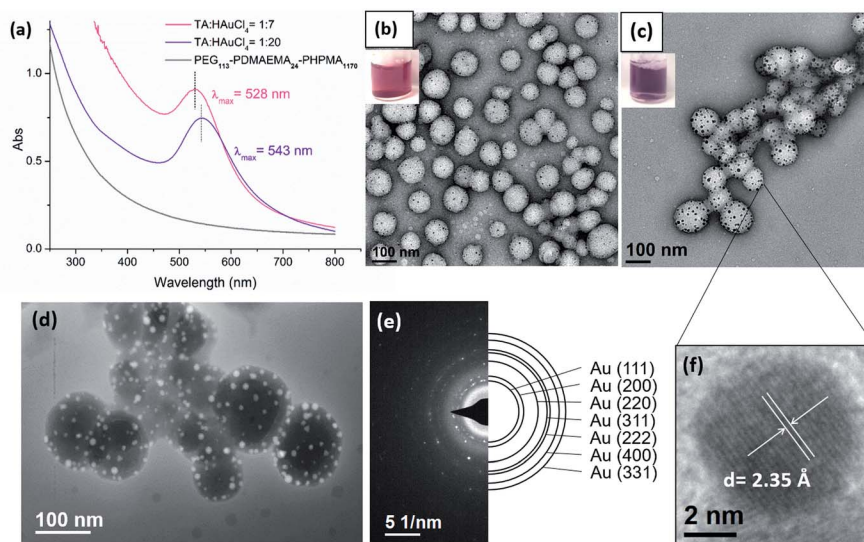$$nAu^0 \rightarrow Au_n \quad (5)$$

The immobilization of AuNPs on polymeric nanoparticles is confirmed by TEM, UV-Vis and high-angle annular dark-field imaging (HAADF). As shown in TEM images (Fig. 3b and c) of
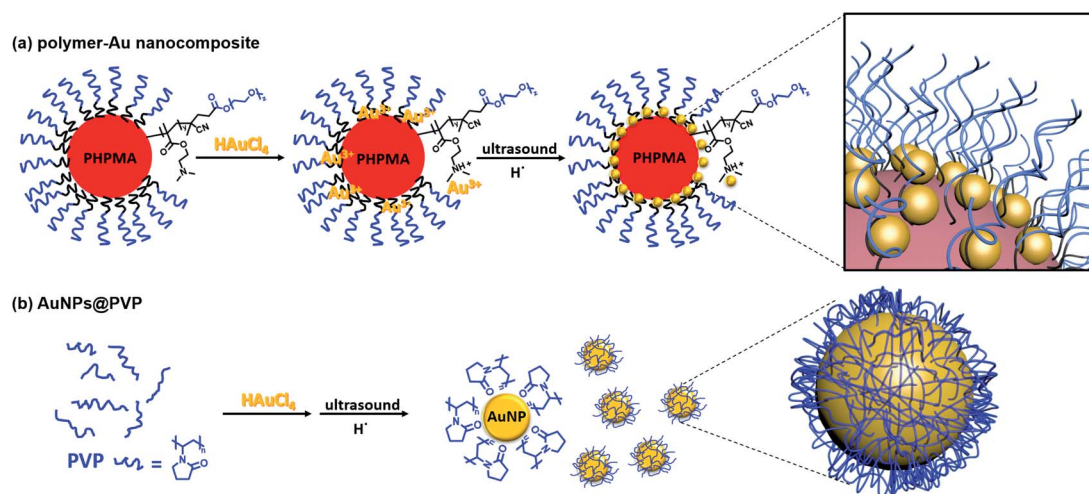
Fig. 2 Schematic illustration of the preparation of (a) polymer–Au nanocomposites and (b) PVP-stabilized AuNPs (AuNPs@PVP) *via* ultrasound sonication.

Fig. 3 (a) UV-Vis spectra of polymer–Au nanocomposites. Digital photos and TEM images of polymer–Au composites with (b) TA : Au = 1 : 7 and (c) TA : Au = 1 : 20. (d) STEM HAADF image and (e) SAED patterns of polymer–Au nanocomposites (TA : Au = 1 : 20). (f) High resolution TEM image of a gold nanoparticle.

polymer–Au nanocomposites (Au@PEG$_{113}$-b-PDMAEMA$_{24}$-b-PHPMA$_{1170}$) (TA : Au = 1 : 7 and 1 : 20), the spherical AuNPs were uniformly dispersed on the shell layer of the polymeric nanoparticles. Thermal gravimetric analysis (TGA) of purified nanocomposites was conducted to determine the Au mass loading on the polymer colloidal matrix. The determined mass loading of Au present in the nanocomposites is approximately equal to the theoretical Au content (Table S2, Fig. S10†). The size of AuNPs was dependent on the TA : Au ratio; the size of AuNPs was measured as 4–6 nm when TA : Au = 1 : 7, and 7–14 nm when TA : Au = 1 : 20. In UV-Vis analysis (Fig. 3a), the absorption spectra exhibited a surface plasmon resonance (SPR) band shifting from λ_{max} = 529 nm to 542 nm when the TA : Au ratio changed from 1 : 7 to 1 : 20. This also reflects the size increment of AuNPs, which is in good agreement with the result measured by TEM. The formation of AuNPs was further confirmed by High-angle annular dark-field (HAADF) microscopy. HAADF is a STEM technique that is highly sensitive to variations of atomic number in the sample. For elements with a higher atomic number, the HAADF detector senses a stronger signal, causing them to appear brighter in the resulting image. Due to the high atomic number of Au compared to the polymer matrix, the AuNPs appeared brighter under HAADF (Fig. 3d). Meanwhile, this study evidently demonstrated the uniform distribution of AuNPs on the surface of the polymer nanoparticles. Fig. 3e shows the selected area electron diffraction (SAED) obtained from polymer–Au composites, which exhibits concentric rings with intermittent bright spots corresponding to (111), (200), (220), (311), (222), (400), and (331). The high-resolution TEM (HRTEM) image (Fig. 3f) of a gold nanoparticle shows that the lattice spacing for the (111) planes is measured to be 2.35 Å (measurement in Fig. S11a†). This reflects the polycrystalline and face-centered-cubic nature of the AuNP and provides direct evidence for the presence of AuNPs in the nanocomposite.

Next, the further size evolution of AuNPs was attempted by adjusting the molar ratio of TA : Au. However, by simply adjusting the initial TA : Au ratio from 1 : 7 or 1 : 20 to 1 : 100, the generated AuNPs were not uniform in size nor were they uniformly dispersed on the shell layer of the polymer nanoparticles (Fig. S12†). Thus, the originally prepared polymer–Au nanocomposite was used as seeds for further growth of AuNPs by stepwise growth methodology. Specifically, the initially prepared AuNPs in a lower TA : Au ratio (1 : 7) were used as seeds and a certain amount of HAuCl$_4$ solution was added. In the next, reducing agent NH$_2$OH was added to reduce the Au precursor and to form larger AuNPs. This step was repeated up to 7–9 times until the nanocomposites became unstable and formed precipitates. Meanwhile, UV-Vis spectroscopy and TEM were applied to monitor the growth of AuNPs. The UV-Vis spectra (Fig. 4a) showed that the λ_{max} of the SPR band red-shifted about 4–6 nm per step and totally shifted up to 53 nm (from ~530 nm to 583 nm) upon the growth of 7 steps. This result indicated that the size of the AuNPs increases with each growth step, because the SPR absorption of small AuNPs increases with their diameters.[37] Furthermore, TEM analysis evidently revealed the AuNP size evolution; the size grew from ~5 nm at the beginning to 20–30 nm at the final step (Fig. 4b–f). It was observed that the overall quantity of the AuNPs on each polymeric nanoparticle remained approximately constant, suggesting that the Au precursors were primarily consumed in the production of larger AuNPs and no new particle nucleation occurred.[38,39]

The densely clustered AuNPs on the surface of polymer–Au nanocomposites are expected to generate electromagnetic hot spots between the AuNPs, making the nanocomposite a potential surface-enhanced Raman scattering (SERS) substrate candidate for localized probe molecules. Therefore, the SERS effect of the polymer–Au nanocomposite after step 7 was further
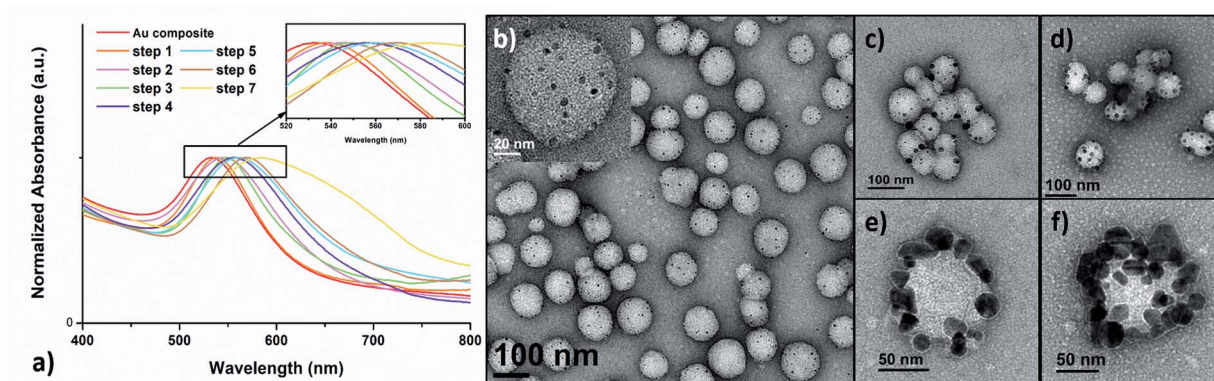
Fig. 4 (a) UV-Vis absorption spectra of plasmonic Au nanocomposites prepared by the stepwise growth. TEM images of the (b) initial polymer–Au nanocomposites and after (c) step 1, (d) step 2, (e) step 6 and (f) step 7.

analyzed. We performed the SERS measurement on the drop-cast polymer–Au nanocomposite using 4-aminothiophenol (4-ATP) as the probe molecule. As shown in Fig. 5, two dominant peaks at 1078 and 1587 cm^{-1} were observed from the SERS spectra of the polymer–Au nanocomposite diffused by 4-ATP vapor for 1 min and 48 h. These correspond to the a$_1$ vibrational modes of ν(C–S) and ν(C–C).[40] The weaker enhancement of b$_2$ modes at 1147, 1180, 1328 and 1438 cm^{-1} were also observed from the SERS spectra.[40] This preliminary SERS measurement confirmed the application of the polymer–Au nanocomposite as a SERS substrate.

The oxidation of alcohols to aldehydes or ketones is a pivotal functional group transformation in organic chemistry. A prior study has found that AuNPs with a smaller size exhibit higher catalytic activity.[41] Thus, the catalytic ability of the polymer–Au nanocomposite with smaller AuNPs (Au@PEG$_{113}$-b-PDMAEMA$_{24}$-b-PHPMA$_{1170}$, TA : Au = 1 : 7) was testified through the oxidation reaction of 1-phenylethanol to aceto-phenone (Fig. 6). The reactions were conducted in water at 80 °C by fixing the reaction time to 2 hours and varying the catalyst quantities. The yield of acetophenone was calculated by the analysis of the ^{1}H NMR spectra (Fig. 6). It was found that the doublet located at 1.52 ppm, which corresponds to the methyl group of 1-phenylethanol, gradually decreased in intensity with

the increase of catalyst amount. Meanwhile, a new singlet located at 2.62 ppm, which corresponds to the methyl group of acetophenone, increased gradually in intensity. Without the presence of a catalyst, the reaction could only proceed with 10.8% yield (Table 2, entry 1), however, with the presence of 0.05 mol% polymer–Au nanocomposites the reaction proceeded with 98.2% yield in 2 hours (Table 2, entry 5). In addition, the catalytic efficiency of the polymer–Au nanocomposite was compared with that of PVP-stabilized AuNPs (Au@PVP) having the same average AuNP size (Fig. S16b†). Both catalysts could achieve full conversion within 2 h at 0.1 mol% of catalysts (Table 2, entries 2 and 3). However, by decreasing the catalyst concentration, Au@PVP exhibited lower catalytic efficiency compared to the polymer–Au nanocomposite. When the catalyst equivalent was 0.01 mol%, the yields were 21.0% for Au@PVP and 32.7% for the polymer–Au nanocomposite (Table 2, entries 8 and 9). The polymer–Au nanocomposite affords a higher turnover frequency (TOF) value of 1.64×10^3 h^{-1}, compared to 1.05×10^3 h^{-1} of Au@PVP (calculated by the 0.01 mol% total Au atoms at 2 h). Generally, the catalytic efficiency of the polymer–Au nanocomposite is higher than that of AuNPs. The reason for this phenomenon is that PVP can dampen the catalytic activity by blocking active sites (e.g., edges, corners, and terraces)
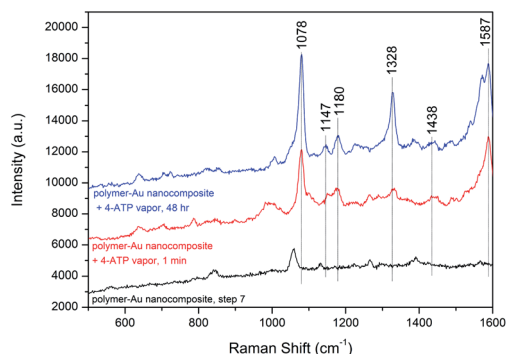

Fig. 5 SERS spectra of 4-ATP vapor from the polymer–Au nano-composite substrate and the original polymer–Au nanocomposite.
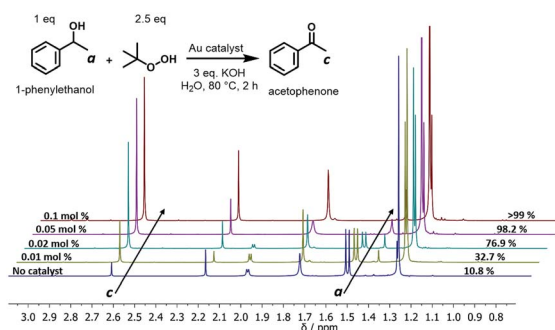

Fig. 6 ^{1}H NMR spectra of 1-phenylethanol oxidation (2.63 ppm: methyl group of acetophenone; 1.51 ppm: methyl group of 1-phe-nylethanol) (the full spectrum and the NMR yield calculation equation are available in Fig. S13†).

Table 2 Aerial oxidation reaction of 1-phenylethanol to acetophenone using the Au catalyst

| Entry	Catalyst	Catalyst eq.[a] (mol%)	NMR yield (%)
1	None	—	10.8
2	Au@PVP	0.1	>99
3	Polymer–Au nanocomposite	0.1	>99
4	Au@PVP	0.05	92.6
5	Polymer–Au nanocomposite	0.05	98.2
6	Au@PVP	0.02	71.4
7	Polymer–Au nanocomposite	0.02	76.9
8	Au@PVP	0.01	21.0
9	Polymer–Au nanocomposite	0.01	32.7

[a] Catalyst eq. (mol%) = [catalyst]/[1-phenylethanol] × 100%.

(Fig. 2b).[9,42] For the polymer–Au nanocomposite (Fig. 2a), only a very small amount of PVP was added, and the AuNPs were embedded on the hydrophilic block of polymeric nano-spheres, leaving the relatively larger area of "naked" Au surface and thus more accessible active sites. The immobilization of AuNPs on the hydrophilic chains also allows good contact with reactants in the aqueous medium.

Another significant aspect of the nanocomposite catalyst is the reusability. Therefore, the performance of the reused nanocomposite was also studied, and the data are presented in Fig. S17,† the polymer–Au composite maintained its well stability and dispersity after separation. In addition, the composite was reused without a notable loss of catalytic activity with near full conversion in the first four batches and good yield in the fifth batch (Fig. S17 and S18†).

In situ synthesis of polymer–Pd nanocomposites

The presence of TA groups in the shell of polymer nanoparticles also allows the immobilization of Pd nanoparticles (PdNPs) through the coordination between the amino groups with Pd ions and subsequent reduction by ultrasound generated reducing species. The successful immobilization of PdNPs on the polymer matrix was confirmed by TEM, UV-Vis spectroscopy and SAED. Specifically, the TEM images (Fig. 7a and b) reveal that PdNPs with a size of 1–4 nm (TA : Pd: tertiary amine = 1 : 7) and 3–5 nm (TA : Pd: tertiary amine = 1 : 20) were uniformly dispersed on the shell layer of the polymeric nanoparticles. In addition, the UV-Vis spectra (Fig. 7c) show the absorption band at 420 nm corresponding to Pd^{2+} ions disappeared after sonication, indicating that Pd(II) has been completely reduced to Pd(0). Furthermore, the HRTEM image (Fig. 7b inset) of a PdNP shows that the lattice spacing for the (111) planes is measured to be 2.25 Å (measurement in Fig. S11b†). The SAED pattern (Fig. 7d) of the nanocomposites exhibits concentric rings, corresponding to the (111), (200), (220), and (311) crystal planes of the face-centered-cubic structure of Pd, which further demonstrate the presence of PdNPs.
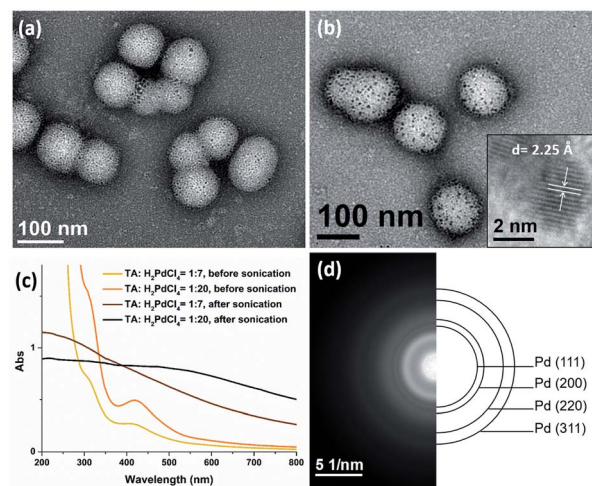
Fig. 7 TEM images of Pd@PEG$_{113}$-*b*-PDMAEMA$_{24}$-*b*-PHPMA$_{1170}$ nanocomposites with a TA : Pd ratio of (a) 1 : 7 and (b) 1 : 20. (c) UV-vis spectra of the palladium nanocomposite before and after sonication. (d) The selected area electron diffraction pattern of the nanocomposites.

Pd(0) catalysts have been broadly utilized in the Suzuki–Miyaura cross-coupling reaction, which is the C–C bond formation between aryl halides and aryl boronic acids, and is a powerful tool in organic syntheses.[43] Recently, many studies have synthesized new types of Pd catalysts, including Pd with different ligands, Pd immobilized on MOFs and other new matrices, which had good catalytic efficiency.[44–47] Herein, the polymer–Pd nanocomposite (Pd@PEG$_{113}$-*b*-PDMAEMA$_{24}$-*b*-PHPMA$_{1170}$, TA : Pd = 1 : 7) catalyzed Suzuki–Miyaura cross-coupling of 4-iodophenol and phenylboronic acid was examined and compared with commercial palladium on activated carbon (Pd/C) and Pd@PVP (Fig. S16d†). In the absence of any Pd catalysts, the coupling reaction could only proceed with 8.5% yield (Table 3, entry 1) in 1 hour. All Pd catalysts were found to exhibit excellent efficiency, with almost complete conversions achieved at catalyst concentrations above 0.18 mol% (Table 3, entries 2–4). Because of the high efficiency of Pd catalysts, the concentration of catalysts was reduced step by step to compare their catalytic efficiency at a lower dosage. As shown in Table 3, the efficiency of Pd@PVP and polymer–Pd nanocomposites remained at excellent levels, achieving a nearly complete conversion even when the concentration was reduced to 0.04 mol% (Table 3, entries 6, 7, 9 and 10). In contrast, the yield decreased to 44.8% for Pd/C at the catalyst concentration of 0.09 mol% (Table 3, entry 5), and it further reduced to 12.5% (Table 3, entry 8), which is close to the control group without any Pd catalyst, at the catalyst concentration of 0.04 mol%.

Polymer–Pd nanocomposites and Pd@PVP could achieve high conversions even at catalyst concentration as low as 0.01 mol% (100 ppm, Table 3, entries 13 and 14). Therefore, to compare the catalytic efficiency of polymer–Pd nanocomposites and Pd@PVP at extremely low concentrations, the reactions were conducted with 100 ppm and 40 ppm of corresponding catalysts, and the kinetics were monitored by NMR analysis with

Table 3 Summary of the Suzuki–Miyaura cross coupling reaction using different types of Pd catalysts

Entry	Catalyst	Catalyst eq.^{a} (mol%)	NMR yield^b (%)
1	None	—	8.5
2	Pd/C	0.18–0.72	>99
3	Pd@PVP	0.18–0.72	>99
4	Polymer–Pd nanocomposite	0.18–0.72	>99
5	Pd/C	0.09	44.8
6	Pd@PVP	0.09	>99
7	Polymer–Pd nanocomposite	0.09	>99
8	Pd/C	0.04	12.5
9	Pd@PVP	0.04	>99
10	Polymer–Pd nanocomposite	0.04	>99
11	Pd@PVP	0.02	96.8
12	Polymer–Pd nanocomposite	0.02	97.4
13	Pd@PVP	0.01	92.6
14	Polymer–Pd nanocomposite	0.01	93.8
15	Pd@PVP	0.004 (40 ppm)	51.5
16	Polymer–Pd nanocomposite	0.004 (40 ppm)	65.8
17	Pd@PVP	0.002 (20 ppm)	21.5
18	Polymer–Pd nanocomposite	0.002 (20 ppm)	33.6

^{a} Catalyst eq. (mol%) = [catalyst]/[4-iodophenol] × 100%. ^{b} Yield was calculated by comparing the NMR spectrum of reaction, and the detailed calculation equation is listed in Fig. S15.

periodic sampling. As shown in Fig. 8, the efficiency performances of both catalysts were very close at the concentration of 100 ppm. Nevertheless, the polymer–Pd nanocomposite was more efficient than Pd@PVP at the concentration of 40 ppm, and it has a higher TOF value of 4.3×10^4 h^{-1}, compared to 2.5×10^4 h^{-1} of Pd@PVP (calculated by the 0.004 mol% total Pd atoms at 10 min). Notably, the polymer–Pd nanocomposite still achieved a yield of 33.6% within 1 h at 20 ppm (Table 3, entry 18) compared to the 21.5% yield of Pd@PVP under the same conditions (Table 3, entry 17). Overall, the catalytic efficiency of the immobilized Pd nanocatalyst was verified to be higher than those of Pd/C and Pd@PVP in this 4-iodophenol and

phenylboronic acid Suzuki–Miyaura cross-coupling reaction. This can be explained by the same rationales as discussed for polymer–Au nanocomposites. On the other hand, the catalytic activity of polymer–Pd nanocomposites gradually decreased after several reuse tests (Fig. S19 and S20†). The yield decreased from 98.8 to 82.1% after 5 times, however, the yields are still within the acceptable range for practical application.

Conclusions

It was demonstrated that polymer–metal nanocomposites could be prepared by utilizing ultrasound as the initiation and reducing source for the synthesis of polymer and metal nanoparticles, respectively. The use of sono-PISA provides an effective *in situ* self-assembly strategy for the scalable preparation of copolymer nano-spheres PEG$_{113}$-*b*-PDMAEMA$_{24}$-*b*-PHPMA$_n$. It was also shown that the sizes of the polymeric nano-spheres can be easily modified by increasing the DP of the PHPMA block. In addition, using ultrasound as the reducing source, it is possible to prepare polymer–Au and polymer–Pd nanocomposites with AuNPs and PdNPs being immobilized on the hydrophilic shell of the polymer matrix. It was found that the size of metal nanoparticles is closely related to the ratio of tertiary amine groups in the polymer matrix to metal atoms. These polymer–metal nanocomposite materials are particularly attractive as nano-catalysts, and the catalytic applications of both polymer–Au and polymer–Pd nanocomposites were demonstrated for the aerobic oxidation of alcohol and Suzuki–Miyaura cross-
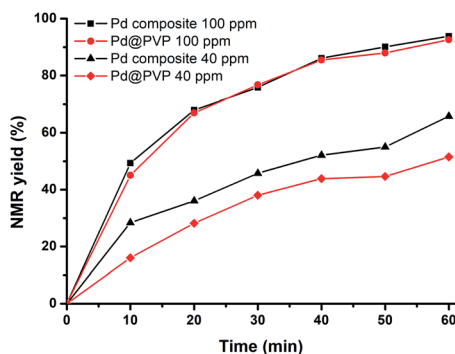

Fig. 8 Time-dependent NMR yield of 4-phenylphenol in the Suzuki–Miyaura coupling catalyzed by polymer–Pd nanocomposites and Pd@PVP.

coupling reactions, respectively. Meanwhile, these metal nanocomposites exhibit superior catalytic efficiency to PVP-stabilized metal nanoparticles or commercially available Pd/C. Furthermore, it was also demonstrated that the sizes of AuNPs on the polymer matrix could be further grown incrementally to afford potential applications such as SERS substrates. Overall, this study should open many new prospects for the field of polymer–metal nanocomposites due to the "green" nature of sonochemistry and scalable feature of the PISA process. Future work will involve the *in situ* formation of metal nanoparticles on the stabilizing macro-RAFT agent by ultrasound followed by the sono-PISA process, or even a "one-pot" synthesis of polymer–metal composites by forming metal nanoparticles and sono-PISA in the same reaction flask.

Conflicts of interest

There are no conflicts to declare.

Acknowledgements

Notes and references

1 O. S. Muddineti, B. Ghosh and S. Biswas, *Int. J. Pharm.*, 2015, **484**, 252–267.

2 M. Han, X. Gao, J. Z. Su and S. Nie, *Nat. Biotechnol.*, 2001, **19**, 631–635.

3 I. V. Kityk, J. Ebothé, I. Fuks-Janczarek, A. A. Umar, K. Kobayashi, M. Oyama and B. Sahraoui, *Nanotechnology*, 2005, **16**, 1687–1692.

4 Y. Liu, B. Fan, Q. Shi, D. Dong, S. Gong, B. Zhu, R. Fu, S. H. Thang and W. Cheng, *ACS Nano*, 2019, **13**, 6760–6769.

5 D. M. Vriezema, M. Comellas Aragonès, J. A. A. W. Elemans, J. J. L. M. Cornelissen, A. E. Rowan and R. J. M. Nolte, *Chem. Rev.*, 2005, **105**, 1445–1490.

6 P. Shi, C. Gao, X. He, P. Sun and W. Zhang, *Macromolecules*, 2015, **48**, 1380–1389.

7 S. Ogasawara and S. Kato, *J. Am. Chem. Soc.*, 2010, **132**, 4608–4613.

8 P. N. Eyimegwu, J. A. Lartey and J.-H. Kim, *ACS Appl. Nano Mater.*, 2019, **2**, 6057–6066.

9 W. Jang, J. Yun, L. Ludwig, S. G. Jang, J. Y. Bae, H. Byun and J.-H. Kim, *Front. Chem.*, 2020, **8**, 834.

10 Y. Li, A. E. Smith, B. S. Lokitz and C. L. McCormick, *Macromolecules*, 2007, **40**, 8524–8526.

11 P. Lim Soo and A. Eisenberg, *J. Polym. Sci., Part B: Polym. Phys.*, 2004, **42**, 923–938.

12 Z. Deng and S. Liu, *Polymer*, 2020, **207**, 122914.

13 B. Fan, R. E. Yardley, J. F. Trant, A. Borecki and E. R. Gillies, *Polym. Chem.*, 2018, **9**, 2601–2610.

14 B. Fan, J. F. Trant, G. Hemery, O. Sandre and E. R. Gillies, *Chem. Commun.*, 2017, **53**, 12068–12071.

15 J. F. Trant, N. Jain, D. M. Mazzuca, J. T. McIntosh, B. Fan, S. M. Haeryfar, S. Lecommandoux and E. R. Gillies, *Nanoscale*, 2016, **8**, 17694–17704.

16 B. Fan, J. Wan, J. Zhai, X. Chen and S. H. Thang, *ACS Nano*, 2021, **15**, 4688–4698.

17 B. Fan, Y. Liu, J. Wan, S. Crawford and S. H. Thang, *ACS Mater. Lett.*, 2020, **2**, 492–498.

18 Y. Zhang, P. Filipczak, G. He, G. Nowaczyk, L. Witczak, W. Raj, M. Kozanecki, K. Matyjaszewski and J. Pietrasik, *Polymer*, 2017, **129**, 144–150.

19 Y. Zhang, Z. Wang, K. Matyjaszewski and J. Pietrasik, *Eur. Polym. J.*, 2019, **110**, 49–55.

20 R. Bleach, B. Karagoz, S. M. Prakash, T. P. Davis and C. Boyer, *ACS Macro Lett.*, 2014, **3**, 591–596.

21 J. Wan, B. Fan, Y. Liu, T. Hsia, K. Qin, T. Junkers, B. M. Teo and S. H. Thang, *Polym. Chem.*, 2020, **11**, 3564–3572.

22 R. A. Caruso, M. Ashokkumar and F. Grieser, *Langmuir*, 2002, **18**, 7831–7836.

23 K. Okitsu, M. Ashokkumar and F. Grieser, *J. Phys. Chem. B*, 2005, **109**, 20673–20675.

24 K. Okitsu, A. Yue, S. Tanabe, H. Matsumoto and Y. Yobiko, *Langmuir*, 2001, **17**, 7717–7720.

25 S. A. Yeung, R. Hobson, S. Biggs and F. Grieser, *J. Chem. Soc., Chem. Commun.*, 1993, **4**, 378–379.

26 Y. Mizukoshi, K. Okitsu, Y. Maeda, T. A. Yamamoto, R. Oshima and Y. Nagata, *J. Phys. Chem. B*, 1997, **101**, 7033–7037.

27 B. Fan, J. Wan, A. McKay, Z. Qu and S. H. Thang, *Polym. Chem.*, 2020, **11**, 5649–5658.

28 J. Chiefari, Y. K. Chong, F. Ercole, J. Krstina, J. Jeffery, T. P. T. Le, R. T. A. Mayadunne, G. F. Meijs, C. L. Moad, G. Moad, E. Rizzardo and S. H. Thang, *Macromolecules*, 1998, **31**, 5559–5562.

29 B. Fan and E. R. Gillies, *Mol. Pharmaceutics*, 2017, **14**, 2548–2559.

30 N. J. W. Penfold, J. Yeow, C. Boyer and S. P. Armes, *ACS Macro Lett.*, 2019, **8**, 1029–1054.

31 J. D. S. Newman and G. J. Blanchard, *Langmuir*, 2006, **22**, 5882–5887.

32 J. Hu, G. Zhang, Z. Ge and S. Liu, *Prog. Polym. Sci.*, 2014, **39**, 1096–1143.

33 S. Luo, J. Xu, Y. Zhang, S. Liu and C. Wu, *J. Phys. Chem. B*, 2005, **109**, 22159–22166.

34 J.-J. Yuan, A. Schmid, S. P. Armes and A. L. Lewis, *Langmuir*, 2006, **22**, 11022–11027.

35 G. Zhao, X. Ran, X. Zhou, X. Tan, H. Lei, X. Xie, L. Yang and G. Du, *ACS Sustainable Chem. Eng.*, 2018, **6**, 3938–3947.

36 X. Tan, Y. Fan, S. Wang, Y. Wu, W. Shi, T. Huang and G. Zhao, *Electrochim. Acta*, 2020, **335**, 135706.

37 W. Haiss, N. T. K. Thanh, J. Aveyard and D. G. Fernig, *Anal. Chem.*, 2007, **79**, 4215–4221.

38 K. R. Brown and M. J. Natan, *Langmuir*, 1998, **14**, 726–728.

39 K. R. Brown, D. G. Walter and M. J. Natan, *Chem. Mater.*, 2000, **12**, 306–313.

40 K. J. Si, D. Sikdar, L. W. Yap, J. K. K. Foo, P. Guo, Q. Shi, M. Premaratne and W. Cheng, *Adv. Opt. Mater.*, 2015, **3**, 1710–1717.

41 H. Tsunoyama, H. Sakurai, Y. Negishi and T. Tsukuda, *J. Am. Chem. Soc.*, 2005, **127**, 9374–9375.

42 K. M. Koczkur, S. Mourdikoudis, L. Polavarapu and S. E. Skrabalak, *Dalton Trans.*, 2015, **44**, 17883–17905.

43 S. E. Hooshmand, B. Heidari, R. Sedghi and R. S. Varma, *Green Chem.*, 2019, **21**, 381–405.

44 R. Martin and S. L. Buchwald, *Acc. Chem. Res.*, 2008, **41**, 1461–1473.

45 B. Yuan, Y. Pan, Y. Li, B. Yin and H. Jiang, *Angew. Chem., Int. Ed.*, 2010, **49**, 4054–4058.

46 W. Dong, L. Zhang, C. Wang, C. Feng, N. Shang, S. Gao and C. Wang, *RSC Adv.*, 2016, **6**, 37118–37123.

47 M. W. Easson, J. H. Jordan, J. M. Bland, D. J. Hinchliffe and B. D. Condon, *ACS Appl. Nano Mater.*, 2020, **3**, 6304–6309.

Polymerization-Induced Hierarchical Self-Assembly: From Monomer to Complex Colloidal Molecules and Beyond

Jing Wan, Bo Fan,* Kevin Putera, Jinhee Kim, Mark M. Banaszak Holl, and San H. Thang*

Read Online

ACCESS | Metrics & More | Article Recommendations | SI Supporting Information

ABSTRACT: The nanoscale hierarchical design that draws inspiration from nature's biomaterials allows the enhancement of material performance and enables multifarious applications. Self-assembly of block copolymers represents one of these artificial techniques that provide an elegant bottom-up strategy for the synthesis of soft colloidal hierarchies. Fast-growing polymerization-induced self-assembly (PISA) renders a one-step process for the polymer synthesis and *in situ* self-assembly at high concentrations. Nevertheless, it is exceedingly challenging for the fabrication of hierarchical colloids *via* aqueous PISA, simply because most monomers produce kinetically trapped spheres except for a few PISA-suitable monomers. We demonstrate here a sequential one-pot synthesis of hierarchically self-assembled polymer colloids with diverse morphologies *via* aqueous PISA that overcomes the limitation. Complex formation of water-immiscible monomers with cyclodextrin *via* "host−guest" inclusion, followed by sequential aqueous polymerization, provides a linear triblock terpolymer that can *in situ* self-assemble into hierarchical nanostructures. To access polymer colloids with different morphologies, three types of linear triblock terpolymers were synthesized through this methodology, which allows the preparation of AX_n-type colloidal molecules (CMs), core−shell−corona micelles, and raspberry-like nanoparticles. Furthermore, the phase separations between polymer blocks in nanostructures were revealed by transmission electron microscopy and atomic force microscopy-infrared spectroscopy. The proposed mechanism explained how the interfacial tensions and glass transition temperatures of the core-forming blocks affect the morphologies. Overall, this study provides a scalable method of the production of CMs and other hierarchical structures. It can be applied to different block copolymer formulations to enrich the complexity of morphology and enable diverse functions of nano-objects.

KEYWORDS: *hierarchical self-assembly, polymerization-induced self-assembly, colloidal molecule, cyclodextrin, dispersion polymerization*
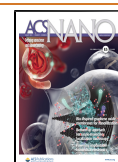
Biological systems feature sophisticated levels of hierarchical structures, as exemplified by proteins, enzymes, and DNA, which govern the precise functions of life. This phenomenon has inspired researchers to design and fabricate artificial nanomaterials with complex structures through bottom-up hierarchical self-assembly for the applications of electronics, photonics, and sensors.[1−9] In the past decade, a myriad of hierarchical nanostructures composed of various building blocks, both organic and inorganic ones, have been achieved through the interactions, such as electrostatic attraction,[10] DNA hybridization,[11] ligand reaction,[4,12] hydrogen bonding,[13] and hydrophobic interactions.[14−17] Polymer assemblies represent one class of soft colloidal particles. Currently, a series of polymer nanostructures,[18,19] including micelle,[20,21] worm, vesicle,[22] lamellae,[23] tecto-(dendrimers),[24,25] cubosome,[26−28] and hexosome[29] have

been realized *via* solution self-assembly of diblock copolymers. However, for more complex nanostructures, such as hierarchical polymer colloids, they require the rational design of polymer structures containing three or more blocks with distinct physical properties.[30−32] For example, Müller and co-workers showed that by synthesizing linear triblock terpolymers with properly designed length ratios of the blocks, a wide range of compartmentalized morphologies could be

achieved, such as spheres, cylinders, sheets, and vesicles, all equipped with a variety of patch morphologies.[33−35] In addition, they demonstrated the application of these nanoscale structures to be soft colloidal building blocks that can be further self-assembled on a higher-level complexity. Nevertheless, conventional self-assembly of block copolymers involves synthesis and self-assembly in separate steps, and the latter step is usually achieved under low concentration (*e.g.*, 0.1−1.0 wt %), which poses difficulties for large-scale applications.[36]

Polymerization-induced self-assembly (PISA) has been exploited as a robust and scalable technique for the preparation of diblock copolymers nanomaterials with different morphologies at high solid contents (up to 40−50 wt %).[37−49] More importantly, the PISA technique can achieve the chemical synthesis and self-assembly in one step without further purification, especially for those prepared in the aqueous environment. However, it has been demonstrated that the utilization of PISA for the fabrication of complex patchy particles composed of triblock terpolymers was extremely challenging in the aqueous medium, mainly because of the limited monomers that are suitable for this process.[50,51] The existing examples all require the utilization of PISA-suitable monomers, which are soluble in water, whereas the formed polymer should be hydrophobic for *in situ* self-assembly.[52,53] Water-immiscible monomers like styrene[54] and *tert*-butyl acrylate[55] commonly generate kinetically trapped spheres. This tremendously limits the diversity of formulations involving water-immiscible monomers when preparing anisotropic or hierarchical colloids *via* the PISA process.

Fortunately, some seminal works have demonstrated the possibility of utilizing cyclodextrin (CD) to convert hydrophobic monomers into water-soluble complexes over the past decades. For example, Ritter *et al.* conducted an extensive investigation on the polymerization of CD/monomer "guest−host" complexes[56−62] and reported the synthesis of amphiphilic block copolymer by reversible addition−fragmentation chain-transfer (RAFT) polymerization of CD/monomer complex in water.[63] Yuan *et al.* reported the direct dispersion polymerization of the CD/styrene complex to form different nano-objects including nanotubes and dumbbell-like micelles.[50] However, no effort has been devoted to synthesize triblock terpolymer-based hierarchical structures by PISA through the formation of CD complex. The achievement of this research will not only solve the problems such as multistep synthesizes and low particle concentration of conventional solution self-assembly process but also provide various soft colloidal building blocks for further self-assembly into higher order nanostructures.

Herein, we demonstrate a promising strategy for the scalable preparation of ABC linear triblock terpolymer-based nanomaterials through RAFT-PISA of CD/hydrophobic monomer complex in the aqueous environment. Methylated-*β*-cyclodextrin (M*β*CD) was complexed with a hydrophobic monomer to make a homogeneous aqueous solution by "host−guest" inclusion. The RAFT dispersion polymerization of the M*β*CD/monomer complex was performed with a poly(ethylene glycol) (PEG) macromolecular chain transfer agent (macro-CTA) to form colloidal seeds. The diblock colloidal seeds were further chain extended by dispersion polymerization of another M*β*CD/monomer complex to produce triblock colloids *in situ*. With the rational selection of monomers, including styrene (st), *tert*-butyl acrylate (tBA),

tert-butyl methacrylate (tBMA), a series of triblock terpolymers, such as poly(ethylene glycol)-*b*-polystyrene-*b*-poly(*tert*-butyl acrylate) (PEG-*b*-PS-*b*-PtBA), poly(ethylene glycol)-*b*-poly(*tert*-butyl acrylate)-*b*-polystyrene (PEG-*b*-PtBA-*b*-PS), and poly(ethylene glycol)-*b*-poly(*tert*-butyl methacrylate)-*b*-polystyrene (PEG-*b*-PtBMA-*b*-PS) were successfully synthesized. Because of the distinct physical compatibilities, interfacial tensions, and glass transition temperatures (T_g) of each block, the aqueous PISAs resulted in diverse particle morphologies, including anisotropic "Janus" particles and corresponding colloidal molecules (CMs) with different valence bonds, core−shell−corona micelles, and raspberry-like micelles. This facile strategy realized a sequential one-pot synthesis of anisotropic colloids by PISA utilizing water-immiscible monomers, which provides the possibility for large-scale production of CMs or other hierarchical structures. As a result, it can be readily applied to different block copolymer formulations to enrich the complexity in morphologies and functions of *in situ* hierarchically self-assembled nano-objects.

RESULTS AND DISCUSSION

The Rational Selection of Monomers. The hierarchical self-assembly of ABC triblock terpolymers are governed by several factors, including physical compatibility, interfacial energy, T_g, composition orders, *etc.* Therefore, the selection of monomers is extremely important for achieving target morphologies. PEG was chosen as block A as it renders excellent hydrophilicity to stabilizing hydrophobic blocks in the aqueous medium. To access hierarchical structures, the phase separation between blocks B and C is required. Moreover, the interfacial energies of blocks B and C with the water molecules also play critical roles in the self-assembly process. When the interfacial tension between block B and solution is higher than that between block C and solution (γ_{BS} > γ_{CS}), a CM can be achieved; conversely, raspberry-like micelles will likely be formed.[52] In addition, the T_g of core-forming blocks could impact the chain mobility and thus the morphology transition.[64] By carefully reviewing these factors, st, tBA, and tBMA were selected as core-forming monomers. The phase separations between PS (S) and PtBA (T)[65] and PS and PtBMA (M)[66] were reported previously (PEG, PS, PtBA, PtBMA are abbreviated to E, S, T, M in the next discussion, respectively). The interfacial tension and T_g of these blocks are distinct as well (Figure 1); the calculation of interfacial tension is showed in Table S1, Supporting Information).

More importantly, due to the proper molecular size and hydrophobic nature of these monomers (Figure 1), they can
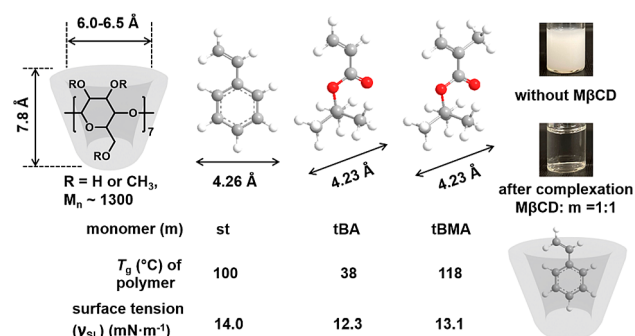
Figure 1. Structure of M*β*CD and chosen monomers forming inclusion complexes with M*β*CD host.
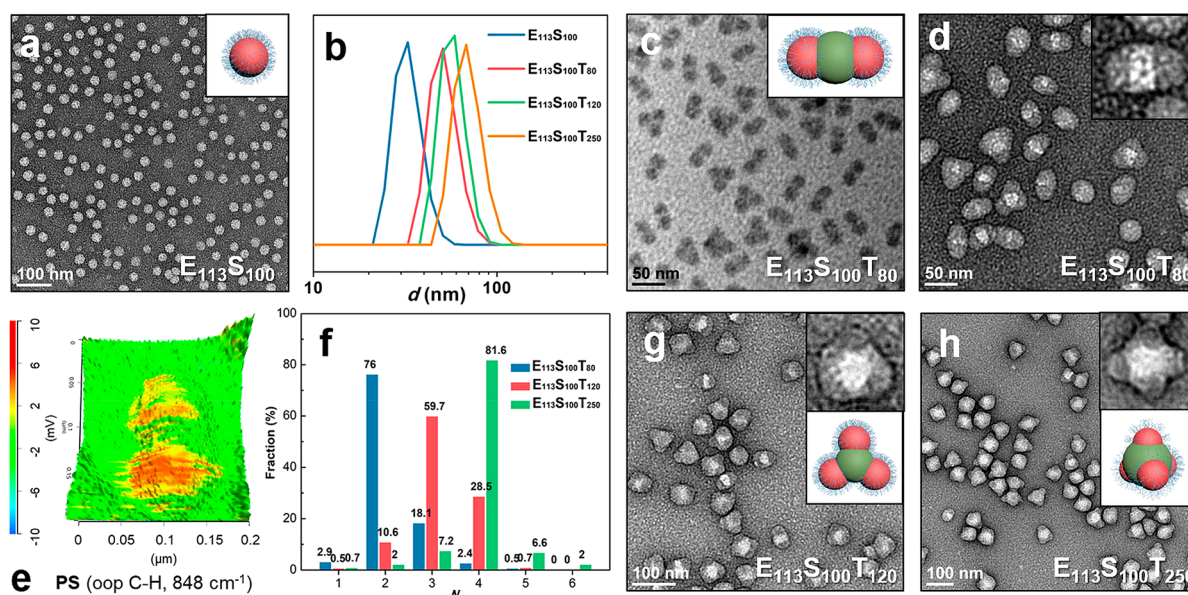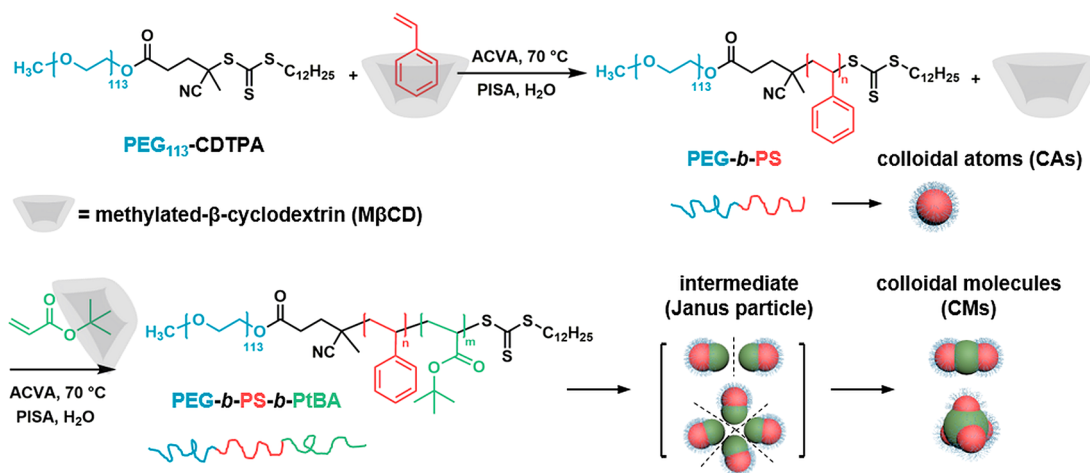
Scheme 1. Synthesis of PEG-*b*-PS CAs and PEG-*b*-PS-*b*-P*t*BA CMs using M*β*CD/Monomer Complex *via* PISA

Figure 2. Representative TEM images and 3D structures (E, blue; S, red; T, green) of (a) $E_{113}S_{100}$ (UA stained), (c) $E_{113}S_{100}T_{80}$ (unstained), (d, g, h) $E_{113}S_{100}T_x$ (x = 80, 120, 250) (UA-RuO$_4$ stained). (b) DLS profiles of $E_{113}S_{100}T_x$ (x = 0, 80, 120, 250) colloids. (e) AFM-IR 3D overlay of topography and IR maps of $E_{113}S_{100}T_{80}$ obtained at 848 cm^{-1} wavenumbers. (f) Valence number (N) distribution of AX$_n$-type CMs of $E_{113}S_{100}T_x$ (x = 80, 120, 250), obtained by analyzing >500 random particles by UA-RuO$_4$ stained TEM.

form "host–guest" complexes with M*β*CD.[50,67] The formed monomer/M*β*CD complexes are water-soluble as confirmed by turbidity tests and ^{1}H NMR spectra (Figures S3–S5). It was found the ratio of M*β*CD:monomer = 1:1 is required to make optimum water-soluble complexes. In addition, the impact of M*β*CD:monomer ratio on the PISA process was also systematically studied. The results indicate it allows the formation of uniform and stable nanoparticles at 1:1 ratio; otherwise, the less addition of M*β*CD produces unstable agglomerates due to superswelling effects in the emulsion polymerization (Figures S9 and S10, Table S2).[68] Consequently, the ratio of M*β*CD: monomer was maintained at 1:1 throughout this study. After forming polymers, the increased steric hindrance and the strong hydrophobic interaction of neighboring repeating units (*e.g.*, aromatic rings and *tert*-butyl moieties) will compete with the interaction of M*β*CD,[69] which results in the dissociation between M*β*CD and polymer. The M*β*CD unthreaded from polymer chains is

freely soluble in water and can be removed without changing the morphology of particles (Figure S10e,j).

Synthesis of AX$_n$-Type CMs Comprised of Triblock Terpolymer PEG-*b*-PS-*b*-P*t*BA. First, macro-RAFT agent comprised of PEG$_{113}$ and widely used RAFT agent 4-cyano-4-(((dodecylthio)carbonothioyl)thio)pentanoic acid (CDTPA)[70,71] was synthesized through Steglich esterification (Figure S1). The PEG$_{113}$-CDTPA was then chain-extended with st by dispersion polymerization of M*β*CD/st complex (1:1) in water (Scheme 1) at 70 °C with 4,4′-azobis(4-cyanopentanoic acid) (ACVA) as initiator. The reaction temperature was selected, as it is relatively high to allow good mobility and still below the lower critical solution temperature (LCST) of PEG (LCST > 100 °C).[72] Figure S11 shows the kinetics data of PEG$_{113}$-CDTPA mediated polymerization of M*β*CD/st (targeting DP 100), the plot of $\ln([M]_0/[M])$ *vs* time depicts two regimes, which are in agreement with the typical kinetics of PISA process reported previously.[38] The intersection of two kinetics lines indicates the micellar

nucleation, at which point the unreacted monomer enters into the core to solvate the hydrophobic polymer chains.[73,74] The cloudiness of suspension and hydrodynamic diameter as measured by dynamic light scattering (DLS) increased with the conversion rate (Figure S13). The gel permeation chromatography (GPC) traces (Figure S14) progressively shifted toward higher retention time, which indicates the increase of molecular weight of the PEG-b-PS with the increment of reaction time and showed a linear relationship with the monomer conversion (Figure S11b). Meanwhile, the dispersity ($Đ$) increased slightly with the chain length of polymer (Figure S11b), however, remained relatively low ($Đ <$ 1.2). These characteristics indicate that the dispersion polymerization proceeded in a well-controlled manner.

For the synthesized colloidal atoms (CAs), TEM image (Figure 2a) shows the morphology of PEG_{113}-b-PS_{100} ($E_{113}S_{100}$) is spherical with an average diameter of 26.4 nm. Spheres with same morphology and size were synthesized at 50 °C (Figure S15), which implies the thermos-responsive behavior of PEG has a limited impact on this PISA process. Next, the further chain extension with PtBA as the third block leads to the increase in hydrodynamic diameter (Figure 2b) and transformation of CAs from 26.4 nm spheres to 50−55 nm cylinder-like clusters (Figure 2c). The TEM image of PEG_{113}-b-PS_{100}-b-$PtBA_{80}$ ($E_{113}S_{100}T_{80}$) (Figure 2c) shows three-segment cylinder-like particles with two dark gray segments on each end and a light gray domain in the central part, suggesting the PS domain in both ends and PtBA domain in the core, because PS with aromatic rings appears darker than PtBA under TEM. The width of PS segments ($w \sim$ 27 nm) also matching with the average particle diameter of $E_{113}S_{100}$ CAs ($d \sim$ 26.4 nm). To further study this morphology and confirm the composition of $E_{113}S_{100}T_{80}$ particles, the sample was stained with uranyl acetate (UA) and then ruthenium tetroxide (RuO$_4$). The UA negative staining can reveal the overall morphology, whereas RuO$_4$ can react with PS to enhance electron absorption. The stained TEM image (Figure 2d) substantiates that PS domain appears in the peripheral region and PtBA in the central region (UA staining: a 'halo' of stain forms around the particle; RuO$_4$ staining: PS, dark gray; PtBA, white; PEG, not visible). This rarely achieved hierarchical structure was coined as a colloidal molecule (CM),[75] and this specific one resembles the molecular structure of CO_2 with a formulation of X−A−X (or AX$_2$) (valence number N = 2) and a bond angle of 180°. CMs are clusters of particles or CAs that mimic the symmetry of molecular structures and have attracted extensive interest due to their specific properties.[1,76−78] These CMs could potentially function as building blocks for the direct assembly of complex hierarchically organized materials.[79−81]

To further confirm the composition of the CMs, atomic force microscopy-infrared spectroscopy (AFM-IR) was employed as an advanced technique to map the nanoparticle component distribution. The AFM-IR spectra of background and nanoparticles were recorded in the range between 1850 and 800 cm^{-1} (Figure S16a). Two specific IR regions were selected as fingerprints for PS and PEG/PtBA. The ester and ether C−O stretching at 1044 cm^{-1} resulted from both PtBA and PEG. The out-of-plane (oop) bending of the aromatic C−H bond at 848 cm^{-1} is typical of PS. Subsequently, IR chemical mappings of CM were recorded at the selected 1044 and 848 cm^{-1} wavenumbers, making the distribution of polymer domains easily distinguishable (Figure 2e and Figure S16b).

The green color in the three-dimensional (3D) topographies indicates no IR absorption, and the color shifts from yellow to red with the increasing of signal. It was found that PS signal (848 cm^{-1}) was detectable on both peripheral sides of CM (Figure 2e), which is consistent with the TEM results. Noteworthy, the dimension of the CM estimated by AFM topography is larger than that by TEM because of the lateral broadening of surface protrusions, which results from the AFM imaging artifact due to the tip convolution effect.[82,83] Overall, the combined TEM images and AFM-IR results verified the successful preparation of AX$_2$-type CMs in analogy to CO_2.

The $E_{113}S_{100}T_{80}$ mainly produced AX$_2$ CMs (76%), with small portion of CM intermediate (N = 1, 2.9%), AX$_3$ (N = 3, 18.1%), and AX$_4$ (N = 4, 2.4%) CMs (distribution shown in Figure 2f). With the further growth of the third block (PtBA, DP = 120), significantly more AX$_3$ and AX$_4$ were observed in the TEM image (Figure 2g); the fraction of AX$_2$ (10.6%) decreased drastically along with the increase of AX$_3$ (59.7%) and AX$_4$ (28.5%) portions. When the degree of polymerization (DP) of PtBA increased to 250, AX$_4$ became the dominant structure (81.6%) (Figure 2f, 2h). Considering the polymer solid content (3 wt %) and the fraction of each type of CMs, the $E_{113}S_{100}T_{80}$ and $E_{113}S_{100}T_{250}$ suspensions yielded 22.8 g/L AX$_2$ and 24.5 g/L AX$_4$, respectively. These values are much higher than previously reported methodology through the solution self-assembly process (typically <1 g/L).[35,84] More importantly, in the colloids of $E_{113}S_{100}T_x$ (x = 80−250), CMs with different valences ranging from 2 to 6 (linear, triangular, tetrahedral, trigonal bipyramidal, square pyramidal, octahedral) were successfully captured by both TEM and SEM (Figure 3a). These artificial CMs are analogues of molecules such as CO_2, BCl_3, CH_4, PCl_5, BrF_5, and SF_6, which further demonstrates the potential of this technique in the preparation of CMs with high diversity. Meanwhile, it has been demonstrated that MβCD plays a critical role in the formation of AX$_n$-type CMs, as the control group ($E_{113}S_{100}$) with MβCD is removed by dialysis, the synthesized $E_{113}S_{100}T_{200}$ in water only resulted in kinetically trapped spherical nanoparticles without obvious patches (Figure S17).

Using the same approach, CMs composed of $E_{113}S_{200}T_x$ with $E_{113}S_{200}$ as CAs ($d \sim$ 32.9 nm, Figure 3b) were fabricated as well. Colloidal intermediate (AX, "Janus" particle) and AX$_2$ were observed (Figure 3c) as the major products for $E_{113}S_{200}T_{89}$. The width of the dark gray PS domain ($w \sim$ 32−35 nm) matches the average diameter of $E_{113}S_{200}$ CAs. Meanwhile, some short chain-like clusters containing 3−4 CAs in a row were observed (Figure 3c). For $E_{113}S_{200}T_{235}$, with longer PtBA, CMs with high valence numbers (N > 6) were identified as the dominant morphology (Figure 3d). By verifying the valence number distribution of $E_{113}S_{100}T_x$ and $E_{113}S_{200}T_x$, there is a general trend that the average valence number (N_{avg}) of CMs increases with the DP of PtBA, which is directly related to the volume ratio of PtBA to PS (V_C/V_B) (calculation of V_C/V_B showed in ESI and Table S3). However, even for CMs with the very close V_C/V_B, $e.g.$ $E_{113}S_{100}T_{120}$ (V_C/V_B = 1.55) and $E_{113}S_{200}T_{235}$ (V_C/V_B = 1.52), the morphology and N_{avg} could be distinct due to different CAs were employed (Figure 2a and 3b). The particular reason for this circumstance is that the packing number of $E_{113}S_{200}$ CA is larger than $E_{113}S_{100}$, thus the number of diblock polymer chains in a single CA is different for $E_{113}S_{100}$ and $E_{113}S_{200}$, leading to different CM intermediates and different clustering in the seeded dispersion polymerization. Thus, the influence of volume ratio
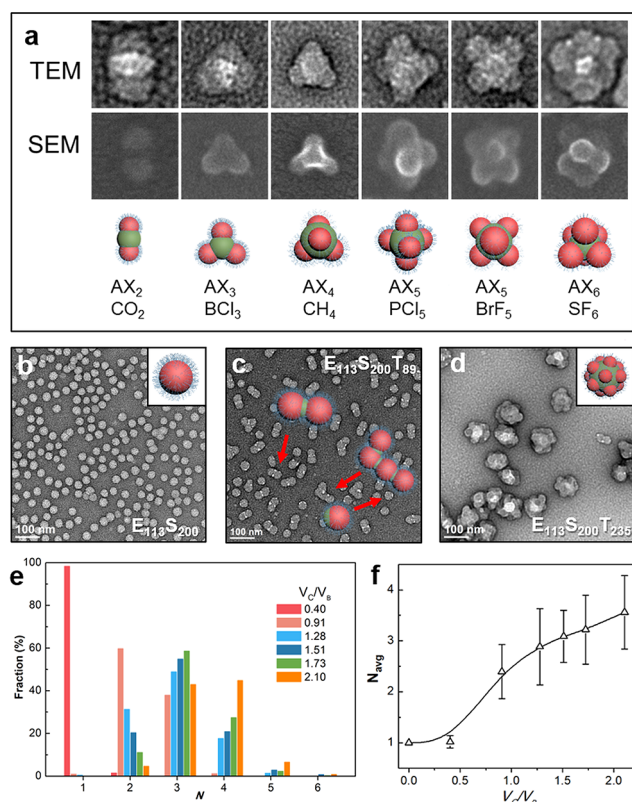
Figure 3. (a) Representative TEM and SEM images of AX_n-type (n = 2−6) CMs observed from $E_{113}S_{100}T_x$ (x = 80−250) colloids. (b−d) TEM images of $E_{113}S_{200}$, $E_{113}S_{200}T_{89}$, and $E_{113}S_{200}T_{235}$. (e) Valence number (N) distribution of CMs with various V_C/V_B ratio (0.40−2.10) during PISA (targeting $E_{113}S_{100}T_{200}$). (f) Plot of mean average valence number (N_{avg}) against V_C/V_B. Error bars are standard deviation of population σ (calculation of N_{avg} and σ showed in the Supporting Information).

V_C/V_B can only be discussed for the CMs prepared from CAs with the same length of PS block.

Next, to understand the morphological evolution, aliquots were collected at specific time points of seeded dispersion polymerization ($E_{113}S_{100}$ to $E_{113}S_{100}T_x$, targeting x = 200), and a series of $E_{113}S_{100}T_x$ (x = 31−163) samples were obtained (Table S4 and Figure S18). The kinetic study depicts a linear pseudo-first-order rate plot, indicating a constant propagating radical concentration during the polymerization (Figure S19a).

As expected, no micellar nucleation state was found due to the micelle formation has been achieved in the synthesis of CAs. The GPC traces exhibited small shoulders (Figure S20), which might be due to the presence of impurity from commercial PEG_{113} (Figure S2) and high molecular weight polymers produced by recombination termination or chian transfer reactions. This phenomenon is well-documented and constantly observed for the RAFT polymerization of acrylate monomers.[85] However, the progress of GPC curves with reaction time, the liner increase of molecular weight with conversion as well as the low Đ indicate the living characteristics and the good control of the seeded dispersion polymerization (Figure S19b). The growth of PtBA blocks leads to an increase in the hydrodynamic diameter (Figure S21) and the transformation of morphology (Figure S22). Figure 3e shows the distribution of CMs valence number (N) shifts toward higher N value with the increasing of V_C/V_B. Specifically, $E_{113}S_{100}B_{31}$ remained as spheres with only 1.5% of AX_2 CMs because PtBA is too short to form domains that lead to clustering. For $E_{113}S_{100}T_{70}$ with a longer PtBA chain (higher V_C/V_B), the intermediate "Janus" particles were no longer stable and further assembled into 59.8% AX_2, 38.0% AX_3, and only 1.2% spheres were observed. The relationship between the average valence (N_{avg}) and V_C/V_B was further revealed in Figure 3f; as V_C/V_B increase from 0.4 to 2.1, the N_{avg} gradually increase from 1.02 to 3.6. This finding is in good agreement with the principle of solvent-based preparation of multi-compartment micelles (MCMs) by Müller et al.,[84] as well as the mechanism of CMs formation proposed by Yuan and co-workers.[52] For an ABC triblock terpolymer, when the ratio between block C and block B is higher than 1 ($V_C/V_B > 1$), the unstable monovalent Janus intermediates assembly into AX_n-type colloidal molecules or cluster-like MCMs, the valence n of CMs is determined by V_C/V_B. When the $V_C/V_B \leq 1$, divalent intermediates with two attractive patches could form colloidal chains (Figure 3c). Different from previous studies, the CM morphology in this study was implemented based on an EST formulation in aqueous medium. In addition, the present study outperformed previous methods in terms of facilitation and efficiency. Unlike previous methods involving multistep synthesis/purification and solvent exchange or low monomer conversion, this study achieved a one-pot synthesis of high-purity CM with almost complete monomer conversion using water as the only solvent, making it perfectly suitable for large-scale production.
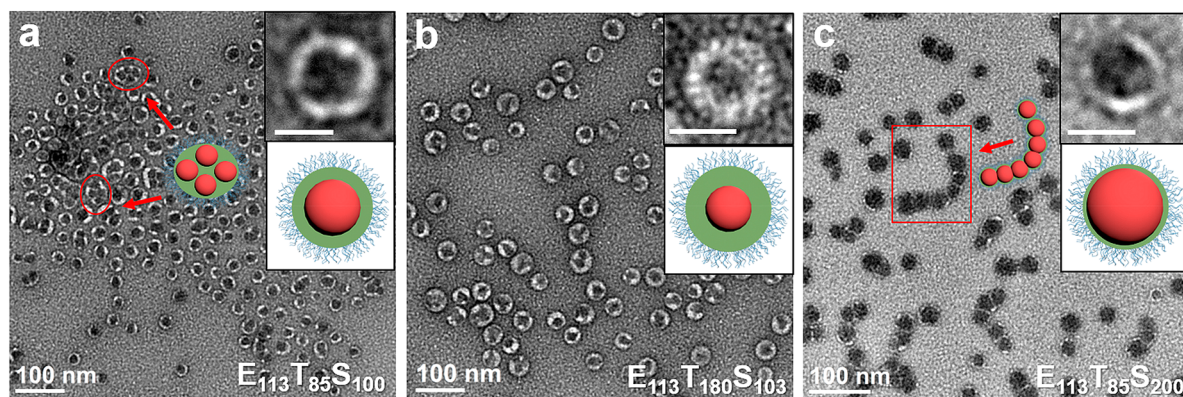
Figure 4. Representative TEM images and 3D structures (E, blue; T, green; S, red) of (a) $E_{113}T_{85}S_{100}$, (b) $E_{113}T_{180}S_{103}$, and (c) $E_{113}T_{85}S_{200}$ (UA-RuO$_4$ stained). Scale bars are 20 nm in the insets.

Synthesis of Core−Shell−Corona Micelles Comprised of Triblock Terpolymer PEG-*b*-P*t*BA-*b*-PS. Another advantage of this MβCD/monomer complex PISA system is that all complexed monomers with different properties are soluble in water, thus the composition of blocks B and C can be readily switched, achieving a different type of hierarchical structures. Therefore, PEG-*b*-P*t*BA ($E_{113}T_x$) diblock copolymer nanoparticles were also synthesized by dispersion polymerization of the MβCD/*t*BA complex. $E_{113}T_{85}$ and $E_{113}T_{180}$ are nanospheres with sizes around 25 and 40 nm, respectively (Figure S23a,b). Next, both nanospheres were employed as seeds for polymerization of MβCD/st complex to form PEG-*b*-P*t*BA-*b*-PS ($E_{113}T_xS_y$) triblock terpolymers nanoparticles in water. With the increasing of PS block (Figure S24), only spheres were observed, and no evident phase separation was observed in the unstained and UA stained particles (Figure S23c,d). Nevertheless, with the staining of RuO$_4$ vapor, the multicompartment nature of particles was unambiguously visualized in TEM images, revealing the presence of PS composition within the core of the nanospheres (Figure 4a). The phase separation between PS and P*t*BA blocks inside the spheres resulting in the formation of the core−shell−corona micelles (PS-core, black; P*t*BA-shell, white; PEG-corona, not visible). This confirms that PS block grew inside the P*t*BA shell rather than between the interface of P*t*BA and water. The shell thickness of $E_{113}T_{85}S_{100}$ is around 5 nm (Figure 4a), and it increased to ∼9 nm for $E_{113}T_{180}S_{103}$ (Figure 4b). However, the core sizes for $E_{113}T_{85}S_{100}$ and $E_{113}T_{180}S_{103}$ are both around 20 nm (Figure 4a,b), as they have approximately the same length of PS. Since P*t*BA has a low T_g (38 °C), the shell can be easily expanded with the increasing of the core size. This is reflected in $E_{113}T_{85}S_{200}$, which has a core size of ∼25 nm and a thin shell layer (Figure 4c). Meanwhile, due to the good mobility of P*t*BA block, the shell layer of some of these particles had merged, resulting in the formation of multicore spheres and peapod-like structures (Figure 4a,c).

The substantial morphological differences between PEG-*b*-PS-*b*-P*t*BA CMs and PEG-*b*-P*t*BA-*b*-PS core−shell−corona micelles indicate that the sequence of the second and third blocks would significantly impact the obtained particles in the PISA process. A similar conclusion was drawn in the solution self-assembly of triblock terpolymers. Laschewsky *et al.* reported the self-assembly of ABC, ACB, and BAC types of triblock terpolymers and discovered the formation of different types of particles, including core−shell−corona micelles and double patched nanoparticles.[14,15] In this study, the solid−water surface tension and T_g of PS and P*t*BA are both different, thus altering the sequence will impact the eventual self-assembly results. The influence of these factors will be further discussed next.

Synthesis of Raspberry-like Nanoparticles Comprised of Triblock Terpolymer PEG-*b*-P*t*BMA-*b*-PS. The polymer chain mobility is greatly decreased at a temperature below T_g, which prevents the transformation from spherical micelles to higher order morphology.[86−89] P*t*BMA has a relatively high T_g (118 °C) and is too stiff to fuse with other particles at the reaction temperature (70 °C). Therefore, by replacing block B (P*t*BA) with P*t*BMA, which is also incompatible with PS, block C (PS) would likely protrude from the P*t*BMA shell. To verify this hypothesis, ABC block terpolymers composed of PEG-*b*-P*t*BMA-*b*-PS were synthesized *via* PISA as well. First, the seed suspension composed of PEG-*b*-P*t*BMA ($E_{113}M_{97}$) was

prepared. The diblock copolymer formed spheres with a rough surface and diameter ∼80 nm (Figure S25a). Next, a series of PEG-*b*-P*t*BMA-*b*-PS (with targeting PS DP of 30−300, Figure S25) were synthesized using $E_{113}M_{97}$ as seed and MβCD/st complex as chain extended monomer. When the DP of block C reached 100 (Figure 5a), the PS domains were
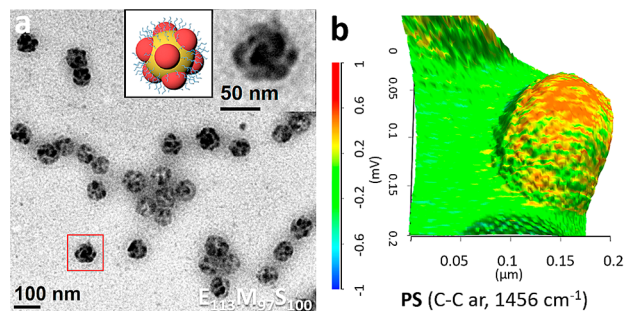
Figure 5. (a) TEM images of $E_{113}M_{97}S_{100}$ raspberry-like particles (unstained). (b) AFM-IR 3D overlay of topography and IR maps of $E_{113}M_{97}S_{100}$ obtained at 1456 cm^{-1} wavenumbers.

observed as dark gray patches on the particle, which result in the formation of a raspberry-like structure. This phenomenon resulted from the microphase separation between P*t*BMA and PS and also because of the high T_g of P*t*BMA. At the beginning of polymerization, PS microdomains aggregate inside the P*t*BMA core. With the growth of PS chain length and volume, the P*t*BMA core is not sufficient to conceal the PS domain, it is too rigid to expand or fuse with other particles (forming multicore micelles as ETS), and the PS domain will crack the P*t*BMA shell and protrude to form small patches at the interface between P*t*BMA and water. To further verify this raspberry-like structure, AFM-IR analysis (Figure 5b) was conducted. It was found the PS signal was detected over scattered regions on the sphere, suggesting that PS dispersed as microdomains on the particle. With the further growth of the PS block ($E_{113}M_{97}S_{200}$), a similar raspberry-like structure with more PS domains on each particle was found due to increased PS volume (Figure S26b).

Assembly Mechanism of ABC Triblock Copolymer during PISA. The universal self-assembly driving force is to reach thermodynamic equilibrium by minimization of the free energy,[34] including the circumstance in this study. The free energy can be presented as

$$F = F_{corona} + F_{core} + F_{interface}$$

where F_{corona} describes repulsive interactions between coronal chains A, whereas F_{core} accounts for the conformational entropy losses in the collapsed core-forming segments.[84] In this study, all triblock copolymers contain the same coronal block A, and F_{core} is negligibly small, thus the interfacial energy $F_{interface}$ determines the morphology of ABC linear triblock terpolymers. It can be presented as

$$F_{interface} = \gamma_{BS}S_{BS} + \gamma_{CS}S_{CS} + \gamma_{BC}S_{BC}$$

where γ_{BS}, γ_{CS}, and γ_{BC} are the surface tensions, and S_{BS}, S_{CS}, S_{BC} are the interfacial areas at the B−solvent, C−solvent, and B−C interfaces, respectively. As shown in Figure 6, for the ABC linear triblock terpolymer, if the interfacial tension $\gamma_{BS} > \gamma_{CS}$, the block C tends to aggregate at the interface between the block B−solvent interface to minimize S_{BS} and the total $F_{interface}$. As a result, it forms CM intermediates and
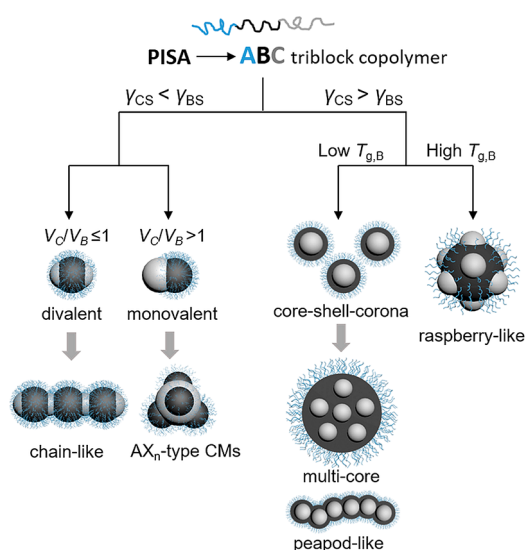
Figure 6. ABC triblock terpolymer hierarchically self-assembly mechanisms under the current PISA conditions.

hierarchically self-assembles into AX$_n$-type CMs. In the PISA of EST, as the surface tension at the PS and water interface is higher than that at PtBA and water interface ($\gamma_{S-W} > \gamma_{B-W}$), P$t$BA aggregates in the interface of PS and water to minimize unfavorable PS—water interface (the surface tensions were calculated from Girifalco—Good equation as shown in Table S1). On the contrary, if $\gamma_{BS} < \gamma_{CS}$, block C tends to grow inside the core of block B, forming the core—shell—corona micelles first. With the further growth of block C, and for the case with block B that has a relatively low T_g, the good mobility of B allows the fusion of particle shells to form multicore and peapod-like MCMs; for the case with block B that has a high T_g, the fusion between B is limited, and block C will protrude from the core to form raspberry-like MCMs. This explains the morphological evolutions for ETS and EMS (Figures 4a and 5a).

This study not only introduced a facile methodology for the preparation of hierarchical polymer nanostructures with diverse morphologies but also systematically studied various factors, including surface tension, polymer composition order, and the glass transition temperature of polymers that could affect the morphologies of triblock terpolymers. Therefore, the proposed mechanism derived from this study could serve as a guideline of triblock terpolymer self-assembly to predict the morphologies of different formulations. Meanwhile, it is conceivable that many other hydrophobic monomers with specific functional groups that are capable of complexing with β-CD can also be applied to conduct dispersion polymerization in water. Beyond β-CD, it is well-known that α- and γ-CD with different inner hydrophobic cavity sizes can also complex with a variety of guest molecules and monomers. For instance, the complex between aliphatic groups and α-CD[90] and two pyrenyl groups with one γ-CD[91] were reported previously. It is foreseeable that monomers with these functional groups could also be applied in the aqueous PISA process to furnish the library of polymer self-assembly.

CONCLUSIONS

It was demonstrated that through the formation of MβCD/monomer complex, well-defined ABC triblock terpolymer colloids with diverse morphologies could be conveniently

prepared *via* aqueous PISA. The water-immiscible monomers could be readily converted into water-soluble complexes at a 1:1 molar ratio of monomer:MβCD, therefore providing a series of additional monomer options for aqueous PISA. Furthermore, the kinetic study confirmed the dispersion polymerization process of st (1:1 to MβCD) with PEG-CDTPA as the chain transfer agent. A series of ABC triblock copolymer nanoparticles are achieved by the addition of a third monomer (1:1 to MβCD) in the seeded dispersion polymerization process. Depending on the polymer component and order, a series of different particle morphologies have been achieved. Specifically, EST self-assembled into rarely achieved AX$_n$-type colloidal molecules *in situ* with high purity and concentration (*e.g.*, 81.6% AX$_4$, 24.5 g/L), which provides a scalable possibility for the synthesis of CMs. ETS and EMS form core—shell—corona micelles and raspberry-like micelles, respectively. In addition, the particle formation mechanism driven by minimization of interfacial energy was summarized, which provides a guideline for the rational design of ABC triblock terpolymer nanoparticles. Overall, the robust, scalable nature of this aqueous formulation is expected to provide opportunities in the growing field of block copolymer self-assembly, since they allow access to diverse particle morphologies at relatively high-solid contents.

EXPERIMENTAL SECTION

Typical Synthesis of PEG-*b*-PS Colloidal Atoms. A typical protocol for the preparation of PEG$_{113}$-*b*-PS (targeting DP = 100): PEG$_{113}$-CDTPA (102.4 mg, 0.0190 mmol) and MβCD (2470 mg, 1.90 mmol) were dissolved in 7.23 mL of DI H$_2$O, then st (197.6 mg, 1.90 mmol) was added, and the solid content was maintained at 3 wt %. The mixture was then sonicated for 10 min and stirred vigorously for 30 min at room temperature to obtain a homogeneous MβCD/st solution. ACVA (1.6 mg, 0.0057 mmol, ACVA/CTA = 0.3) was then added. The solution was deoxygenated by three cycles of freeze—vacuum—thaw and immersed into a 70 °C oil bath for 16 h. The solution was then cooled to room temperature and exposed to air. For the kinetic study, the solution was purged with argon for 15 min, sealed, and immersed into a 70 °C oil bath. Aliquots of solution were collected at specific time point for analysis. ^{1}H NMR spectra of the dried crude suspension were obtained using CDCl$_3$ as solvent. PEG-*b*-PtBA and PEG-*b*-PtBMA diblock copolymers were synthesized using the same procedure.

Typical Synthesis of PEG -*b*-PS-*b*-PtBA Colloidal Molecules. A typical protocol for the preparation of PEG$_{113}$-*b*-PS$_{100}$-*b*-PtBA (targeting DP = 250): 991.4 mg of PEG$_{113}$-*b*-PS$_{100}$ suspension (3 wt %, containing 1.88×10^{-3} mmol of PEG$_{113}$-*b*-PS$_{100}$ and 0.188 mmol MβCD), tBA (60.3 mg, 0.470 mmol), and MβCD (366.6 mg, 0.282 mmol) were mixed with 1.58 mL of DI H$_2$O to make a 3 wt % solid content suspension. The mixture was then sonicated for 10 min and stirred for 30 min to obtain a homogeneous suspension, and ACVA (26 μL of 6 mg ACVA/mL methanol solution, ACVA/CTA = 0.3) was added. The suspension was deoxygenated by three cycles of freeze—vacuum—thaw and immersed into a 70 °C oil bath for 16h. The suspension was then cooled to room temperature and exposed to air. Kinetic study was conducted using the same procedure as PEG-*b*-PS. PEG-*b*-PtBA-*b*-PS and PEG-*b*-PtBMA-*b*-PS triblock terpolymers were synthesized using the same procedure.

Synthesis of PEG-*b*-PtBMA *via* PISA of MβCD/tBMA Complex with Various Ratios. Synthesis of PEG$_{113}$-*b*-PtBMA (targeting DP = 100): PEG$_{113}$-CDTPA (24.8 mg, 4.6×10^{-3} mmol) and various amounts of MβCD (0 mg for 0:1 MβCD:tBMA ratio, 119.2 mg for 1:5, 298 mg for 1:2, 596 mg for 1:1) were dissolved in 2.91 mL of DI H$_2$O (amount varying with MβCD to maintain polymer solid content at 3 wt %), then tBMA (65.2 mg, 0.46 mmol) was added. The mixture was then sonicated for 10 min and stirred vigorously for 30 min at room temperature to obtain a homogeneous

MβCD/tBMA solution and turbid tBMA emulsions. ACVA (0.4 mg, 1.4 × 10⁻³ mmol, ACVA/CTA = 0.3, 67 μL of 6 mg/mL methanol solution) was then added. The solution was deoxygenated by three cycles of freeze−vacuum−thaw and immersed into a 70 °C oil bath for 16 h. The solution was then cooled to room temperature and exposed to air. Synthesis of PEG₄₅-b-PtBMA (targeting DP = 50) was conducted using the same procedure by replacing PEG₄₅-CDTPA and adjusting the amount of reagents accordingly. The groups with 1:1 MβCD/tBMA were dialyzed against DI H₂O using a 3.5 kDa MWCO membrane for 2 days to remove MβCD. All suspensions were analyzed by ¹H NMR, GPC, DLS, and TEM (summarized in Figures S8−S10 and Table S2).

Characterization Methods. *Transmission electron microscopy.* The images were taken using an FEI Tecnai G2 T20 TWIN transmission electron microscopy (TEM) instrument equipped with Orius SCD200D wide-angle CCD camera operating at 200 keV. Copper grids (Formvar/carbon coated, 400 mesh) were plasma glow-discharged for 10 s to create a hydrophilic surface. After glow discharge, the grid was contacted with a drop (about 15 μL) of 0.10% w/v aqueous dispersions containing the diblock copolymer nano-objects for 3 min. Excess sample solution was removed by blotting, and the residual was left on the grid to dry completely. The negative staining process was done by allowing 3 μL of uranyl acetate solution (2.0% w/v) to stay on the grid for 1 min, then blotted and dried. Ruthenium tetroxide vapor staining: Freshly prepared 25 μL of RuCl₃ solution (~4% w/v) and 25 μL of NaClO solution (10−15% w/v) were mixed, and the solution and grids were placed in a sealed container at ambient temperature for overnight.

Scanning electron microscopy. The scanning electron microscopy (SEM) sample was prepared by casting a drop (about 10 μL) of 0.10% w/v aqueous dispersions containing the diblock copolymer nano-objects on a silicon wafer. The dispersion was then dried using a gentle nitrogen blow. The sample was then coated with a thin layer (~2 nm) of iridium to make it conductive. Imaging was performed using an FEI Magellan 400 FEGSEM instrument operating at 5.0 kV.

Atomic force microscopy-infrared spectroscopy. The atomic force microscopy-infrared spectroscopy (AFM-IR) sample was prepared by casting a drop (about 10 μL) of 0.10% w/v aqueous dispersions on a silicon wafer and studied using a Bruker NanoIR3 system. AFM scanning was performed at 0.3 Hz line scan rate with 100−150 pixel density on each edge using the noncontact tapping mode probes capable of IR mapping (Model: PR-EX-TnIR-A-10). IR spectra within the range of 790−1850 cm⁻¹ were taken on the nanoparticles with 100% laser power, 3% duty cycle, and 2429 pt IR focus spot.

ASSOCIATED CONTENT

Ⓢ Supporting Information

The Supporting Information is available free of charge at https://pubs.acs.org/doi/10.1021/acsnano.1c05089.

Additional experimental details; NMR, GPC, DLS, TEM, AFM-IR and other measurements; contact angle of homopolymers and calculation of interfacial tensions; cyclodextrin-monomer complexation study; calculation of CMs average valence (PDF)

AUTHOR INFORMATION

Corresponding Authors

Bo Fan − *School of Chemistry, Monash University, Clayton, Victoria 3800, Australia*; Email: bo.fan@monash.edu

San H. Thang − *School of Chemistry, Monash University, Clayton, Victoria 3800, Australia*; ⓘ orcid.org/0000-0003-2629-3895; Email: san.thang@monash.edu

Authors

Jing Wan − *School of Chemistry, Monash University, Clayton, Victoria 3800, Australia*

Kevin Putera − *Department of Chemical Engineering, Monash University, Clayton, Victoria 3800, Australia*

Jinhee Kim − *Department of Chemical Engineering, Monash University, Clayton, Victoria 3800, Australia*

Mark M. Banaszak Holl − *Department of Chemical Engineering, Monash University, Clayton, Victoria 3800, Australia*; ⓘ orcid.org/0000-0001-7759-7456

Complete contact information is available at:
https://pubs.acs.org/10.1021/acsnano.1c05089

Author Contributions

Conceptualization was performed by J.W., B.F., and S.H.T. Data acquisition and curation were performed by J.W. and K.P. The original manuscript was written by J.W. and B.F. The manuscript review and editing were performed by S.H.T., M.M.B.H., K.P., and J.K. Funding acquisition was performed by S.H.T. All authors have given approval to the final version of the manuscript.

Notes

The authors declare no competing financial interest.

REFERENCES

(1) Zeng, C.; Chen, Y.; Kirschbaum, K.; Lambright, K. J.; Jin, R. Emergence of Hierarchical Structural Complexities in Nanoparticles and Their Assembly. *Science* **2016**, *354* (6319), 1580−1584.

(2) von Freymann, G.; Kitaev, V.; Lotsch, B. V.; Ozin, G. A. Bottom-Up Assembly of Photonic Crystals. *Chem. Soc. Rev.* **2013**, *42* (7), 2528−2554.

(3) Inan, H.; Poyraz, M.; Inci, F.; Lifson, M. A.; Baday, M.; Cunningham, B. T.; Demirci, U. Photonic Crystals: Emerging Biosensors and Their Promise for Point-of-Care Applications. *Chem. Soc. Rev.* **2017**, *46* (2), 366−388.

(4) Yi, C.; Liu, H.; Zhang, S.; Yang, Y.; Zhang, Y.; Lu, Z.; Kumacheva, E.; Nie, Z. Self-Limiting Directional Nanoparticle Bonding Governed by Reaction Stoichiometry. *Science* **2020**, *369* (6509), 1369−1374.

(5) Tomalia, D. A.; Khanna, S. N. A Systematic Framework and Nanoperiodic Concept for Unifying Nanoscience: Hard/Soft Nano-elements, Superatoms, Meta-Atoms, New Emerging Properties, Periodic Property Patterns, and Predictive Mendeleev-Like Nano-periodic Tables. *Chem. Rev.* **2016**, *116* (4), 2705−2774.

(6) Wen, W.; Ouyang, W.; Guan, S.; Chen, A. Synthesis of Azobenzene-Containing Liquid Crystalline Block Copolymer Nano-particles *via* Polymerization Induced Hierarchical Self-Assembly. *Polym. Chem.* **2021**, *12* (3), 458−465.

(7) Guan, S.; Zhang, C.; Wen, W.; Qu, T.; Zheng, X.; Zhao, Y.; Chen, A. Formation of Anisotropic Liquid Crystalline Nanoparticles *via* Polymerization-Induced Hierarchical Self-Assembly. *ACS Macro Lett.* **2018**, *7* (3), 358−363.

(8) Xu, Q.; Huang, T.; Li, S.; Li, K.; Li, C.; Liu, Y.; Wang, Y.; Yu, C.; Zhou, Y. Emulsion-Assisted Polymerization-Induced Hierarchical Self-Assembly of Giant Sea Urchin-Like Aggregates on a Large Scale. *Angew. Chem., Int. Ed.* **2018**, *57* (27), 8043−8047.

(9) Skelhon, T. S.; Chen, Y.; Bon, S. A. F. Hierarchical Self-Assembly of 'Hard−Soft' Janus Particles into Colloidal Molecules and Larger Supracolloidal Structures. *Soft Matter* **2014**, *10* (39), 7730−7735.

(10) Hong, L.; Cacciuto, A.; Luijten, E.; Granick, S. Clusters of Charged Janus Spheres. *Nano Lett.* **2006**, *6* (11), 2510−2514.

(11) Wang, Y.; Wang, Y.; Breed, D. R.; Manoharan, V. N.; Feng, L.; Hollingsworth, A. D.; Weck, M.; Pine, D. J. Colloids with Valence and Specific Directional Bonding. *Nature* **2012**, *491* (7422), 51−55.

(12) van Dongen, M. A.; Vaidyanathan, S.; Banaszak Holl, M. M. PAMAM Dendrimers as Quantized Building Blocks for Novel Nanostructures. *Soft Matter* **2013**, *9* (47), 11188−11196.

(13) Hu, J.; Liu, G. Chain Mixing and Segregation in B−C and C−D Diblock Copolymer Micelles. *Macromolecules* **2005**, *38* (19), 8058−8065.

(14) Skrabania, K.; Berlepsch, H. v.; Böttcher, C.; Laschewsky, A. Synthesis of Ternary, Hydrophilic−Lipophilic−Fluorophilic Block Copolymers by Consecutive RAFT Polymerizations and Their Self-Assembly into Multicompartment Micelles. *Macromolecules* **2010**, *43* (1), 271−281.

(15) Marsat, J.-N.; Heydenreich, M.; Kleinpeter, E.; Berlepsch, H. v.; Böttcher, C.; Laschewsky, A. Self-Assembly into Multicompartment Micelles and Selective Solubilization by Hydrophilic−Lipophilic−Fluorophilic Block Copolymers. *Macromolecules* **2011**, *44* (7), 2092−2105.

(16) Shi, P.; Li, Q.; He, X.; Li, S.; Sun, P.; Zhang, W. A New Strategy To Synthesize Temperature- and pH-Sensitive Multi-compartment Block Copolymer Nanoparticles by Two Macro-RAFT Agents Comediated Dispersion Polymerization. *Macromolecules* **2014**, *47* (21), 7442−7452.

(17) He, X.; Qu, Y.; Gao, C.; Zhang, W. Synthesis of Multi-compartment Nanoparticles of a Triblock Terpolymer by Seeded RAFT Polymerization. *Polym. Chem.* **2015**, *6* (35), 6386−6393.

(18) Deng, Z.; Liu, S. Emerging Trends in Solution Self-Assembly of Block Copolymers. *Polymer* **2020**, *207*, 122914.

(19) Xiao, J.; Du, J. Tetrapod Polymersomes. *J. Am. Chem. Soc.* **2020**, *142* (14), 6569−6577.

(20) Fan, B.; Yardley, R. E.; Trant, J. F.; Borecki, A.; Gillies, E. R. Tuning the Hydrophobic Cores of Self-Immolative Polyglyoxylate Assemblies. *Polym. Chem.* **2018**, *9* (19), 2601−2610.

(21) Fan, B.; Gillies, E. R. Poly(ethyl Glyoxylate)-Poly(ethylene Oxide) Nanoparticles: Stimuli-Responsive Drug Release *via* End-to-End Polyglyoxylate Depolymerization. *Mol. Pharmaceutics* **2017**, *14* (8), 2548−2559.

(22) Mai, Y.; Eisenberg, A. Self-Assembly of Block Copolymers. *Chem. Soc. Rev.* **2012**, *41* (18), 5969−5985.

(23) Gädt, T.; Ieong, N. S.; Cambridge, G.; Winnik, M. A.; Manners, I. Complex and Hierarchical Micelle Architectures from Diblock Copolymers Using Living, Crystallization-Driven Polymerizations. *Nat. Mater.* **2009**, *8* (2), 144−150.

(24) Tomalia, D. A.; Brothers, H. M.; Piehler, L. T.; Durst, H. D.; Swanson, D. R. Partial Shell-Filled Core-Shell Tecto(Dendrimers): A Strategy to Surface Differentiated Nano-Clefts and Cusps. *Proc. Natl. Acad. Sci. U. S. A.* **2002**, *99* (8), 5081−5087.

(25) Uppuluri, S.; Swanson, D. R.; Piehler, L. T.; Li, J.; Hagnauer, G. L.; Tomalia, D. A. Core−Shell Tecto(Dendrimers): I. Synthesis and Characterization of Saturated Shell Models. *Adv. Mater.* **2000**, *12* (11), 796−800.

(26) La, Y.; Park, C.; Shin, T. J.; Joo, S. H.; Kang, S.; Kim, K. T. Colloidal Inverse Bicontinuous Cubic Membranes of Block Copolymers with Tunable Surface Functional Groups. *Nat. Chem.* **2014**, *6* (6), 534−541.

(27) Lin, Z.; Zhou, J.; Cortez-Jugo, C.; Han, Y.; Ma, Y.; Pan, S.; Hanssen, E.; Richardson, J. J.; Caruso, F. Ordered Mesoporous Metal−Phenolic Network Particles. *J. Am. Chem. Soc.* **2020**, *142* (1), 335−341.

(28) Ha, S.; La, Y.; Kim, K. T. Polymer Cubosomes: Infinite Cubic Mazes and Possibilities. *Acc. Chem. Res.* **2020**, *53* (3), 620−631.

(29) Lyu, X.; Xiao, A.; Zhang, W.; Hou, P.; Gu, K.; Tang, Z.; Pan, H.; Wu, F.; Shen, Z.; Fan, X.-H. Head−Tail Asymmetry as the Determining Factor in the Formation of Polymer Cubosomes or Hexasomes in a Rod−Coil Amphiphilic Block Copolymer. *Angew. Chem., Int. Ed.* **2018**, *57* (32), 10132−10136.

(30) Lu, Y.; Lin, J.; Wang, L.; Zhang, L.; Cai, C. Self-Assembly of Copolymer Micelles: Higher-Level Assembly for Constructing Hierarchical Structure. *Chem. Rev.* **2020**, *120* (9), 4111−4140.

(31) Zhang, K.; Miao, H.; Chen, D. Water-Soluble Monodisperse Core−Shell Nanorings: Their Tailorable Preparation and Interactions with Oppositely Charged Spheres of a Similar Diameter. *J. Am. Chem. Soc.* **2014**, *136* (45), 15933−15941.

(32) Cheng, L.; Zhang, G.; Zhu, L.; Chen, D.; Jiang, M. Nanoscale Tubular and Sheetlike Superstructures from Hierarchical Self-Assembly of Polymeric Janus Particles. *Angew. Chem., Int. Ed.* **2008**, *47* (52), 10171−10174.

(33) Gröschel, A. H.; Walther, A.; Löbling, T. I.; Schacher, F. H.; Schmalz, H.; Müller, A. H. E. Guided Hierarchical Co-Assembly of Soft Patchy Nanoparticles. *Nature* **2013**, *503* (7475), 247−251.

(34) Gröschel, A. H.; Müller, A. H. E. Self-Assembly Concepts for Multicompartment Nanostructures. *Nanoscale* **2015**, *7* (28), 11841−11876.

(35) Löbling, T. I.; Borisov, O.; Haataja, J. S.; Ikkala, O.; Gröschel, A. H.; Müller, A. H. E. Rational Design of ABC Triblock Terpolymer Solution Nanostructures with Controlled Patch Morphology. *Nat. Commun.* **2016**, *7* (1), 12097.

(36) Rahman, M. A.; Cha, Y.; Yuan, L.; Pageni, P.; Zhu, T.; Jui, M. S.; Tang, C. Polymerization-Induced Self-Assembly of Metallo-Polyelectrolyte Block Copolymers. *J. Polym. Sci.* **2020**, *58* (1), 77−83.

(37) Fan, B.; Liu, Y.; Wan, J.; Crawford, S.; Thang, S. H. Polymerization-Induced Self-Assembly (PISA) and "Host−Guest" Complexation-Directed Polymer/Gold Nanocomposites. *ACS Mater. Lett.* **2020**, *2* (5), 492−498.

(38) Wan, J.; Fan, B.; Liu, Y.; Hsia, T.; Qin, K.; Junkers, T.; Teo, B. M.; Thang, S. H. Room Temperature Synthesis of Block Copolymer Nano-Objects with Different Morphologies *via* Ultrasound Initiated RAFT Polymerization-Induced Self-Assembly (sono-RAFT-PISA). *Polym. Chem.* **2020**, *11* (21), 3564−3572.

(39) Fan, B.; Wan, J.; Zhai, J.; Chen, X.; Thang, S. H. Triggered Degradable Colloidal Particles with Ordered Inverse Bicontinuous Cubic and Hexagonal Mesophases. *ACS Nano* **2021**, *15* (3), 4688−4698.

(40) Wan, J.; Fan, B.; Thang, S. H. Sonochemical Preparation of Polymer−Metal Nanocomposites with Catalytic and Plasmonic Properties. *Nanoscale Adv.* **2021**, *3* (11), 3306−3315.

(41) Liu, C.; Hong, C.-Y.; Pan, C.-Y. Polymerization Techniques in Polymerization-Induced Self-Assembly (PISA). *Polym. Chem.* **2020**, *11* (22), 3673−3689.

(42) Zhang, W.-J.; Hong, C.-Y.; Pan, C.-Y. Formation of Hexagonally Packed Hollow Hoops and Morphology Transition in RAFT Ethanol Dispersion Polymerization. *Macromol. Rapid Commun.* **2015**, *36* (15), 1428−1436.

(43) Dai, X.; Zhang, Y.; Yu, L.; Li, X.; Zhang, L.; Tan, J. Seeded Photoinitiated Polymerization-Induced Self-Assembly: Cylindrical Micelles with Patchy Structures Prepared *via* the Chain Extension of a Third Block. *ACS Macro Lett.* **2019**, *8* (8), 955−961.

(44) Huo, M.; Zeng, M.; Li, D.; Liu, L.; Wei, Y.; Yuan, J. Tailoring the Multicompartment Nanostructures of Fluoro-Containing ABC Triblock Terpolymer Assemblies *via* Polymerization-Induced Self-Assembly. *Macromolecules* **2017**, *50* (20), 8212−8220.

(45) Lv, F.; An, Z.; Wu, P. Scalable Preparation of Alternating Block Copolymer Particles with Inverse Bicontinuous Mesophases. *Nat. Commun.* **2019**, *10* (1), 1397.

(46) Xu, S.; Yeow, J.; Boyer, C. Exploiting Wavelength Orthogonality for Successive Photoinduced Polymerization-Induced Self-Assembly and Photo-Crosslinking. *ACS Macro Lett.* **2018**, *7* (11), 1376−1382.

(47) Charleux, B.; Delaittre, G.; Rieger, J.; D'Agosto, F. Polymerization-Induced Self-Assembly: From Soluble Macromolecules to Block Copolymer Nano-Objects in One Step. *Macromolecules* **2012**, *45* (17), 6753−6765.

(48) Shi, P.; Gao, C.; He, X.; Sun, P.; Zhang, W. Multicompartment Nanoparticles of Poly(4-Vinylpyridine) Graft Block Terpolymer:

Synthesis and Application as Scaffold for Efficient Au Nanocatalyst. *Macromolecules* **2015**, *48* (5), 1380−1389.

(49) Penfold, N. J. W.; Whatley, J. R.; Armes, S. P. Thermoreversible Block Copolymer Worm Gels Using Binary Mixtures of PEG Stabilizer Blocks. *Macromolecules* **2019**, *52* (4), 1653−1662.

(50) Chen, X.; Liu, L.; Huo, M.; Zeng, M.; Peng, L.; Feng, A.; Wang, X.; Yuan, J. Direct Synthesis of Polymer Nanotubes by Aqueous Dispersion Polymerization of a Cyclodextrin/Styrene Complex. *Angew. Chem., Int. Ed.* **2017**, *56* (52), 16541−16545.

(51) Warren, N. J.; Armes, S. P. Polymerization-Induced Self-Assembly of Block Copolymer Nano-Objects *via* RAFT Aqueous Dispersion Polymerization. *J. Am. Chem. Soc.* **2014**, *136* (29), 10174−10185.

(52) Li, D.; Chen, X.; Zeng, M.; Ji, J.; Wang, Y.; Yang, Z.; Yuan, J. Synthesis of ABₙ-Type Colloidal Molecules by Polymerization-Induced Particle-Assembly (PIPA). *Chem. Sci.* **2020**, *11* (10), 2855−2860.

(53) Chambon, P.; Blanazs, A.; Battaglia, G.; Armes, S. P. Facile Synthesis of Methacrylic ABC Triblock Copolymer Vesicles by RAFT Aqueous Dispersion Polymerization. *Macromolecules* **2012**, *45* (12), 5081−5090.

(54) Zhang, W.; D'Agosto, F.; Boyron, O.; Rieger, J.; Charleux, B. One-Pot Synthesis of Poly(methacrylic Acid-*Co*-Poly(ethylene Oxide) Methyl Ether Methacrylate)-*B*-Polystyrene Amphiphilic Block Copolymers and Their Self-Assemblies in Water *via* RAFT-Mediated Radical Emulsion Polymerization. A Kinetic Study. *Macromolecules* **2011**, *44* (19), 7584−7593.

(55) Gurnani, P.; Sanchez-Cano, C.; Abraham, K.; Xandri-Monje, H.; Cook, A. B.; Hartlieb, M.; Lévi, F.; Dallmann, R.; Perrier, S. RAFT Emulsion Polymerization as a Platform to Generate Well-Defined Biocompatible Latex Nanoparticles. *Macromol. Biosci.* **2018**, *18* (10), 1800213.

(56) Jeromin, J.; Ritter, H. Cyclodextrins in Polymer Synthesis: Free Radical Polymerisation of Cyclodextrin Complexes of Cyclohexyl and Phenyl Methacrylate in Aqueous Medium. *Macromol. Rapid Commun.* **1998**, *19* (7), 377−379.

(57) Cinar, H.; Kretschmann, O.; Ritter, H. Synthesis of Novel Fluorinated Polymers *via* Cyclodextrin Complexes in Aqueous Solution. *Macromolecules* **2005**, *38* (12), 5078−5082.

(58) Köllisch, H.; Barner-Kowollik, C.; Ritter, H. Living Free Radical Polymerization of Cyclodextrin Host-Guest Complexes of Styrene *via* the Reversible Addition Fragmentation Chain Transfer (RAFT) Process in Aqueous Solution. *Macromol. Rapid Commun.* **2006**, *27* (11), 848−853.

(59) Kretschmann, O.; Choi, S. W.; Miyauchi, M.; Tomatsu, I.; Harada, A.; Ritter, H. Switchable Hydrogels Obtained by Supramolecular Cross-Linking of Adamantyl-Containing LCST Copolymers with Cyclodextrin Dimers. *Angew. Chem., Int. Ed.* **2006**, *45* (26), 4361−4365.

(60) Kretschmann, O.; Steffens, C.; Ritter, H. Cyclodextrin Complexes of Polymers Bearing Adamantyl Groups: Host−Guest Interactions and the Effect of Spacers on Water Solubility. *Angew. Chem., Int. Ed.* **2007**, *46* (15), 2708−2711.

(61) Schmidt, B. V. K. J.; Hetzer, M.; Ritter, H.; Barner-Kowollik, C. Cyclodextrin-Complexed RAFT Agents for the Ambient Temperature Aqueous Living/Controlled Radical Polymerization of Acrylamido Monomers. *Macromolecules* **2011**, *44* (18), 7220−7232.

(62) Schmidt, B. V. K. J.; Hetzer, M.; Ritter, H.; Barner-Kowollik, C. Modulation of the Thermoresponsive Behavior of Poly(*N,N*-Diethylacrylamide) *via* Cyclodextrin Host/Guest Interactions. *Macromol. Rapid Commun.* **2013**, *34* (16), 1306−1311.

(63) Köllisch, H. S.; Barner-Kowollik, C.; Ritter, H. Amphiphilic Block Copolymers Based on Cyclodextrin Host−Guest Complexes *via* RAFT-Polymerization in Aqueous Solution. *Chem. Commun.* **2009**, *9*, 1097−1099.

(64) Penfold, N. J. W.; Yeow, J.; Boyer, C.; Armes, S. P. Emerging Trends in Polymerization-Induced Self-Assembly. *ACS Macro Lett.* **2019**, *8* (8), 1029−1054.

(65) Hirai, Y.; Wakiya, T.; Yabu, H. Virus-Like Particles Composed of Sphere-Forming Polystyrene-*Block*-Poly(*t*-Butyl Acrylate) (PS-*b*-P*t*BA) and Control of Surface Morphology by Homopolymer Blending. *Polym. Chem.* **2017**, *8* (11), 1754−1759.

(66) Yao, D.; Zhang, K.; Chen, Y. Microphase Separation of Poly(*tert*-Butyl Methacrylate)-*Block*-Polystyrene Diblock Copolymers to Form Perforated Lamellae. *Polymer* **2016**, *94*, 1−7.

(67) Madison, P. H.; Long, T. E. Carbohydrate/Monomer Complexes in Aqueous Polymerizations: Methylated-*β*-Cyclodextrin Mediated Aqueous Polymerization of Hydrophobic Methacrylic Monomers. *Biomacromolecules* **2000**, *1* (4), 615−621.

(68) Luo, Y.; Tsavalas, J.; Schork, F. J. Theoretical Aspects of Particle Swelling in Living Free Radical Miniemulsion Polymerization. *Macromolecules* **2001**, *34* (16), 5501−5507.

(69) Taura, D.; Taniguchi, Y.; Hashidzume, A.; Harada, A. Macromolecular Recognition of Cyclodextrin: Inversion of Selectivity of *β*-Cyclodextrin toward Adamantyl Groups Induced by Macromolecular Chains. *Macromol. Rapid Commun.* **2009**, *30* (20), 1741−1744.

(70) Fan, B.; Wan, J.; Liu, Y.; Tian, W. W.; Thang, S. H. Functionalization of Liquid Metal Nanoparticles *via* the RAFT Process. *Polym. Chem.* **2021**, *12* (20), 3015−3025.

(71) Fan, B.; Wan, J.; McKay, A.; Qu, Z.; Thang, S. H. Facile Synthesis of Well-Controlled Poly(1-Vinyl Imidazole) by the RAFT Process. *Polym. Chem.* **2020**, *11* (35), 5649−5658.

(72) Saeki, S.; Kuwahara, N.; Nakata, M.; Kaneko, M. Upper and Lower Critical Solution Temperatures in Poly(ethylene Glycol) Solutions. *Polymer* **1976**, *17* (8), 685−689.

(73) Warren, N. J.; Mykhaylyk, O. O.; Mahmood, D.; Ryan, A. J.; Armes, S. P. RAFT Aqueous Dispersion Polymerization Yields Poly(ethylene Glycol)-Based Diblock Copolymer Nano-Objects with Predictable Single Phase Morphologies. *J. Am. Chem. Soc.* **2014**, *136* (3), 1023−1033.

(74) Tan, J.; Zhang, X.; Liu, D.; Bai, Y.; Huang, C.; Li, X.; Zhang, L. Facile Preparation of CO₂-Responsive Polymer Nano-Objects *via* Aqueous Photoinitiated Polymerization-Induced Self-Assembly (Photo-PISA). *Macromol. Rapid Commun.* **2017**, *38* (13), 1600508.

(75) van Blaaderen, A. CHEMISTRY: Colloidal Molecules and Beyond. *Science* **2003**, *301* (5632), 470−471.

(76) Colorado, R.; Villazana, R. J.; Lee, T. R. Self-Assembled Monolayers on Gold Generated from Aliphatic Dithiocarboxylic Acids. *Langmuir* **1998**, *14* (22), 6337−6340.

(77) Fan, J. A.; Wu, C.; Bao, K.; Bao, J.; Bardhan, R.; Halas, N. J.; Manoharan, V. N.; Nordlander, P.; Shvets, G.; Capasso, F. Self-Assembled Plasmonic Nanoparticle Clusters. *Science* **2010**, *328* (5982), 1135−1138.

(78) Barrow, S. J.; Wei, X.; Baldauf, J. S.; Funston, A. M.; Mulvaney, P. The Surface Plasmon Modes of Self-Assembled Gold Nanocrystals. *Nat. Commun.* **2012**, *3* (1), 1275.

(79) Zhang; Keys, A. S.; Chen, T.; Glotzer, S. C. Self-Assembly of Patchy Particles into Diamond Structures through Molecular Mimicry. *Langmuir* **2005**, *21* (25), 11547−11551.

(80) Hosein, I. D.; Ghebrebrhan, M.; Joannopoulos, J. D.; Liddell, C. M. Dimer Shape Anisotropy: A Nonspherical Colloidal Approach to Omnidirectonal Photonic Band Gaps. *Langmuir* **2010**, *26* (3), 2151−2159.

(81) Sacanna, S.; Pine, D. J. Shape-Anisotropic Colloids: Building Blocks for Complex Assemblies. *Curr. Opin. Colloid Interface Sci.* **2011**, *16* (2), 96−105.

(82) Betley, T. A.; Banaszak Holl, M. M.; Orr, B. G.; Swanson, D. R.; Tomalia, D. A.; Baker, J. R. Tapping Mode Atomic Force Microscopy Investigation of Poly(amidoamine) Dendrimers: Effects of Substrate and pH on Dendrimer Deformation. *Langmuir* **2001**, *17* (9), 2768−2773.

(83) Schwarz, U.; Haefke, H.; Reimann, P.; Güntherodt, H. J. Tip Artefacts in Scanning Force Microscopy. *J. Microsc.* **1994**, *173* (3), 183−197.

(84) Gröschel, A. H.; Schacher, F. H.; Schmalz, H.; Borisov, O. V.; Zhulina, E. B.; Walther, A.; Müller, A. H. E. Precise Hierarchical Self-

Assembly of Multicompartment Micelles. *Nat. Commun.* **2012**, *3* (1), 710.

(85) Chiefari, J.; Jeffery, J.; Mayadunne, R. T.; Moad, G.; Rizzardo, E.; Thang, S. H. Chain Transfer to Polymer: A Convenient Route to Macromonomers. *Macromolecules* **1999**, *32*, 7700−7702.

(86) Zhou, J.; Zhang, W.; Hong, C.; Pan, C. Promotion of Morphology Transition of Di-Block Copolymer Nano-Objects *via* RAFT Dispersion Copolymerization. *Polym. Chem.* **2016**, *7* (19), 3259−3267.

(87) Figg, C. A.; Carmean, R. N.; Bentz, K. C.; Mukherjee, S.; Savin, D. A.; Sumerlin, B. S. Tuning Hydrophobicity to Program Block Copolymer Assemblies from the Inside Out. *Macromolecules* **2017**, *50* (3), 935−943.

(88) Yeow, J.; Chapman, R.; Xu, J.; Boyer, C. Oxygen Tolerant Photopolymerization for Ultralow Volumes. *Polym. Chem.* **2017**, *8* (34), 5012−5022.

(89) Wen, W.; Chen, A. Influence of Single Chain Nanoparticle Stabilizers on Polymerization Induced Hierarchical Self-Assembly. *Polym. Chem.* **2021**, *12* (18), 2743−2751.

(90) Barrientos, L.; Lang, E.; Zapata-Torres, G.; Celis-Barros, C.; Orellana, C.; Jara, P.; Yutronic, N. Structural Elucidation of Supramolecular Alpha-Cyclodextrin Dimer/Aliphatic Monofunctional Molecules Complexes. *J. Mol. Model.* **2013**, *19* (5), 2119−2126.

(91) Li, N.; Qi, L.; Qiao, J.; Chen, Y. Ratiometric Fluorescent Pattern for Sensing Proteins Using Aqueous Polymer-Pyrene/γ-Cyclodextrin Inclusion Complexes. *Anal. Chem.* **2016**, *88* (3), 1821−1826.